

1-1-2013

Ionization In Diesel Combustion For On-Board Diagnostics And Engine Control

Tamer Hassan Badawy
Wayne State University,

Follow this and additional works at: http://digitalcommons.wayne.edu/oa_dissertations

 Part of the [Oil, Gas, and Energy Commons](#), and the [Other Mechanical Engineering Commons](#)

Recommended Citation

Badawy, Tamer Hassan, "Ionization In Diesel Combustion For On-Board Diagnostics And Engine Control" (2013). *Wayne State University Dissertations*. Paper 634.

This Open Access Dissertation is brought to you for free and open access by DigitalCommons@WayneState. It has been accepted for inclusion in Wayne State University Dissertations by an authorized administrator of DigitalCommons@WayneState.

**IONIZATION IN DIESEL COMBUSTION FOR
ON-BOARD DIAGNOSTICS AND ENGINE CONTROL**

by

TAMER H. BADAWY

DISSERTATION

Submitted to the Graduate School

of Wayne State University,

Detroit, Michigan

in partial fulfillment of the requirements

for the degree of

DOCTOR OF PHILOSOPHY

2013

MAJOR: MECHANICAL ENGINEERING

Approved by:

Advisor

Date

© COPYRIGHT BY

TAMER H. BADAUY

2013

All Rights Reserved

ACKNOWLEDGEMENTS

I would like to express my deepest appreciation and sincere gratitude to my adviser Prof. Naeim A. Henein, who has given me the opportunity to be a part of his research team at Wayne State University. He continually and influentially guided me in all aspects of my research and given me extraordinary experiences throughout the work. His truly scientist intuition has exceptionally inspire and enrich my growth as a student, a researcher and a scientist want to be. I will be indebted to him for the rest of my life.

I thank Dr. Dinu Taraza and Dr. Marcis Jansons for their constant support and help. I also thank Dr. Fadi Estefanous for providing me help in modeling and simulation. I acknowledge help from Lidia Nedeltcheva for providing technical support, Eugene, Marvin and Dave for the machine shop support in machining components and tools for the engine.

I have been fortunate to work with many colleagues and friends that always helped me and supported me in particular Ashish Gupta, Nilesh Rai, Suman Gargo, Amit Shrestha, Sridhar Koushik, and Sanket Gujarathi. Finally, I would like to thank all members of Center for Automotive Research for their cooperation and support.

Tamer Badawy

Dec. 19th 2012, Detroit, Michigan

TABLE OF CONTENTS

Acknowledgements	iii
List of Figures	ix
List of Tables	xviii
CHAPTER 1 SCOPE OF THE WORK	1
1.1 Introduction	1
1.2 Thesis outline	2
CHAPTER 2 LITERATURE REVIEW	5
2.1 Introduction	5
2.2 Ionization in Spark ignition engines.....	5
2.3 Ionization in HCCI engines	7
2.4 Ionization in diesel engines	8
2.5 Correlations between the ion current and engine operating parameters	11
2.5.1 Intake temperature and equivalence ratio.....	11
2.5.2 In cylinder temperature and engine speed.....	12
2.5.3 Ignition delay vs. ion current delay	13
2.6 Ion current as a feedback signal for engine control.....	13
2.6.1 Closed-loop ignition control architecture.....	14
2.6.2 Peak pressure position (PPP) control	15
2.7 Conclusion.....	17
CHAPTER 3 ENGINE SETUP AND INSTRUMENTATIONS	18
3.1 Engine instrumentation	18

3.1.1	Engine setup	19
3.1.2	Ion current measuring circuit	20
3.1.3	Emission test bench.....	20
3.2	Engine control unit	22
CHAPTER 4 STUDY OF THE ION CURRENT FOR COMBUSTION CONTROL		
	24
4.1	Introduction	24
4.2	Ion current characteristics for feedback control	25
4.2.1	Cycle-to-cycle variations.....	27
4.2.2	Experimental results	28
4.3	Misdedetection of the ion current signal	36
4.4	Optical analysis of the ion current signal	38
4.4.1	Optical engine test at light load.....	42
4.4.2	Optical engine test at medium load.....	43
4.5	Summary	48
CHAPTER 5 CLOSE LOOP COMBUSTION CONTROL		50
5.1	Engine ECU.....	50
5.2	Algorithm for SIC detection.....	52
5.2.1	Results for SIC Detection.....	58
5.3	Combustion Phasing Control	60
5.3.1	Controller design	60
5.3.2	Steady state and transient operation logic	62

5.4	Experimental results	65
5.4.1	Operation under steady state conditions.....	66
5.4.2	Operation under transient conditions	68
5.4.3	Operation under low loads	71
5.4.4	Operation with one injector deactivated at low load.....	73
5.4.5	Operation under different fuels	75
5.5	Summary	79
CHAPTER 6 COMBUSTION RESONANCE IN DIESEL ENGINES.....		81
6.1	Experimental setup.....	81
6.2	Background and literature review	82
6.3	Signal processing.....	84
6.3.1	Analytical approach.....	84
6.3.2	Analysis of combustion resonance	86
6.3.3	Advanced combustion resonance interpretation	95
6.4	Summary	103
CHAPTER 7 ANALYSIS OF TIME-RESOLVED RESONANCE, COMBUSTION AND EMISSION PARAMETERS.....		104
7.1	Effect of injection pressure	105
7.2	Effect of EGR.....	109
7.3	Effect of pilot injection	112
7.3.1	Effect of pilot injection quantity at different engine loads at a constant SOPI timing of 25 ⁰ bTDC.....	113

7.3.2	Effect of pilot injection timing at different engine loads	129
7.4	Summary	139
CHAPTER 8 NO_x AND SOOT ESTIMATION MODELS.....		141
8.1	Introduction	142
8.2	Characteristics of the ion current signal in diesel engine.....	145
8.3	Basic concept of the soot and NO estimation.....	147
8.4	NIMR model.....	148
8.5	Results and discussion for the soot model	149
8.5.1	Sensitivity analysis for the ion current parameters	149
8.5.2	Ion current/ soot sensor	152
8.6	Results and discussion for the NO model	159
8.7	Summary	162
CHAPTER 9 3D CFD MODEL SIMULATION AND VALIDATION OF IONIZATION.....		163
9.1	Literature review	163
9.1.1	Ions formation in flames	164
9.1.2	Modeling ions formation in internal combustion engines.....	165
9.2	Simulation model and assumption	167
9.3	Ionization mechanism and ion current probe configuration.....	169
9.4	Effect of probe diameter and protrusion in the CFD results	171
9.5	Effect of probe location in the CFD results.....	174
9.6	Simulation results validation with experimental data	176

9.6.1	Effect of engine load	176
9.6.2	Effect of injection pressure	180
9.7	Swirl ratio effect on the ion current using CFD simulation	183
9.7.1	Correlation between the swirl ratio and the ion current signal	185
9.8	SIC and peak I_{\max} distribution inside the chamber.....	190
9.8.1	Swirl ratio.....	190
9.8.2	Engine load.....	198
9.8.3	Injection pressure	199
9.9	Summary	201
CHAPTER 10 CONCLUSIONS.....		203
References		207
Abstract.....		229
Autobiographical Statement		231

LIST OF FIGURES

Figure 2.1. Typical ion current signal in SI engine [Speed= 1300 RPM, torque= 22 Nm, $\lambda = 0.89$] (18)	6
Figure 2.2. Cylinder pressure, RHR and ion current traces in an HCCI engine (23)	8
Figure 2.3. Ion Current, burn rate and soot concentration traces in a diesel engine operating on split injection (10).....	9
Figure 2.4. Cylinder pressure, Temperature, RHR, N.L., and ion current traces in a diesel engine operating on single injection (29)	10
Figure 2.5. Peak chemi and thermal ion current at different intake temperatures and equivalence ratios (HCCI 0-D simulation, 1800 rpm) (30)	11
Figure 2.6. Trend for the peak cylinder mean temperature versus I_{max} (29).....	12
Figure 2.7. Ignition delay plotted (I.D) versus ion current delay(ICD) (29)	13
Figure 2.8. Control architecture for advance and retard limit control in an SI engine (32).....	15
Figure 2.9. Peak pressure position (PPP) control in 4 cylinders SI engine (39).....	16
Figure 3.1. Engine test cell	18
Figure 3.2. Layout of engine instrumentations	21
Figure 3.3. Ion current measuring circuit.....	22
Figure 3.4. Open ECU layout	23
Figure 4.1. Cylinder gas pressure, needle lift, RHR, ion current and the derivative of the ion current traces in a diesel engine [IMEP=8 bar, Const. Speed=1800RPM, SOI=10° bTDC, Inj. Pres=900bar].....	26
Figure 4.2. Boxplot for different ion current parameters [IMEP= 8 bar, Const. Speed=1800RPM, SOI=10° bTDC, Inj. Pres=900bar, # Cycles = 100].....	28

Figure 4.3. Sweep of loads and injection pressures [IMEP= 3.3 - 8 bar, Speed= 1800RPM, Inj. Pressure= 250 to 1100 bar, Const. SOI= 10°bTDC].....	29
Figure 4.4. Correlation between SIC and LPPC at sweep loads and injection pressures [IMEP= 3.3 - 8 bar, Speed= 1800RPM, Inj. Pres= 250 to 1100 bar, SOI= 10°bTDC].....	29
Figure 4.5. Histogram of LPPC-SIC [IMEP= 3.3 - 8 bar, Speed= 1800 RPM, Inj. Pres= 250 to 1100 bar, SOI= 10°bTDC].....	30
Figure 4.6. Sweep of loads and injection pressures [IMEP= 2.8 - 7.8 bar, Speed= 1800RPM, Inj. Pres= 600 bar, SOI= -29° to -4° bTDC]	32
Figure 4.7. Boxplot for SIC, LPPC, and LPP for different injection timing [IMEP= 4 bar, Const. Speed=1800RPM, SOI=10° bTDC, Inj. Pres=600bar, # Cycles = 100]	32
Figure 4.8. Correlation between SIC & LPPC at sweep loads [IMEP= 2.8 - 7.8 bar, Const. Speed = 1800RPM, Inj. Pres= 600 bar, SOI= -29° to -4° bTDC]	33
Figure 4.9. Histogram of LPPC - SIC [IMEP= 2.8 - 7.8 bar, Const. Speed = 1800RPM, Inj. Pres= 600 bar, SOI= -29° to -4° bTDC].....	33
Figure 4.10. Correlation between the SIC and LPPC (JD).....	35
Figure 4.11. Correlation between the SIC and LPPC standard deviations (JD).....	35
Figure 4.12. Cylinder gas pressure and ion current signals at light load condition of two arbitrary cycles [JD, IMEP=2.1 bar, Const. Speed=1800 RPM, Inj. Press =550 bar]	36
Figure 4.13. Percentage of ion current signal detection in 100 cycles at various engine loads	37
Figure 4.14. Cylinder gas pressure, ion current signal, RHR, and need lift signals [OPT, IMEP=3 bar, Const. Speed=1000RPM, SOI= 8° bTDC, Inj. Press =400 bar]	39
Figure 4.15. High speed images of the visible light from the combustion process [OPT, IMEP=3 bar, Const. Speed=1000RPM, SOI= 8° bTDC, Inj. Press=400 bar]	40
Figure 4.16. Correlation between the start of ion current (SIC) and timing of the maximum blue flame intensity (OPT, transient test) (42)	42

Figure 4.17. High speed images of the visible light produced from the combustion process (Light load: Detection of the ion current) [OPT, IMEP= 1 bar, Const. Speed=1000RPM, SOI= 8° bTDC, Inj. Press= 800 bar]	45
Figure 4.18. High speed images of the visible light produced from the combustion process (Light load: Misdetection of the ion current) [OPT, IMEP= 1 bar, Const. Speed=1000RPM, SOI= 8° bTDC, Inj. Press= 800 bar]	46
Figure 4.19. High speed images of the visible light produced from the combustion process (Medium load: Detection of the ion current) [OPT, IMEP= 3 bar, Const. Speed=1000RPM, SOI= 8° bTDC, Inj. Press= 800 bar]	47
Figure 5.1. Combustion phasing controller using the ion current as a feedback signal .	51
Figure 5.2. Signal processing for the ion current signal before applying SIC detection algorithm [JD, IMEP=5.5bar, Const. Speed=1800RPM, SOI=10° bTDC, Inj. Press=650 bar]	54
Figure 5.3. Derivative of the ion current signal of arbitrary cycles under steady state operation [JD, IMEP=5.5bar, Const. Speed=1800RPM, Inj. Press=1100 bar]	56
Figure 5.4. flow chart for "SIC detection" correction at idling and light engine loads ..	57
Figure 5.5. a- Calculated threshold for the detection of the ion current signal and b- the detected SIC [IMEP=5.5bar, Const. Speed=1800RPM, Inj. Pres=1100 bar, # Cycles = 100]	59
Figure 5.6. Block diagram for the fuzzy logic control system.....	60
Figure 5.7. Rule surface of the combustion phasing fuzzy control system	62
Figure 5.8. Block diagram for the fuzzy controller with scheduled gains	63
Figure 5.9. Performance of the fuzzy controller [JD, IMEP=7.5 bars, Const. Speed=1800RPM, SOI= Variable, Inj. Press=800bars]	65
Figure 5.10. Open loop with constant start of injection [JD, IMEP=6bar, Const. Speed=1800RPM, Inj. Press=800bar, # Cycles = 300]	66
Figure 5.11. Closed loop IFLC enabled [JD, IMEP=6bar, Const. Speed=1800RPM, Inj. Press=800bar, # Cycles = 300]	67

Figure 5.12. Response to desired changes in SIC in different steps between 0 and 10 CAD aTDC [JD, IMEP=6bar, Const. Speed=1800RPM, SOI=variable, Inj. Press=800bar]	68
Figure 5.13. Response to change of the injection pressure from 350 to 1200bar @Const. SIC 5° aTDC [JD, IMEP= 8bar, Const. Speed=1800RPM, SOI=Variable] 69	
Figure 5.14. Change engine speed from 1000 to 2000RPM @Const. SIC 5° aTDC [JD, IMEP= 2 - 7bar, SOI=Variable, Inj. Press=800bar]	70
Figure 5.15. Change desired SIC from 1 to 11° aTDC [IMEP= 2bar, Const. Speed=1800RPM, SOI=Variable]	72
Figure 5.16. Traces for ion current, LPPC, and engine speed, with one deactivated cylinder [Constant. SIC at 4° aTDC, IMEP= 2.5bar, Speed=1800RPM, SOI=Variable].....	74
Figure 5.17. Response to change of the supplied fuel using open loop and close loop controller [JD, Const. Speed=1500RPM]	77
Figure 5.18. Traces for needle lift, cylinder pressure, and ion current using USLD and transition to JP-8 under the command of the open loop controller [JD, Const. Speed=1500RPM, Inj. Press=600bar]	78
Figure 5.19. Traces for needle lift, cylinder pressure, and ion current using USLD and transition to JP-8 under the command of the close loop controller [JD, Const. Speed=1500RPM, Inj. Press=600bar]	78
Figure 6.1. Typical cylinder pressure trace, ion current and vibration signals, [JD, Cyl#1, ULSD, 0% EGR, 1800 RPM, LPPC 4° aTDC, Inj. Press. 800 bar, and IMEP 6 bar].....	86
Figure 6.2. FFTs analysis for the unfiltered signals for cylinder pressure, ion current and engine vibration	88
Figure 6.3. Filtered cylinder pressure, ion current and vibration signals using a band pass filter 3 to 9 kHz	89
Figure 6.4. (a) FFTs analysis for the filtered and unfiltered signals for cylinder pressure, ion current and engine vibration, (b) Power spectra of the filtered signals. 91	
Figure 6.5. STFTs analysis for the filtered signals, [JD, Cyl#1, ULSD, 0% EGR, 1800 RPM, LPPC 5° bTDC, Inj. Press: 800 bar, and IMEP: 6 bar].....	93
Figure 6.6. Combustion resonances 1 st mode determined from the ion current plotted versus resonance determined from the pressure and vibration signals	94

Figure 6.7.	CWT analysis for the band pass filtered signals, [JD, Cyl#1, ULSD, 0% EGR, 1800 RPM, LPPC 5° bTDC, Inj. Press: 800 bar, and IMEP: 6 bar] ..	96
Figure 6.8.	(a) cylinder pressure, RHR, ion current and needle lift signals, (b) cylinder pressure, ion current and vibration signals, and (c) their corresponding resonance [Cyl#1, ULSD, 0% EGR, 1800 RPM, LPPC 4° aTDC, Inj. Press. 900 bar, IMEP 6 bar, Single injection]	99
Figure 6.9.	(a) cylinder pressure, RHR, ion current and needle lift signals, (b) cylinder pressure, ion current and vibration signals, and (c) their corresponding resonance [Cyl#1, ULSD, 0% EGR, 1800 RPM, LPPC 4° aTDC, Inj. Press. 1200 bar, IMEP 6 bar, Pilot + Main injection]	102
Figure 7.1.	Effect of injection pressure on the combustion process [JD, ULSD, 0% EGR, 1800 RPM, LPPC 4° aTDC, and IMEP 6 bar]	106
Figure 7.2.	(a) Indicated and brake specific fuel consumption, NO emissions and Opacity percentage (b) peak pressure, peak of pressure rise and combustion resonance at different injection pressures	107
Figure 7.3.	Effect exhaust gas recirculation on the combustion process [JD, ULSD, 1800 RPM, LPPC 4° aTDC, inj. Press 1200 bar, and IMEP 6 bar].....	110
Figure 7.4.	(a) Indicated and brake specific fuel consumption, NO emissions and Opacity percentage (b) peak pressure, peak of pressure rise and combustion resonance at different rates of EGR	111
Figure 7.5.	(a) Indicated specific fuel consumption, NO emissions and Opacity percentage (b) peak pressure, peak of pressure rise and combustion resonance at different amounts of pilot injection [IMEP 4 bar]	114
Figure 7.6.	Different amounts of pilot injection at constant SOPI 25° bTDC [JD, ULSD, 1800 RPM, LPPC 4° aTDC, Inj. Press 1200 bar SOPI 25° bTDC, and IMEP 4 bar]	115
Figure 7.7.	Ion current delay versus different amounts of pilot injection at constant SOPI 25° bTDC [IMEP 4 bar].....	117
Figure 7.8.	(a) Indicated specific fuel consumption, NO emissions and Opacity percentage (b) peak pressure, peak of pressure rise and combustion resonance at different amounts of pilot injection [IMEP 6 bar]	120
Figure 7.9.	Different amounts of pilot injection at constant SOPI 25° bTDC [JD, ULSD, 1800 RPM, LPPC 4° aTDC, Inj. Press 1200 bar SOPI 25° bTDC, and IMEP 6 bar].....	121

Figure 7.10. Ion current delay versus different amounts of pilot injection at constant SOPI 25° bTDC [IMEP 6 bar].....	121
Figure 7.11. (a) Indicated specific fuel consumption, NO emissions and Opacity percentage (b) peak pressure, peak of pressure rise and combustion resonance at different amounts of pilot injection [IMEP 8 bar]	123
Figure 7.12. Different amounts of pilot injection at constant SOPI 25° bTDC [JD, ULSD, 1800 RPM, LPPC 4° aTDC, Inj. Press 1200 bar SOPI 25° bTDC, and IMEP 8 bar]	124
Figure 7.13. Ion current delay versus different amounts of pilot injection at constant SOPI 25° bTDC [IMEP 8 bar].....	125
Figure 7.14. (a) Indicated specific fuel consumption, NO emissions and Opacity percentage (b) peak pressure, peak of pressure rise and combustion resonance at different amounts of pilot injection [IMEP 12 bar]	126
Figure 7.15. Different amounts of pilot injection at constant SOPI 25° bTDC [JD, ULSD, 1800 RPM, LPPC 4° aTDC, Inj. Press 1200 bar SOPI 25° bTDC, and IMEP 12 bar]	127
Figure 7.16. Ion current delay versus different amounts of pilot injection at constant SOPI 25° bTDC [IMEP 12 bar].....	128
Figure 7.17. Combustion resonance at different SOPI [JD, ULSD, 1800 RPM, LPPC 4° aTDC ,inj. Press 1200 bar, and Pilot Q. 30% of the main inj.].....	132
Figure 7.18. Different timings of pilot injection with pilot quantity of 5.2 mg/cycle [JD, ULSD, 1800 RPM, LPPC 4° aTDC, ,inj. Press 1200 bar, various SOPI , and IMEP 4 bar].....	133
Figure 7.19. Different timings of pilot injection with pilot quantity of 10 mg/cycle [JD, ULSD, 1800 RPM, LPPC 4° aTDC, ,inj. Press 1200 bar, various SOPI , and IMEP 12 bar].....	134
Figure 7.20. Peak cylinder pressure at different SOPI [JD, ULSD, 1800 RPM, LPPC 4° aTDC,inj. Press 1200 bar, and Pilot Q. 30% of the main injection].....	135
Figure 7.21. NO emissions at different SOPI [JD, ULSD, 1800 RPM, LPPC 4° aTDC, ,inj. Press 1200 bar, and Pilot Q. 30% of the main injection].....	135
Figure 7.22. Soot percentage at different SOPI [JD, ULSD, 1800 RPM, LPPC 4° aTDC, ,inj. Press 1200 bar, and Pilot Q. 30% of the main injection].....	137

Figure 7.23. Brake specific fuel consumption at different start of pilot injection. [JD, ULSD, 1800 RPM, LPPC 4° aTDC, ,inj. Press 1200 bar, and Pilot Q. 30% of the main inj.].....	137
Figure 8.1. Cylinder gas pressure, needle lift, RHR, and ion current traces in a diesel engine [JD, IMEP=10 bar, Const. Speed=1800RPM, SOI=10° bTDC, Inj. Pres=600bar]	146
Figure 8.2. Engine Instrumentation for the ion current sensor, in-line opacity meter, and CLD.....	147
Figure 8.3. Layout of the NLMR model	148
Figure 8.4. Estimated versus measured soot percentage using different inputs to the NLMR model	152
Figure 8.5. Testing the NLMR model layout.....	153
Figure 8.6. Engine Load data [JD, Const. Speed=1800RPM, EGR= 0%]	154
Figure 8.7. Histogram for the residual error between estimated and measured soot percentage for engine Load data	155
Figure 8.8. Measured versus estimated soot percentage for engine Load data.....	155
Figure 8.9. Engine speed data [JD, EGR= 0%]	156
Figure 8.10. Histogram for the residual error between estimated and measured soot percentage for engine speed data	156
Figure 8.11. Measured versus estimated soot percentage for engine speed data.....	157
Figure 8.12. Engine speed data [JD, Speed=1800 rpm, Load=140 Nm , EGR= 0%]	158
Figure 8.13. Histogram for the residual error between estimated and measured soot percentage for MAP data	158
Figure 8.14. Measured versus estimated soot percentage for MAP data.....	159

Figure 8.15. Estimated versus measured NO concentration using different inputs to the NLMR model	160
Figure 8.16. Estimated and measured NO concentration under different operating conditions	161
Figure 9.1. Piston bowl profile used in the CFD simulation	167
Figure 9.2. Computational Sector mesh used in the engine simulation at TDC	168
Figure 9.3. Virtual probes defined in the CFD model	171
Figure 9.4. Different probe diameter CFD simulation [JD, 1800 RPM, LPPC 4° aTDC, ,inj. press 1200 bar, and IMEP 4 bar]	172
Figure 9.5. Different probe protrusion in the CFD simulation [JD, 1800 RPM, LPPC 4° aTDC, ,inj. press 1200 bar, and IMEP 4 bar]	173
Figure 9.6. Different probe location in the CFD simulation [JD, 1800 RPM, LPPC 4° aTDC, ,inj. press 1200 bar, and IMEP 4 bar]	174
Figure 9.7. Simulation at different loads [JD, 1800 RPM, LPPC 4° aTDC, and inj. press 1200 bar]	177
Figure 9.8. Simulated and experimental NO emissions at different loads [JD, 1800 RPM, LPPC 4° aTDC, and inj. press 1200 bar]	178
Figure 9.9. Simulated soot precursor and experimental opacity emissions at different loads [JD, 1800 RPM, LPPC 4° aTDC, and inj. press 1200 bar]	178
Figure 9.10. Simulation at different injection pressures [JD, 1800 RPM, LPPC 4° aTDC, and IMEP 6 bar]	181
Figure 9.11. Simulated and experimental NO emissions at different injection pressure [JD, 1800 RPM, LPPC 4° aTDC, and IMEP 6 bar]	182
Figure 9.12. Simulated soot precursor and experimental opacity emissions at different injection pressure [JD, 1800 RPM, LPPC 4° aTDC, and inj. IMEP 6 bar]	182
Figure 9.13. Simulation at different swirl ratios [JD, 1800 RPM, LPPC 4° aTDC, inj. press 1200 bar and IMEP 6 bar]	183
Figure 9.14. Schematic of fuel spray injected in a swirl air of a diesel engine (156).....	186

Figure 9.15. Correlation between difference in SIC of two probes and swirl ratio at different operating conditions	187
Figure 9.16. Electron concentration (Ion Current) and swirl ratio profile during a combustion cycle (SR = 3.72).....	189
Figure 9.17. Correlation between the rates of ion formation and dissociation and swirl ratio at different operating conditions.....	190
Figure 9.18. SIC and I_{\max} distribution inside the combustion chamber by multiple ion probes at different swirl ratios [inj. press 1200 bar, and IMEP 6 bar].....	194
Figure 9.19. SIC and I_{\max} distribution inside the combustion chamber by multiple ion probes at different engine loads [Inj. press 1200 bar].....	196
Figure 9.20. SIC and I_{\max} distribution inside the combustion chamber by multiple ion probes at different injection pressures [IMEP 6 bar]	197

LIST OF TABLES

Table 3.1.	Engine specifications and injection system configuration.....	19
Table 5.1.	Statistics for operation with constant start of injection.....	67
Table 5.2.	Closed loop IFLC enabled statistics	68
Table 6.1.	Vibration mode shapes for a cylindrical chamber and their corresponding resonance frequencies	85
Table 7.1.	Percentage increase or decrease of different combustion and emissions output at the minimum combustion resonance achieved by varying the quantity of pilot injection, SOPI at 25° bTDC and LPPC at 4° aTDC.....	129
Table 7.2.	Percentage increase or decrease of different combustion and emissions output at the minimum combustion resonance achieved by varying the timing of the pilot injection.....	139
Table 8.1.	Operation range for experimental tests used in the study.....	149
Table 8.2.	Results for MSE and R ² for the NLMR model using different combination of the ion current parameters.....	151
Table 9.1.	Simulation parameters setting.....	169

CHAPTER 1

SCOPE OF THE WORK

1.1 Introduction

Diesel engines have been known for their high thermal efficiency and specific power output, but there is concern about high levels of engine-out NO_x and particulate matter emissions. To meet the current emission standards, diesel engines are fitted with electronically controlled fuel injection systems and sophisticated, bulky and expensive after treatment devices. But, still there is demand for further improvements in fuel economy and meeting more stringent emission standards, while operating on diesel fuel that has narrow specifications. Another problem that need to be addressed by future diesel engines is related to the national concern about the increase in imported petroleum crude and the trade deficit. This would require future diesel engines to operate properly on alternate and renewable fuels that have different physical and chemical properties. To meet these demands there is a need for the control of the combustion process to reduce the engine out emissions while operating on different fuels. This requires a signal indicative of the in-cylinder conditions to be fed in the ECU (Engine Control Unit). The most promising sensors in internal combustion engines are the cylinder gas pressure transducer and the combustion produced ion current sensor. Ion current probes are less

expensive, more rugged, and are sensitive to the in cylinder gas temperature, and composition of the combustion products.

The ion current technique has been used in some SI engines, based on an understanding of the sources of ionization in a homogeneous charge burned by a propagating flame front. This is not the case in diesel engines where different types of flames are produced from the combustion of the heterogeneous charge developed from the fuel sprays which produce a heterogeneous charge.

This dissertation covers a detailed investigation of the characteristics of the ion current signal in diesel engines and its use for combustion diagnostics and feedback control of the engine. Experimental investigations and CFD simulation models are used to understand the characteristics of the ion current signal under different operating conditions. In addition, mathematical models are developed to monitor cylinder related combustion and emission parameters in real-time for the purpose of on-board diagnostics.

1.2 Thesis outline

This thesis is structured as follows: chapter 2 is literature reviews on the ions production in internal combustion engines and its applications for feedback control. It also covers review on the main characteristics of the ion current with respect to the combustion process. Engine instrumentation, data acquisition system, and emissions test bench used in this study are described in chapter 3.

The contributions of this thesis are covered in chapters 4 - 9. In Chapter 4, a detailed study that investigates the characteristics of the ion current signal under different operating conditions is conducted and correlations to combustion process are established for engine feedback control. An advanced fuzzy logic combustion controller is developed in chapter 5 that control the combustion phasing based on the feedback of the ion current signal. The performance of the controller was tested under different operating conditions as well as different fuels to maintain combustion phasing and engine power at the desired targets.

The combustion resonance is an important phenomenon in internal combustion engines as it is considered the main source of engine noise, vibration and harshness. In chapter 6 and 7, the ion current signal is analyzed for resonance detection, where it was benchmarked with the cylinder pressure transducer and accelerometer. Moreover, the ion current signal revealed more details of combustion resonance evolution during different stages of combustion which was not the case for the pressure transducer and the accelerometer. Further, combustion resonance produced from the ion current signal was studied under different pilot injection strategies at different engine loads; this study showed the possibility of using the ion current sensor for combustion resonance diagnostics and potential engine control to meet production targets with improvement in engine performance, fuel economy, and reducing engine out emissions.

A non-linear multiple regression model (NLMR) is developed in chapter 8 to estimate NO_x concentration in PPM and opacity percentage from the ion current signal. The ion current signal acquired in each cycle is analyzed, and a number of parameters are

extracted and used as inputs to the NLMR model. Further, a sensitivity analysis for these parameters is evaluated to optimize the estimation accuracy. The NLMR model is tested and results show that the ion current signal can effectively be used to estimate NO_x and soot percentage produced in diesel engines.

In order to understand ionization produced in diesel combustion, a 3D CFD model is developed in chapter 9 using commercial computational fluid dynamics software. The CFD cycle simulation is coupled with a chemical kinetic solver (DARS-CFD) to compute the chemical reactions taking place inside the combustion. A validation of the model is verified by experimental data. A local virtual probe is defined to simulate the real ion current probe installed in the combustion chamber. The analysis of the CFD results gives explanations for the local ions production under different operating conditions. Also, an attempt to correlate ion current parameters to combustion parameters such as swirl ratio is explored using different approaches and validated under different engine loads and injection pressures. Finally, chapter 10 covers an overall summary and conclusions for all the dissertation findings.

CHAPTER 2

LITERATURE REVIEW

2.1 Introduction

Spark ignition and compression ignition engines are required to meet stringent emission standards, without penalty in performance and fuel economy. Moreover, the concern about global warming is adding another demand on engine manufacturers to reduce carbon dioxide emissions. To meet these demands, close loop in-cylinder combustion control strategies are needed. Many sensing techniques have been used to produce signals indicative of the combustion process in both engines. These techniques include the use of pressure sensors (1-3), glow plugs modified to measure cylinder gas pressure (4; 5), optical sensors (6-8) and ion current sensors (9-11). In this chapter a review that covers the characteristics of the ion current and prior research that implemented the signal for feedback control.

2.2 Ionization in Spark ignition engines

The ion current in hydrocarbon flames are considered to form from a chemi and a thermal ionization processes (9; 12-15). The ions produced through the chemi and thermal-ionization dependent on the air-fuel ratio of the charge mixture and the in-cylinder combustion temperature (9; 16). SI engines operate on a homogeneous mixture

close to the stoichiometric air-fuel ratio. As a result, the production of ions through chemi-ionization is high as flame front propagates inside the combustion chamber. Also, a high ion current is produced in the post flame zone due to thermal-ionization. Figure 2.1 shows a typical ion current signal measured by using the spark plug as an ion current sensor and the corresponding cylinder gas pressure. The ion current signal shows a spike that occurs at 26° bTDC which indicates the ignition discharging phase. This is immediately followed by the first peak of the ion current at 14° bTDC. The second ion current peak coincides with the cylinder gas peak pressure at 12° aTDC. The two peaks have been reported in many investigations. In some cases, the two peaks merge into one peak due to several factors such as sensor configuration (17; 18), lean burn of natural gas (19) and high rates of EGR in two stroke engines (20; 21).

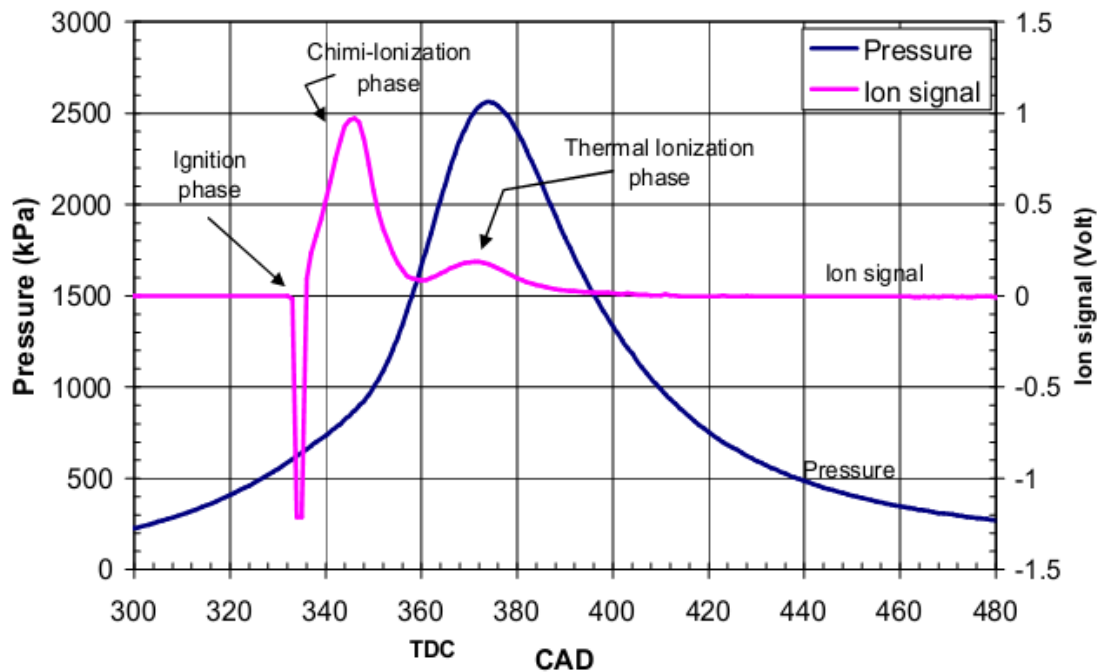


Figure 2.1. Typical ion current signal in SI engine [Speed= 1300 RPM, torque= 22 Nm, $\lambda = 0.89$] (18)

2.3 Ionization in HCCI engines

The ion current formation in HCCI engines is the result of combustion of a premixed charge similar to the charge in SI engine, but the equivalence ratio in HCCI is limited to much lower values of about 0.45 to avoid the high rates of pressure rise and peak pressures that could be reached after auto-ignition and volumetric combustion of most of the charge (22). In spark ignition engines the first peak of the ion current signal is caused by chemi ionization in the flame front and reaches high values compared to HCCI. Figure 2.2 shows ion current, measured by using the spark plug as an ion current sensor, cylinder pressure and RHR in an HCCI engine at $\phi = 0.35$ and an inlet air temperature of 176°C (23). The ion current starts to rise at a very high rate and reaches a peak at 17° aTDC after which it drops during the expansion stroke. As shown in Figure, the ion current has single peak and reaches lower values compared to SI engines because of the lower temperatures reached from the combustion of a lean mixture (11; 12; 23; 24). However, it carries valuable information that can be utilized for feedback control of HCCI combustion (25).

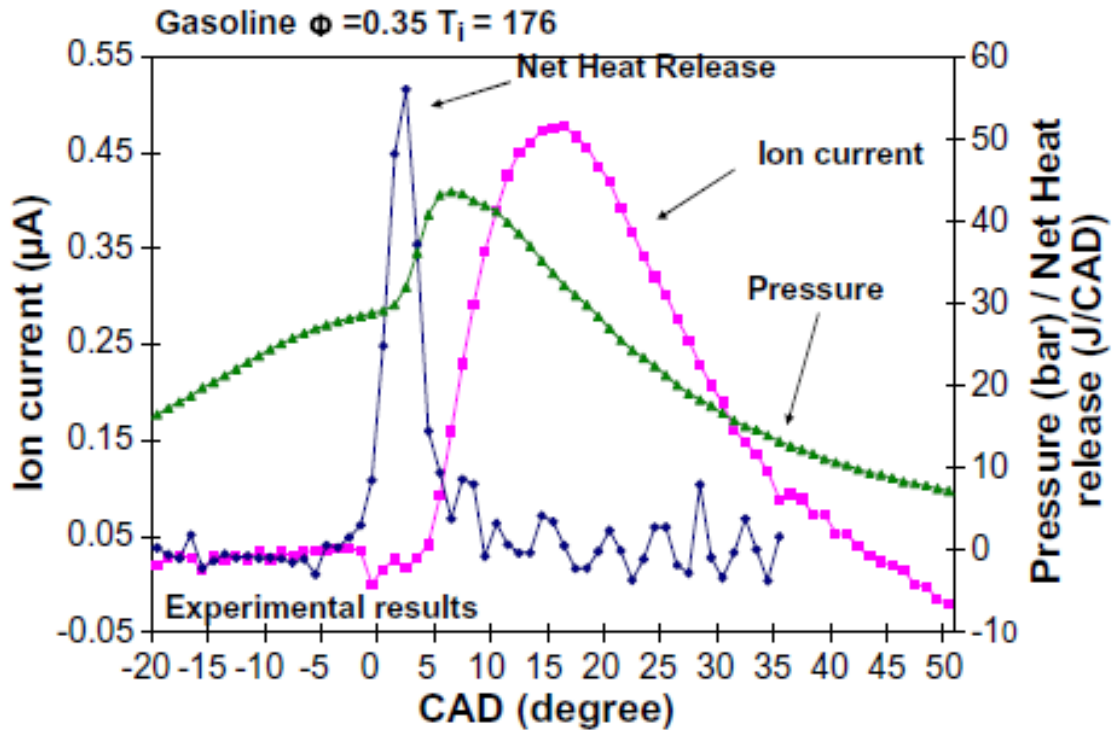


Figure 2.2. Cylinder pressure, RHR and ion current traces in an HCCI engine (23)

2.4 Ionization in diesel engines

Unlike HCCI and gasoline engines, ionization in diesel engines is the result of a complex combustion process of a heterogeneous charge. The ion current signal in diesel engines depicts one, two or more peaks (9; 26). Glavmo et al. were the first to modify a glow plug to measure the ion current produced during combustion and to use it as a feedback signal to control the start of combustion in diesel engines (27). The ion current in diesel engine has been studied using an optically accessible engine by Keßler (28),

where a comparison is made between the ion current signal, OH Luminance and soot under different engine conditions.

Kubach et al. investigated the effect of the probe design and its location in the combustion chamber on the ion current produced in a diesel engine using pilot injection (10) in a attempt to understand the source of ionization at different stages of combustion. Figure 2.3 shows the ion current signal produced from a split injection strategy, and its corresponding burn rate and soot concentration.

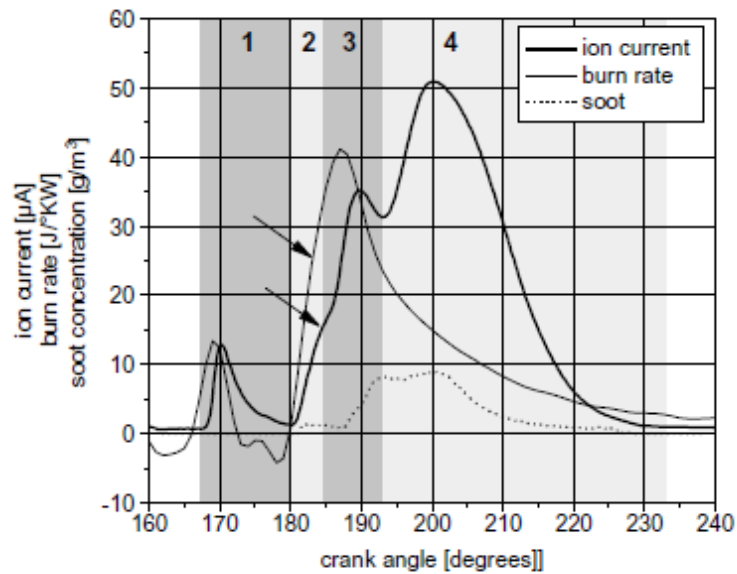


Figure 2.3. Ion Current, burn rate and soot concentration traces in a diesel engine operating on split injection (10)

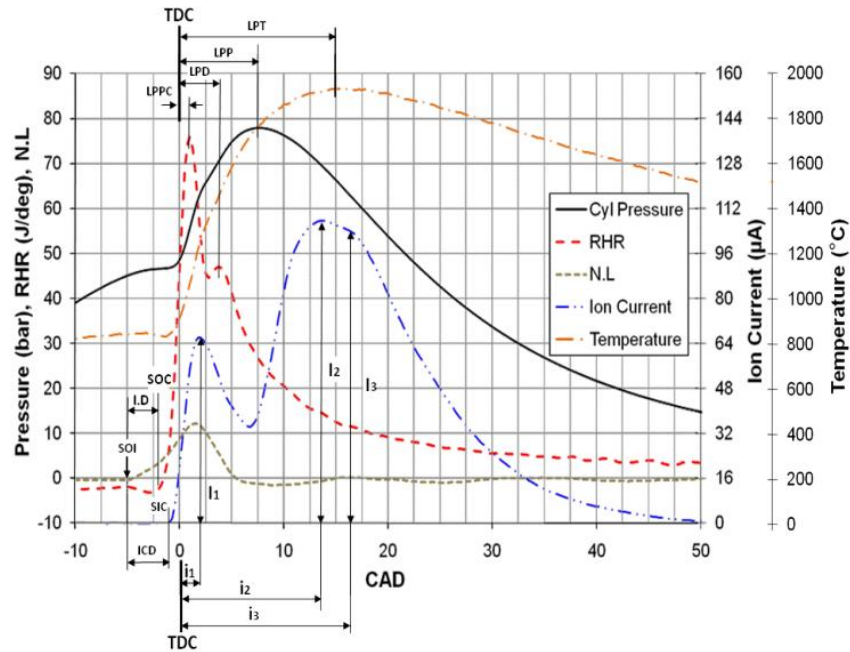


Figure 2.4. Cylinder pressure, Temperature, RHR, N.L., and ion current traces in a diesel engine operating on single injection (29)

Figure 2.4 shows a typical ion current signal in a diesel engine operating on single injection (29). The first peak of the ion current signal I_1 occurs just after the peak of the rate of heat release due to the premixed combustion. The second peak I_2 occurs in the region of the maximum temperature inside the cylinder. A third peak I_3 appears after the second peak later during the expansion stroke. I_3 was reported to be the result of the flame bouncing back from the piston bowl toward the ion sensor probe (9; 10; 28). The 3rd peak I_3 can clearly be identified at high loads in the presence of flames characterized by soot formation and oxidation.

2.5 Correlations between the ion current and engine operating parameters

2.5.1 Intake temperature and equivalence ratio

Figure 2.5 is a plot of the peaks of the chemi-ions and thermal-ions versus equivalence ratio at different inlet temperatures obtained from Chemkin-Pro simulation of HCCI engine operation (30). The engine configuration used in simulation has a bore of 79.5mm, stroke of 95.5mm and compression ratio of 19:1. The chemi-ionization at any equivalence ratio is the main source of the ion current in a homogenous mixture, and probably so in the premixed combustion fraction in diesel engines. The peak of the thermal ionization is around the stoichiometric ratio between $\phi = 0.7$ and $\phi = 0.12$ and the peak of the chemi-ions is on the rich side between $\phi = 1.1$ and $\phi = 1.4$.

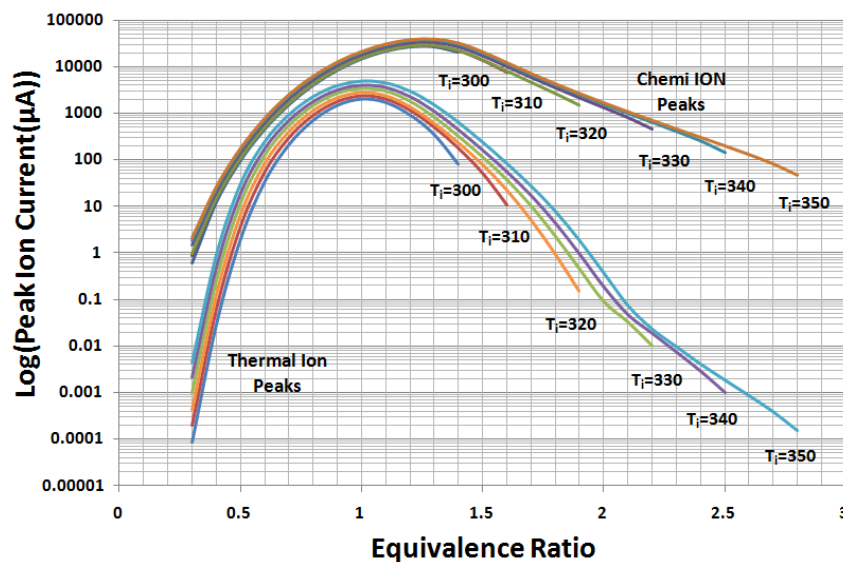


Figure 2.5. Peak chemi and thermal ion current at different intake temperatures and equivalence ratios (HCCI 0-D simulation, 1800 rpm) (30)

2.5.2 In cylinder temperature and engine speed

Figure 2.6 shows the highest amplitude of the ion current signal I_{\max} plotted versus the peak cylinder temperature in (K) at three different speeds in a diesel engine (29). The engine used in the experimental tests is a single cylinder 0.67L Hatz. The engine has 100 mm bore, 85 mm stroke and 20.5:1 compression ratio. The plot shown in Figure 2.6 covers a wide range of engine operation (IMEP from 2.5 to 7.5 bar and injection pressure from 300 to 900 bar). It is noticed that at different engine speeds, I_{\max} increased exponentially with the mass average cylinder gas temperature and correlation coefficient R^2 higher than 0.90. The ion current produced at higher speeds has lower amplitude at higher temperatures because the formation rate is reduced due to the reduction in residence time for the ionization process at that temperature.

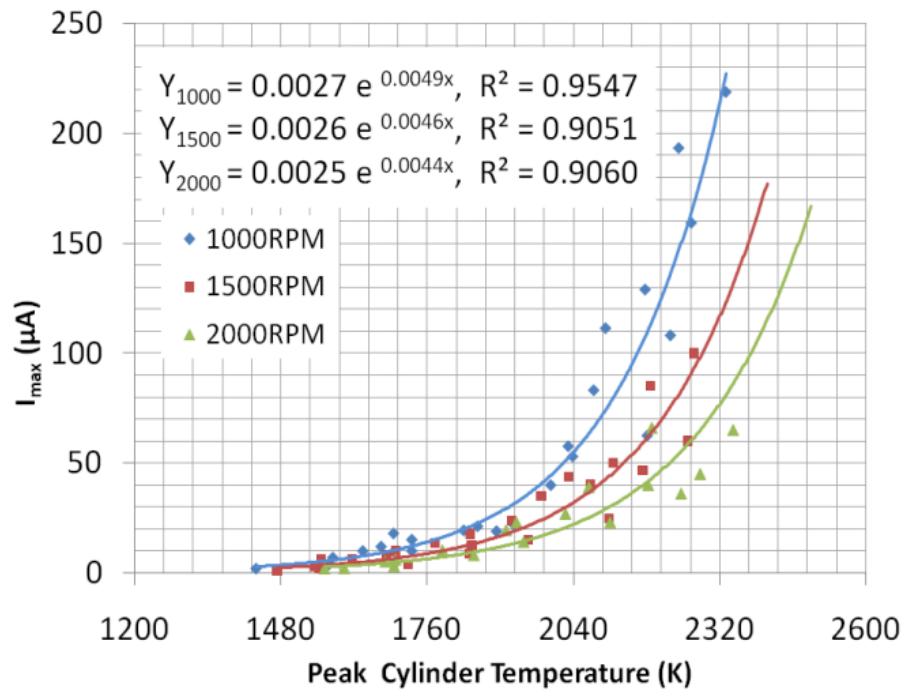


Figure 2.6. Trend for the peak cylinder mean temperature versus I_{\max} (29)

2.5.3 Ignition delay vs. ion current delay

In Figure 2.7, the ignition delay (I.D) is plotted versus the ion current delay (ICD) (29). A linear trend was established between I.D and ICD with correlation coefficient $R^2=0.988$. It is observed that the delay increases at higher engine speeds.

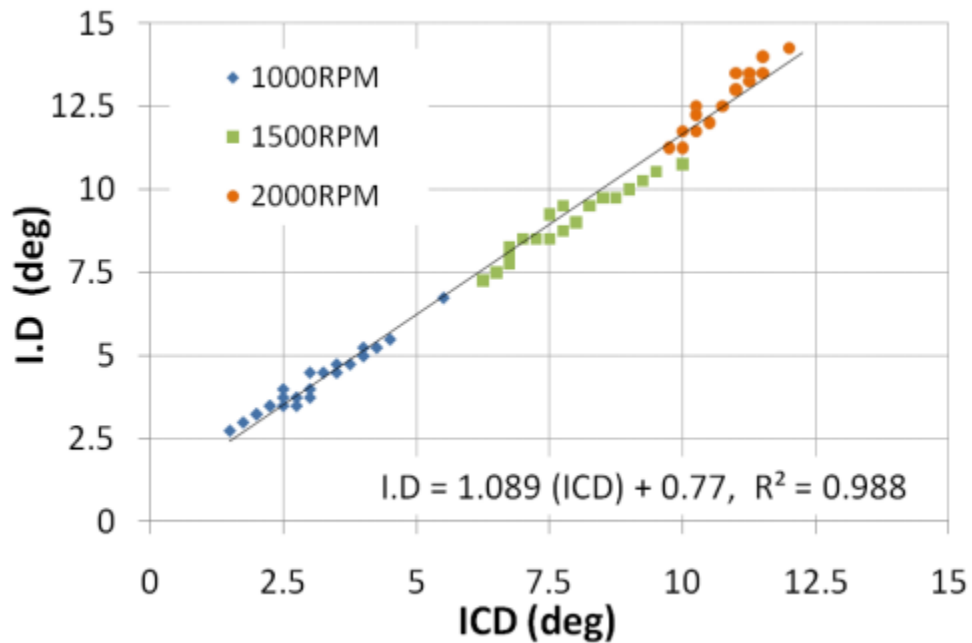


Figure 2.7. Ignition delay plotted (I.D) versus ion current delay(ICD) (29)

2.6 Ion current as a feedback signal for engine control

The ion current signal has been used as feedback for close loop engine control in SI and HCCI engines. In SI engines, the ion current signal was effectively used to control location of peak pressure for mean brake torque (MBT) (31; 32), ignition timing for knock limit (33), optimize engine stability (34), control of EGR percentage (31; 35), and

misfire control (36). In HCCI engine, the use of ion current was focused on controlling combustion timing and peak pressure for stable engine operation (37; 38). Two successful cases from literature for close loop control using ion current feedback are illustrated.

2.6.1 Closed-loop ignition control architecture

Figure 2.8 shows a closed-loop ignition control implemented in an SI engine (32) that utilize the ion current feedback to adjust the spark timing to achieve engine MBT and avoid knock occurrence. The control architecture includes a closed-loop MBT timing control, borderline knock limit control, and retard limit control. This allows the engine to operate at its true MBT timing when it is not limited by borderline knock limit and operate at its borderline knock limit when it is knock limited. The ionization signals is utilized as feedback to a closed loop stochastic limit controller to regulate both borderline knock and retard spark limits, where MBT timing is controlled using an MBT criterion derived from in-cylinder ionization signals.

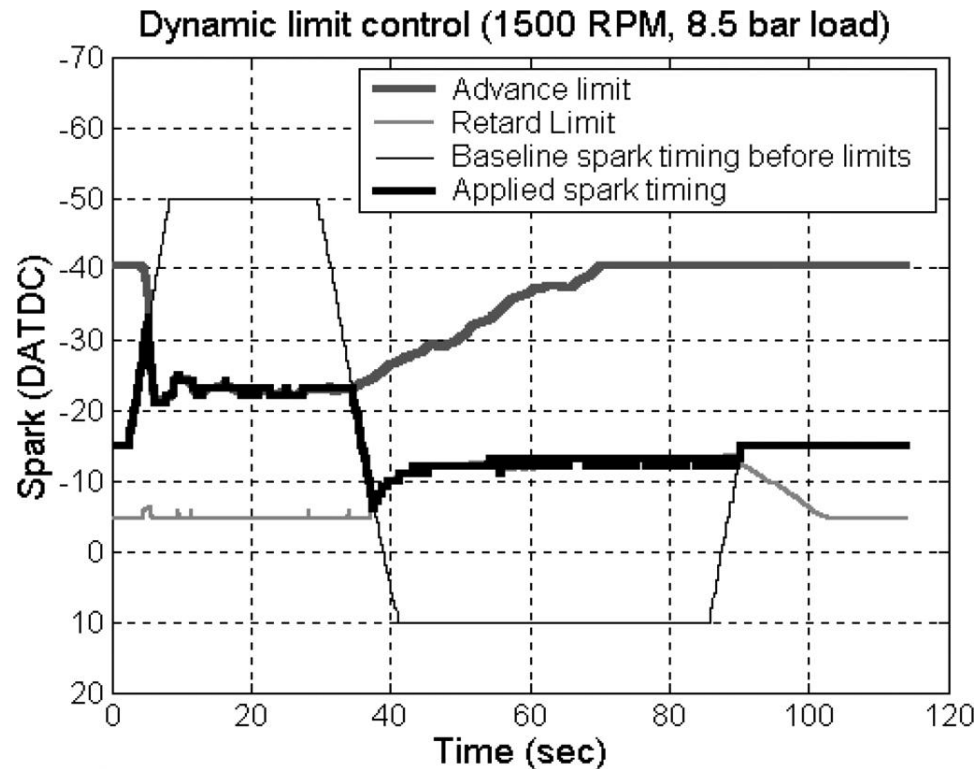


Figure 2.8. Control architecture for advance and retard limit control in an SI engine (32)

2.6.2 Peak pressure position (PPP) control

Figure 2.9 shows a closed-loop feedback control of PPP that uses the feedback from the ion current (39). PPP is estimated on each cylinder using the ion current signal using a NARX neural networks which are trained in steady state transient ranges. The results shows that by subjecting an appropriate PPP demand signal, MBT can thereby be achieved on each cylinder independently through the feedback scheme. The success in applying this technique is very dependent on the appropriate test signals and neural

network training. The limitation of this technique is that it is only reliable within the boundaries of the identification test data used in the training.

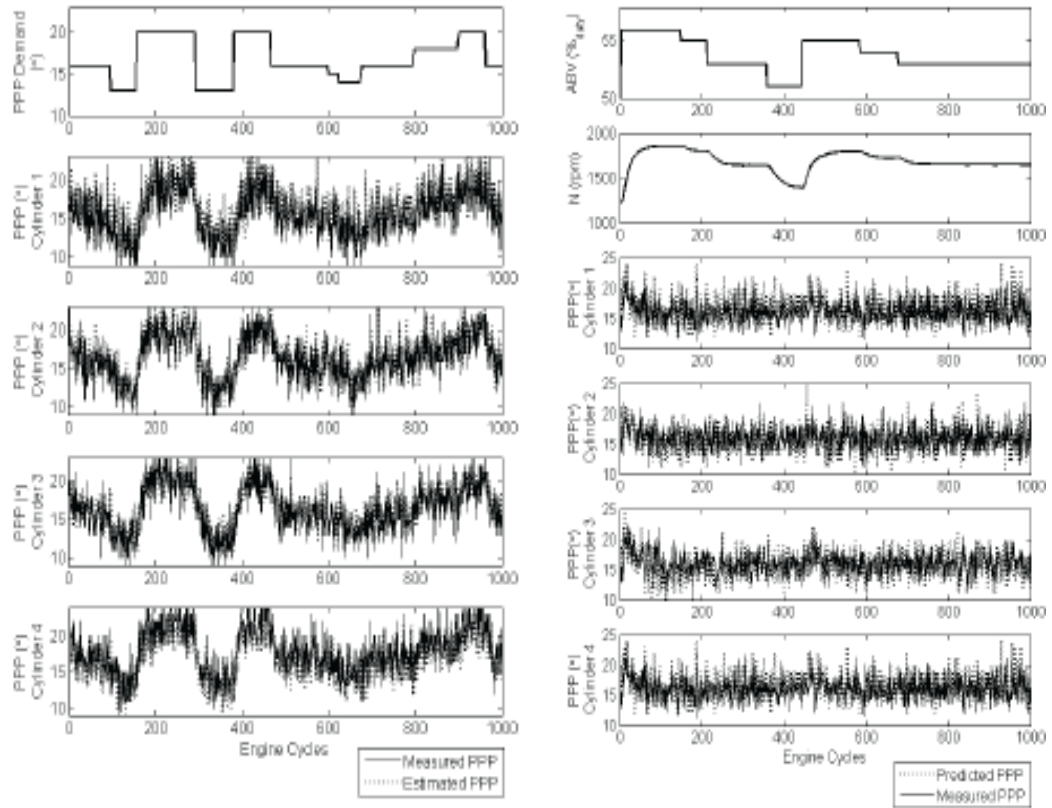


Figure 2.9. Peak pressure position (PPP) control in 4 cylinders SI engine (39)

2.7 Conclusion

The literature review on the ion current signal shows the potential of using the signal for feedback control. Most of the research work has been conducted on spark ignition and HCCI engines. Limited number of publications dealt with the ion current in diesel engine. This mainly due to the complexity of the heterogeneous combustion produced, the irreproducibility of the signal, and the cycle to cycle variations.

The ion current signal showed a very strong dependency on the cylinder gas temperature confirmed by simulation and experimental results. Although the second peak of the ion current correlates with the peak pressure in SI and HCCI engines, the correlation is not valid in case of diesel engines. But ignition delay shows a strong correlation with the ion current delay under all operating conditions.

More analysis of the ion current signal in diesel engine is need to understand its characteristics under different operating conditions for possible implementation in close loop engine control.

CHAPTER 3

ENGINE SETUP AND INSTRUMENTATIONS

John Deere 4.5 L turbo charged heavy duty diesel engine was used in this study; the engine has high pressure common rail (HPCR) injection system, solenoid injectors, variable geometry turbocharger, and exhaust gas circulation valve (EGR). A GO-POWER hydraulic dynamometer was coupled to the engine flywheel by a flexible coupling to apply load on the engine. Engine specifications are shown in Table 3.1. The solenoid injector having 6 hole nozzle with 60° equally spaced spray angle. The engine test cell and instrumentation are shown in Figure 3.1.

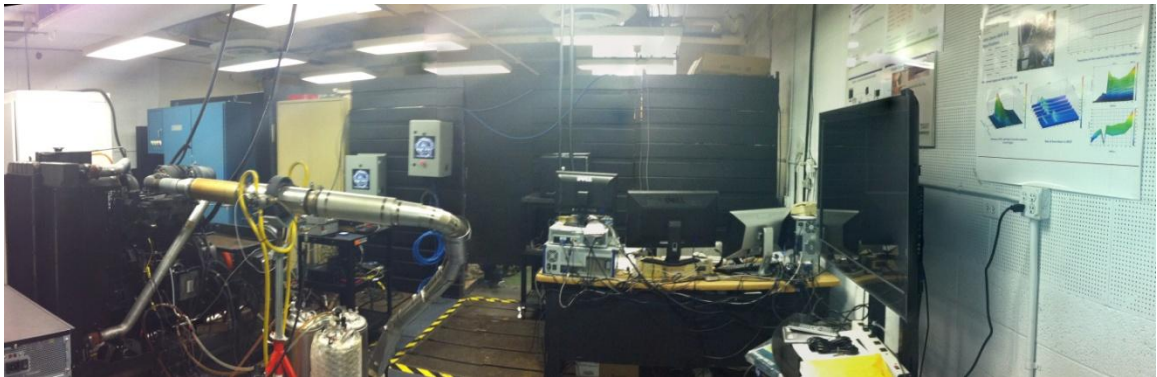


Figure 3.1. Engine test cell

3.1 Engine instrumentation

A brief description for engine setup and instrumentation is given in this section and a layout of various instruments and measuring equipment is shown in Figure 3.2.

Detailed description of each sensor, measuring equipments, DAQ systems, and emissions test benches can be found in Ref. (40).

Table 3.1. Engine specifications and injection system configuration

Model	4045HF485
Aspiration	Turbocharger
No. of Cylinder	4
Displacement (L)	4.5
Bore x Stroke (mm)	106 x 127
Compression Ratio	17.0 : 1
Con-Rod (mm)	203
Engine Type	4 stroke
Max. Power (kW)	147
Injection System	HCPR

3.1.1 Engine setup

The engine has been instrumented to monitor different engine parameters as shown in Figure 3.2. The cylinder head is instrumented with a Kistler pressure transducer to detect the gas pressure developed inside the combustion chamber of cylinder # 1. The high fuel pressure in the common rail system has been monitored using a Kistler piezo-resistive sensor, where the sensor was mounted as near as possible to injector #1 to observe closely the change in pressure during engine cycle.

An intake manifold pressure transducer was used to monitor the intake air pressure to provide pegging to the in cylinder pressure trace due engine boosting by VGT. A load cell is installed between the engine shaft and the hydraulic dynamometer which provides the instantaneous load developed by the engine. A fuel measuring system based on Coriolis mass flow meter was used to measure the fuel mass flow rate. The

injector of cylinder #1 was instrumented with a needle lift sensor to detect the needle lift during different injection strategies. A optical encoder is installed on the crank shaft to measure the instantaneous crank angle position and speed, where the encoder resolution was 0.25 CAD. Several high speed and low speed response thermocouples are installed in the engine to monitor change in temperature including intake, exhaust, cooling water, oil sump, and test cell. Dewe-800 combustion analyzer was used to recorded varies signals based on the crank angle degree; the system is capable of recording 16 channels at a rate of 1MS/sec per channel simultaneously, where many engine parameters are displayed continuously online.

3.1.2 Ion current measuring circuit

The ion current sensor used in this study is a modified glow plug. The glow plug heater is insulated from the engine ground to form one electrode, and the cylinder head acts as the other electrode. The ion current circuit is shown in Figure 3.3. The ion current circuit is coupled with a switching circuit to heat up the glow plug when required. The ion current signal produced during combustion passes through a 50 ohm resistor; the voltage across the resistor is amplified and recorded by the DAQ system.

3.1.3 Emission test bench

A fast CLD was used to measure nitric oxide in exhaust port. Also, a fast NDIR was used to measure CO and CO₂ in intake and exhaust port. An Opacity meter was installed on the tailpipe to measure the soot percentage in the exhaust gases. Description of each system in details is in Ref. (40).

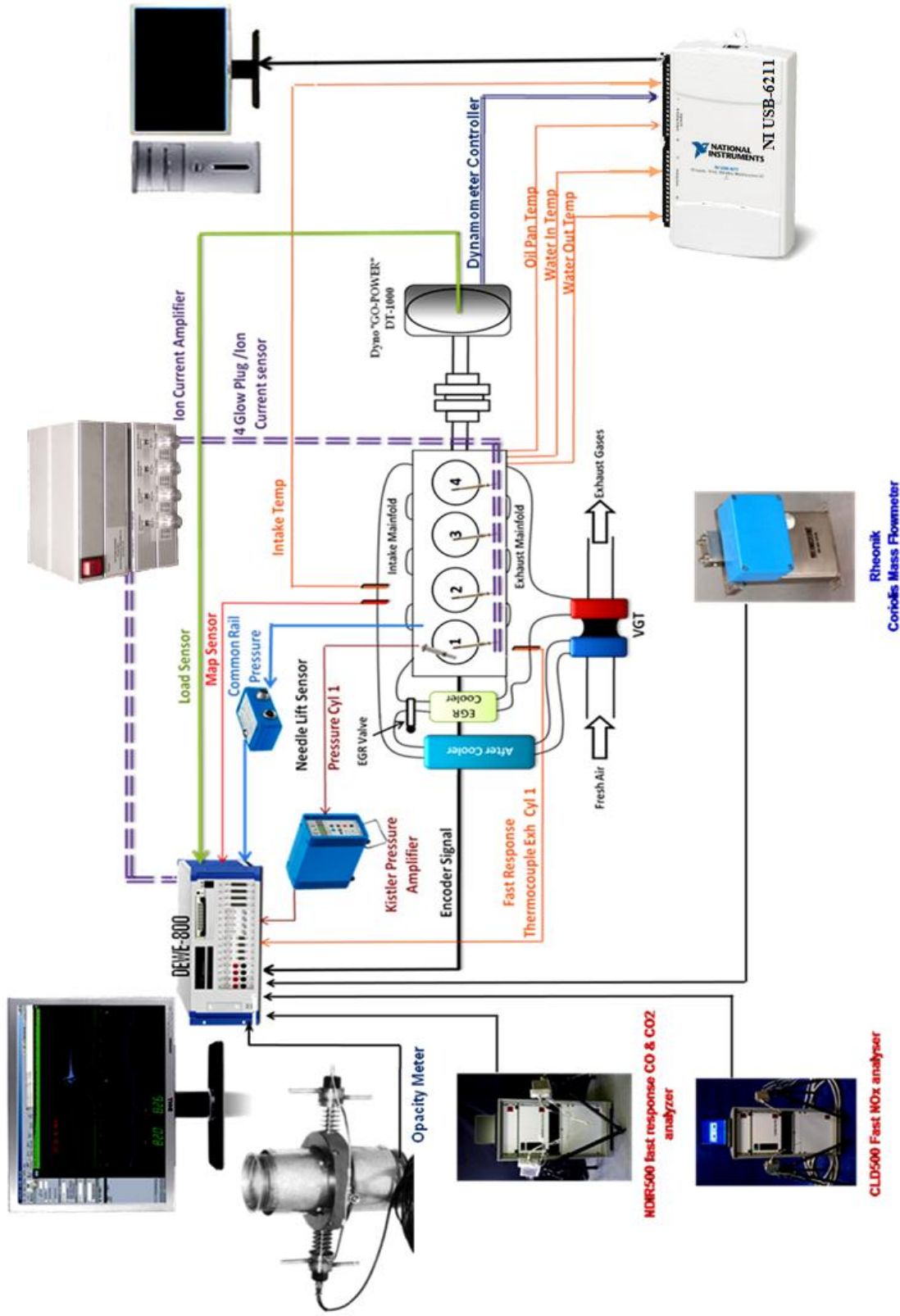


Figure 3.2. Layout of engine instrumentations

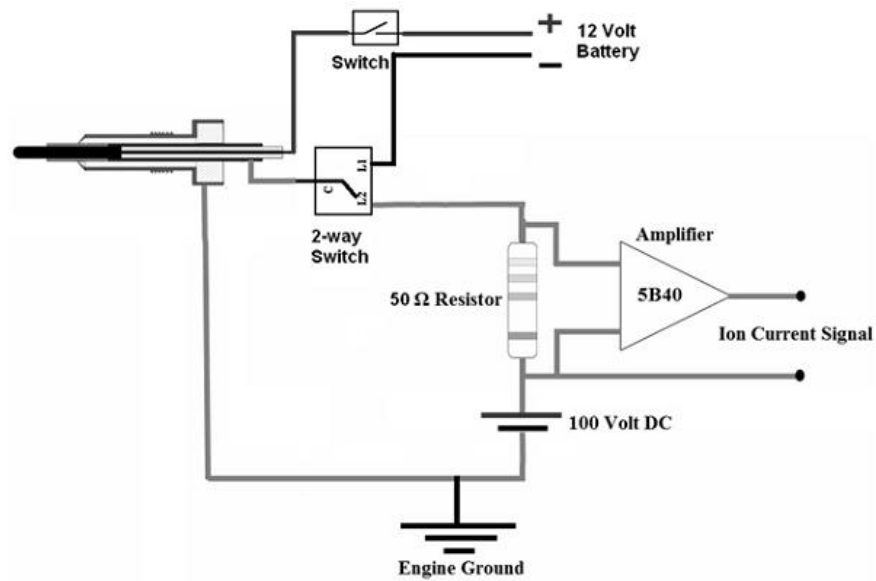


Figure 3.3. Ion current measuring circuit

3.2 Engine control unit

The engine has been instrumented with real-time high-speed measurement and control unit (AD5435), the system was provided from A&D technology Inc. for the aim of full bypass the original ECU. The open ECU runs under a real-time performance through the medium of MATLAB/Simulink control models and the GUI generating and experimentation support tool. Figure 3.4 shows a layout of the open ECU and various sensors and actuators in communication with the ECU. Further, Labview software and NI USB-6259 data acquisition system are used to analyze the in-cylinder combustion signal and send a feedback to the open ECU for the close loop combustion control.

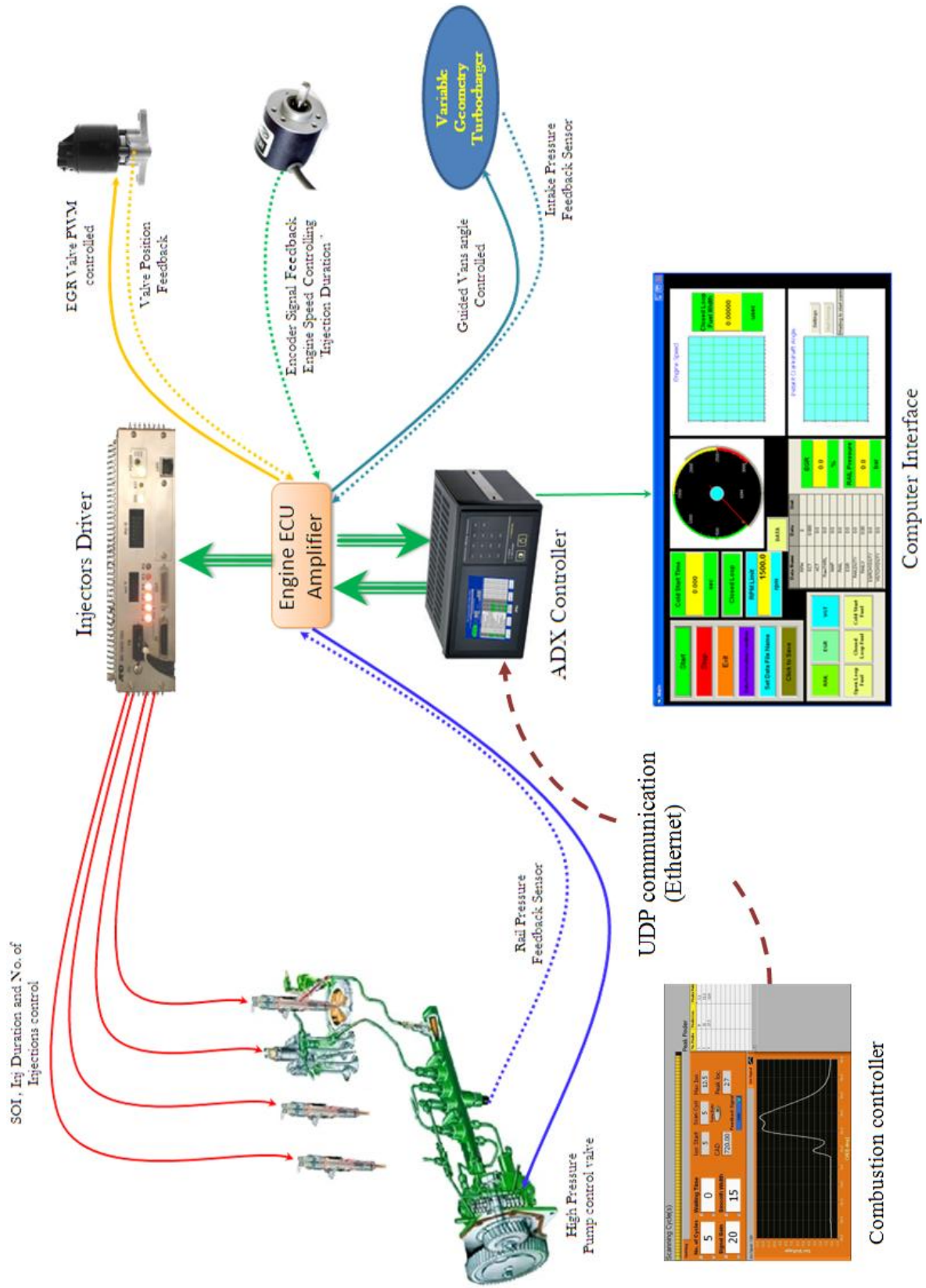


Figure 3.4. Open ECU layout

CHAPTER 4

STUDY OF THE ION CURRENT FOR COMBUSTION CONTROL

This chapter covers a broad analysis of the ion current signal in diesel engines with the purpose of using the signal for feedback close loop engine control. The characteristics and the parameters of the ion current are investigated under steady state and transient operating conditions. Also, the cycle-to-cycle variations of a number of ion current parameters are examined under steady state conditions. Furthermore, correlations between parameters of the ion current and the combustion parameters from the cylinder gas pressure are established. In addition, the detection of the ion current signal is explored with the aid of optical imaging of the combustion process which adds to the understanding of the characteristics of the ion current signal concurrent with the combustion images of the flame color and intensity.

4.1 Introduction

The ion current has the potential to be used for sensing diesel combustion using the integrated glow plug/ ion current sensor. The combustion in diesel engine consists of two zones; the premixed combustion, and the diffusion and mixing controlled combustion. Both zones are detected by the ion current signal (9; 40). The 1st peak in the

ion current represents the ions produced from the premixed combustion, and the ion current 2nd peak represents the ions produced during the diffusion and mixing controlled combustion.

Engine load, injection pressure, and injection timing have a great influence on the ion current peaks amplitude and timing (29; 40). Increasing the injection pressure, the premixed combustion fraction and the peak in-cylinder gas temperature increase; therefore, the rate of ion production is higher and the 1st and 2nd peaks amplitude of the ion current increase.

4.2 Ion current characteristics for feedback control

Figure 4.1 shows cylinder gas pressure, needle lift, RHR, ion current and the derivative of the ion current traces. The following is an explanation of the combustion cycle. The fuel delivery starts very shortly after the start of the rise in the needle lift signal (41), at 10° bTDC, followed by an ignition delay period. The start of combustion, indicated by the pressure trace and RHR, is at 1.5° bTDC. It is followed by the start of the ion current (SIC) depicted at 0.5° aTDC. This small shift between SOC and SIC depends, mainly on the location of the probe relative to the closest fuel spray and the swirl direction. The sharp increase in cylinder gas pressure is caused by the volumetric burning of the premixed charge; this is associated with a slow rise in the ion current reaching its first peak. The difference between the relatively small rise in the ion current first peak and the premixed combustion peak of the RHR is due to the fact that the latter is caused by a global rise in pressure due to combustion of six sprays, while the ion

current signal is produced by the combustion of the neighboring spray (9). After the first peaks of the premixed combustion in the RHR and the ion current signal, both dropped indicating the end of the premixed combustion and started to increase again to their second peaks during the mixing and diffusion controlled combustion. The second ion current peak reached much higher amplitude compared to the first peak due to the higher concentration of the ionized species and local temperatures reached in the cycle shortly after reaching to the peak cylinder pressure (LPP).

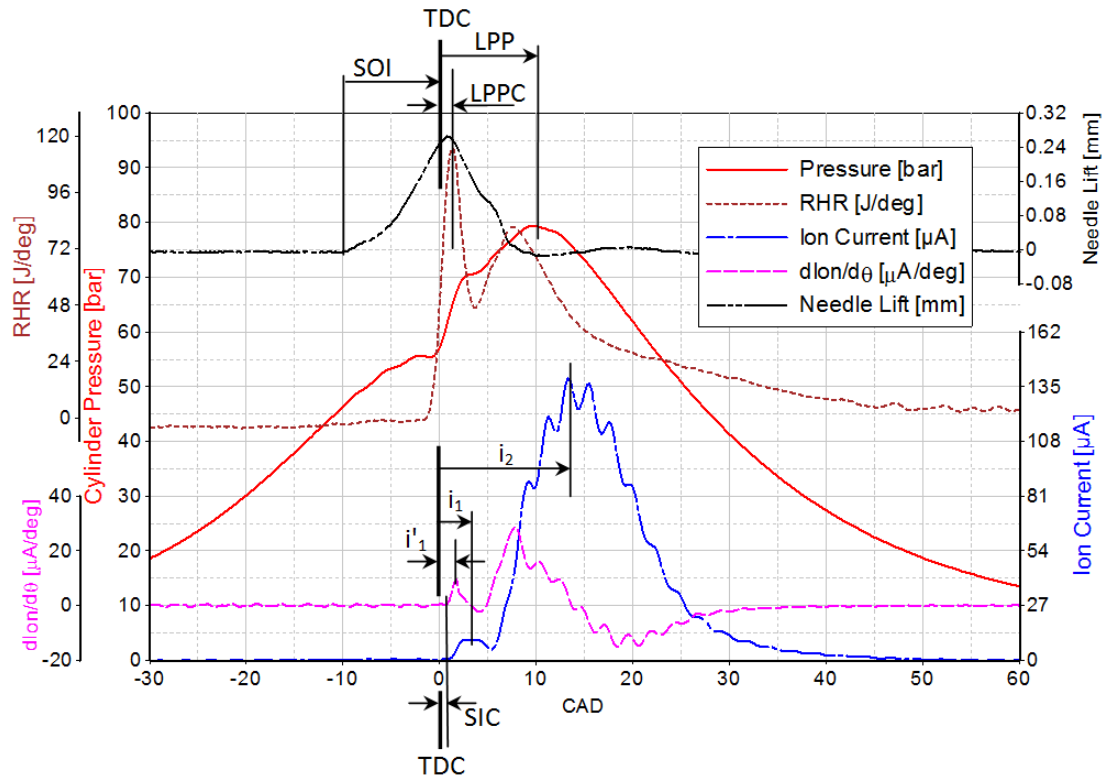


Figure 4.1. Cylinder gas pressure, needle lift, RHR, ion current and the derivative of the ion current traces in a diesel engine [IMEP=8 bar, Const. Speed=1800RPM, SOI=10° bTDC, Inj. Press=900bar]

Developing correlations between RHR and ion current parameters for the control of combustion by utilizing the ion current signal can be achieved according to the similarities found between the two signals. The RHR parameters for which their locations are of interest include: the start of RHR due to the premixed combustion, the first peak, the second peak, the highest rate of rise to each of the two peaks and the 50% of the total heat release. Similarly, the locations of the following ion current parameters are of interest: the start of ion current (SIC), the first peak of the derivative of the ion current (i'_1), the first ion current peak (i_1), the second ion current peak (i_2), the highest rate of rise to the two peaks and the 50% of the total ion current.

4.2.1 Cycle-to-cycle variations

In order to develop a stable combustion controller based on the feedback of the ion current signal, four of the ion current parameters SIC, i_1 , i_2 and i'_1 are examined for their reproducibility and cycle-to-cycle variations under steady state operation. Figure 4.2 shows a boxplot for SIC, i_1 , i_2 and i'_1 ; where the boxplot is constructed using 100 consecutive cycles. The figure shows that the SIC has the smallest spread and mid-spread compared to the other ion current parameters. i'_1 has slightly higher spread than SIC, but i_1 and i_2 exhibit high spread and mid-spread during steady state conditions. It is noticed that the variations in the ion current signal increases as signal progresses in CAD.

The ion current signal has mainly two distinguished peaks representing premixed and diffusion combustion similar in their characteristics to the RHR. Despite these similarities, the lag of the ion current signal is still considerable. On the other hand, it is observed that LPPC is located between the SIC and i'_1 as shown in Figure 4.1 and the SIC

exhibited the lowest variations as shown in Figure 4.2. It should be noted that LPPC represents the location at which the combustion reaches its maximum rate of burning, where the ion current is detected a fraction of crank angle degree earlier. Therefore, experimental tests are conducted to verify any existing correlation between LPPC and SIC under different operating conditions.

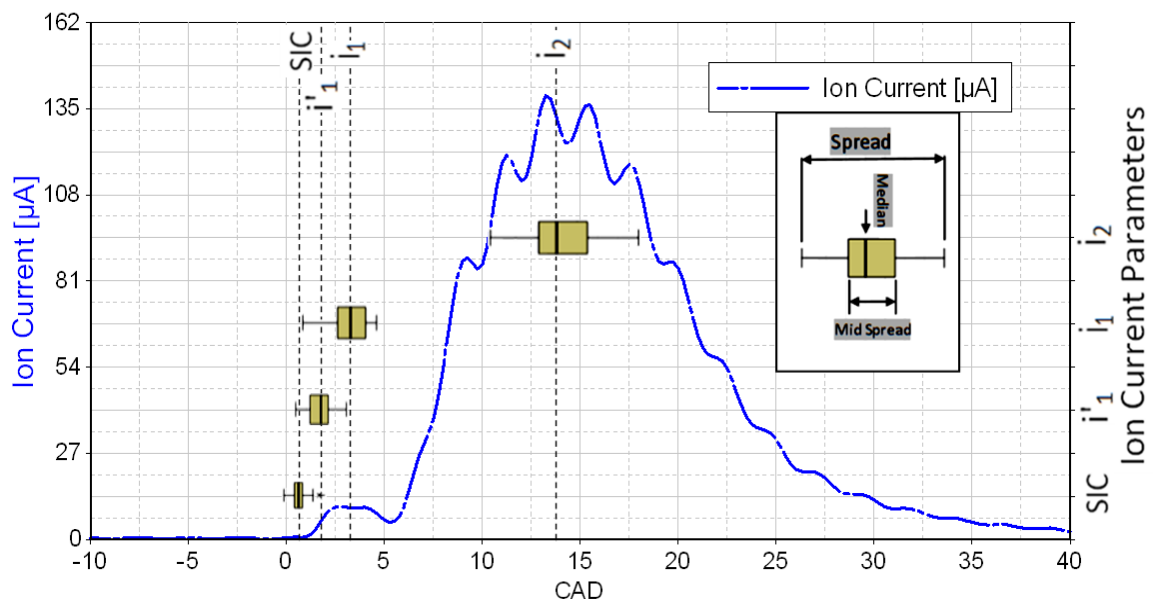


Figure 4.2. Boxplot for different ion current parameters [IMEP= 8 bar, Const. Speed=1800RPM, SOI=10° bTDC, Inj. Pres=900bar, # Cycles = 100]

4.2.2 Experimental results

Tests at constant SOI timing and variable loads and injection pressures

A series of steady state tests are conducted at a constant SOI under different loads and injection pressures as shown in Figure 4.3. IMEP is varied from 3.3 to 8 bar in seven steps, and the injection pressure is varied at each load from 250 to 1100 bar in ten steps.

Under these conditions, the manifold absolute pressure (MAP) is varied from 1.16 to 1.4 bar in four steps. Start of injection is constant at 10° bTDC, and engine is operated at speed of 1800 RPM.

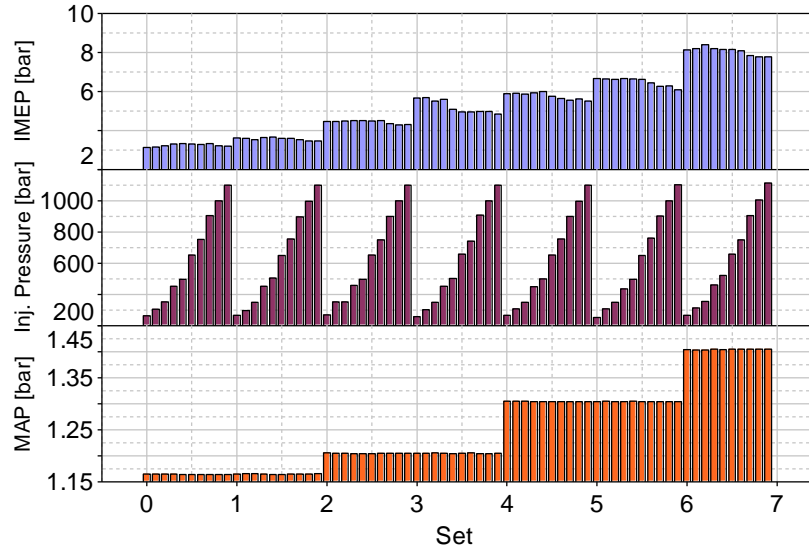


Figure 4.3. Sweep of loads and injection pressures [IMEP= 3.3 - 8 bar, Speed= 1800RPM, Inj. Pressure= 250 to 1100 bar, Const. SOI= 10° bTDC]

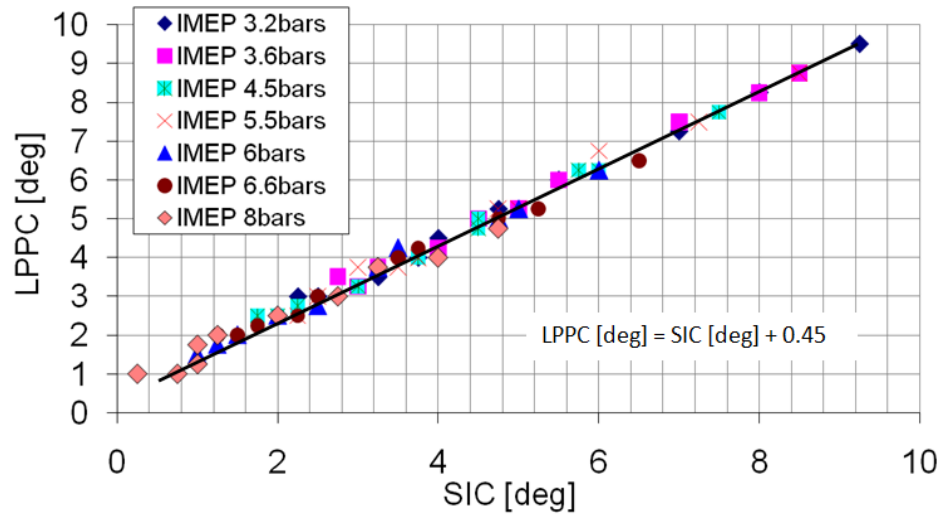


Figure 4.4. Correlation between SIC and LPPC at sweep loads and injection pressures [IMEP= 3.3 - 8 bar, Speed= 1800RPM, Inj. Pres= 250 to 1100 bar, SOI= 10° bTDC]

Figure 4.4 shows LPPC plotted versus SIC, where a linear relationship is found with SIC lagging the LPPC by 0.45 CAD. Since the SIC is directly proportional to the LPPC with constant offset, a histogram is plotted for their difference, as shown in Figure 4.5. The histogram shows the mean is about 0.45 deg, and the standard deviation is 0.2 deg. This trend shows that the location of the premixed combustion peak in the RHR can be located by the SIC.

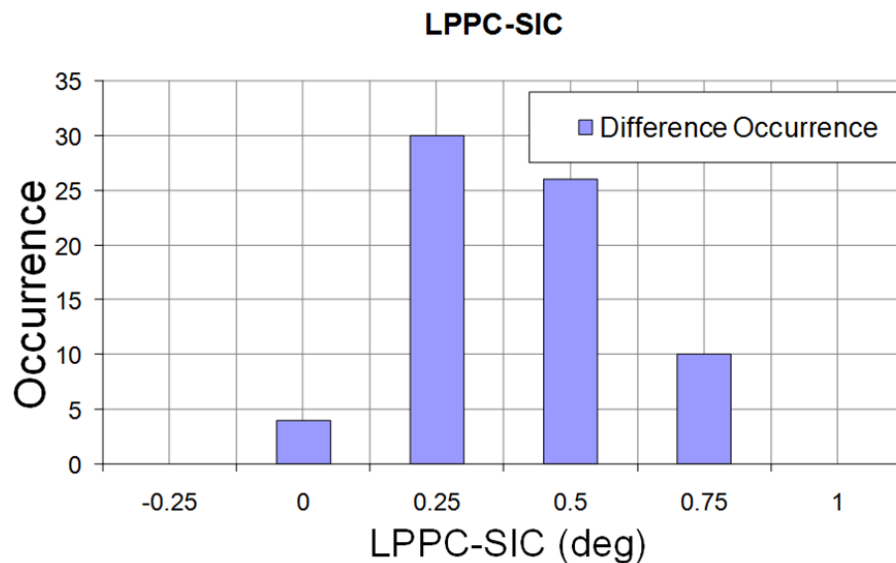


Figure 4.5. Histogram of LPPC-SIC [IMEP= 3.3 - 8 bar, Speed= 1800 RPM, Inj. Pres= 250 to 1100 bar, SOI= 10°bTDC]

Tests at constant injection pressure under variable loads and SOI timings

A series of steady state sweep tests are conducted at a constant injection pressure under different engine loads and injection timings as shown in Figure 4.6. The IMEP is varied from 2.8 to 7.8 bar in seven steps and SOI is varied at each load from 29 to 4° bTDC in six steps. Under these conditions the MAP is increased with load from 1.05 to

1.24 bar in four steps. The injection pressure is kept constant at 600 bar and the engine is operated at speed of 1800 RPM.

The cycle to cycle variations in the SIC, LPPC and LPP are plotted in a boxplot as shown in Figure 4.7. At the earliest SOI of 24° bTDC, the mean SIC is detected at 5.75° bTDC with a spread of 2 divisions, the mean LPPC is located at 6.25° bTDC with a spread of 3 divisions, and LPP is located at 1.75° aTDC with a spread of 2 divisions. These location of SIC, LPPC and LPP change according to the SOI timing. It should be noted that variations of these location are affected by the position of the piston from TDC when combustion takes place. Therefore retarding the SOI from 24 to 14° bTDC, causes combustion to start shortly after TDC and all the three parameters SIC, LPPC and LPP are located with very narrow spread. The mean SIC, LPPC and LPP are located at 5.25° , 5.75° and 9.75° aTDC respectively, where their spreads are within one division or even less. The trend is twisted back at a late SOI of 4° bTDC. The late injection caused combustion to occur fairly late in the expansion stroke. The SIC, LPPC and LPP are located at 14° , 15° and 17.5° respectively. The corresponding spreads increased to 4, 3 and 2 divisions respectively.

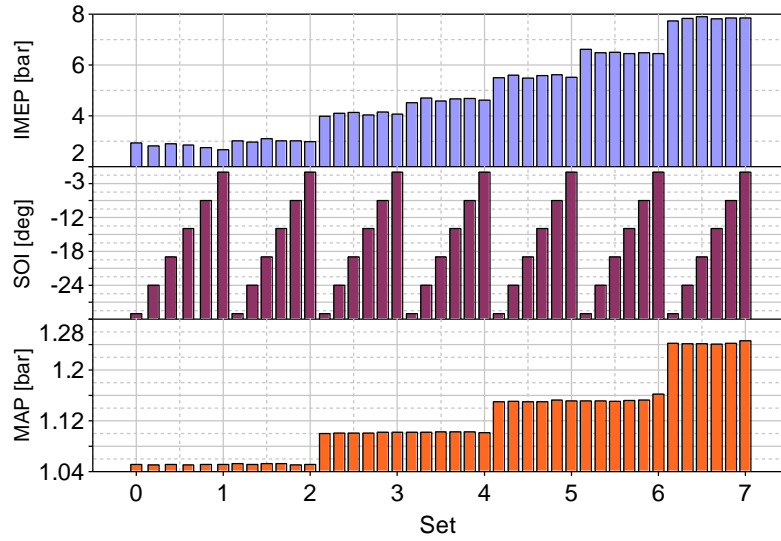


Figure 4.6. Sweep of loads and injection pressures [IMEP= 2.8 - 7.8 bar, Speed= 1800RPM, Inj. Pres= 600 bar, SOI= -29° to -4° bTDC]

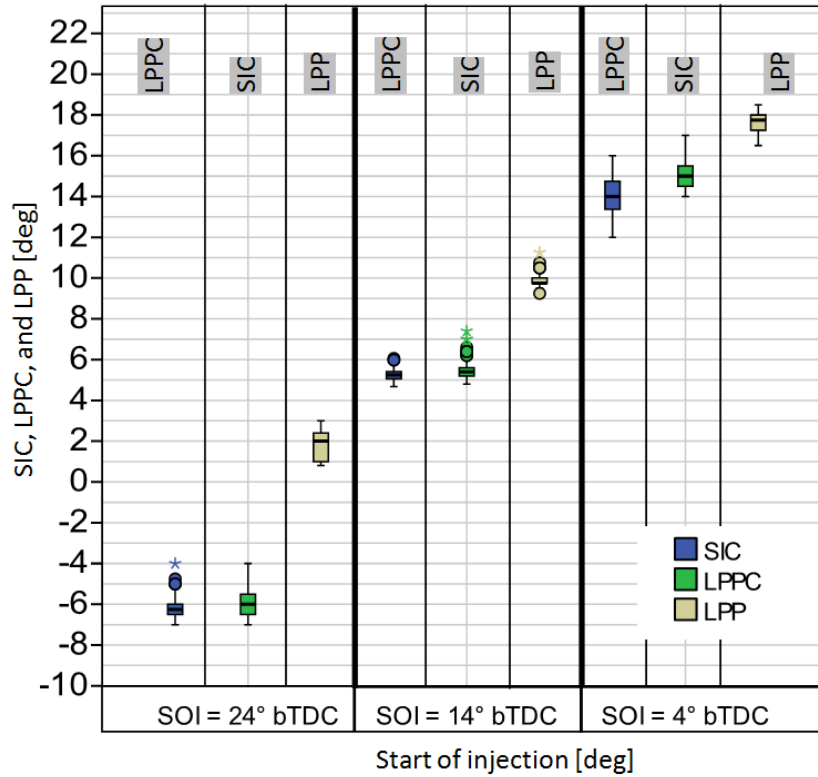


Figure 4.7. Boxplot for SIC, LPPC, and LPP for different injection timing [IMEP= 4 bar, Const. Speed=1800RPM, SOI=10° bTDC, Inj. Pres=600bar, # Cycles = 100]

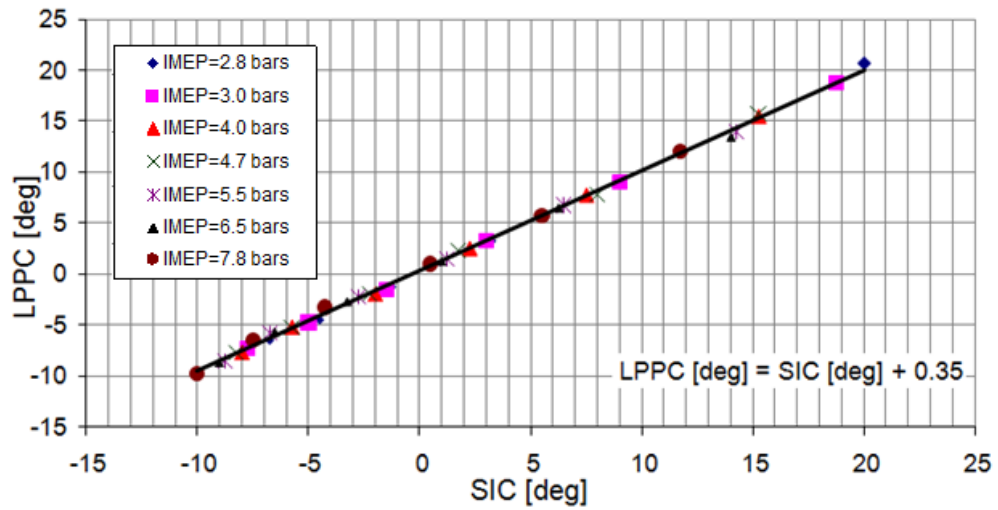


Figure 4.8. Correlation between SIC & LPPC at sweep loads [IMEP= 2.8 - 7.8 bar, Const. Speed = 1800RPM, Inj. Pres= 600 bar, SOI= -29° to -4° bTDC]

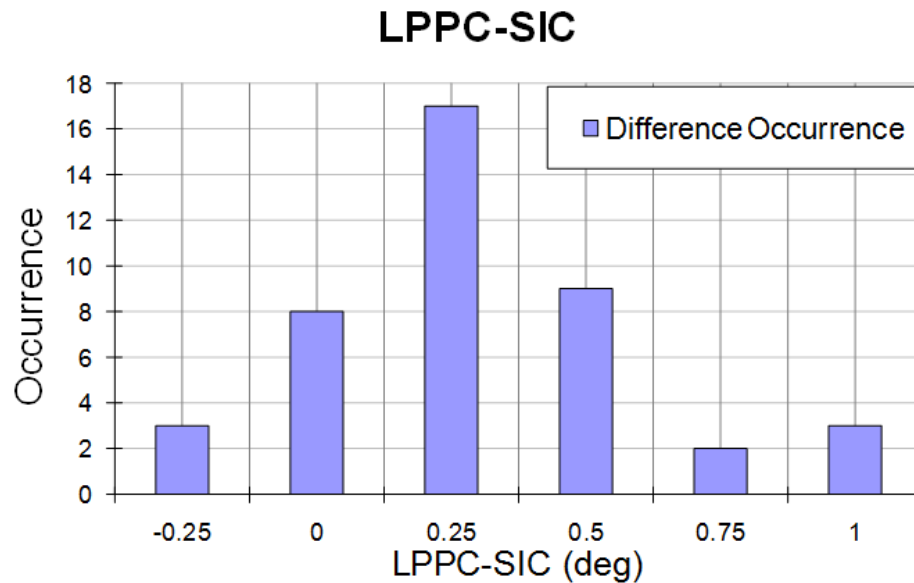


Figure 4.9. Histogram of LPPC - SIC [IMEP= 2.8 - 7.8 bar, Const. Speed = 1800RPM, Inj. Pres= 600 bar, SOI= -29° to -4° bTDC]

Figure 4.8 shows the correlation between the SIC and LPPC at a constant injection pressure of 600 bar at different SOI timings and engine loads. The LPPC has a linear relationship with SIC timing and lagged by about 0.35 CADs. The histogram for this lag period is shown in Figure 4.9 and it depicts a normal distribution with a mean of 0.3 CAD and a standard deviation of about 0.32 CAD.

Correlation between SIC and LPPC

Figure 4.10 shows the CAD corresponding to the start of ion current plotted versus LPPC of the rate of heat release. A correlation between the SIC and LPPC is shown with a coefficient of determination $R^2 = 0.985$. The linear equation shows that the SIC is directly proportional to the LPPC and lags it by about 0.35 CAD. Such correlation can be used to control the combustion phasing at any desired location by utilizing the SIC as a feedback to the engine ECU.

Figure 4.11 shows the standard deviation for the SIC plotted versus LPPC. Five consecutive cycles are considered for calculating the standard deviation for various operating conditions. The plot shows that standard deviation for SIC has a linear relationship with the standard deviation for LPPC with $R^2 = 0.8$. Moreover, the slope between standard deviations for SIC and LPPC shows that the ion current sensor is more sensitive to combustion variations compared the pressure transducer.

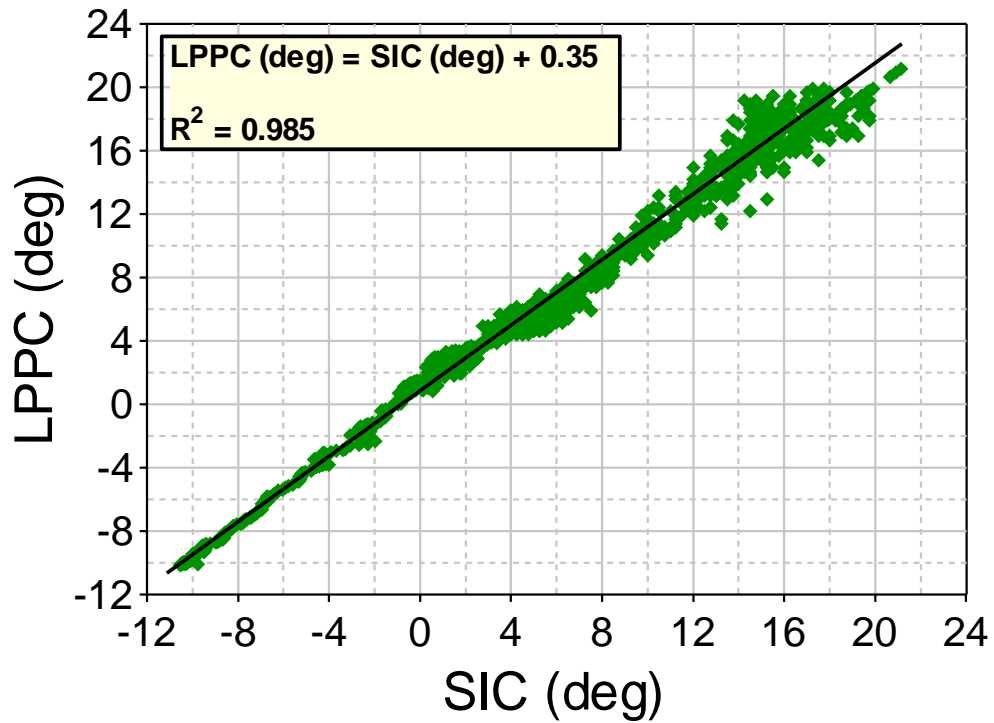


Figure 4.10. Correlation between the SIC and LPPC (JD)

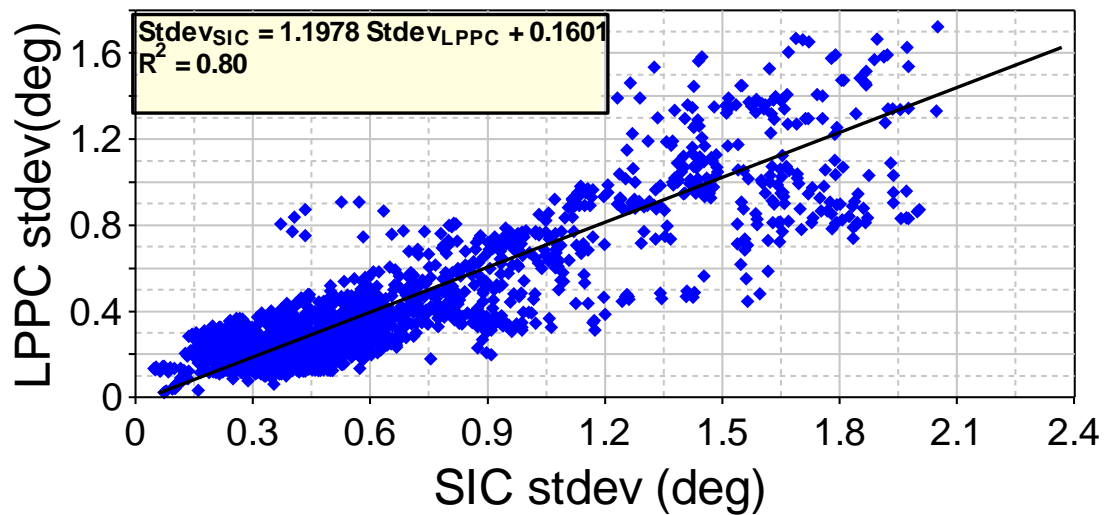


Figure 4.11. Correlation between the SIC and LPPC standard deviations (JD)

4.3 Misdetection of the ion current signal

The analysis of the ion current signal in diesel engines showed that ion current signal is undetected by the ion current sensor in some random cycles although combustion is detected by the cylinder gas pressure transducer. This phenomenon of misdetection of the ion current signal is observed more often during idling and light load operations. This phenomenon can be contributed to the nature of diesel combustion characterized by the heterogeneity of the charge, very lean mixture, and low in-cylinder gas temperature at these operating conditions. Figure 4.12 shows traces for the cylinder gas pressure and ion current recorded in John Deere engine at IMEP = 2.1 bar and injection pressure = 550 bar. Two combustion events produced two identical and superimposed pressure traces, however; the ion current probe produced a signal for only one cycle and was missing for the other cycle.

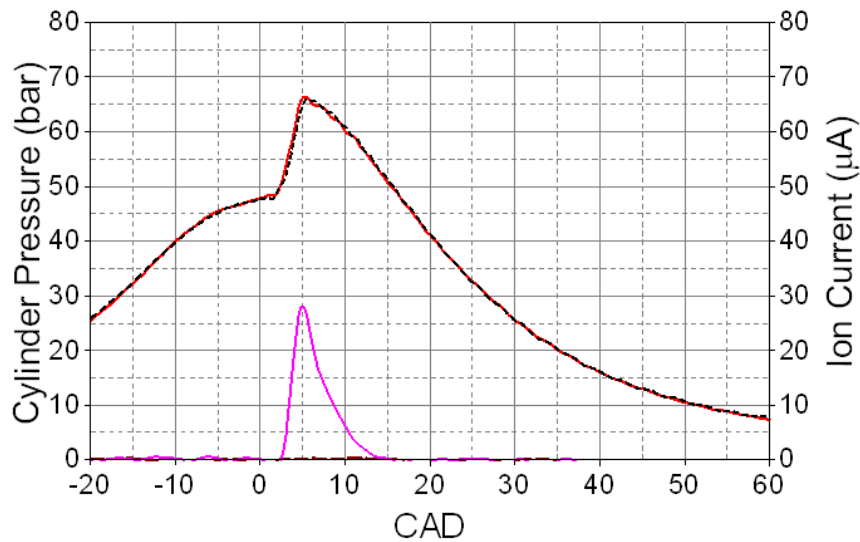


Figure 4.12. Cylinder gas pressure and ion current signals at light load condition of two arbitrary cycles [JD, IMEP=2.1 bar, Const. Speed=1800 RPM, Inj. Press =550 bar]

Figure 4.13 shows the percentage of ion current detection for a 100 consecutive cycles at different loads, starting from idling at IMEP= 1 bar to high loads at IMEP = 15.5 bar. All test points are conducted at steady state conditions at an engine speed of 1800 RPM. It is observed that the number of cycles having ion current misdetection is the highest at idling operation. The misdetection phenomena gradually decreases at higher loads and it wanes at IMEP >3 bar. A zoomed box plot in Figure 4.13 shows a high dispersion for the percentage of ion current detected at very low loads where this dispersion is exponential diminishing with increase in load.

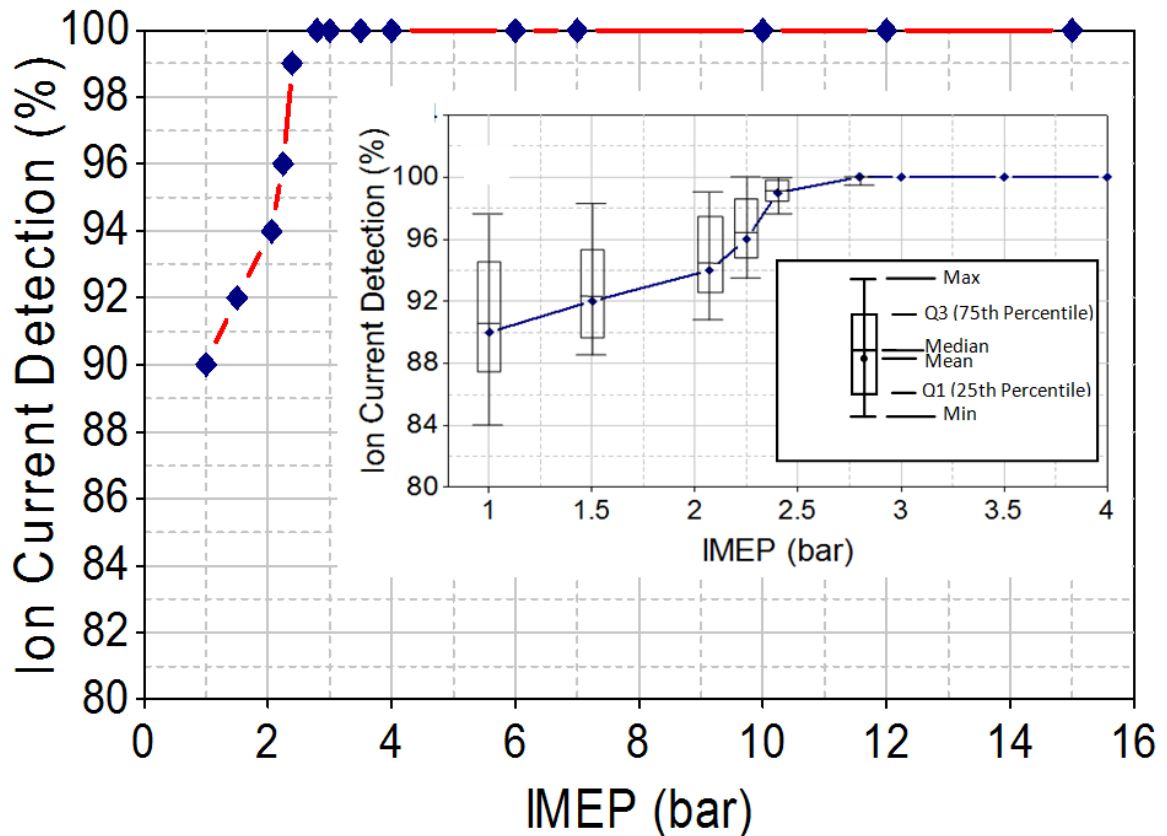


Figure 4.13. Percentage of ion current signal detection in 100 cycles at various engine loads

4.4 Optical analysis of the ion current signal

In order to investigate the characteristics of the ion current signal, images are taken in an optically accessible direct injection single cylinder diesel engine to study the effect of combustion evolution on the production of the ion current signal. The engine has a cylinder bore of 85 mm and stroke 90 mm. A centrally located injector is modified to act as an ion current sensor. The details of the engine instrumentation, optical setup, and ion sensor implementation are given in reference (42; 43). The investigation was carried out in the optical engine using a 30,000 frame/sec high speed PHANTOM camera. This camera is able to obtain colored pictures of combustion, on a cycle basis; within the visible ranges every one sixth of a crank angle degree. A set of information can be extracted from these pictures which includes the liquid fuel jets as well as the fuel impingement on the wall, the premixed combustion characterized by the blue flame, and the diffusion controlled combustion illustrated by the sooty yellow flames.

Figure 4.14 shows needle lift signal, RHR, cylinder gas pressure and temperature traces, and ion current signal measured from the optical engine. Characteristics of the ion current signal explained earlier are clearly identified regardless of the sensor location or engine bowl design.

Figure 4.15 shows the images of the combustion evolution within a single cycle obtained in the visible range using a high speed “Phantom” camera, where the ion current signal was measured and represented in Figure 4.14.

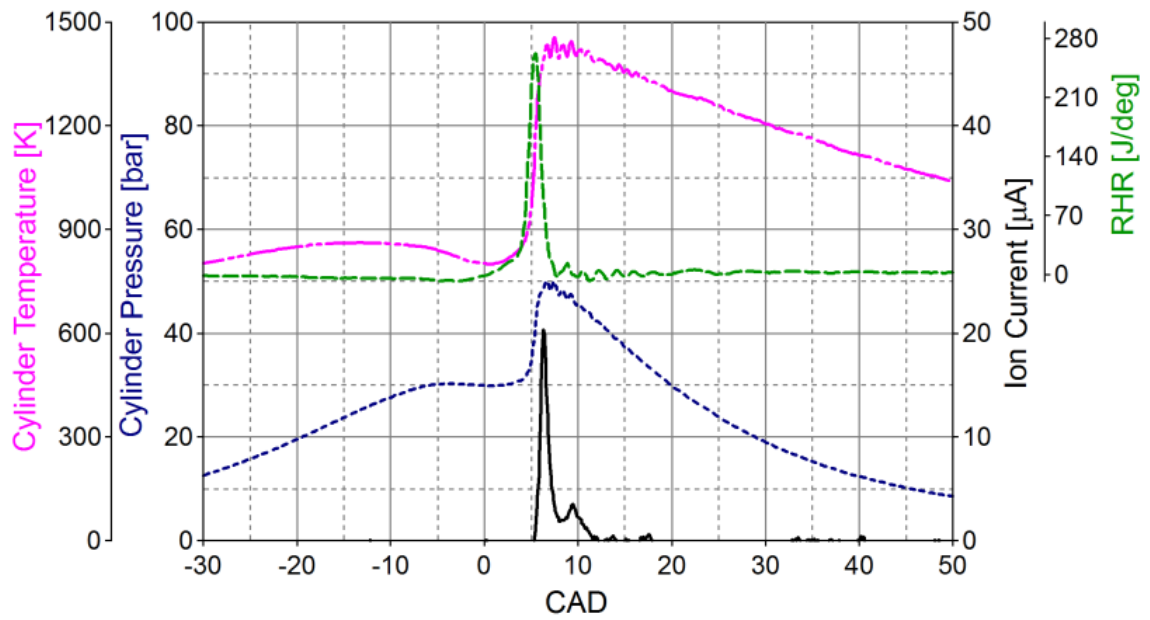


Figure 4.14. Cylinder gas pressure, ion current signal, RHR, and need lift signals [OPT, IMEP=3 bar, Const. Speed=1000RPM, SOI= 8° bTDC, Inj. Press =400 bar]

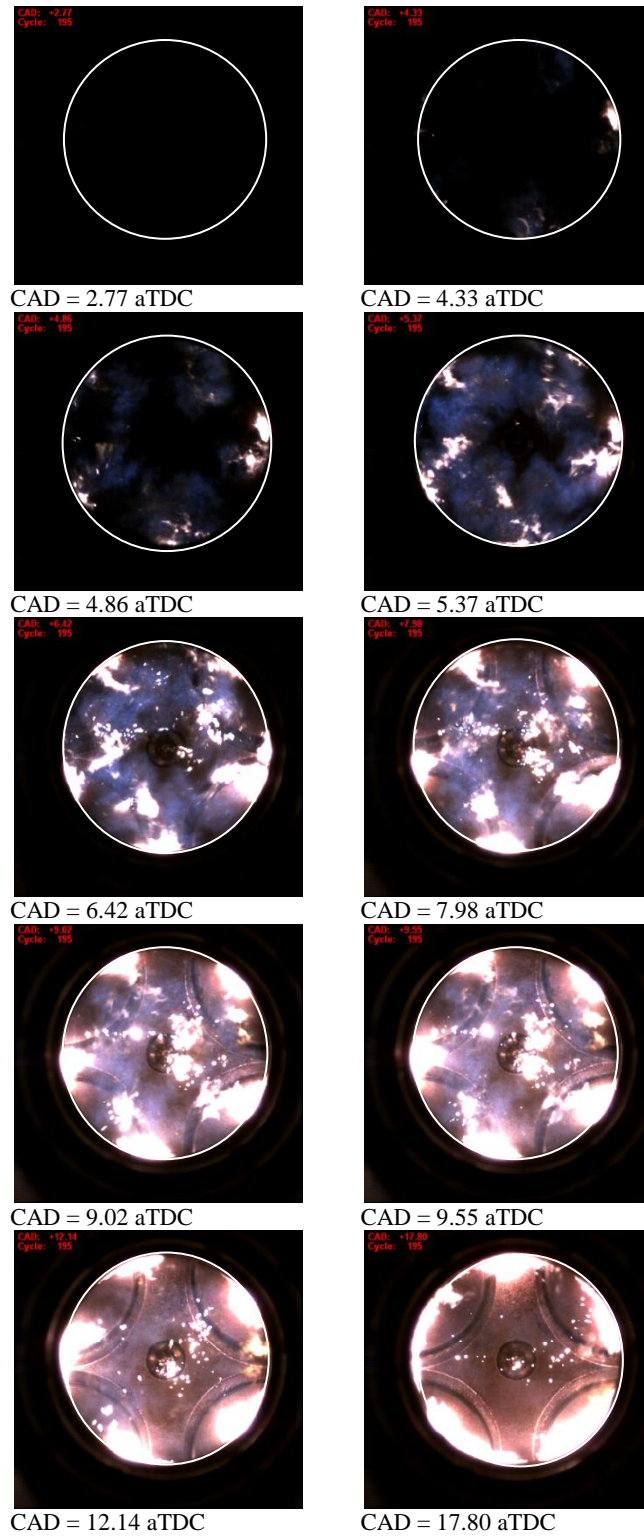


Figure 4.15. High speed images of the visible light from the combustion process [OPT, IMEP=3 bar, Const. Speed=1000RPM, SOI= 8° bTDC, Inj. Press=400 bar]

Figure 4.15 shows at 2.77° aTDC, a complete dark image. The ion current signal is absent at this point. At 4.86° aTDC, the image shows spots of faint blue light and spots of bright yellow light in one side of the combustion chamber indicating early stages of high temperature combustion (HTC); this is indicated by a start of rise in the in-cylinder pressure and temperature in Figure 4.14. The blue light very rapidly propagates, where it covers the entire combustion chamber at 5.37° aTDC. The blue light represents the volumetric combustion referred to as the premixed combustion. At this point, the ion current signal starts to rise as shown in Figure 4.14, and the RHR reaches its peak of premixed combustion. It should be noted that the ion current production is mainly governed by the local cylinder gas temperature and local equivalence ratio. As the cycle advances, combustion images indicate an increase in the bright light inside the combustion chamber; where the cylinder temperature and the ion current signal kept increasing until the ion current reached a maximum at 6.42° aTDC. At 7.98° aTDC, the image shows an increase of the bright yellow light which represents the diffusion controlled type of combustion as the blue flame starts to fade. After 9.55° aTDC, the combustion process is thermally close to termination although bright light is present along the combustion chamber wall. This yellow color indicates a sooty flame. (9; 44; 45). The ion current signal decays during this period as seen in Figure 4.14.

According to the observation made for the optical images of the combustion evolution and the ion current signal, a correlation between the blue flame and the start of ion current was found (42). Figure 4.16 shows a transient test conducted on the optical engine, where it indicates a good agreement between the start of ion current signal (SIC)

and the timing of the maximum intensity of the blue flame. Therefore, the presence of the blue flame with high intensity is essential to detect the ion current signal in diesel engines. This optical observation confirms the correlation found between SIC and LPPC shown in Figure 4.10.

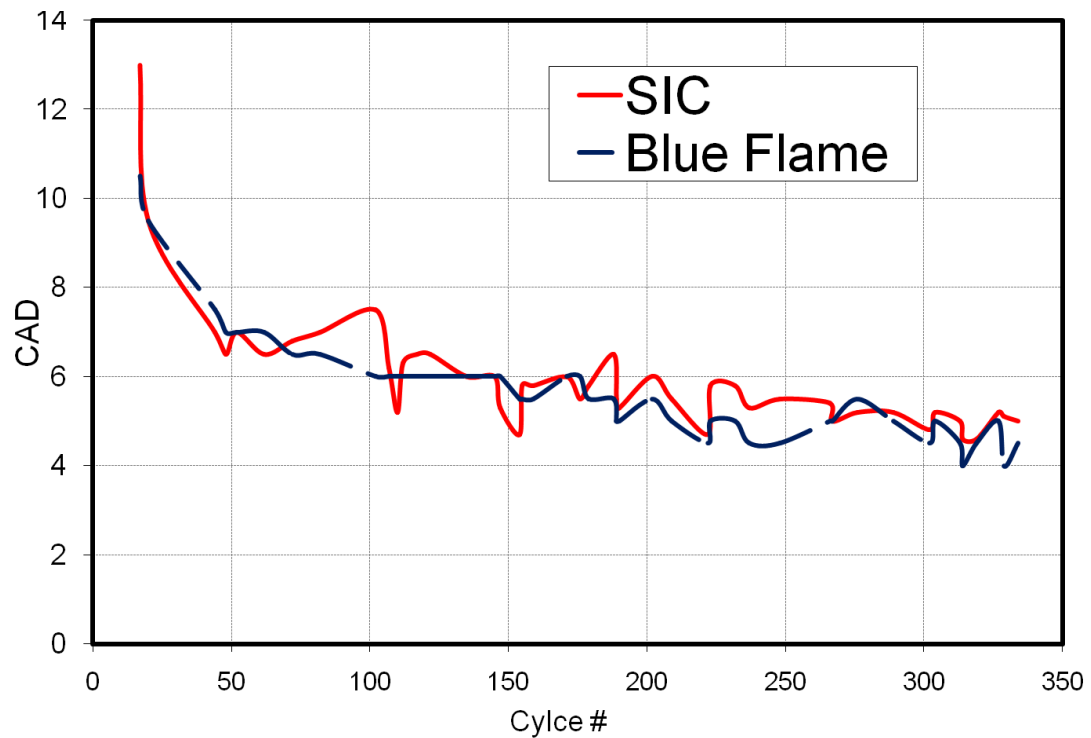


Figure 4.16. Correlation between the start of ion current (SIC) and timing of the maximum blue flame intensity (OPT, transient test) (42)

4.4.1 Optical engine test at light load

Figure 4.17 and Figure 4.18 show a close examination of visible light produced during combustion in two random cycles, under the same running conditions, IMEP= 1 bar, and engine speed of 1000 rpm. Both cycles produce the same cylinder gas pressure

and RHR although the ion current is not detected in the cycle of images in Figure 4.18. The combustion starts in both cycles at 2.2° aTDC where the blue flame starts to be seen. Figure 4.17, at 6.12° aTDC, the blue light dominates nearly the whole combustion chamber, where the ion current signal is detected by the sensor. After 8.41° aTDC, the blue light fades away and it completely disappears at 16.07° aTDC. This indicates that the combustion terminates at this light load in a premixed combustion fashion of a very lean mixture, where the ion current terminates as well. It should be noted that the local temperature around the ion sensor was high enough to develop an ion signal as indicated by the presence of the blue flame.

On the other hand in Figure 4.18, the intensity of the blue lights is concentrated in two separate areas inside the chamber. The spread of the blue light is limited and did not cover the whole combustion chamber. Although the peak of premixed combustion is reached at 6.50° aTDC, the ion current signal was not detected. The images also indicate that the combustion terminates at 16.61° aTDC, where the blue light completely disappeared. In this cycle, the combustion indicates less fuel/air mixing compared to the cycle in Figure 4.17 as the blue light did not propagate in the whole chamber. As a result, inadequate local temperature for ion current formation and poor or no flame developed locally around the ion current sensor lead to the misdetection of the ion current signal.

4.4.2 Optical engine test at medium load

Figure 4.19 shows images of the visible light of the combustion process at a medium load of 3bar IMEP, and engine speed of 1000 rpm. It should be noted that images time step is not constant. The combustion starts at 2.25° aTDC, where the blue

light starts to be seen. The blue light very rapidly spreads in the whole combustion chamber as seen at 2.25° aTDC. The high intensity of the blue light indicates the high premixed combustion fraction burned at high temperatures above 2500 K. This results in production of ion current signal which is strongly detected by the ion current sensor. As combustion proceeds, the intensity of the blue flame reduces and the bright light increase due to the diffusion and mixing controlled combustion. The diffusion combustion burns much slower than the premixed combustion, where the bright light is present along the walls of the combustion chambers till 47.76° aTDC.

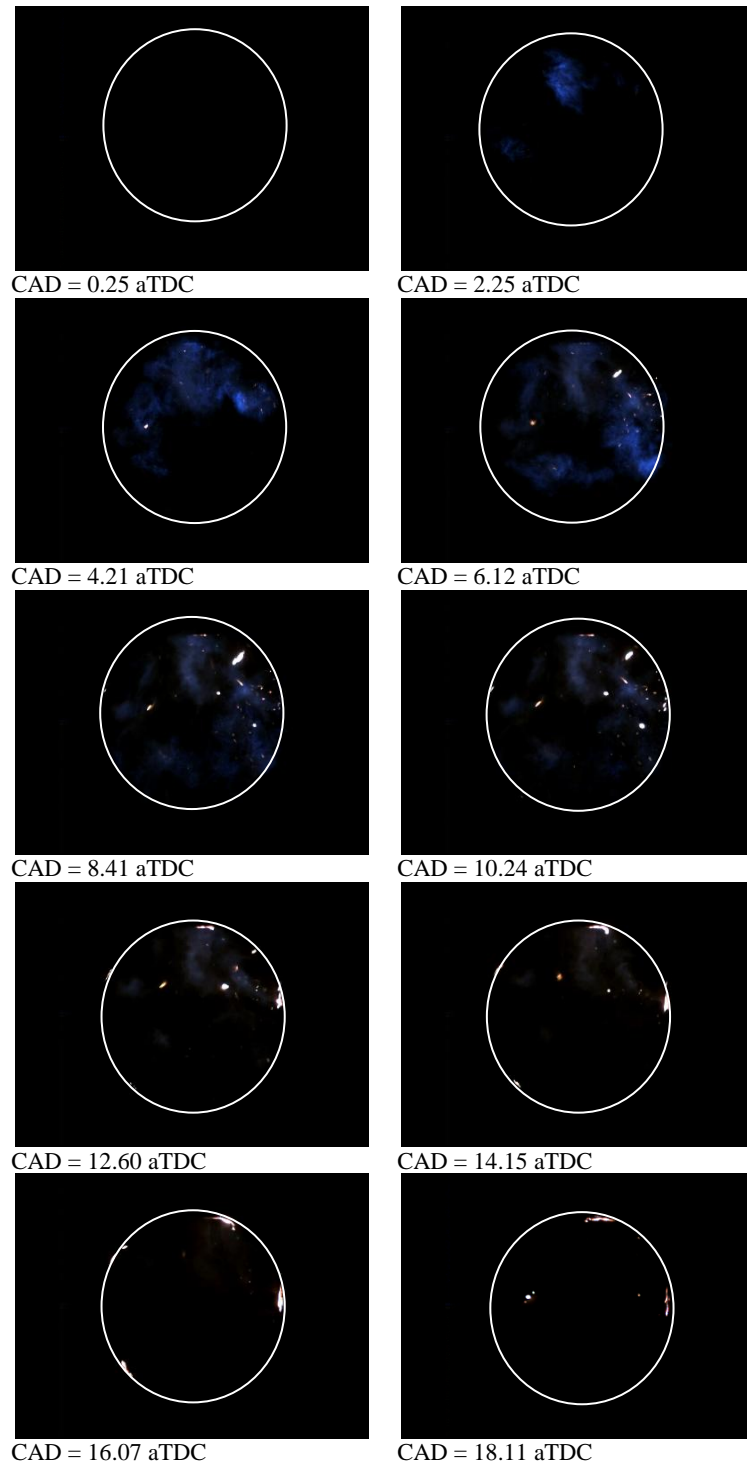


Figure 4.17. High speed images of the visible light produced from the combustion process (Light load: Detection of the ion current) [OPT, IMEP= 1 bar, Const. Speed=1000RPM, SOI= 8° bTDC, Inj. Press= 800 bar]

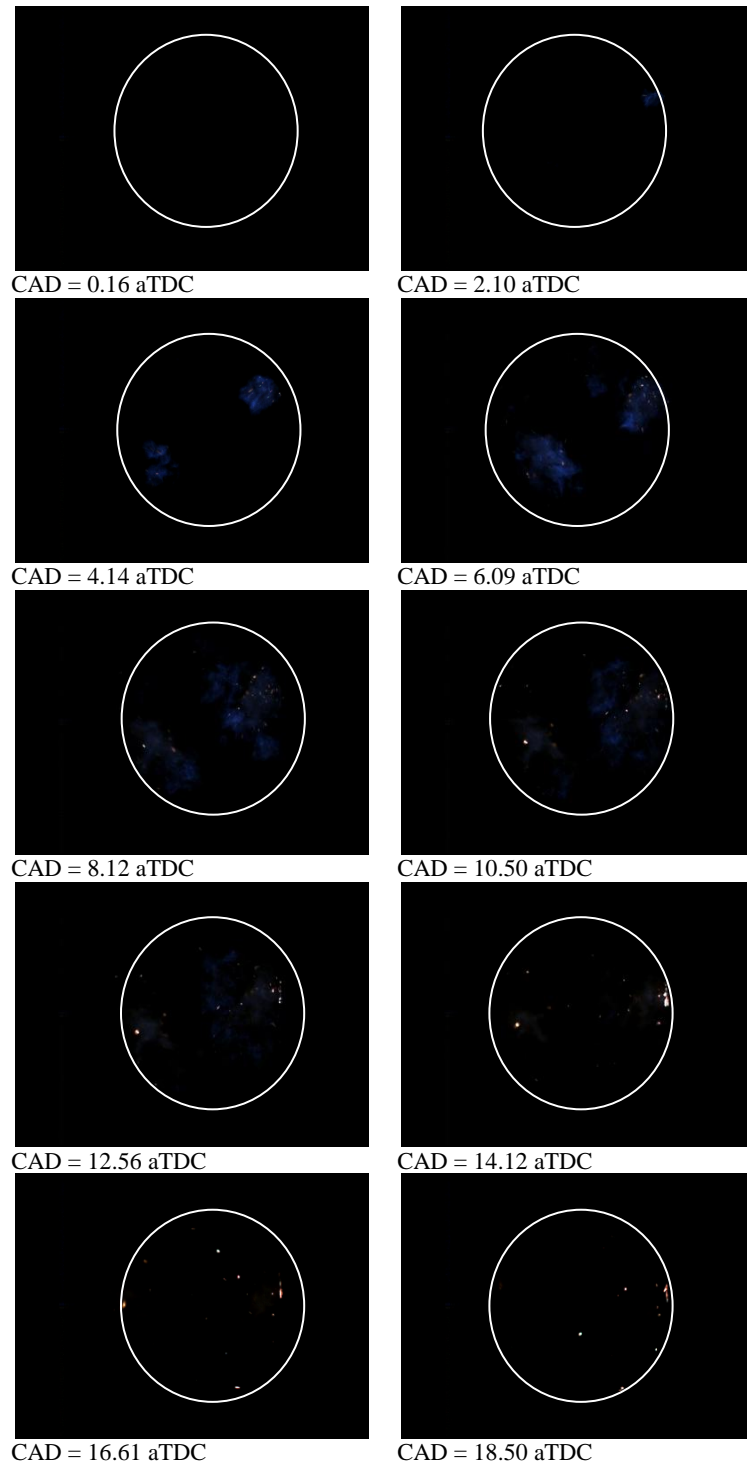


Figure 4.18. High speed images of the visible light produced from the combustion process (Light load: Misdetection of the ion current) [OPT, IMEP= 1 bar, Const. Speed=1000RPM, SOI= 8° bTDC, Inj. Press= 800 bar]

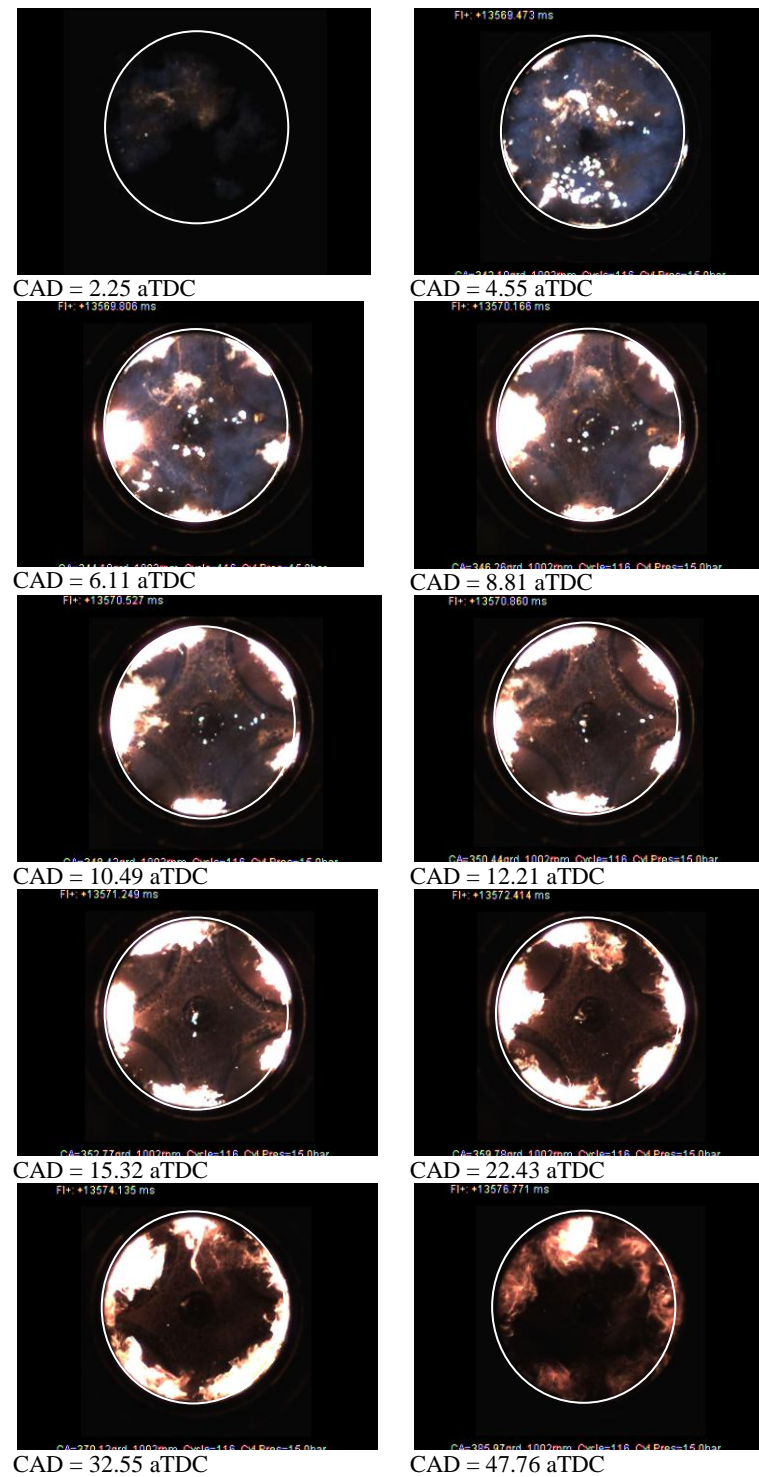


Figure 4.19. High speed images of the visible light produced from the combustion process (Medium load: Detection of the ion current) [OPT, IMEP= 3 bar, Const. Speed=1000RPM, SOI= 8° bTDC, Inj. Press= 800 bar]

4.5 Summary

This chapter walked through the possibilities of using different parameters of the ion current signal for the electronic control of diesel engines. One of the main concerns of the ion current signal is the cycle-to-cycle variations, number of peaks detected and their amplitudes. The correlation between the location for the start of the ion current sensed locally by the ion probe and the location of the maximum rate of heat release during the premixed combustion has been discussed. The experimental investigation is conducted on 4.5L heavy-duty diesel engine and a single cylinder optical accessible engine. The optical imaging provided a justification for the misdetection of the ion current signal. In addition, it showed different types of flames that produces the ions during different stages of combustion. There is a strong evidence of ion current misdetection in diesel engine at low loads, where the overall equivalence ratio is very lean. The following are the main conclusions:

1. There is cycle-to-cycle variation in the ion current signal peak location, shape and amplitude but the start of the ion current signal provides a reproducible characteristic at various engine operating conditions.
2. A linear relationship between the start of the ion current (SIC) and the location of the peak of the rate of heat release (LPPC) due to premixed combustion is established. Therefore, it is a good indicator of combustion phasing (LPPC).
3. Misdetection of the ion current signal is possible at idling and low engine loads due to the heterogeneity of a very lean mixture.

4. The investigation in the optically accessible engine helped to explain the nature of the ion current signal at different phases of combustion and to differentiate between different flames producing ions.
5. Optical imaging at different loads explains the misdetection of the ion current is caused by the absence of a viable visible flame in parts of the combustion chamber at low engine loads.

CHAPTER 5

CLOSE LOOP COMBUSTION CONTROL

An incremental fuzzy logic controller that adjusts the combustion phasing to meet production goals is demonstrated in this chapter. A sequence of signal processing methods is applied to improve the quality of ion current signal on cyclic basis. The algorithm developed in this study optimizes the ion current feedback to increase its reliability for stable engine control while maintaining fast controller response, and high accuracy. The response of the controller is evaluated from experimental data obtained by running the engine under different steady, and transient operating conditions.

5.1 Engine ECU

The original engine ECU is replaced by an open code ECU "ADX controller" that uses MATLAB/Simulink control models as illustrated in chapter 3. The open ECU is used to fully bypass the original ECU. An optical encoder is used to measure the angular position of the crank shaft with a resolution of 0.25 CAD. The ECU controls a number of engine parameters such as injection pressure, injection duration, injection timing, injection events, intake pressure, and engine speed.

A Labview code is developed to acquire and analyze the ion current signal, where the processed data is sent to the open ECU. The code can acquire and provide feedback

based on one cycle or average of a number of cycles. The code can also find the peak values in the ion current signal and their CAD locations.

Figure 5.1 shows a schematic diagram for the open ECU and the combustion phasing control system. The ion current signal is analyzed, where a set-point controller and the ion current feedback are used by the closed loop combustion controller to adjust the injection timing. Both the engine control system and the combustion analyzer are synchronized by the timing of the encoder. The engine is controlled based on the feedback signal from the first cylinder to adjust the injection timing for all four cylinders considering the phase shift between the four cylinders. It is to be noted that using the ion current feedback for each individual cylinder would eliminate the error from cylinder to cylinder variations. However, the scope of this study is to examine the possibilities to enable a closed loop combustion phasing control by using the feedback of the ion current signal.

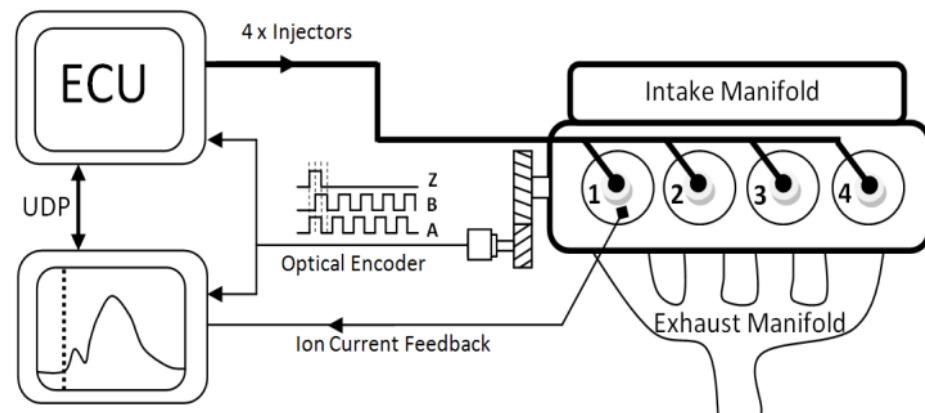


Figure 5.1. Combustion phasing controller using the ion current as a feedback signal

5.2 Algorithm for SIC detection

The ion current signal is processed and conditioned before applying the detection algorithm. The signal processing consists of the following five steps:

(i) Offset:

The ion current signal could have an offset due to soot accumulation on the sensing probe, which can be eliminated by turning on the glow plug heater for a few seconds if the signal datum crosses a certain threshold (29). The soot accumulation has two effects. The first is increasing the resistance to the ions and electrons path to the electrodes, which decreases the signal amplitude. The second is producing a short circuit between the two electrodes which result in an offset of the signal. These two effects result in the deterioration of the signal quality and increase the signal noise and distortion. The ion current threshold settings, above which the glow plug needs to be activated, can be defined in the range from 5-10 μA . The ion current signal datum need to be reset to zero μA by offsetting the ion current at SOI according to Equation 5.1 and depicted in Figure 5.2a.

Equation 5.1 Ion Current = $[\text{Ion Current}_{\text{raw}} - |\text{Ion Current@ SOI}|]$

(ii) Filter:

In this investigation, the analysis is made on a cycle to cycle basis rather than average of many cycles. For a single cycle, the ion current signal exhibits a number of oscillations caused by the local change in the concentration of ionized species around the

probe. This change is the result of pressure waves produced from the sharp rate of pressure rise due the volumetric type of combustion resulted from the premixed charge formed during the ID period. These oscillations have been found to be an indication of combustion resonance as it will be explained in details in CHAPTER 6. In this case, an accurate detection of the SIC requires a smooth ion current signal. Therefore, the high frequency components need to be filtered from the ion current signal. Figure 5.2b shows the ion current signal and the signal after applying a low pass filter. A low pass filter with a phase correction is used, which has a cut-off frequency of 2 kHz, and a generalized hamming window.

(iii) Derivative:

After resetting the ion current signal datum and applying the low pass filter, the algorithm for detecting the SIC can be used directly. However, a further step of computing the derivative of the ion current signal ($dI_{ion}/d\theta$) is shown in Figure 5.2c. It is observed that the detection of the start of $dI_{ion}/d\theta$ is more accurate due to the sharp rise of the signal, and a lower threshold level.

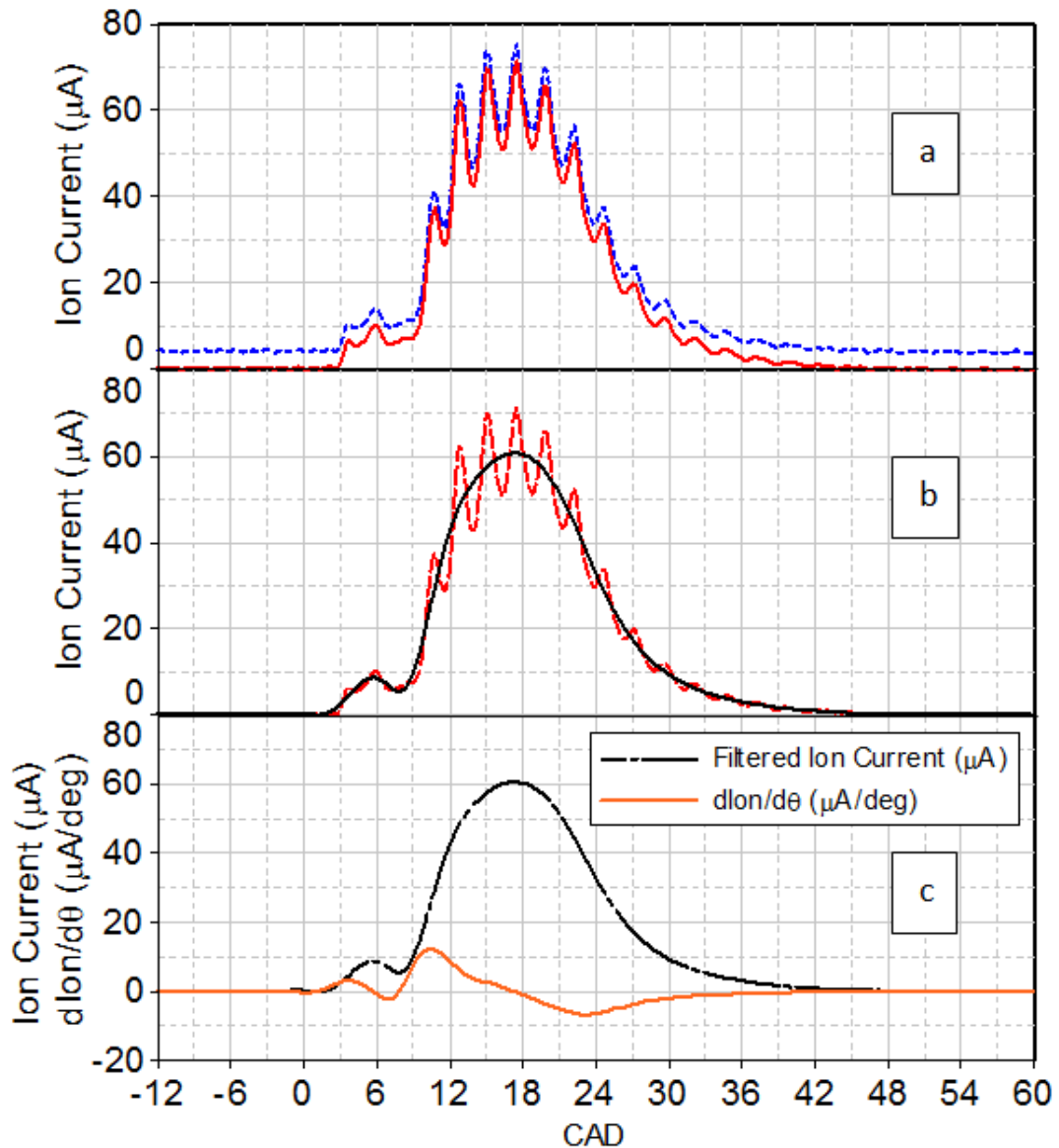


Figure 5.2. Signal processing for the ion current signal before applying SIC detection algorithm [JD, IMEP=5.5bar, Const. Speed=1800RPM, SOI=10° bTDC, Inj. Press=650 bar]

(vi) Dynamic threshold for the SIC:

The accuracy for detecting the SIC depends on many factors. Some of these factors have been addressed in the previous subsections but one of the important factors

is the threshold level set to detect the SIC. Although the signal datum is reset to zero and the high frequency components have been filtered, the ion current signal could have some noise level that can deplete the accuracy of detecting the SIC. Figure 5.3 is a plot of an experimental result recorded for 100 consecutive cycles. $dI_{ion}/d\theta$ is calculated after resetting the datum offset and applying the filter. It is observed that signal has random noise before the start of combustion which varies from cycle to cycle. Therefore, a dynamic threshold calculation is necessary to have an accurate detection of the SIC.

The SIC threshold can be computed by considering the signal $\frac{dI_{ion}}{d\theta}$ for a certain period of CAD, triggered by the start of injection. The data used for the threshold estimation (DTE) is obtained by considering 6 CAD after SOI as stated in Equation 5.2. The maximum and coefficient of variation (COV) are calculated for this period to determine the maximum value and the degree of variation during the present cycle. Further, the threshold level is calculated for each cycle as stated in Equation 5.3. The SIC is detected by determining first location in crank angle degree, where the signal crosses the threshold level as stated in Equation 5.4. The dynamic calculation of the threshold provides better accuracy than the static threshold because it avoids the detection of false peaks that might be present before start of combustion.

Equation 5.2 $DTE = \frac{dI_{ion}}{d\theta} [SOI, SOI + 6]$

Equation 5.3 $Threshold = [Max(DTE) + COV(DTE) \times 4 + 0.005] \times 2.1$

Equation 5.4 $SIC = Min.Location \left(\frac{dI_{ion}}{d\theta} > Threshold \right)$

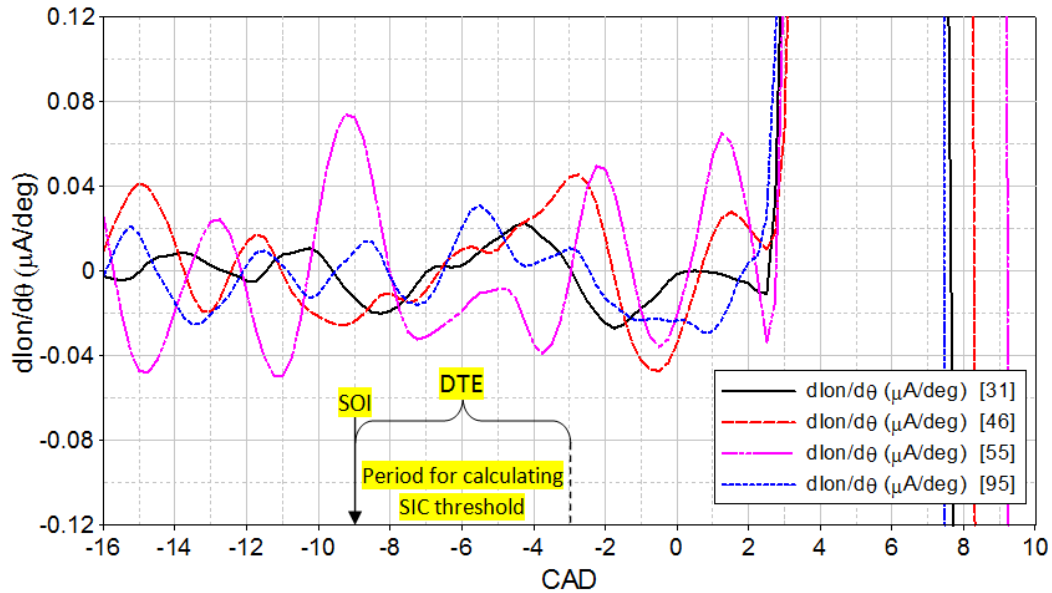


Figure 5.3. Derivative of the ion current signal of arbitrary cycles under steady state operation [JD, IMEP=5.5bar, Const. Speed=1800RPM, Inj. Press=1100 bar]

(v) Correction for the ion current misdetection:

The misdetection of ionization during idling and light loads represents a problem in using the ion current signal as feedback for engine control under these conditions. This problem needs to be solved and this paper presents one of the solutions.

Figure 5.4 shows a flow chart for the "SIC detection" correction needed at idling and light loads engine operation in order to account for the cycles, where the ion current exhibits misdetection. The SIC detection algorithm is configured to utilize the information obtained from a previous cycle in case of misdetection based on the following terms. If the SIC is detected, the SIC is sent as a feedback to the combustion controller. If misdetection occurs, instantaneous engine speed is consulted in making the decision to differentiate between misfiring and misdetection of the ion current signal.

During steady speed and acceleration, a previous successful detection of SIC is considered. Otherwise, the system indicates a misfire depicted by an instantaneous drop in engine speed.

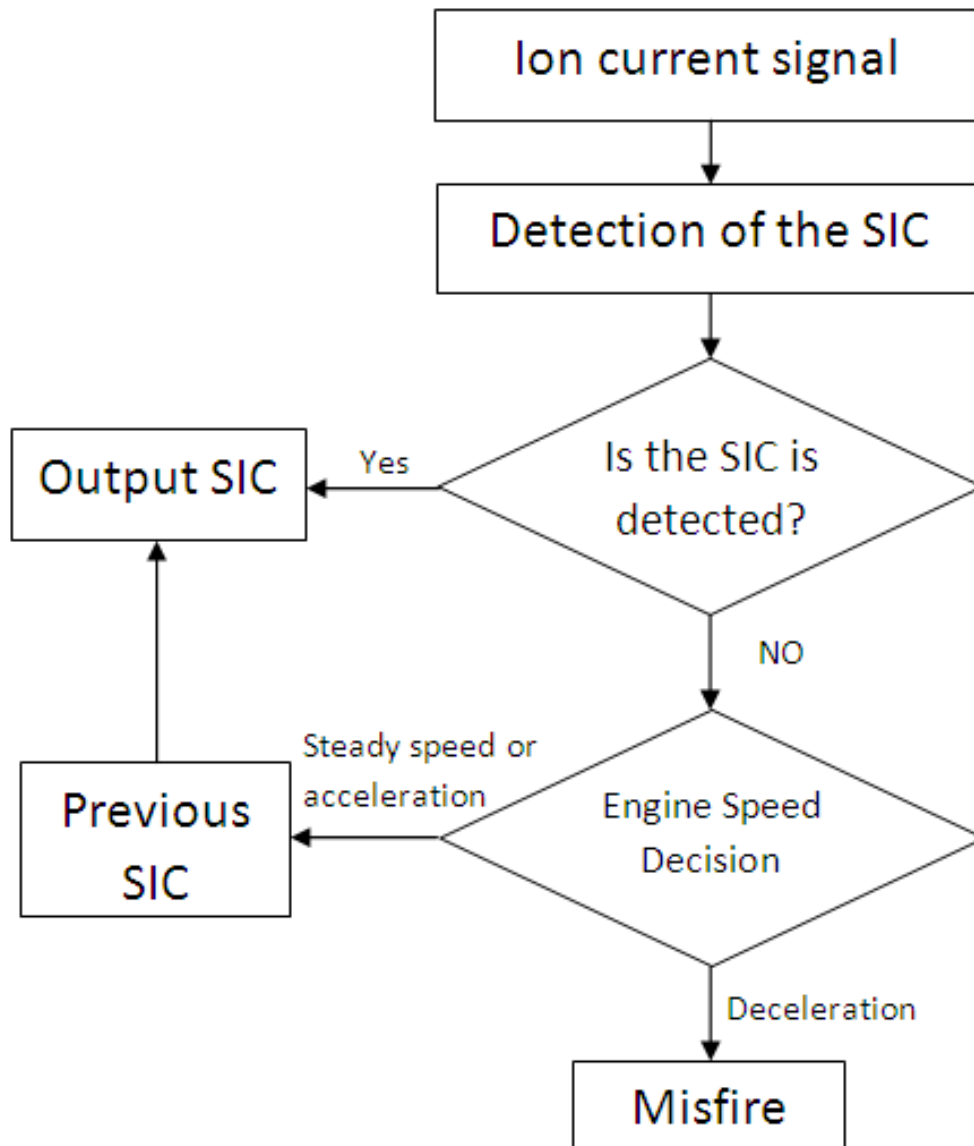
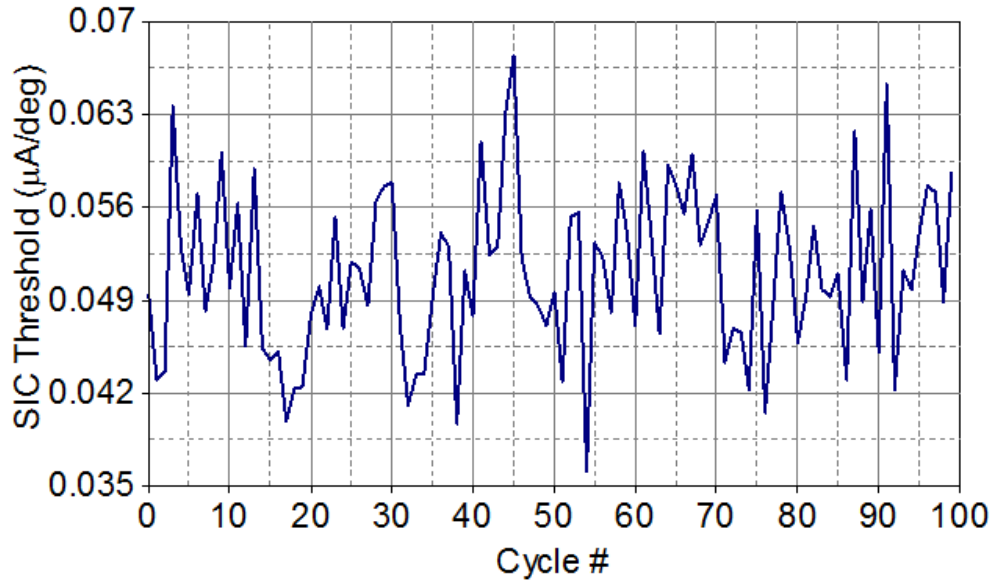


Figure 5.4. flow chart for "SIC detection" correction at idling and light engine loads

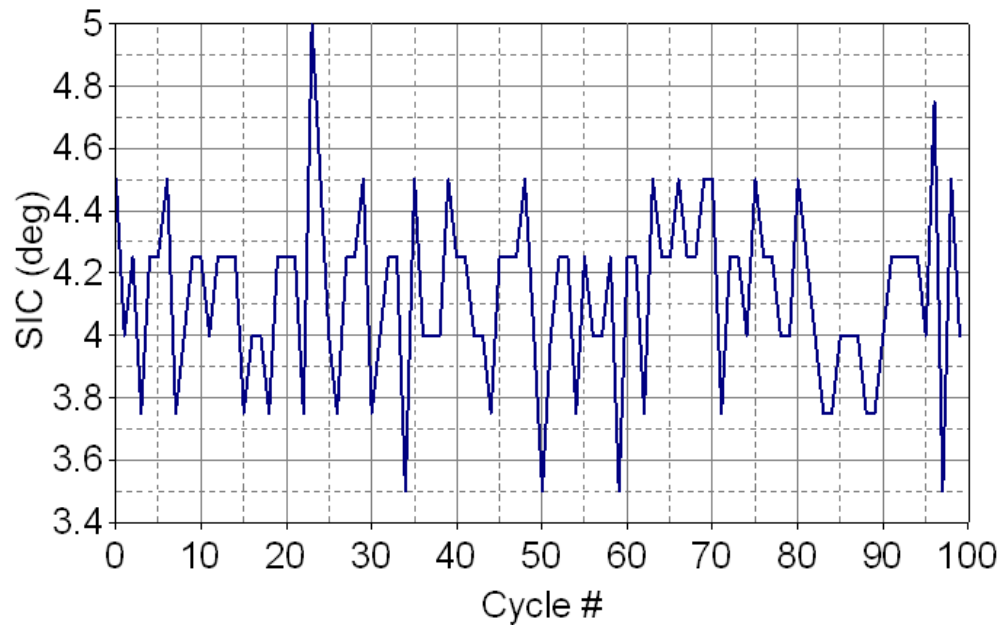
5.2.1 Results for SIC Detection

Figure 5.5a shows threshold values calculated to detect the SIC in a steady state engine operation for 100 consecutive cycles. The threshold is dynamically calculated for each cycle using SIC detection algorithm. The plot shows that the threshold reached a highest value of $0.067\mu\text{A}/\text{degree}$ and a lowest value of $0.036\mu\text{A}/\text{degree}$. The threshold recorded a mean value of $0.051\mu\text{A}/\text{deg}$ and a standard variation of $0.0061\mu\text{A}/\text{deg}$. Variations in the mean and spread of the threshold level are highly dependent on the noise recorded in the DTE after the SOI.

Figure 5.5b shows the SIC detected by using the dynamic threshold calculated and plotted in Figure 5.5a. The data shows a steady engine operation with a mean SIC at 4.1° aTDC and a standard deviation of 0.28 CAD. These results show that the SIC detection algorithm is capable of identifying noise characteristics of each cycle, where threshold levels are set accordingly to detect the SIC as accurate as possible.



(a)



(b)

Figure 5.5. a- Calculated threshold for the detection of the ion current signal and b- the detected SIC [IMEP=5.5bar, Const. Speed=1800RPM, Inj. Pres=1100 bar, # Cycles = 100]

5.3 Combustion Phasing Control

5.3.1 Controller design

The combustion phasing is designed such that the SIC will track a desired reference (SIC_{Ref}). This location can be set to achieve the production targets in fuel economy, efficiency and engine out emissions. Diesel combustion is known for its complexity and high non-linearity; therefore, a nonlinear control scheme is needed to achieve a good tracking performance. Fuzzy logic control has been used increasingly in the past three decades for industrial applications such as image processing for cameras, washers and cruise control for automotive applications (46; 47). In this work, a PD incremental Mamdani fuzzy logic controller (IFLC) is developed to control the phasing of the combustion process using the SIC as the feedback signal.

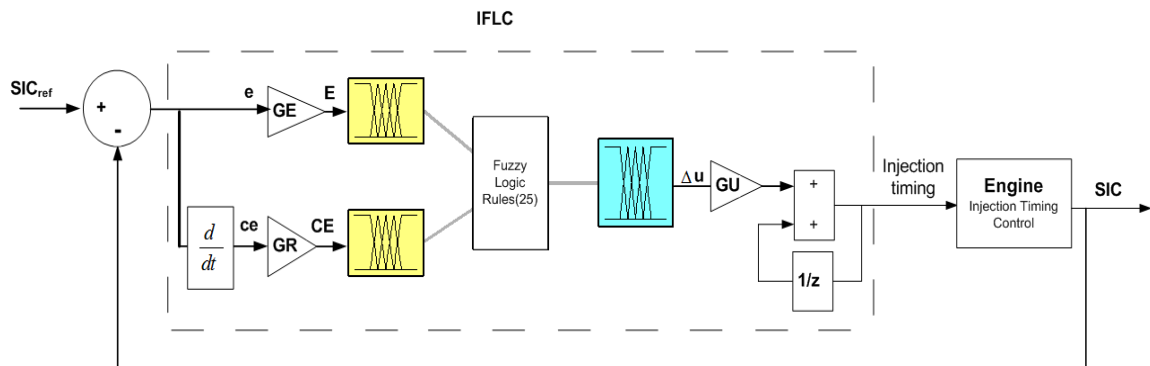


Figure 5.6. Block diagram for the fuzzy logic control system

Figure 5.6 shows the block diagram of the incremental IFLC controller, where normalize error (E) and the normalized error change (CE) are the input IFLC variables, and the injection timing is the IFLC output. The parameters used to tune the IFLC are the scalar factors GE , GR , and GU , which are the weights for the inputs and output variables respectively. Error (e) and error change (ce) are given as follows:

Equation 5.5 $e = SIC_{Ref} - SIC$

Equation 5.6 $ce = \frac{e(t) - e(t-\Delta t)}{\Delta t}$

Where Δt is the time interval between two consecutive cycles

The normalized error (E) is computed form the error as follows:

Equation 5.7 $E = GE \times e$

The normalized change in error (CE) is computed form the change in error as follows:

Equation 5.8 $CE = GR \times ce$

The variables E , CE and Δu have a linguistic sets partitioned into five parts (48). The domain of discourse of input and output variables is $(-1, 1)$. Normalized triangle membership function is used for both input and output membership functions. The number of control rules is 25 in the fuzzy system. The adopted fuzzy operators are the product as AND operator, the bounded sum as OR operator, min as implication method, the center of gravity (COG) as defuzzification method. Figure 5.7 shows a three-dimensional curve that represents the mapping for E , CE and Δu that generates the rule surface of the designed fuzzy control system.

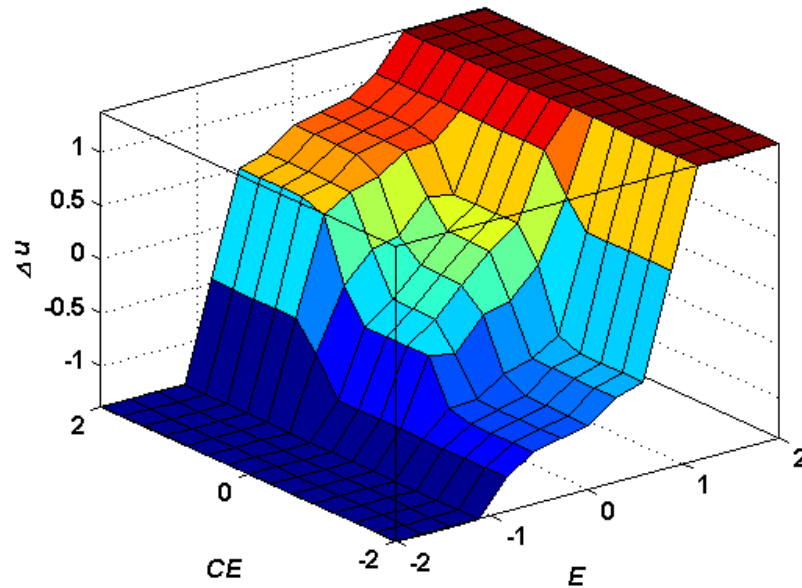


Figure 5.7. Rule surface of the combustion phasing fuzzy control system

5.3.2 Steady state and transient operation logic

In order to improve the performance of the fuzzy controller, a proportional factor is introduced for the output variable which is dependent on engine speed. This factor will adjust the controller response time according to the instantaneous engine speed.

Further, the fuzzy control system is employed with gains schedule by categorizing engine operation into steady or transient modes of operation. Two set of gains of the input and output variables are designed for steady state conditions "Slow mode" and transient state conditions "Fast mode". Figure 5.8 shows a block diagram of the fuzzy controller with scheduled gains. The logic of operation switches from fast to slow mode according to the following rules:

If $SIC_{Ref}(i) \neq SIC_{Ref}(i - 1)$

Switch = Fast Mode

Elseif $SIC - SIC_{Ref} > |Error_{Th}|$

Switch = Fast Mode

Else

Switch = Slow Mode

where (i) is the time step, and ($Error_{Th}$) is constant threshold in CAD.

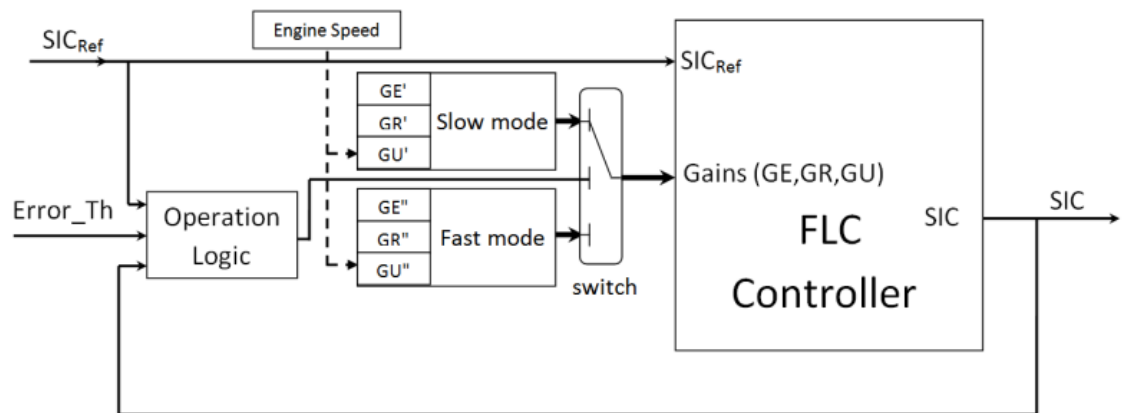


Figure 5.8. Block diagram for the fuzzy controller with scheduled gains

The logic of operation consists of a number of if-statements that starts with comparing the desired start of ion current to its previous value. If the SIC_{Ref} is changed in the ECU to a different location, the logic switches to fast mode gains. If SIC_{Ref} did not change, another condition is executed to compare between the error (e) and the threshold error ($Error_{Th}$). If the error is greater than $Error_{Th}$, the logic switches to fast mode gains.

Otherwise, the logic switches to slow mode gains. Error_{Th} is an absolute threshold value for the error that prevents the logic from switching to fast mode due to inherited cycle to cycle variations in the start of combustion. Thus, this allows the controller to be more stable during steady state engine operations.

Figure 5.9 shows results of a test conducted to evaluate the performance of the modified fuzzy logic controller with scheduled gains. The plot shows desired SIC_{Ref} , SIC, LPPC, and SOI. The desired SIC_{Ref} command was changed from 4 to 10° aTDC using a step function. During steady state operation, all logics are attributing toward the slow mode gains, where variations in the SOI are observed to be minimum. The fuzzy control system switches instantly from low to fast mode gains when the SIC_{Ref} changes from 4 to 10 ° aTDC. As soon as the operation satisfies steady operation, the logic shifts back to low mode gains. Likewise, the controller switches from slow to fast mode gains, when the desired SIC_{Ref} changes from 10 to 4° aTDC. Once again the operation satisfies for a steady state condition, the logic changes back to slow mode gains. It should be noted that the LPPC follows the same trend as the SIC, which is achieved by the controller through adjusting the SOI to the correct timing. Moreover, the change in the combustion phasing from 4 to 10° aTDC shows the system time response to be around 14 cycles at 1800 RPM (0.93 sec). The controller is evaluated by calculating the error (e), where the mean of $e = 4 \times 10^{-4}$ deg, median = 0 deg, and the standard deviation = 1.35 deg. This result indicates that the system has a fast response and high accuracy, and is being on target with a minimum variation during engine operation.

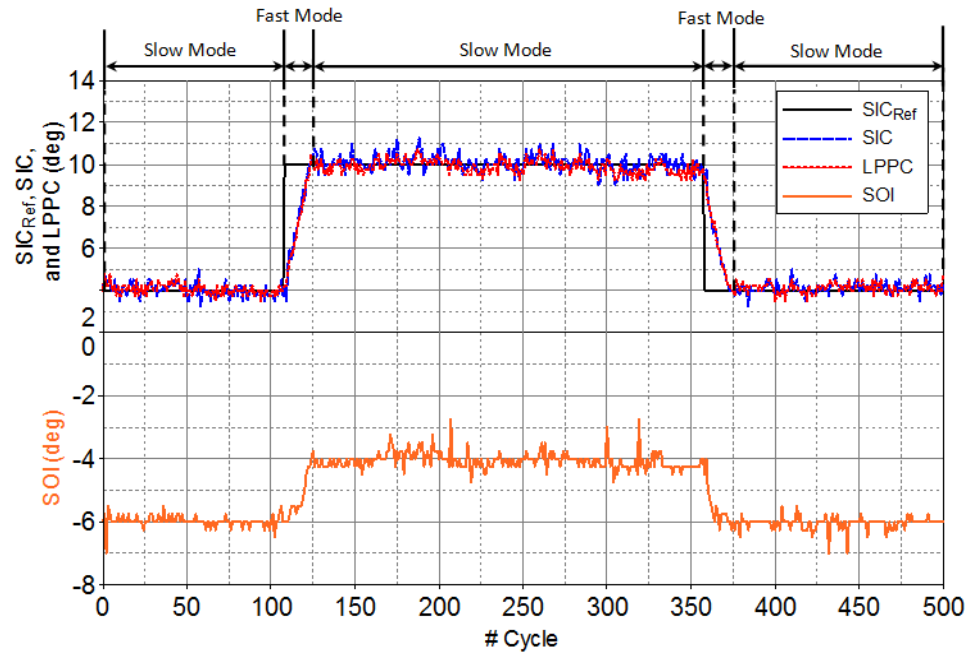


Figure 5.9. Performance of the fuzzy controller [JD, IMEP=7.5 bars, Const. Speed=1800RPM, SOI= Variable, Inj. Press=800bars]

5.4 Experimental results

ECU based on open loop combustion depends on look up tables and tolerance factors for the SOI to establish an estimate for the combustion phasing therefore it rarely operates on the intended combustion phasing. In addition, recalibration is required with engine aging. On the other hand, the closed loop control of the combustion phasing using the ion current signal is an inexpensive tool to monitor and adjust the combustion processes without considering tolerance factors or recalibration to account for engine aging. This section describes the experiments conducted to test the IFLC under steady and transient operations.

5.4.1 Operation under steady state conditions

A comparison is made between the operation under open loop control with constant injection timing and under closed loop using the IFLC. The data was recorded for 300 cycles at speed of 1800 RPM, injection pressure of 800 bar, and IMEP at 6 bar. Figure 5.10 shows the results with a constant SOI at 5.5° bTDC. The combustion phasing is seen constant with SIC and LPPC at 5.15° and 5.39° aTDC respectively. Table 5.1 shows statistical data such as mean, medium, range, and standard deviation. The cycle to cycle variations observed to be minimal with standard deviation for SIC and LPPC of 0.055 and 0.038 CAD respectively.

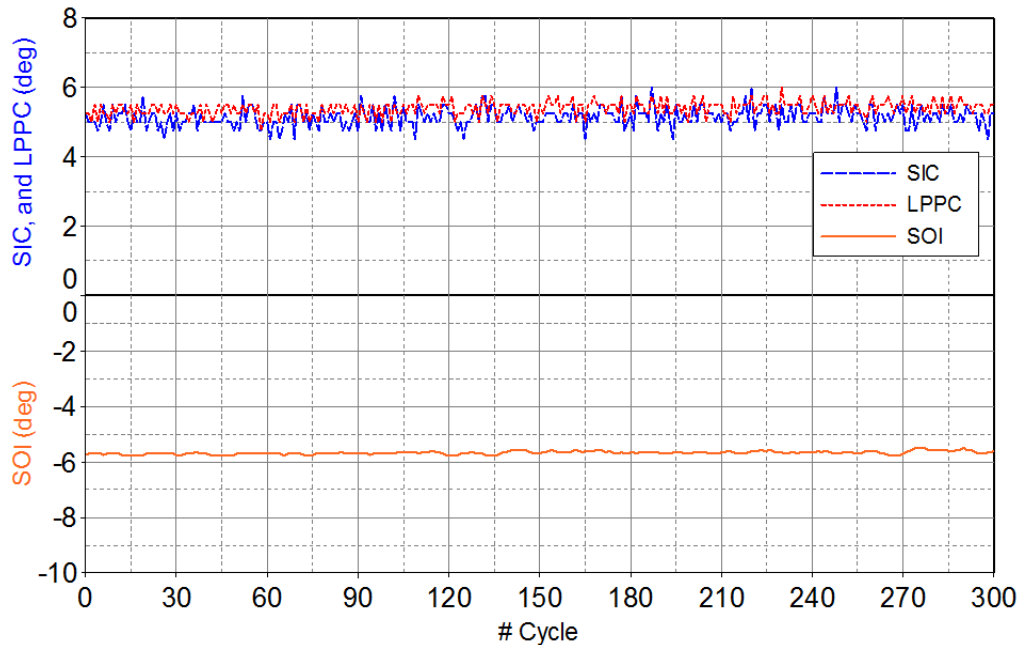


Figure 5.10. Open loop with constant start of injection [JD, IMEP=6bar, Const. Speed=1800RPM, Inj. Press=800bar, # Cycles = 300]

Table 5.1. Statistics for operation with constant start of injection

	SIC	LPPC
Mean (deg)	5.15	5.39
Medium (deg)	5.25	5.50
Range (deg)	1.50	1.25
St. Dev. (deg)	0.285	0.206

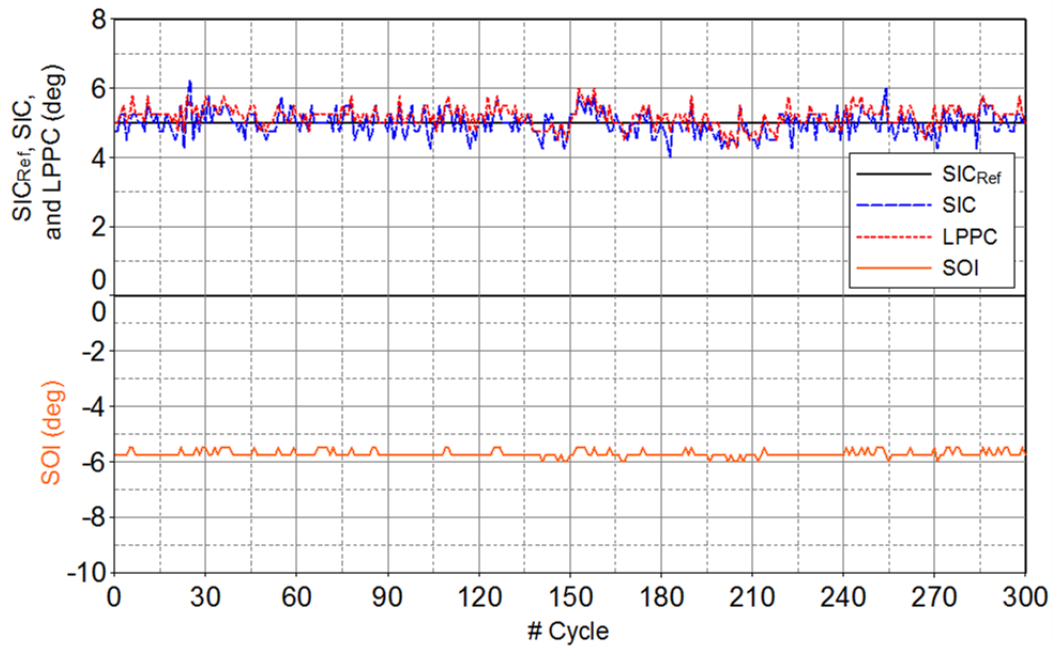


Figure 5.11. Closed loop IFLC enabled [JD, IMEP=6bar, Const. Speed=1800RPM, Inj. Press=800bar, # Cycles = 300]

Figure 5.11, shows the results for operation under the closed loop IFLC at the same conditions of Figure 5.10. The desired SIC_{Ref} is set at 5° aTDC. The IFLC adjusts the SOI accordingly to maintain the SIC at 5° aTDC. It is noticed that the results for the mean and the medium for the SIC are close to the desired SIC_{Ref} . The statistics for the operation under the IFLC are given in Table 5.2. The values for the Mean and Medium for IFLC are slightly closer to the desired setting compared to the open loop control given

in Table 5.1. However, slightly higher values are noticed in the Range and Standard Deviation.

Table 5.2. Closed loop IFLC enabled statistics

	SIC	LPPC
Mean (deg)	4.99	5.17
Medium (deg)	5.00	5.25
Range (deg)	2.25	1.75
St. Dev. (deg)	0.367	0.305

5.4.2 Operation under transient conditions

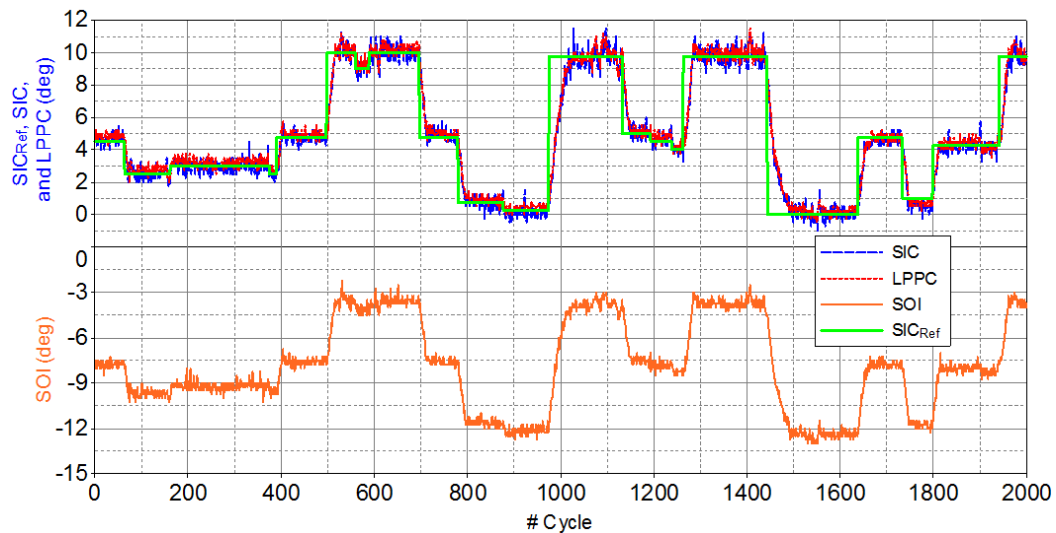


Figure 5.12. Response to desired changes in SIC in different steps between 0 and 10 CAD aTDC [JD, IMEP=6bar, Const. Speed=1800RPM, SOI=variable, Inj. Press=800bar]

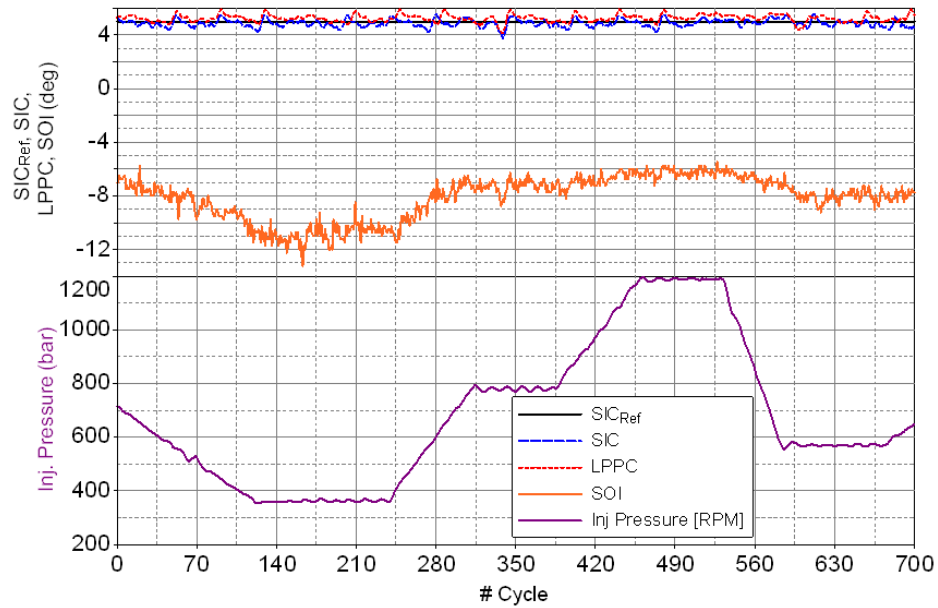


Figure 5.13. Response to change of the injection pressure from 350 to 1200bar @ Const. SIC 5° aTDC [JD, IMEP= 8bar, Const. Speed=1800RPM, SOI=Variable]

Three different types of transient tests were conducted on the engine using the IFLC in order to validate the effectiveness of the closed loop combustion phasing controller.

Figure 5.12 shows the performance of the combustion phasing controller, where the desired SIC_{Ref} is changed in a step function. The SIC_{Ref} is changed from 0 to 10° aTDC arbitrarily. The engine is operated at constant engine speed of 1800 RPM, injection pressure 800 bar, and IMEP = 6 bar. It is observed an advance in the SOI for early combustion phasing and vice versa. The results show a good performance of the controller by shifting smoothly from slow to fast mode depending on operating conditions.

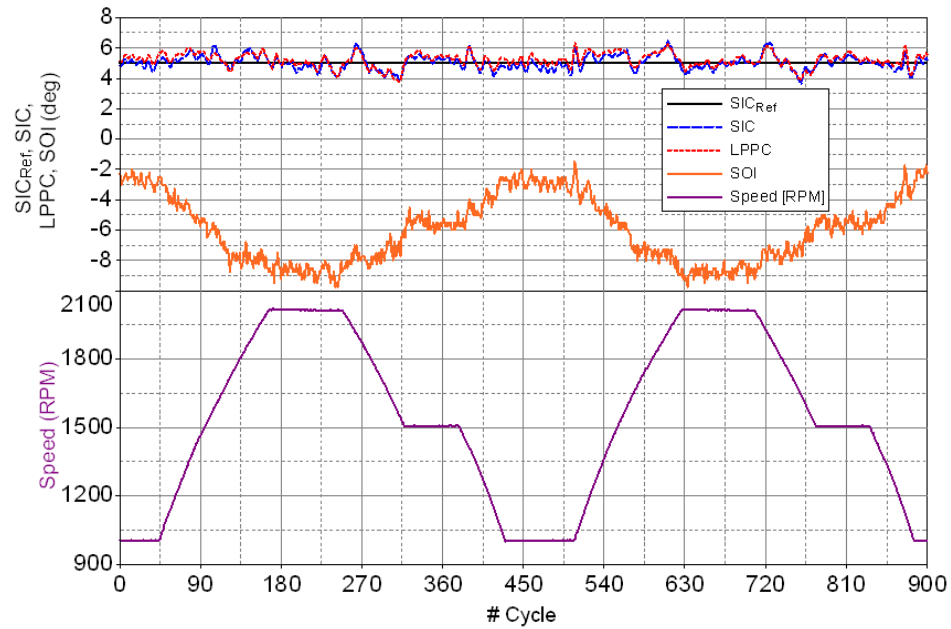


Figure 5.14. Change engine speed from 1000 to 2000RPM @ Const. SIC 5° aTDC [JD, IMEP= 2 - 7bar, SOI=Variable, Inj. Press=800bar]

Figure 5.13 shows the response to changes in the injection pressure, as it was increased and decreased using a ramp function from 350 to 1200 bar, while the desired SIC_{Ref} is pre-set at 5° aTDC. At higher injection pressure, the fuel injected has better atomization and mixing with the air which shorten the ignition delay period and accelerate the combustion process. Figure 5.13 shows that the closed loop combustion controller accounted for the drop in pressure from 700 bar in cycle 0 to 350 bar in cycle 120 by advancing the SOI from 7 to 13° bTDC. Similarly, the increase in injection pressure from 350 to 1200 bar resulted in retarding the SOI to 6°bTDC. It should be noted that changes in the ignition delay, LPPC and SIC are not linear with changes in injection pressure.

Figure 5.14 shows the response to engine acceleration, deceleration, and constant engine speed operation. The speed varied from 1000 to 2000 RPM. The SIC_{Ref} is pre-set at 5° aTDC and the injection pressure is kept constant at 800 bar. The closed loop combustion controller adjusted the SOI to account for the change in speed. The SOI is advanced from 2.5° bTDC to 9° bTDC as the speed increased from 1000 to 2000 RPM. Similarly, SOI retards as the speed dropped back to 1000 RPM.

5.4.3 Operation under low loads

An experiment was conducted at a light load to determine the response of the ion current probe to changes in the combustion process under un-warmed up or relatively low operating temperature conditions. Figure 5.15 shows the response to changes in the SIC from 1 to 11° aTDC at IMEP= 2 bar for 1000 cycles. At this low engine load, the ion current signal was not detected in 14% of the cycles. However, Figure 5.15 demonstrates the ability of the combustion controller to phase the combustion process and keep it on target in spite of the 14% misdetection of the ion current signals. Figure 5.15a shows a step change of the SIC_{Ref} from 1 to 6° aTDC, where the IFLC produced a steady response to achieve the desired target. Similarly, Figure 5.15b and Figure 5.15c show the stability and the response of the IFLC in achieving the desired combustion phasing regardless of the discrete and continuous misdetection of the ion current signal.

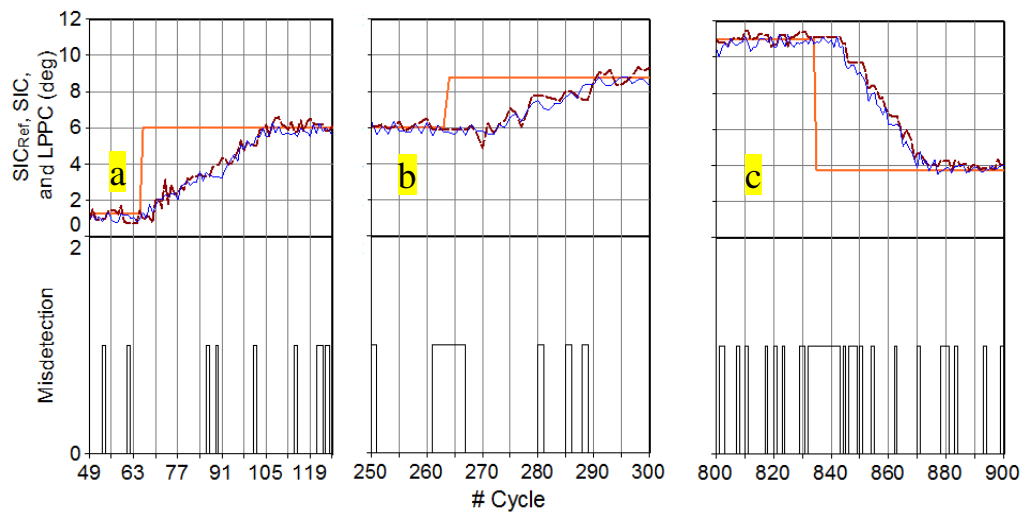
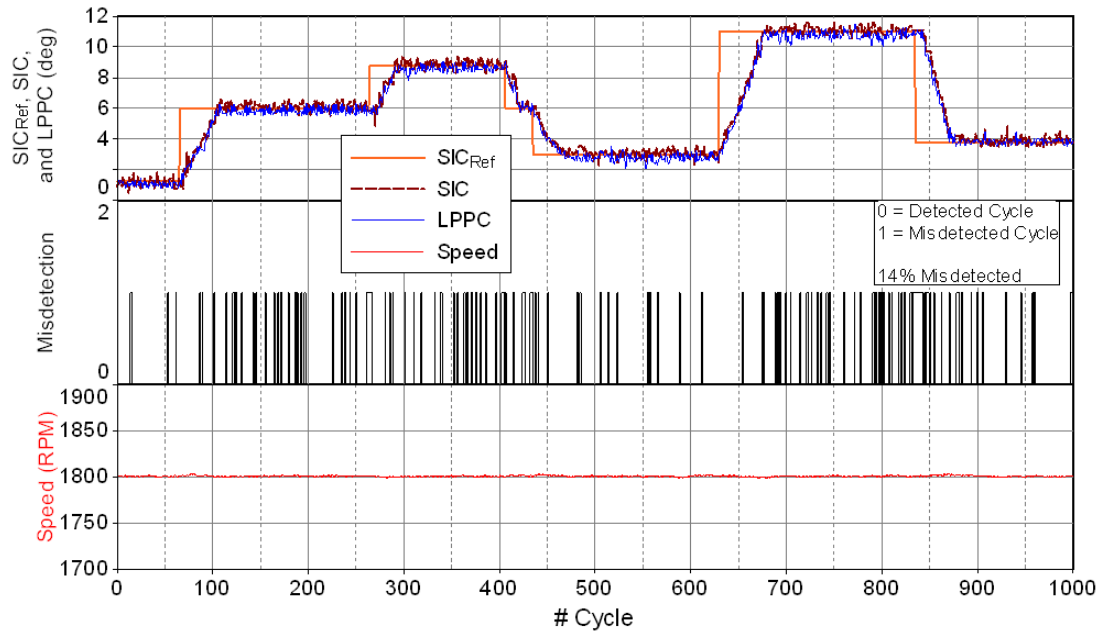


Figure 5.15. Change desired SIC from 1 to 11° aTDC [IMEP= 2bar, Const. Speed=1800RPM, SOI=Variable]

5.4.4 Operation with one injector deactivated at low load

An experiment was conducted to determine the ability of the combustion controller to perform its functions with one deactivated injector while the engine was operating at a low load. Under these conditions, the ion current would not be detected in the cylinder during deactivation as well as during firing due to the low operating temperature as explained in the previous section. Figure 5.16 shows results with the injector of cylinder number 1 deactivated while the engine was operating steadily at a constant speed of 1800 RPM, IMEP =2.5 bar and at constant combustion phasing at 4° aTDC.

Further, the figure shows two deactivation events and the following discussion will deal with the first deactivation. Figure 5.16c shows an engine deceleration starting at cycle 127, as the speed dropped from 1800 rpm to 1780 rpm, followed by acceleration back to 1800 rpm in cycle 193. Figure 5.16a shows traces for the SIC_{Ref} , SIC and LPPC. During injector deactivation, the SIC stayed on target at 4° aTDC, the value of the last detected firing cycle. Also, the LPPC dropped from 4.3° aTDC to a negative value indicating the absence of combustion. This is demonstrated in Figure 5.16e where RHR of the fired and misfired cycles is represented by 0 and 1 respectively. Figure 5.16b shows detected and misdetected cycles represented by 0 and 1 respectively. In this case, the misdetection indicates the absence of the ion current signal due to either misfiring or where combustion occurred, but the temperature was not high enough to produce a detectable ion current signal. The algorithm explained earlier utilizes the absence of ion current signal together with engine deceleration to indicate a misfiring cylinder as shown

in Figure 5.16d. This demonstrates the ability of the system in detecting a misfiring cylinder, or cylinders even at low loads when the ion current is not detected due to the low combustion temperatures.

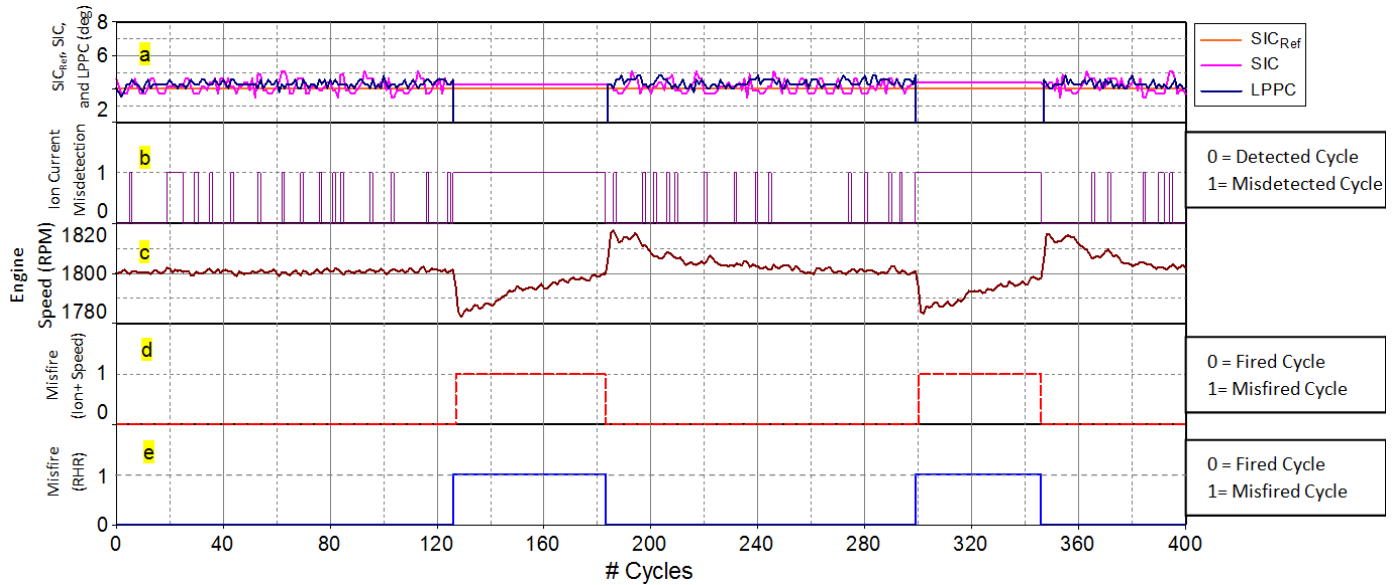


Figure 5.16. Traces for ion current, LPPC, and engine speed, with one deactivated cylinder [Constant. SIC at 4° aTDC, IMEP= 2.5bar, Speed=1800RPM, SOI=Variable]

5.4.5 Operation under different fuels

The following is a demonstration of using IFLC to control the engine and compare it with the open loop control. Figure 5.17 shows traces for peak cylinder pressure, SIC, LPPC, indicated mean effective pressure (IMEP), and SOI. It shows the variation of these parameters during 1900 cycles (3800 revolution in 152 second) in which the engine was supplied with (ULSD) fuel which has cetane number of 47 and a poor ignition quality fuel (JP-8) which has a cetane number of 31. It should be noted that JP-8 (CN=31) takes longer time to auto-ignite compared to ULSD (CN=47).

Figure 5.17 is divided into two sections. The first 750 cycles demonstrate the open loop controller results, represented by the symbol (P), in which the engine is operated under the control of its production ECU. Between cycles 900 to 1900, the engine was switched from the operation under the command of the production ECU to an open ECU that uses the IFLC close loop controller. The operation of using the close loop controller is represented by symbol (C). This experiment demonstrates the ability of the close loop controller to autonomous operate the engine on two fuels which have extremely different properties particularly cetane number.

Engine operation under the open loop controller:

Figure 5.17 shows that the engine operated steadily in the first 350 cycles using ULSD fuel. The value of the peak pressure is about 67 bar. The SIC and LPPC are at 4.5° CAD (crank angle degrees). The indicated mean effective pressure (IMEP) is at 3.85 bar and the start of injection (SOI) is at -7° CAD. After cycle number 350, the fuel supply is

changed from ULSD to JP-8. Using the open loop controller, the engine ECU did not change the SOI but it tried to maintain the IMEP constant by increasing the amount of fuel injected. During the fuel transition period P2, it is noticed that the peak pressure started to drop gradually because of the low ignition quality of the JP-8 fuel and reached a value of 44 bar, and the SIC and LPPC are retarded in the expansion stroke. The third period P3, that starts at cycle number 474, indicates that the engine suffered by operation using the low ignition quality JP-8 fuel since the combustion started very late as indicated by the SIC and LPPC. This caused a drop in the IMEP by 25%, from 3.85 to 2.90 bar.

Transition from the open loop to the close loop combustion controller:

At cycle 750, the fuel supply was shifted back to ULSD fuel, where the combustion started to advance and the engine IMEP increased back to 3.85 bar. At the end of this transition stage, the engine operation began under the close loop controller. The close loop controller operates the engine using the codes and algorithms developed and explained earlier in this chapter.

Engine operation according to IFLC of the close loop controller:

Engine cycles from 900 to 1400 are marked as C1 during which the engine operated steadily under the command of the close loop controller using ULSD fuel. It is noticed that the values for the peak pressure, SIC, LPPC, and SOI reached values similar to those under the open loop controller in P1 period. At cycle 1400, the fuel was changed from ULSD to JP-8. The complete transition to JP-8 fuel in period C2 ends at cycle 1570. It should be noticed that during the transition period C2, the open ECU advanced the SOI

from -7° to -11.5° CAD while the open loop controller did not change the SOI shown in period P2. Also, the peak pressure is kept constant at 67 bar under the command of the close loop controller while it dropped to 44 bar under the command of open loop controller. Furthermore, the IMEP is kept constant at 3.8 bar while it dropped to 2.9 bar under the open loop controller. This represents a drop of 25% in the power output of the engine by using the open loop controller.

The above test shows clearly the ability of the engine to maintain the same power output by using the close loop controller while the fuel changed from the conventional fuel to a fairly low ignition quality fuel.

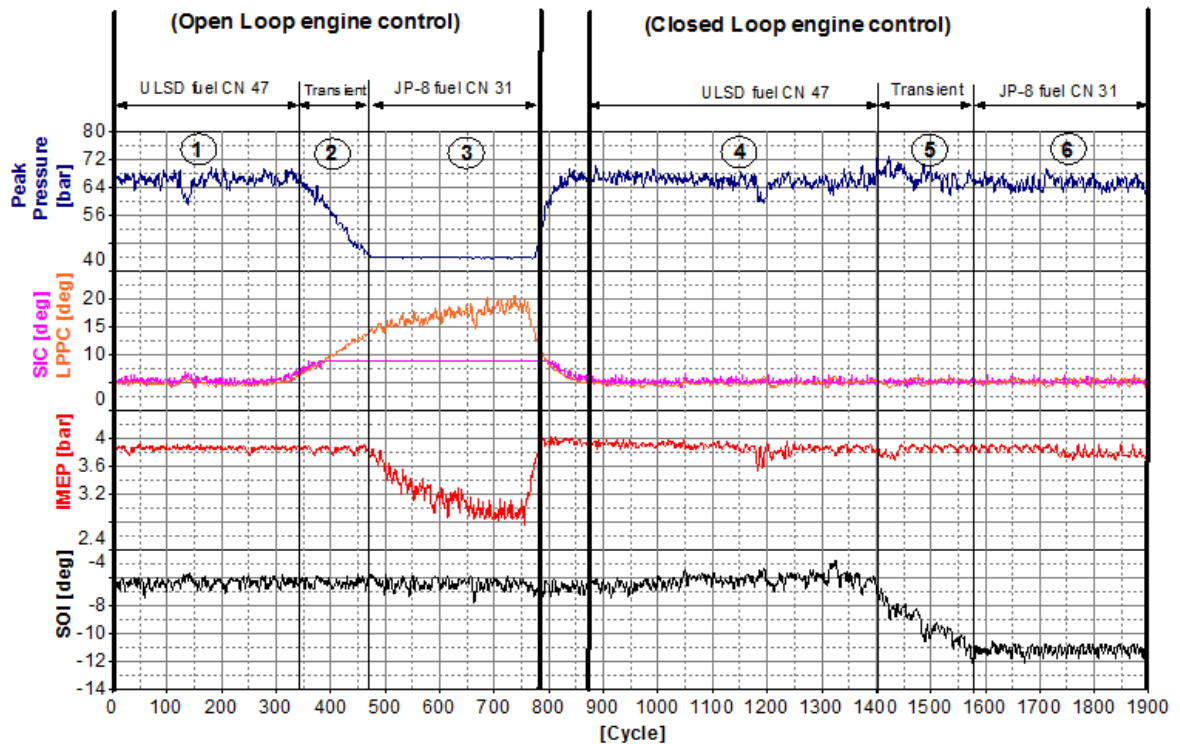


Figure 5.17. Response to change of the supplied fuel using open loop and close loop controller [JD, Const. Speed=1500RPM]

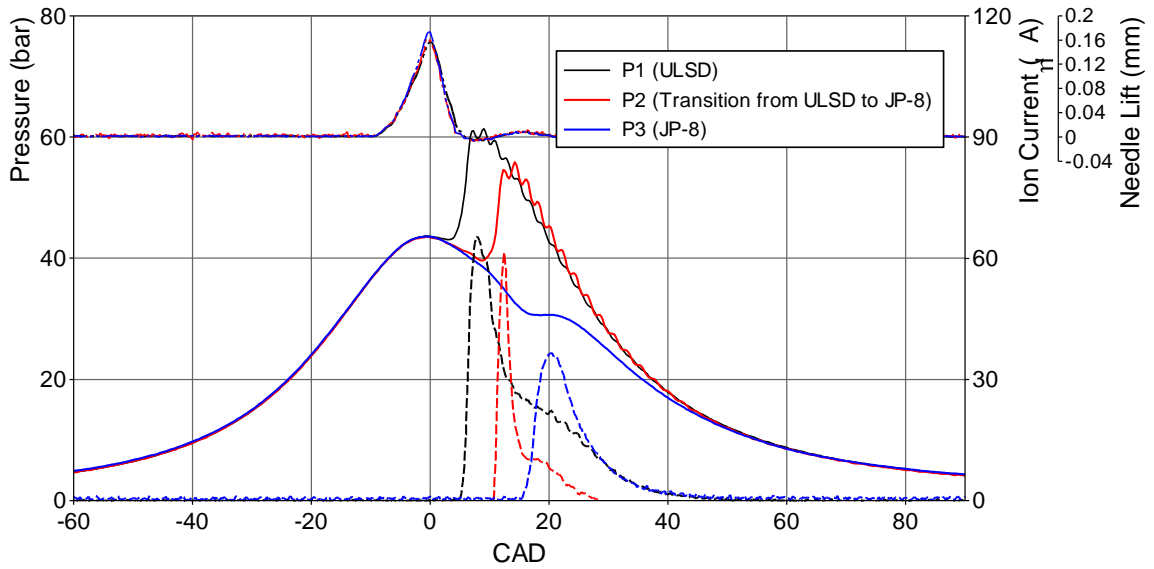


Figure 5.18. Traces for needle lift, cylinder pressure, and ion current using USLD and transition to JP-8 under the command of the open loop controller [JD, Const. Speed=1500RPM, Inj. Press=600bar]

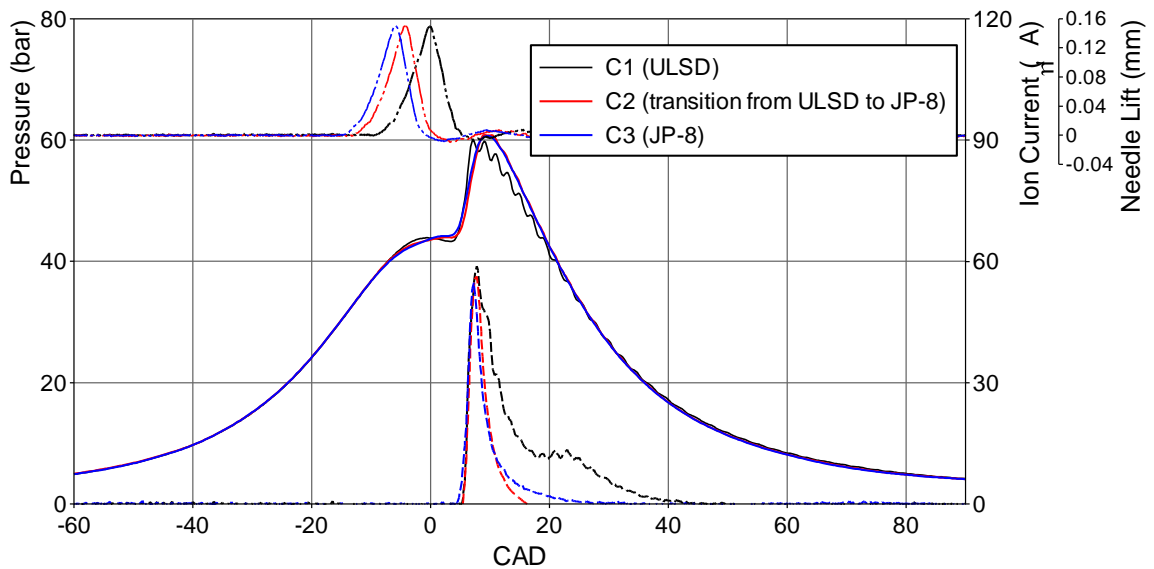


Figure 5.19. Traces for needle lift, cylinder pressure, and ion current using USLD and transition to JP-8 under the command of the close loop controller [JD, Const. Speed=1500RPM, Inj. Press=600bar]

Figure 5.18 and Figure 5.19 show traces for the needle lift, cylinder gas pressure and ion current under the command of the open and close loop controllers respectively. It should be noticed that the start of the needle lift is controlled, based on the feedback for the timing of the ion current signal to keep the combustion phasing the same for the two fuels.

5.5 Summary

The technique of in-cylinder ionization sensing in a diesel engine has been described. The development and implementation are demonstrated for a closed loop combustion phasing controller based on real time cycle-to-cycle feedback, using the start of ion current detection. The main results can be summarized as follows:

1. An incremental fuzzy logic controller (IFLC) is developed to control the phasing of the combustion process in a direct injection diesel engine, utilizing the ion current as feedback signal to the ECU.
2. IFLC demonstrated a fast response in phasing the combustion process under steady and transient operating modes of a warmed up engine.
3. IFLC accounted for the low amplitude or missing ion current signals in some cycles while the engine is operating under light loads and un warmed up conditions. The logic controls the combustion phasing during these cycles as well.

4. IFLC demonstrated its ability to differentiate between missing ion current signals due to low temperatures in fired cycles and due to complete misfiring cycles caused by system malfunctions. Accordingly, it can be used for misfiring detection.
5. Autonomous operation on fuels of different specifications without additional cost in engine production is possible while maintaining the production target in power and fuel economy.

CHAPTER 6

COMBUSTION RESONANCE IN DIESEL ENGINES

Resonance is a phenomenon that occurs due to the oscillations of burned gases in the combustion chamber that produce engine vibration and noise. The combustion resonance is excited at a range of frequencies much higher than the engine structural vibration. These oscillations are generated in gasoline engines due to the auto-ignition of the end gases producing undesirable noise called "Knock". In diesel engines, these oscillations are produced from the high rates of pressure rise due to the premixed combustion.

This chapter covers a detailed analysis of the combustion resonance in a diesel engine that includes a comparison between results obtained from different sensors such as the pressure sensor, accelerometer and the ion current sensor.

6.1 Experimental setup

The experimental test was carried out on the John Deere 4.5 liter, 4-cylinder turbocharged diesel engine. This study covers the analysis of the combustion resonance using three different sensors. The ion current sensor and the pressure transducer are in-cylinder sensors and the accelerometer is mounted on the engine surface. Engine setup and instrumentations are shown in details in Chapter 3.

6.2 Background and literature review

Several investigations used accelerometers mounted on the engine body to measure the vibrations produced from the combustion resonance (49-54). Other investigations used pressure transducers to obtain information about the combustion resonance (49-51; 55).

Payri and Broatch developed a procedure for decomposing the pressure signal into three different components compression signal, combustion signal and resonance signal (56; 57), where they showed that the combustion signal is mostly controlled by engine speed and the resonance signal is controlled by engine load.

Arnone et. al. studied the effect of different accelerometer orientation on the engine block. The horizontal accelerometer indicated less sensitivity to combustion process as mostly was influenced by mechanical components of engine vibration. On the other hand, the accelerometer mounted vertically was sensitive to combustion and resonance produced vibration.

In gasoline engines, the combustion resonance has been thoroughly investigated and found to cause engine knock due to the ignition of the end gases. The analysis and detection of engine knock were conducted using different sensors such as accelerometer, a pressure transducer, or an ion current sensor (33; 58-60).

Asano et. al. modified the ignition circuit of a spark ignition engine to utilize the spark plug as an ion current sensor in order to find a correlation between the ion current signal and knocking (61) and developed an algorithm that depends on resonance variation and ion current peak value to control engine knock.

Ohashi et. al. proposed a different method for counting for the knock detected by the ion current signal by digitalizing the knock period to a counter, where the counter increase at higher knock occurrence (62). A controller based on the spark advance and feedback for the knocking pulse counts was demonstrated.

In diesel engines, the combustion resonance oscillations are produced from the high rates of pressure rise due to the auto-ignition of the premixed combustion (55; 57; 63-65). Khaira et. al. investigated the effect of injection pressure, timing, load and speed on the engine loudness produced resulted from combustion resonance (65), where the rate of pressure rise was found to be the main source for engine loudness.

Different techniques have been developed to interpret the combustion resonance such as the Fast Fourier Transform (FFT) which is used for the frequency domain analysis (66), Short-Time Fourier Transform (STFT) (67) and Discrete Wavelet Transform (DWT) for time-scaled-frequency analysis (68; 69). Other indirect techniques of resonance detection are based on the rate of pressure rise (55; 70) and the rate of heat release (71).

In this study, an ion current sensor is used together with a pressure transducer and an accelerometer to detect combustion resonance produced in a heavy duty direct injection diesel engine.

6.3 Signal processing

6.3.1 Analytical approach

The pressure waves produced from combustion resonate at a certain frequency depend mainly on the speed of sound and geometry of the combustion chamber (56; 72). Assuming that the cylinder is filled with air at 2000 K, the speed of sound, C_{cyl} , is given by:

$$\text{Equation 6.1} \quad C_{cyl} = \sqrt{k.R.T} = \sqrt{1.28 \times 287 \times 2000 K} \approx 857 \frac{m}{sec} \quad C_{cyl} = \sqrt{k.R.T} = \sqrt{1.4 \times 287 \frac{J}{kg.K} \times 2000K} \approx 896 \frac{m}{sec}$$

where

k is specific heats ratio of air at 2000K

R is the air gas constant

T is the gas temperature

Thus, the resonance frequency can be calculated by

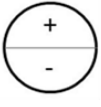
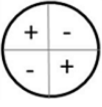
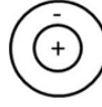
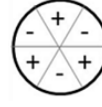
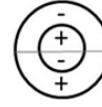
$$\text{Equation 6.2} \quad f_{Res} = \frac{C_{cyl} \cdot \alpha_{m,n}}{\pi \cdot B} = \frac{C_{cyl} \cdot \alpha_{1,0}}{\pi \cdot B} = \frac{857 \frac{m}{sec} \times 1.841}{\pi \cdot 0.106 m} \approx 4.7 kHz$$

Where

$\alpha_{1,0}$ is the wave number for the 1st mode of vibration

B is the cylinder bore in meters

Table 6.1. Vibration mode shapes for a cylindrical chamber and their corresponding resonance frequencies

Mode Shape (m,n)	 1 (1,0)	 2 (2,0)	 3 (0,1)	 4 (3,0)	 5 (1,1)
$\alpha_{m,n}$	1.84	3.054	3.832	4.201	5.332
f_{Res} (kHz)	4.6	7.9	9.9	11.0	13.8

The vibration mode shapes shown in Table 6.1 are calculated using the wave equation to obtain different oscillation mode shapes of pressure waves (58). The pressure waves are assumed to be in an elastic medium enclosed in a circular cylinder. The wave equation is solved for cylindrical coordinates using the Bessel function (33; 58; 73; 74). The first five transverse modes are calculated using Equation 6.2 and listed in Table 6.1, where radial, circumferential oscillations and their combinations are considered. The axial modes are neglected since combustion phasing is constant at LPPC 4° aTDC.

6.3.2 Analysis of combustion resonance

(i) Combustion resonance detection using the ion current signal

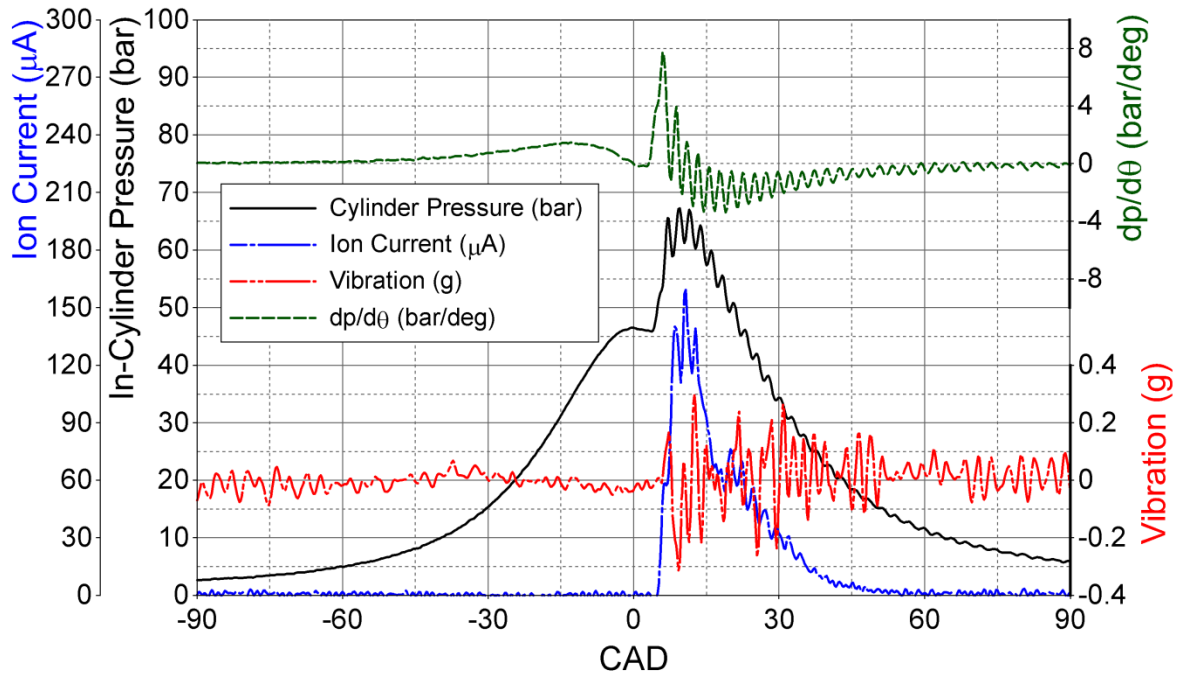


Figure 6.1. Typical cylinder pressure trace, ion current and vibration signals, [JD, Cyl#1, ULSD, 0% EGR, 1800 RPM, LPPC 4° aTDC, Inj. Press. 800 bar, and IMEP 6 bar]

Figure 6.1 shows typical traces acquired in a test at 1800 rpm, IMEP = 6 bar, injection pressure = 800 bar and LPPC (Location of the Peak RHR due to Premixed Combustion) at 4° aTDC. The traces are for the cylinder gas pressure, pressure derivative ($dp/d\theta$), ion current and accelerometer output, during the compression and expansion strokes. Combustion resonance is initiated by a sharp increase in gas pressure rise with a maximum rate of 7.6 bar per crank angle degree, and starts at 3.25° aTDC. This sharp

increase in gas pressure produced a wave with amplitude of 8 bar, followed by waves with lower amplitudes, that eventually disappears after 45 crank angle degrees.

The ion current increased at a sharp rate, almost immediately after the start of the pressure rise due to combustion. This indicates the presence of high concentrations of ions and electrons as a result of a sharp rise in combustion temperature. The waves in the ion current indicate the presence of similar waves in the temperature and the concentration of the chemically ionized and thermally ionized species (9; 26). The ion current waves produced from the premixed combustion fraction decayed at 13 degrees and are followed by another set of waves with lower amplitudes that diminishes after 45 crank angle degrees.

The engine vibration trace produced by the accelerometer starts at 5 CAD after the pressure waves. This is the time taken for the stresses produced by the gas pressure forces to reach the location of the accelerometer on the outer surface of the engine.

(ii) Analysis of unfiltered signals in frequency domain

In order to use the Fast Fourier Transform (FFT), the cylinder gas pressure signal is plotted using a reference of $P_0 = 20\mu\text{Pa}$ (56); this is a reference of the smallest pressure level possible to be heard by a human. Similarly, the ion current and the vibration signals are plotted in FFT using the same reference value.

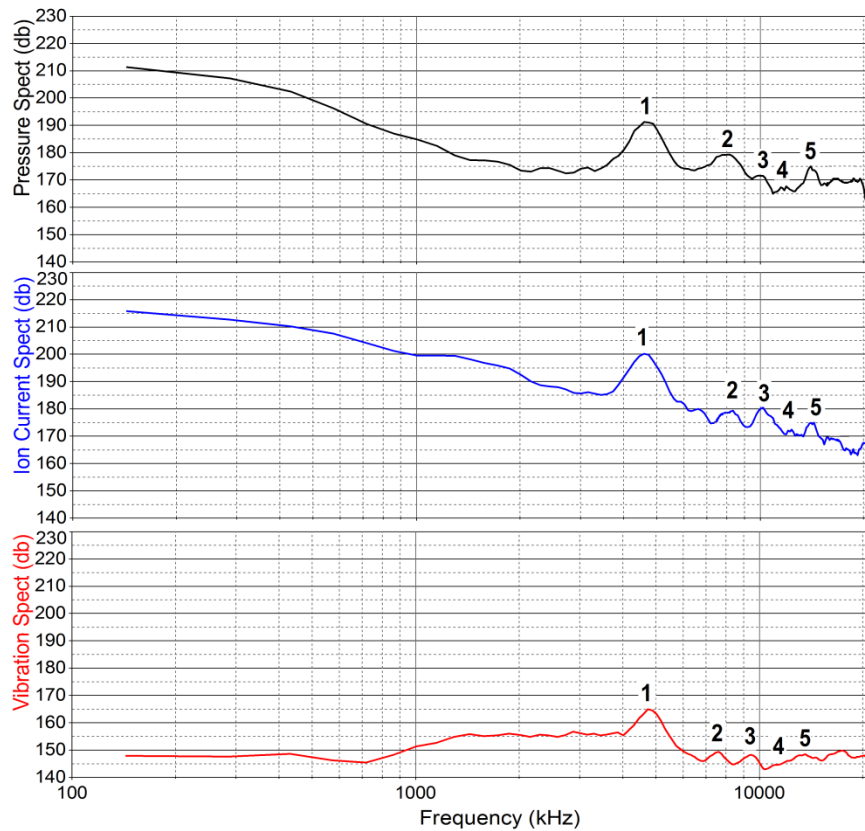


Figure 6.2. FFTs analysis for the unfiltered signals for cylinder pressure, ion current and engine vibration

A Fast Fourier transform is used for the overall spectral analysis of the signals, shown in Figure 6.2, before applying any filters. The resonance frequencies calculated using the analytical approach in Table 6.1 agree with the FFT spectrum of the signals for the cylinder pressure, ion current and engine vibration. It is also clear that the 1st mode which appears at 4.6 kHz has the highest amplitude compared to the other modes. This is followed by the 2nd mode at 7.9 kHz. The resonance frequencies over 9 kHz are subjected to high noise to signal ratio and are not considered in this investigation. In order to

investigate the frequencies of interest, a band pass filter from 3 to 9 kHz applied to the three signals.

(iii) Analysis of filtered signals in time domain

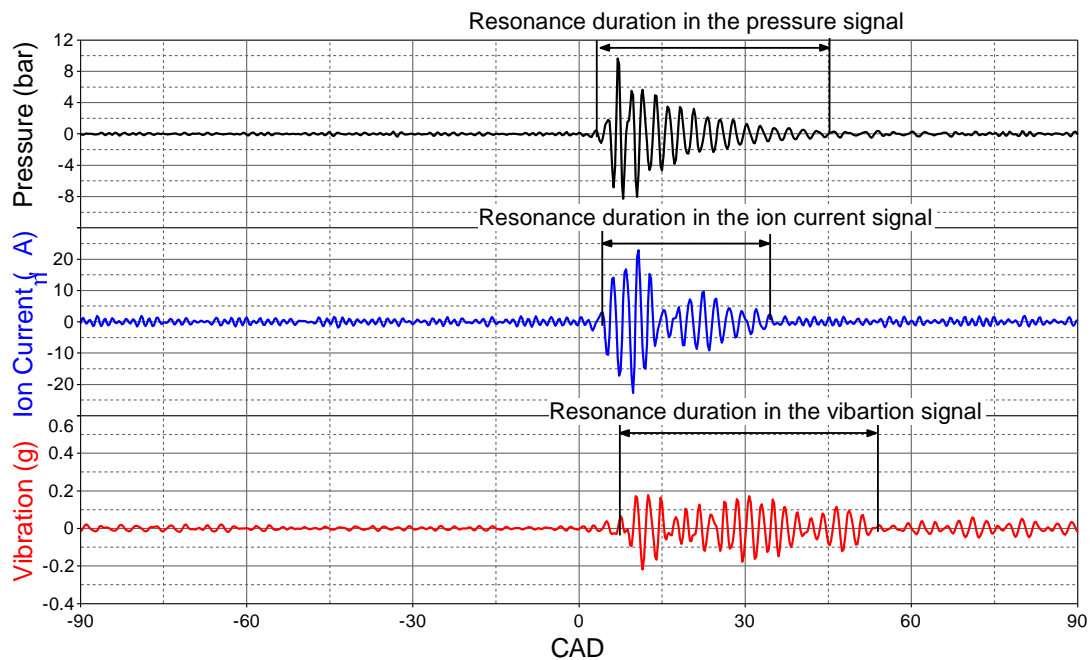


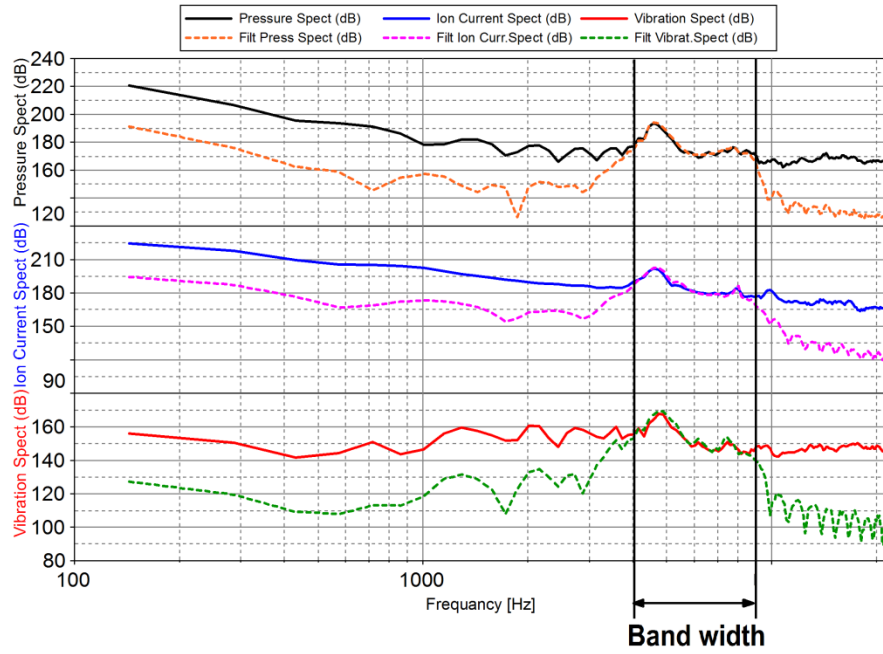
Figure 6.3. Filtered cylinder pressure, ion current and vibration signals using a band pass filter 3 to 9 kHz

Figure 6.3 shows the characteristics of the filtered signals. There is a phase shift in the start of the signals. The cylinder pressure is the first, followed by the ion current and the engine vibration. The delay of the ion current signal after the cylinder pressure signal is related to the position of the probe relative to the fuel sprays, in addition to the local gas temperature (9).

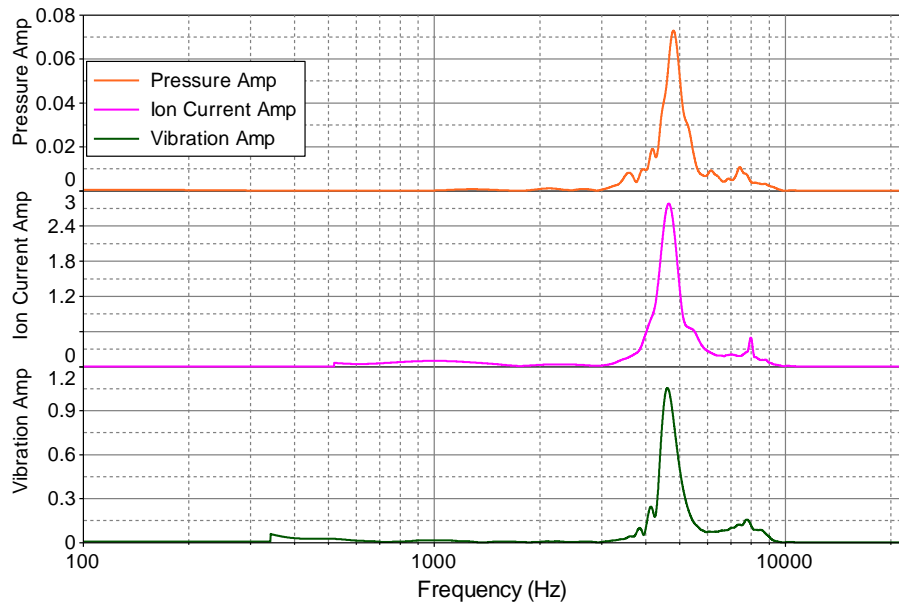
There is a difference in the duration of the signals in Figure 6.3. The longest is the engine vibration, caused by the behavior of the engine elastic components. This is followed by the cylinder gas pressure and the ion current signals. The oscillations in the pressure signal are the result of the pressure waves developed during the combustion process which are being damped later toward the end of combustion. In the case of the ion current signal, the probe detects the oscillations of ions that travel with the pressure waves that decay in the expansion stroke. However, the probe detects another set of oscillations at 15 degrees aTDC and remains for 20 CADs. These oscillations are caused by the ionization produced from the mixing and diffusion controlled combustion.

(iv) Different spectral representations of the signals

The signals are processed using the FFT, where the filter and unfiltered spectra are plotted Figure 6.4a. The filtered spectrums highlight the amplitude of the resonance of the first two vibrating modes. Figure 6.4b also shows the intensity of the combustion resonance for the first two vibration modes, plotted in power spectra. Both plots give an overall representation of the combustion resonance amplitudes and their corresponding frequencies, produced during a combustion cycle.



(a)



(b)

Figure 6.4. (a) FFTs analysis for the filtered and unfiltered signals for cylinder pressure, ion current and engine vibration, (b) Power spectra of the filtered signals.

(v) Time- Frequency analysis of the filtered signals using STFT

The characteristics, explained earlier are shown in Figure 6.5, using the short-time Fourier transform (STFT). The advantage of using STFT over the conventional FFT is that it facilitates the interpretation of the resonant frequencies in a time domain. It permits processing the signal by decomposing it into short frames (window) and computing the spectrum of each frame (69; 75). A Gaussian window is used for the computation with an overlap of 40%. In Figure 6.5, the STFT plot combines the information for, the filtered waveform shown under each plot, and the FFT plot shown on the left side.

Further, the STFT plots for the filtered signals of the ion current, cylinder pressure, and vibration in Figure 6.5 show timings, phase shifts, amplitudes, and frequencies of the combustion resonance for the 1st and 2nd modes during a combustion cycle. Also, the STFT analysis clearly shows that the ion current and pressure signals have distinguished peaks for the first two resonance modes than the vibration signal. The red areas in the figure represent severe combustion resonance which is detected by the three sensors as it persists for about 34° CAD.

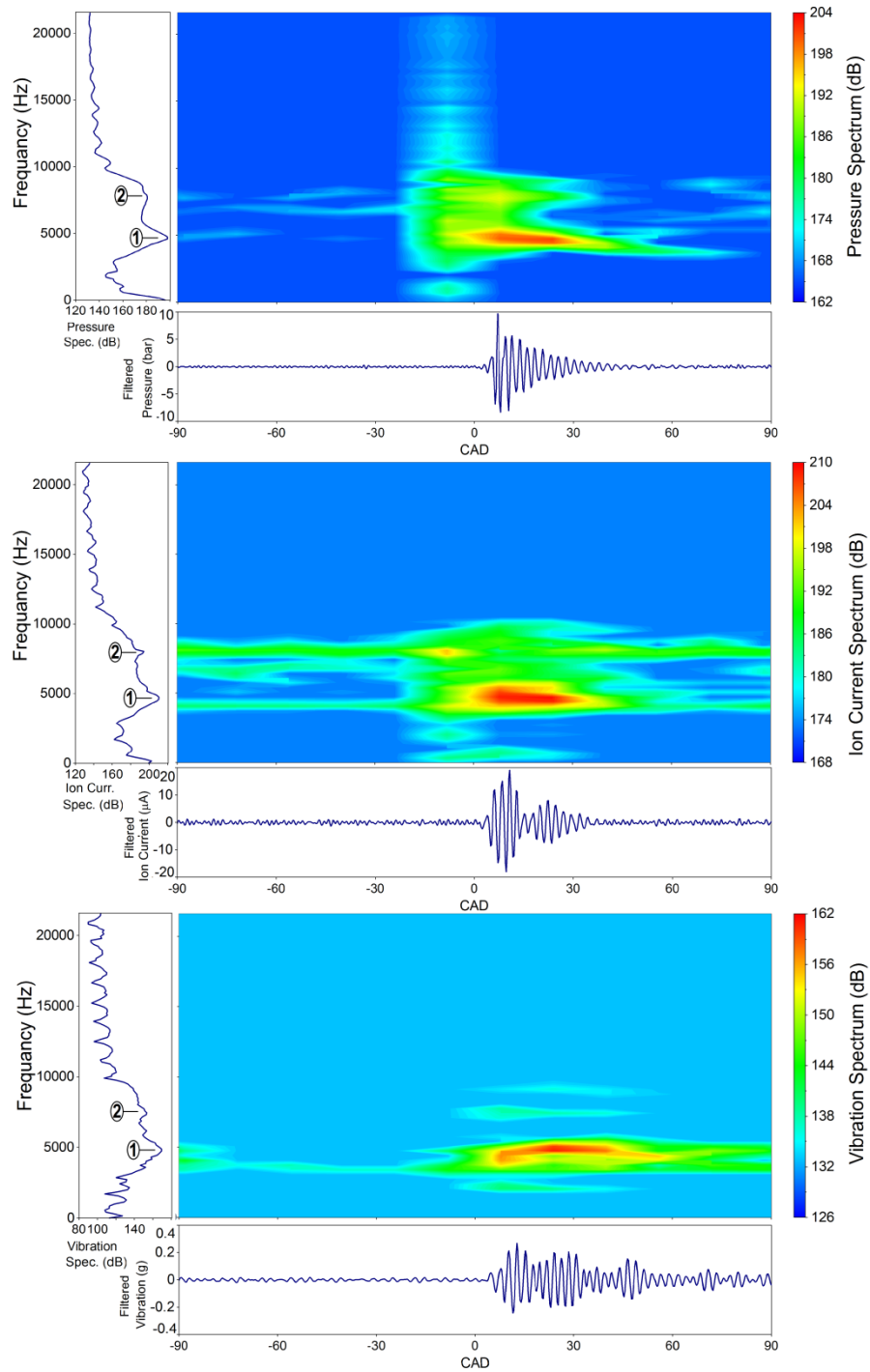


Figure 6.5. STFTs analysis for the filtered signals, [JD, Cyl#1, ULSD, 0% EGR, 1800 RPM, LPPC 5° bTDC, Inj. Press: 800 bar, and IMEP: 6 bar]

(vi) Benchmark combustion resonance of the ion current signal

The 1st mode of the combustion resonance adhere the highest magnitude compared to the other higher frequency modes. Figure 6.6 shows that a linear relationship exist between the 1st mode of the combustion resonance determined from the ion current signal and the resonance determined from the in-cylinder pressure and vibration signals with cofficients of determinations $R^2 = 0.809$ and 0.764 respectively. Thus, the ion current sensor could be used in replacement to the pressure sensor and the accelerometer to detect resonance.

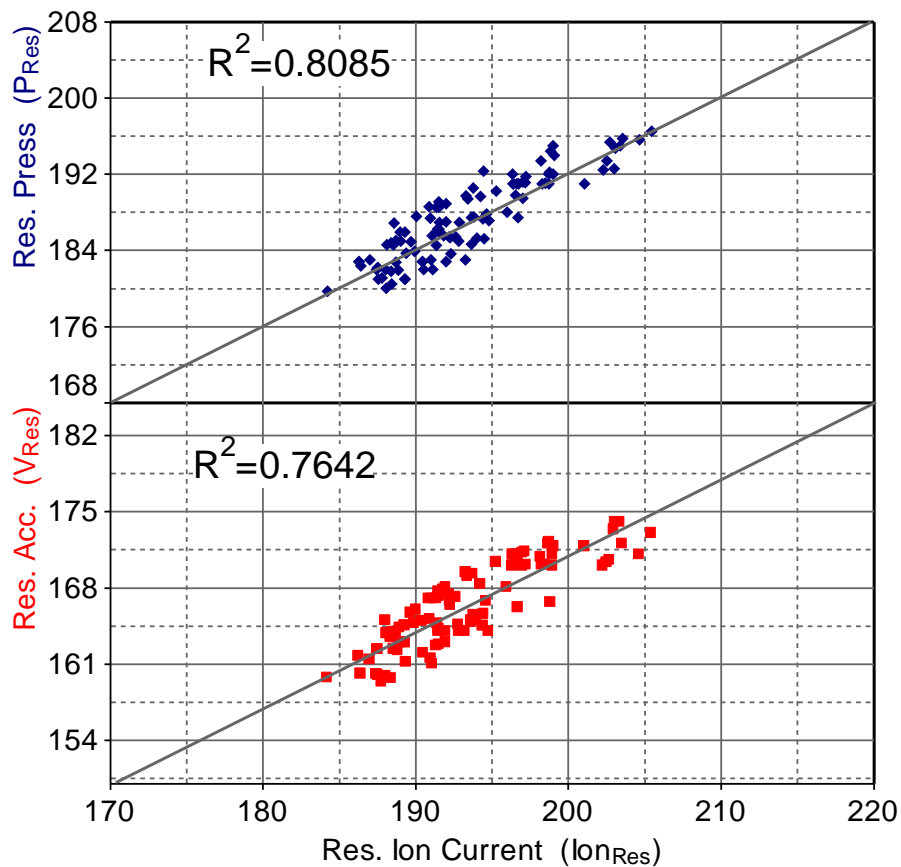


Figure 6.6. Combustion resonances 1st mode determined from the ion current plotted versus resonance determined from the pressure and vibration signals

6.3.3 Advanced combustion resonance interpretation

Further analysis for the detection of combustion resonance is discussed in this section. An accurate method to compute the combustion resonance in time domain is required to gain a deep understanding of combustion resonance produced during a combustion cycle.

(i) Continuous wavelet transform of the filtered signals (CWT)

The continuous wavelet transform (CWT) is used to analyze the frequency evolution of a one-dimensional time signal in the time–frequency plane. Both CWT and STFT are based on linear transformations. The CWT has advantages over the STFT since the spectrogram generated by the STFT is limited in resolution by the extent of the sliding window that has a fixed resolution. In STFT, smaller time window results in better time resolution, but leads to worse frequency resolution, and vice versa. On the contrary, the CWT is capable of achieving variable resolution in one domain (either time or frequency) and multi-resolution in the other domain (76).

Figure 6.7 shows the spectrums for the filtered cylinder pressure, ion current, and vibration signals in CWT spectrogram. The results showed by the CWT for the 1st and 2nd modes of resonance in term of timing, phase shift, amplitude and frequency are more detailed compared to the STFT results shown in Figure 6.5.

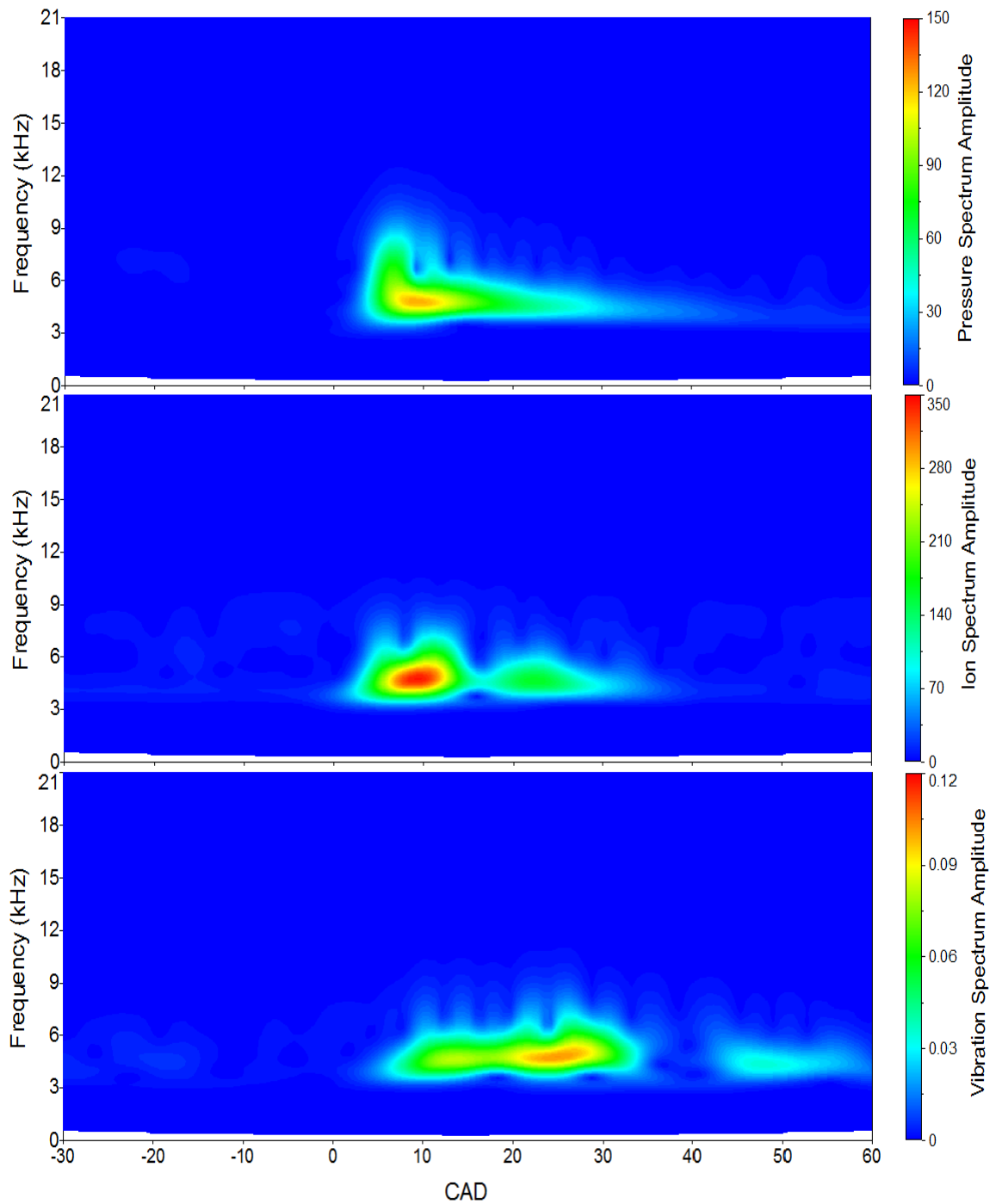


Figure 6.7. CWT analysis for the band pass filtered signals, [JD, Cyl#1, ULSD, 0% EGR, 1800 RPM, LPPC 5° bTDC, Inj. Press: 800 bar, and IMEP: 6 bar]

The resonance detected by the ion current signal in Figure 6.7 is observed to have a particular characteristic not seen in the pressure and vibration spectrums. The pressure spectrum shows high amplitude for the 1st and 2nd modes, where resonance reach a maximum at CAD corresponding to the peak $dp/d\theta$ shown in Figure 6.1. The vibration spectrum shows continuous resonance detection during the combustion process. In the case of the ion current, the resonance detected in time domain indicates different combustion zones. Since the ion current have two distinguished peaks as discussed in chapter 4, the premixed combustion peak and the diffusion combustion peak. Thus, the resonances detected are resonances produced during these different combustion phases. Figure 6.7 shows that the resonance detected by the ion current indicates a high resonance is produced during the premixed combustion and moderate resonance exists during the diffusion combustion.

(ii) Resonance interpretation using CWT

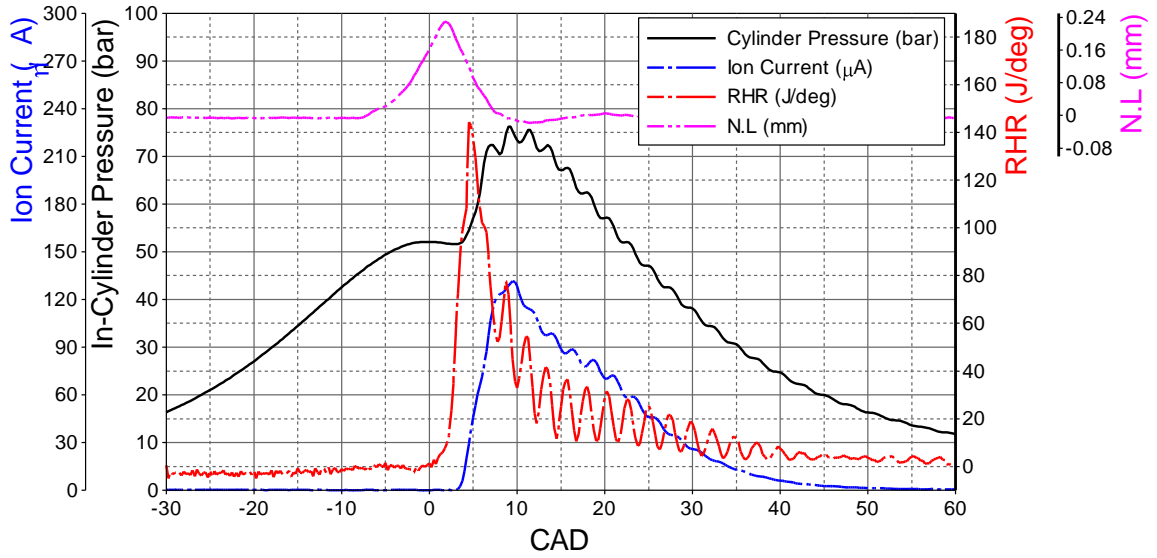
The resonance spectrums shown in Figure 6.7 can be averaged in the range of interest of the combustion resonance frequencies. This can be achieved by calculating the mean values of the resonance amplitudes between 3 to 9 kHz for the three spectrums. This will help to explore the capability of different sensors and to indicate different sources of combustion resonance.

Figure 6.8 and Figure 6.9 show two different combustion scenarios, where the time-resolved resonance calculated from the cylinder pressure, ion current, and vibration signals is presented. It is observed that the ion current gives more details for the source of

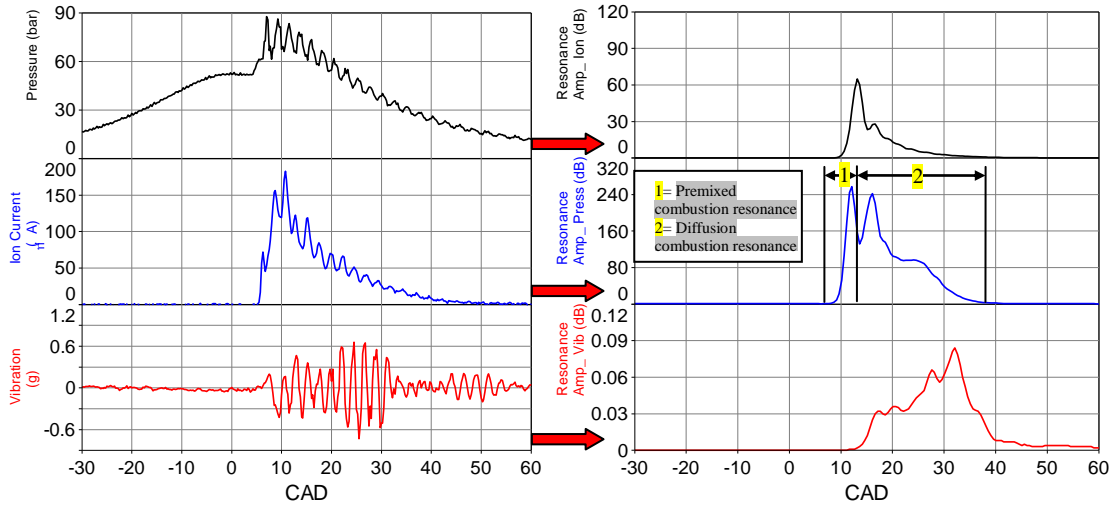
the resonance in different combustion process compared to cylinder pressure and vibration signals.

Figure 6.8a shows cylinder gas pressure, RHR, ion current and needle lift signals for a test conducted at IMEP of 6 bar, injection pressure of 900 bar, and an engine speed of 1800 RPM. The needle lift indicates a single injection with SOI at -6.5° bTDC that outcomes a combustion phasing at LPPC 4° aTDC. As a result of having the ion current delay of 10.5 CAD, the fuel/air mixture developed a very high rate of premixed combustion that produces a sharp rise in the cylinder pressure. The peak of the premixed combustion reaches a peak of 144 J/deg and the first peak of the ion current reaches a peak of 133 μ A. Therefore, the resonance with high amplitude is generated as seen from the oscillations of the three sensors as shown in Figure 6.8b.

The combustion resonance "time-resolved" corresponding to each sensor is plotted in Figure 6.8c. The resonance trace derived from the pressure signal is observed to have a very high peak of 65 dB during the premixed combustion, followed by a second peak of 29 dB during the diffusion combustion. Also, the resonance trace derived from the ion current signal shows two peaks of 255 and 240 dB, followed by a small hump during the expansion stroke. The resonance derived from the ion current indicates a strong presence during the premixed as well as diffusion which is not indicated by the cylinder pressure. The resonance derived from the vibration does not have defined peaks trend and it progresses in an opposite trend to the ion current and cylinder pressure trends. As it has initially low amplitude which increases gradually during expansion stroke and it decay after 35 aTDC.



(a) [Average of 100 cycles]



(b)

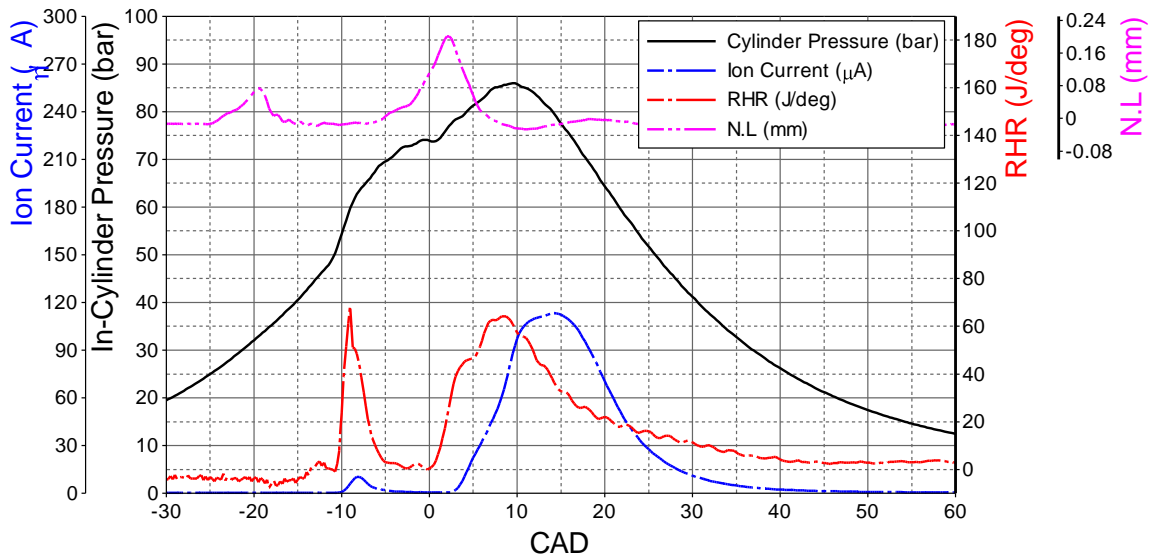
(c)

Figure 6.8. (a) cylinder pressure, RHR, ion current and needle lift signals, (b) cylinder pressure, ion current and vibration signals, and (c) their corresponding resonance [Cyl#1, ULSD, 0% EGR, 1800 RPM, LPPC 4° aTDC, Inj. Press. 900 bar, IMEP 6 bar, Single injection]

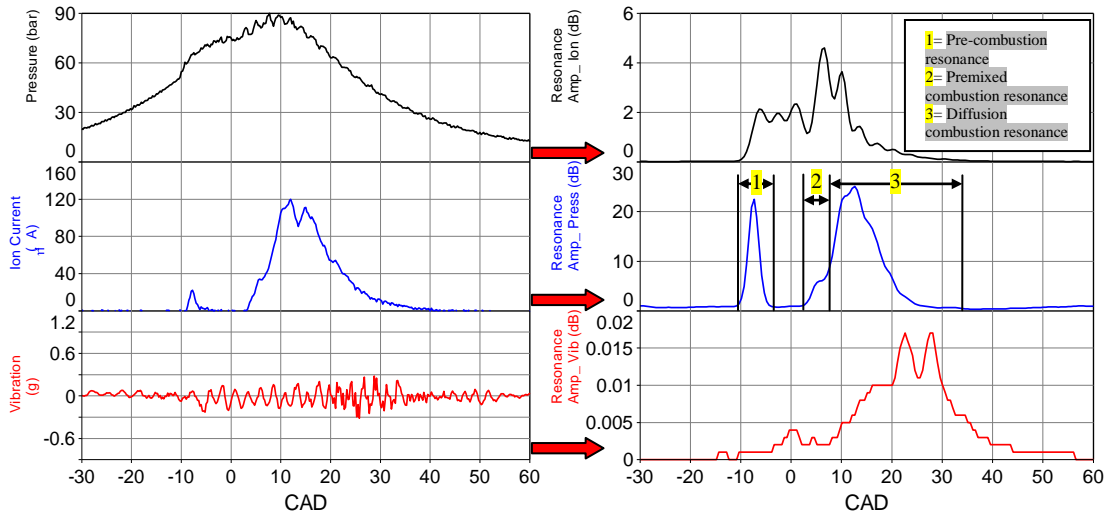
Figure 6.9a shows cylinder gas pressure, RHR, ion current and needle lift signals for a test conducted at IMEP of 6 bar, injection pressure 1200 bar, and engine speed of 1800 RPM. The needle lift indicates multiple injection (pilot + main), where the SOI for the main is at -5° bTDC which results in a combustion phasing at LPPC 4° aTDC. The pilot injection developed a premixed combustion bTDC as a result the ion current delay of the main combustion is 9 CAD. The fuel/air mixture developed after the pilot injection produced a high rate of premixed combustion and increase in cylinder pressure bTDC. Further, the main injection occurs at higher pressure and temperature resulting in a short ignition delay and a slow rate of burn during the main combustion. The peak of the premixed combustion due to the pre-injection reaches a peak of 70 J/deg and the first peak of the ion current reaches a peak of 12 μ A. The main combustion is characterized by a poor premixed combustion and dominating diffusion combustion. The peak of diffusion combustion in the RHR and the ion current are 65 J/deg and 115 μ A. These detail explained in during the progress of the combustion process is reflected in the produced resonance. It should be noted that the rates of pressure rise using multiple injection shown in Figure 6.9 is much lower than single injection shown in Figure 6.8.

Figure 6.9b shows the raw signal for the cylinder pressure, ion current and vibration signal. The signal is further processed using CWT and averaging the resonance frequencies in time domain as shown in Figure 6.9c. It is observed that the resonance in this test is much lower compared to the test in Figure 6.8c.

Figure 6.9c shows the resonance traces derived from cylinder pressure, ion current and vibration signals. The resonance derived from the cylinder pressure starts from the start of pre-combustion for duration of 50 CAD and it peaks during the diffusion combustion during the main combustion with a value of 4.5 dB. The resonance derived from the ion current signal exhibit the same duration showing three distinct peaks; the first is 22 dB due to the pre-combustion, the second is 5 dB due to the premixed of the main combustion, and the third is 25 dB due to the diffusion of the main combustion. The resonance derived from the vibration does not have a defined peaks trend and it increases during the expansion stroke opposite to the ion current and cylinder pressure trends.



(a) [Average of 100 cycles]



(b)

(c)

Figure 6.9. (a) cylinder pressure, RHR, ion current and needle lift signals, (b) cylinder pressure, ion current and vibration signals, and (c) their corresponding resonance [Cyl#1, ULSD, 0% EGR, 1800 RPM, LPPC 4° aTDC, Inj. Press. 1200 bar, IMEP 6 bar, Pilot + Main injection]

6.4 Summary

The ion current signal was investigated to examine its ability to detect the combustion resonance produced inside the combustion chamber. The oscillations observed in the ion current signal are studied in frequency domain using different representation such as FFT, STFT, and CWT. Further, the frequencies of the peaks found using the FFT analysis agrees with the analytical analysis that considers the combustion chamber as a perfect cylinder.

A benchmarking for the combustion resonance for the 1st shape mode (highest resonance amplitude) with its corresponding resonance from the cylinder pressure and vibration signals showed a linear relationship. Therefore, the ion current sensor can be used in replacement to the cylinder pressure sensor or accelerometer to detect combustion resonance for the purpose of engine diagnostics and control.

The time frequency representation of the combustion resonance using STFT and CWT gives more understanding during the development and progress of the combustion resonance using different sensors. Manipulation of the CWT is made in order to have the combustion resonance "time-resolved". The resonance derived from the ion current signal shows clear explanation for the evolution of the combustion resonance at different combustion phases compared to the resonance derived from cylinder pressure or vibration signals.

CHAPTER 7

ANALYSIS OF TIME-RESOLVED RESONANCE, COMBUSTION AND EMISSION PARAMETERS

Modern diesel engines operate on electronic controlled fuel and air delivery systems that allow flexibility in varying operating parameters for fuel such as injection pressure, number of events, timings and durations, and for air such as intake pressure and exhaust gas recirculation. These electronic controlled systems provide opportunity for engineers to develop elaborate engine control strategies to meet production targets in fuel economy and emissions. In order to integrate the ion current signal in a real-time feedback and to utilize it in a close loop control for complex combustion strategies, detailed analysis is made for experiments conducted on JD 4.5L diesel engine under various engine operating conditions. A detailed analysis is made for the ion current signal and the time-resolved combustion resonance at different loads, injection pressures, EGR rates and multiple injection strategies.. The test conducted using the close loop combustion phasing controller demonstrated in chapter 4 and 5, where the combustion phasing is kept constant at 4° aTDC.

7.1 Effect of injection pressure

As it is illustrated in CHAPTER 6, the combustion resonance is produced due to the sudden rise in the cylinder pressure due to combustion. The injection pressure has a very high effect on the ignition delay as well as the rate of pressure rise.

The effect of varying the injection pressure from 300 to 1200 bar on cylinder gas pressure, RHR, ion current traces is shown in Figure 7.1. At higher injection pressures, the ID is shorter and the start of injection is retarded to keep the LPPC at 4° aTDC. The shorter ignition delay is caused by the better atomization and enhanced evaporation of the fuel spray at higher injection pressures.

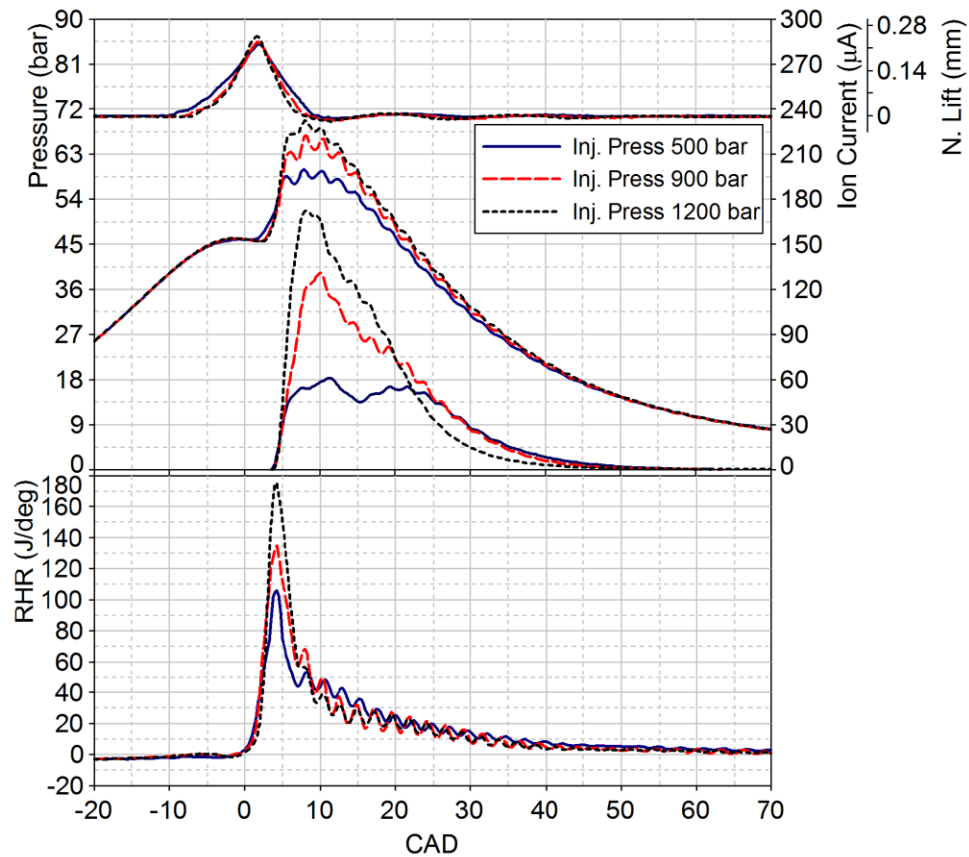


Figure 7.1. Effect of injection pressure on the combustion process [JD, ULSD, 0% EGR, 1800 RPM, LPPC 4° aTDC, and IMEP 6 bar]

Figure 7.1 shows traces for the N.L., cylinder pressure, ion current and RHR at different injection pressures. The N.L. trace shows the retard in the needle opening to keep LPPC at 4° aTDC, and the shortest injection duration at 1200 bar compared to the lower pressures. The traces for the cylinder pressure, ion current and RHR demonstrate the increase in rates of rise and peak values at higher injection pressures. Combustion resonance, following the high rates of pressure rise, is evident in the pressure and ion current traces, as it increases at higher injection pressures.

A more detailed analysis of the effect of injection pressure on combustion resonance detected in the ion current signal is given in Figure 7.2. This figure also shows the ISFC, BSFC, NO emission, Opacity, maximum rate of pressure rise and peak pressure.

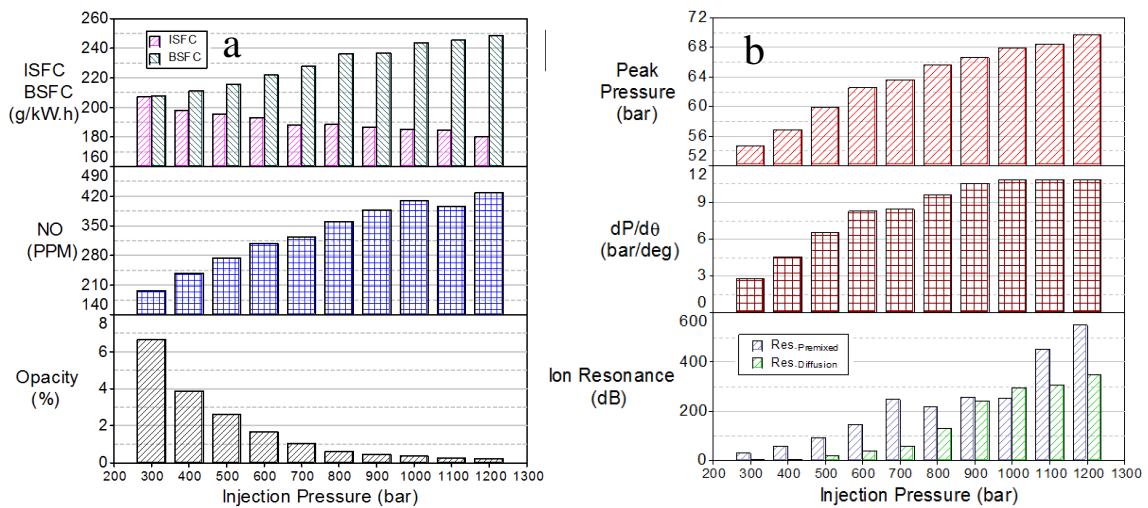


Figure 7.2. (a) Indicated and brake specific fuel consumption, NO emissions and Opacity percentage (b) peak pressure, peak of pressure rise and combustion resonance at different injection pressures

Figure 7.2 shows that increasing the injection pressure from 300 to 1200 bar has the following effects: (i) reduces the indicated specific fuel consumption, (ii) increase the brake specific fuel consumption, (iii) increase NO emissions, (iv) decreases soot emissions as indicated by the reduction in opacity, (v) increase the peak of the rate of cylinder pressure rise, (vi) increase in peak cylinder pressure and (vii) intensifies combustion resonance. These effects can be explained by examining the effect of higher injection pressures on the combustible mixture formation and combustion.

Upon auto-ignition and start of combustion, the larger amount of premixed charge burns at higher rates, closer to TDC, which improves the thermodynamic cycle efficiency as indicated by the reduction of ISFC from 207.3 g/kW.h at 300 bar to 180.0 g/kW.h at 1200 bar. This represents 13% reduction in ISFC. On the contrary, BSFC increased from 207.8 g/kW.h at 300 bar, to 248.7 g/kW.h at 1200 bar. This is due to the increase in the power consumed by the injection pump to deliver the fuel at higher pressures. Moreover, the higher cylinder gas pressure produces more frictional losses in the piston assembly and bearings at higher injection pressures.

The increased quantity of the premixed charge produces locally higher combustion gas temperatures which promote the formation of larger amounts of NO emissions. Also, higher injection pressures increase the residence time of the combustion products in the critical temperature window for NO formation (77) and increase the total amount of NO_x emissions. In addition, the higher quantity of the premixed charge at higher injection pressures reduces soot formation and enhance soot oxidation due to the drop in the amount of fuel injected in the flame (77).

Figure 7.2b shows the combustion resonance produced during the premixed and the mixing-diffusion controlled combustion. Increasing the injection pressure from 300 to 700 bar, increased the resonance during premixed increases due to a significant increase in $dp/d\theta$. Further increase of the injection pressure from 800 to 1100 bar, caused a smaller increase in $dp/d\theta$ and a corresponding slight increase in the combustion resonance during premixed combustion. Meanwhile, a noticeable increase in the level of resonance is

detected during the diffusion combustion starting from 800 bar. At 1000 bar injection pressure, the resonance during diffusion combustion reached a higher level than the one during premixed combustion. In the range of injection pressures from 1000 to 1200 bar, a minor increase in the $dp/d\theta$ is noticed but the resonance during premixed and diffusion combustion kept increasing. The resonance during premixed and diffusion combustion reached their highest level at injection pressure 1200 bar of 550 and 350 dB respectively.

Therefore, the intensity of the combustion resonance in diesel engines can be contributed mainly to two sources (a) the pressure waves developed due to the higher rate of pressure rise caused by the high rates of burning of the premixed combustion fraction, and (b) the pressure waves produced during the mixing and diffusion controlled combustion promoting the primary oscillations. Since the rate of burning is responsible for the level of resonance developed at each phase of combustion. This explains the significant increase in the resonance produced during the diffusion combustion after 700 bar injection pressure, where the resonance level exceeds the one produced during the premixed combustion at 1000 bar injection pressure. Since the increase injection pressure increase the premixed combustion fraction and decrease the diffusion combustion fraction regardless of their higher rate of burning, the resonance during premixed dominate again for injection pressure higher than 1000 bar.

7.2 Effect of EGR

Figure 7.3 shows the effect of increasing the percentage of EGR while keeping LPPC at 4° aTDC. Increasing the EGR rate causes an increase in the ignition delay due to

the following: (a) drop in the compression gas temperature caused by the increase in the specific heats of the gases, (b) drop in the specific reaction rates caused by the drop in temperature and (c) the reduced mole fraction of the oxygen in the charge.

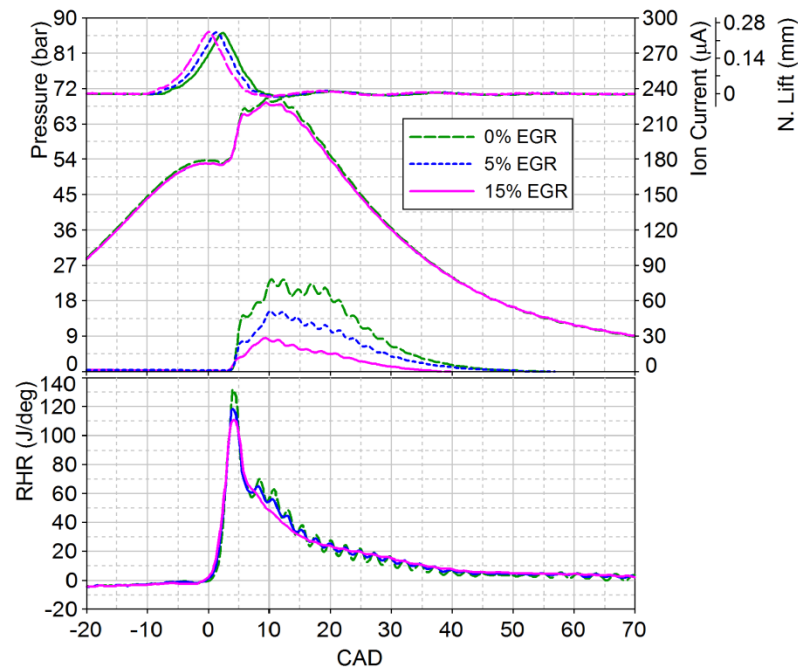


Figure 7.3. Effect exhaust gas recirculation on the combustion process [JD, ULSD, 1800 RPM, LPPC 4° aTDC, inj. Press 1200 bar, and IMEP 6 bar]

The increase in EGR rate has the following effects: (a) reduced the peak of the premixed combustion RHR, in spite of the increase in ID, (b) reduced the rate of pressure rise, (c) reduced the peak pressure and (d) reduced the amplitude and duration of the ion current, and (e) reduced the amplitude of combustion resonance detected from the

pressure trace as well as from the ion current signals. This reduction is the result of the drop in the maximum rate of pressure rise.

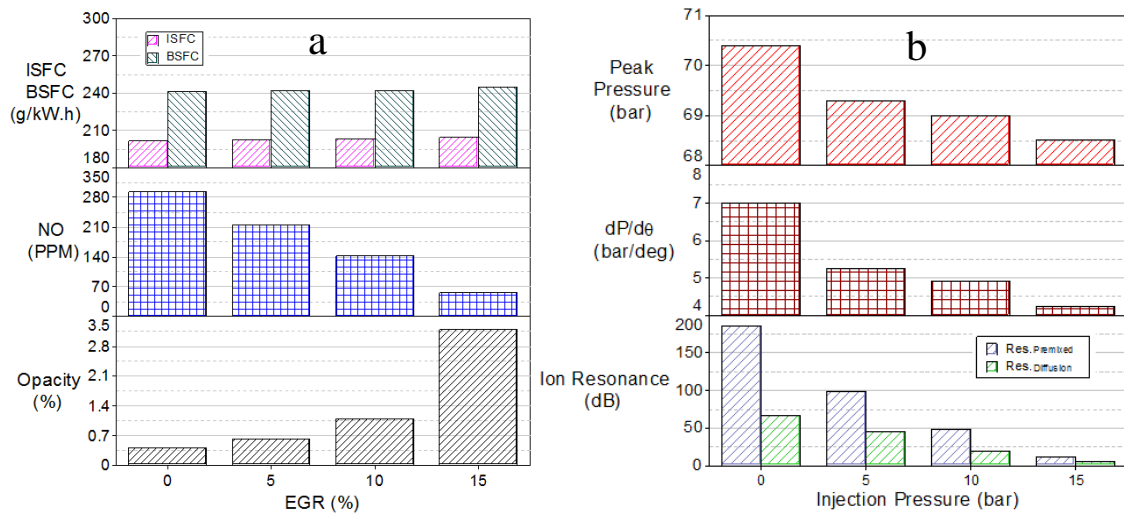


Figure 7.4. (a) Indicated and brake specific fuel consumption, NO emissions and Opacity percentage (b) peak pressure, peak of pressure rise and combustion resonance at different rates of EGR

EGR affects the combustible mixture in two ways. First, it reduces the oxygen content of the charge and slows down the rates of oxidation reactions, and the rate of heat release near TDC. This causes a very small drop in the thermodynamic cycle efficiency and an increase in the ISFC and BSFC. Figure 7.4 shows an increase in ISFC from 201.7 at 0% EGR to 204.2 at 15 % EGR. Similarly, BSFC increases from 241 at 0% EGR to 244 at 15 % EGR. This represents nearly 1.5% increase in both ISFC and BSFC. Second, higher EGR rates increase the specific heat of the charge and reduce the compression temperature as well as the peak cylinder gas temperature and pressure. The peak cylinder

pressure decreases from 70.4 to 68.5 bar. Both these effects reduce the rate of NO formation. NO emission drops down from 292.6 to 56.2 PPM with 81% emissions reduction at 15% EGR.

The reduction of the oxygen content at higher EGR rates, hinder the complete combustion of the fuel and increases soot formation. In addition, the drop in combustion temperature reduces the rate of oxidation of the soot after its formation. Figure 7.4 shows the soot percentage is 0.42% at zero EGR and exponentially escalates to 3.2% at 30% EGR. This represents an increase of 662% in soot emissions.

The peak of cylinder pressure significantly decrease at higher rates of EGR in case of constant SOI but it is not the case for the constant combustion phasing as shown in Figure 7.4, where the peak cylinder pressure drops from 70.4 to 68.5 bar with 2.7% peak pressure reduction . Similarly, the max rate of pressure rise drops from 7 to 4.2 bar/deg with 40% reduction in the maximum $dp/d\theta$.

The combustion resonance produced during the premixed and diffusion combustion dropped at higher rates of EGR resulted from the lower rate of pressure rise. The combustion resonances for the premixed and diffusion drop from 185.69 and 67.017 dB at 0% EGR to 18.8 and 5.06 dB at 15% EGR with a reduction in the resonance level of about 91%.

7.3 Effect of pilot injection

Over the last decade, several research activities have focused on developing methods to modify the combustion process in order to reduce emissions of NO and soot,

fuel consumption, and engine noise and vibration (63; 78-83). Pilot injection strategy is one of such methods which is examined in the current investigation. Injecting the fuel as a pilot in different amounts and at different timings can significantly reduce the combustion noise (79-81; 84). However, the level of reduction depends on the amount of the fuel injected as a pilot, injection timing and other operating variables such as injection pressures and EGR (84). On the other hand, corresponding to the pilot injection quantity and timing for which the combustion noise is the least, the emissions characteristics and other performance variables of the engine may exhibit a different trend at that particular operating condition. For instance, soot percentage usually increases with pilot injection. Therefore, it becomes necessary to carefully study and analyze the data so as to optimize the overall performance of the engine.

7.3.1 Effect of pilot injection quantity at different engine loads at a constant SOPI timing of 25° bTDC

In this work, the quantity of pilot injection is varied from 10% to 50% of the main injection at different loads ranging from an IMEP of 4 to 12 bar. Split injection is a special case of pilot injection where a larger fraction of the fuel is injected closer to the main injection. In this paper, the term “pilot injection” will be used for different amounts of fuel injected earlier to the main injection. The location of the peak RHR due to premixed combustion (LPPC) is kept the same for all tests, by adjusting the start of the main injection. The pilot quantity is varied as a percentage of the main injection from 0 – 50 %, and the pilot timing was kept constant at 25° bTDC.

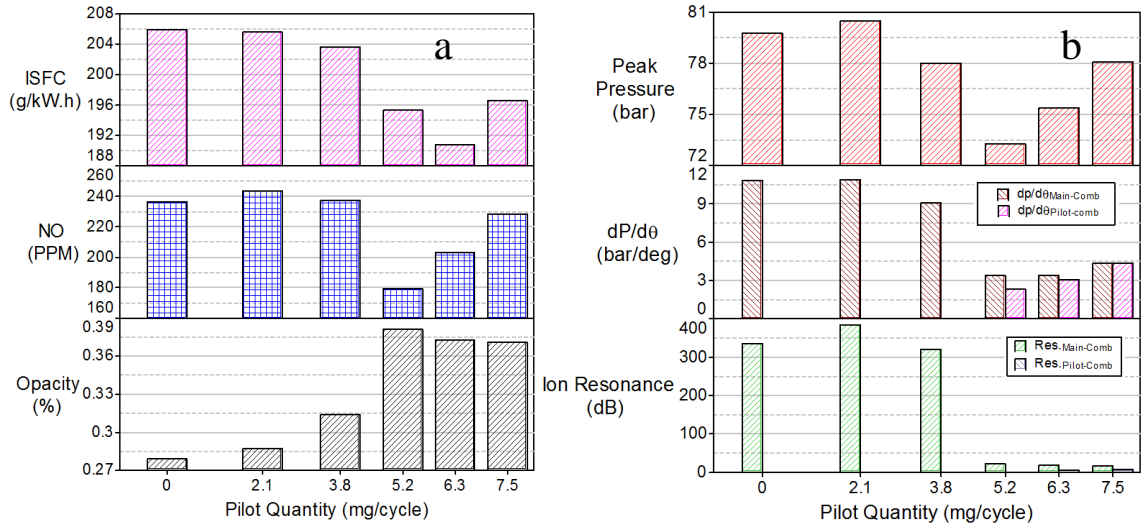
(i) Resonance at IMEP 4 bar

Figure 7.5. (a) Indicated specific fuel consumption, NO emissions and Opacity percentage (b) peak pressure, peak of pressure rise and combustion resonance at different amounts of pilot injection [IMEP 4 bar]

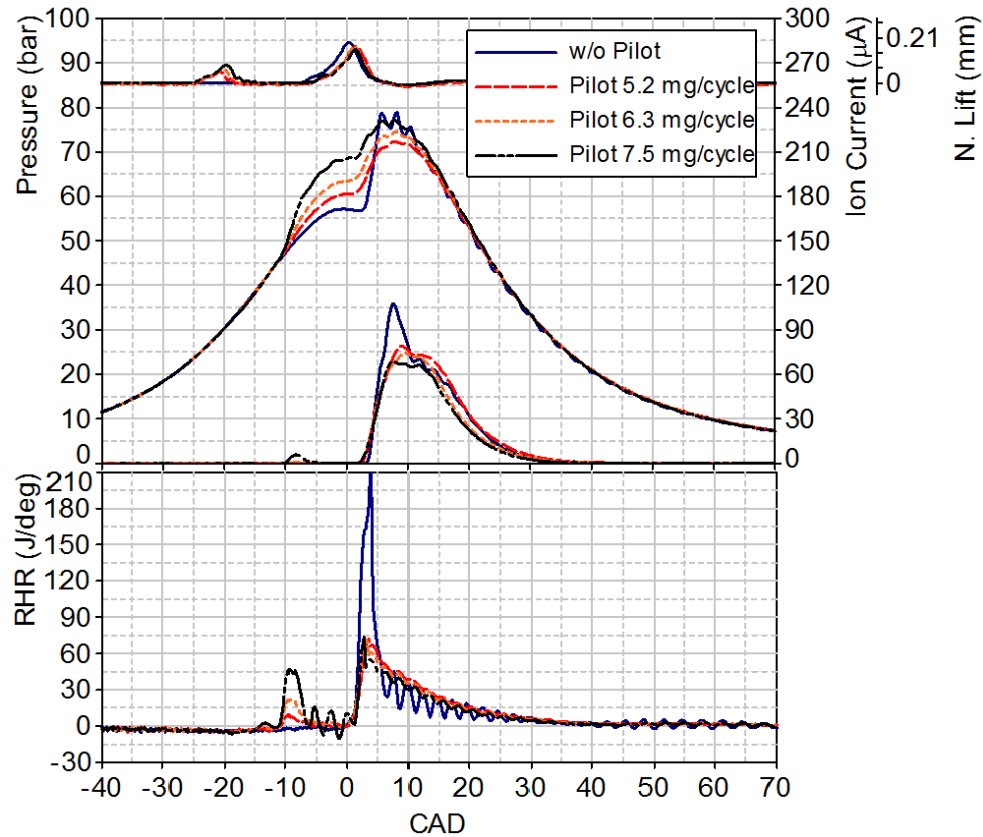


Figure 7.6. Different amounts of pilot injection at constant SOPI 25° bTDC [JD, ULSD, 1800 RPM, LPPC 4° aTDC, Inj. Press 1200 bar SOPI 25° bTDC, and IMEP 4 bar]

Figure 7.5 and Figure 7.6 show the effect of increasing pilot injection on combustion emissions and resonance. Applying the main injection without pilot has the following effects: (a) production of a high level of combustion resonance due a high rate of pressure rise of 10.8 bar/deg, (b) high peak pressure of 79.8 bar, (c) NO emission of 236 ppm, and (d) the lowest soot percentage of 0.28%. Introducing a small amount of 2.1 mg/cycle at 25° bTDC as a pilot injection, increased the premixed combustion fraction which has the following effects: (a) slight increase in combustion resonance as the rate of pressure rise increased to 10.9 bar/degree, (b) increase in the peak pressure to 80.5 bar,

(c) increase in NO to 244 ppm.,(d) higher soot percentage and (e) lower ISFC of 205.5 g/kW.h.

Increasing the quantity of the pilot injection to 30% (5.2 mg/cycle) has the following effects (a) reduced resonance to its lowest level of 22.6 dB, as the rate of pressure rise dropped to its lowest value of 3.39 bar/deg, (b) reduced the peak cylinder pressure to its lowest level of 73.25 bar (c) reduced NO to a low level of 179 ppm, (d), increased soot percentage is the highest level of 0.375 % and (e) reduced ISFC to 195 g/kW.h due to the increase in premixed combustion fraction close to TDC.

Increasing the quantity of pilot injection to 40 % (6.3 mg/cycle) caused the auto-ignition and combustion of the pilot which has the following effects (a) on resonance 17.53 db, (b) on peak pressure 75.36 bar,(c) on NO 203.35 ppm, (d) on Soot 0.373 %, and (e) on ISFC 190.7 g/kW.h.

A further increase in the amount of the pilot injection to 50% (7.5 mg/cycle) has the following effects (a) on resonance 16.773 db, (b) on peak pressure 78.08 bar, (c) on NO 228.48 ppm, (d) on Soot 0.371 %, and (e) on ISFC 196.6 g/kW.h.

The increase in the premixed combustion fraction, produced by the pilot injection, raises the pressure and temperature before the main combustion. This leads to an increase in the peak pressure and temperature of the main combustion causing an increase in the rate of NO formation. The increase in the rate of pressure rise relatively increases the combustion resonance amplitude.

The significant increase in the soot percentage at higher quantity of pilot injection is caused by two factors; (a) the reduction in the ignition delay as a result of the increase in temperature due to pre-combustion, and (b) the larger amount of fuel of the main injection delivered in the flame.

Figure 7.7 shows the ion current delay (ICD) for the main combustion plotted at different quantity of pilot injection. The ICD is 10.5 deg for the single injection. By introducing a small quantity of pilot injection of 2.1 mg/cycle, the ICD increased by 0.5 CAD afterwards the ICD started to drop and reached 7.75 deg at a pilot quantity of 7.5 mg/cycle. The drop in ICD is due to the increase in pressure and temperature as a result of the pre-combustion bTDC.

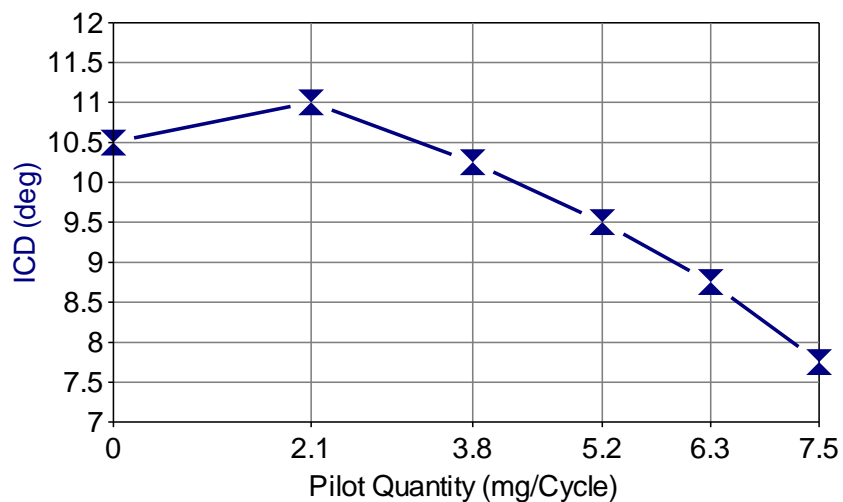


Figure 7.7. Ion current delay versus different amounts of pilot injection at constant SOPI 25° bTDC [IMEP 4 bar]

(ii) Resonance at IMEP 6 bar

Figure 7.8 shows results obtained at engine load IMEP of 6 bar. As load increased, the quantity of fuel delivered in the main and pilot injections relatively increased. In case of the single injection, the combustion produces a high peak pressure of 85.4 bar and ISFC of 190.8 g/kW.h, NO of 340 ppm, and low soot of 0.22 %. By introducing pilot injection and increasing its quantity from 3.2 to 5.9 mg/cycle, the combustion resonance slightly increased along with insignificant change in the maximum rate of pressure rise and peak cylinder pressure.

Increasing pilot injection to 30% (8 mg/cycle), caused the combustion resonance to reach its minimum value of 21.8 dB, where the fuel consumption to reach its lowest value of 188.8 g/kW.h. Further increase in the pilot injection quantity (i.e. more than 8 mg/cycle), a continuous increase in the combustion resonance is observed from pre-combustion due to the highest rate of pressure rise, and highest peak pressure. This results in increasing NO and soot emission, and the indicated specific fuel consumption (ISFC).

Figure 7.9 can give more explanation of the progress of the combustion process under different quantities of pilot injection. The single injection has the longest ID and produces the highest premixed combustion fraction in the RHR. Increasing pilot injection to 5.9 mg/cycle, a slight increase in the cylinder gas pressure near TDC is noticed and a lower peak in the RHR is developed. The rate of heat release produced due to the pilot injection enhances the pressure and temperature conditions inside the cylinder. As a result, ID is shortened, and a sharp drop in the peak of the premixed combustion followed

by an increase in the mixing- diffusion controlled combustion is observed. This resulted in lowering the rate of pressure rise, peak cylinder pressure and NO emission.

Further increase of pilot injection quantity produces higher peak of the rate of heat release during compression stroke and higher cylinder pressure. The maximum rate of pressure rise after 8 mg/cycle is developed from the pilot injection. The formation of soot is mainly controlled by the fuel evaporation and the presence of fuel spray in the flame. At higher quantity of pilot injection, the soot percentage increases mainly because of the presence of the fuel spray during combustion till a pilot quantity of 10 mg/cycle. Thereafter the soot drops at pilot quantity of 12 mg/cycle as a result of less amount of fuel being introduced at the main injection.

It is also noticed that the increase in the heat release before TDC at higher quantities of pilot injection as shown in Figure 7.9 is responsible for the significant increase in the ISFC as part of the work is done in the compression stroke bTDC.

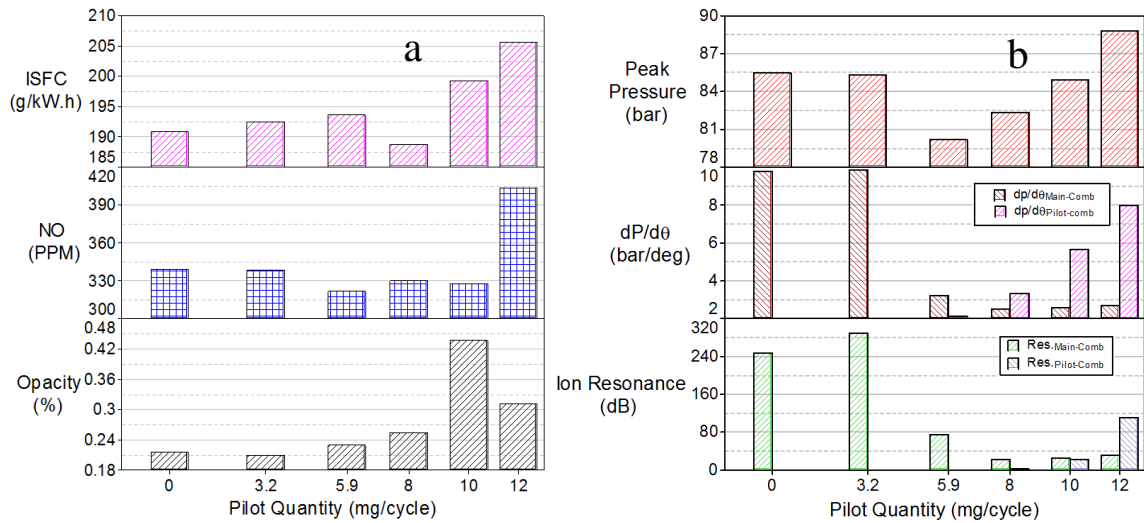


Figure 7.8. (a) Indicated specific fuel consumption, NO emissions and Opacity percentage (b) peak pressure, peak of pressure rise and combustion resonance at different amounts of pilot injection [IMEP 6 bar]

Figure 7.10 shows the ion current delay (ICD) for the main combustion plotted versus different quantity of pilot injection at IMEP 6 bar. The ICD is 10.5 deg at single injection. The ICD kept decreasing with increase in the quantity of pilot injection. The ICD reached its lowest value of 9 deg at IMEP 6 bar for pilot injection above 8 mg/cycle. This supports the early explanation for the factor that affects soot formation by comparing 10 and 12 mg/cycle pilot injection. As the ICD is constant, any reduction of the main injection reduced significantly the soot produced as shown in Figure 7.8a

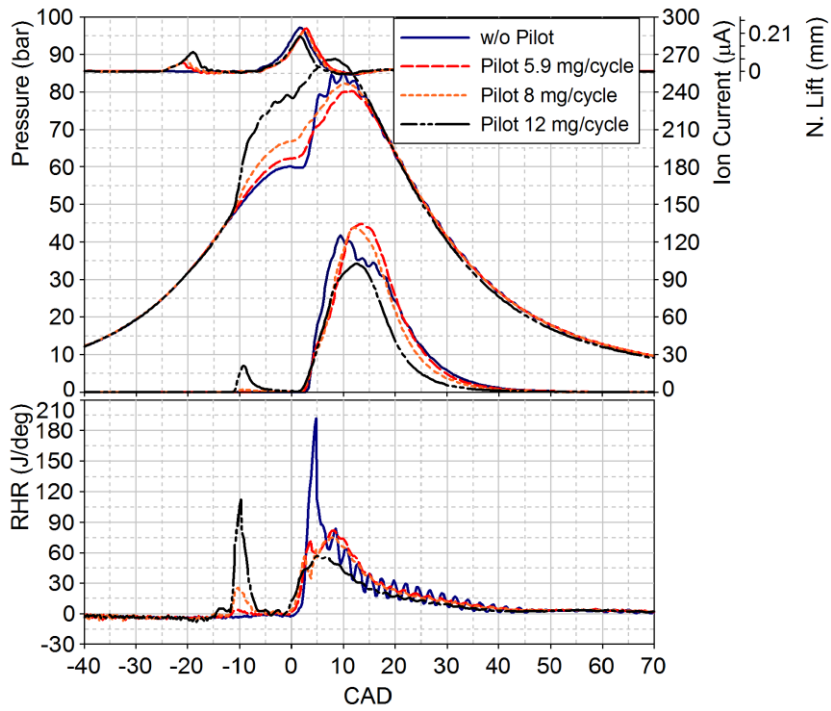


Figure 7.9. Different amounts of pilot injection at constant SOPI 25° bTDC [JD, ULSD, 1800 RPM, LPPC 4° aTDC, Inj. Press 1200 bar SOPI 25° bTDC, and IMEP 6 bar]

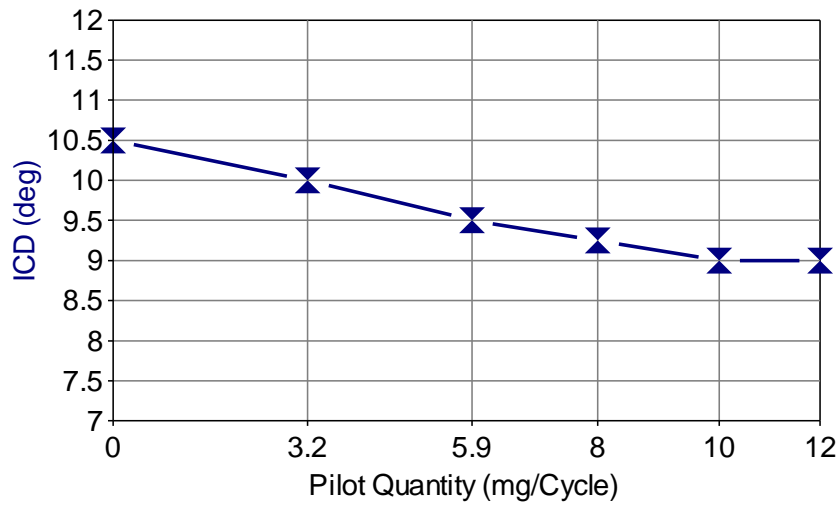


Figure 7.10. Ion current delay versus different amounts of pilot injection at constant SOPI 25° bTDC [IMEP 6 bar]

(iii) Resonance at IMEP 8 bar

The results obtained at IMEP 8 bar are shown in Figure 7.11. The combustion resonance is the highest in case of the single injection. By introducing pilot injection, the combustion resonance reduces, soot percentage increases, peak cylinder pressure and rate of pressure rise drop, and NO emission reduces. The ISFC reaches its minimum values of 187.6 g/kW.h. At pilot quantity of 7.5 mg/cycle, the combustion resonance is significantly reduced which is in agreement with the maximum rate of pressure rise. Increasing the pilot injection above 7.5 mg/cycle has the following effects: (a) increase in the premixed combustion fraction developed from the pilot injection, (b) increase in the maximum rate of pressure rise bTDC, (c) significant increase in the combustion resonance during pre-combustion, (d) decrease in the duration of the main injection, (e) drop in the soot percentage, (f) increase in the peak cylinder pressure, and (g) increase in NO emissions.

Figure 7.12 shows traces for the N.L., cylinder pressure, ion current and RHR at different quantities of pilot injection at IMEP of 8 bar. The single injection has the longest ID and produces the highest premixed combustion fraction in the RHR. At pilot injection of 10 mg/cycle, an increase in the cylinder gas pressure due to the pilot produces the lowest maximum rate of pressure rise and peak cylinder pressure. This develops lower peak cylinder temperature which indicates the reduction in NO formation in Figure 7.11a. It is also very clear that the combustion duration is longest seen by the ion current signal and RHR which explains the high soot percentage at pilot injection of 7.5 mg/cycle.

An overall increasing trend in peak pressure, maximum rate of pressure rise, NO, ISFC and combustion resonance are observed for pilot injection quantity higher than 7.5 mg/cycle. This is mainly due to the pre-combustion that takes place bTDC. Increasing the pilot injection quantity reduces the quantity delivered during the main injection; therefore, less fuel is being injected in the flame which explains the drop in soot percentage after 7.5 mg/cycle.

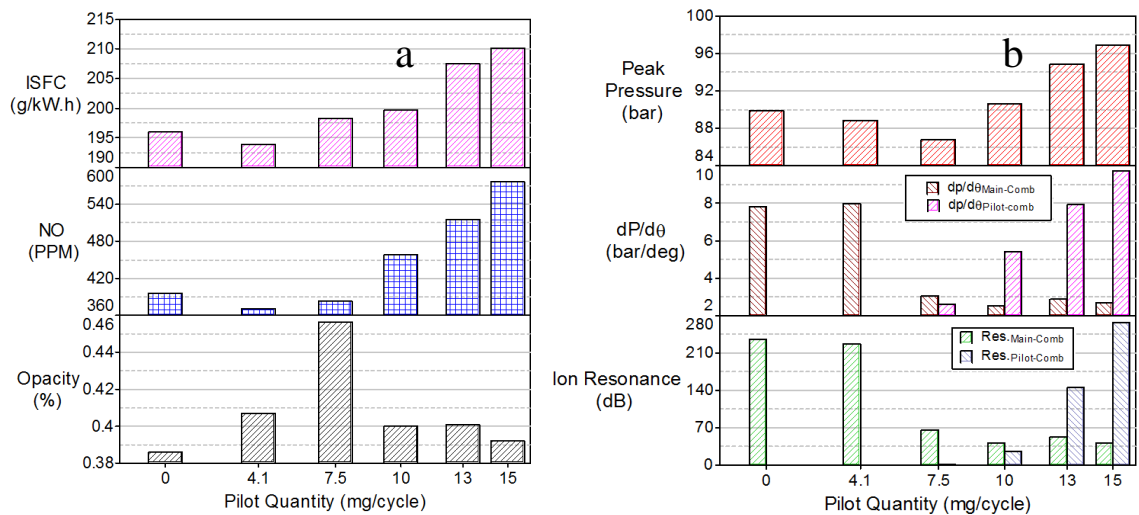


Figure 7.11. (a) Indicated specific fuel consumption, NO emissions and Opacity percentage (b) peak pressure, peak of pressure rise and combustion resonance at different amounts of pilot injection [IMEP 8 bar]

Figure 7.12 gives explanation for the trends shown in Figure 7.11. The rate of pressure rise is the highest during the main combustion in case of single injection which results with highest combustion resonance. A pilot quantity of 10 mg/cycle slightly increases the pressure and temperature during compression, which reduces the ID and

slow down the burning rate. This reduced peak cylinder pressure and NO formation but it also increase the main combustion duration and soot formation. Further, higher quantities of pilot injection develop higher rate of pressure rise during the pre-combustion from the pilot injection which results in higher peak pressures and temperatures, higher NO formation, and higher combustion resonance. Meanwhile, shorter duration of the main injection at higher pilot injection quantity results in earlier combustion termination; therefore, lower soot percentage.

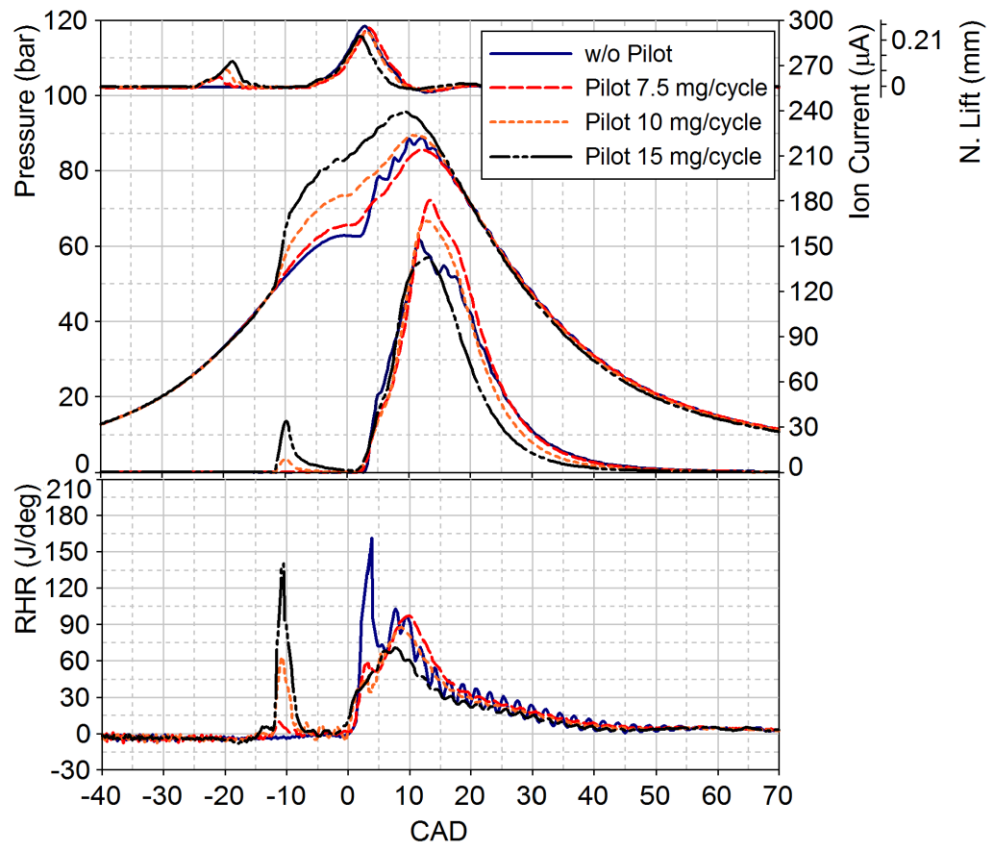


Figure 7.12. Different amounts of pilot injection at constant SOPI 25° bTDC [JD, ULSD, 1800 RPM, LPPC 4° aTDC, Inj. Press 1200 bar SOPI 25° bTDC, and IMEP 8 bar]

Figure 7.13 shows the ion current delay (ICD) for the main combustion plotted against different quantity of pilot injection at IMEP 8 bar. The ICD is 10 deg at single injection. The ICD kept decreasing with increase in the quantity of pilot injection. The ICD reached its lowest possible value of 9.25 deg at IMEP 8 bar for pilot injection above 7.5 mg/cycle. This supports the early explanation for the factor that affects soot formation by comparing 7.5 and 10 mg/cycle pilot injection. As the ICD is constant, any reduction of the main injection reduced significantly the soot produced as shown in Figure 7.11a

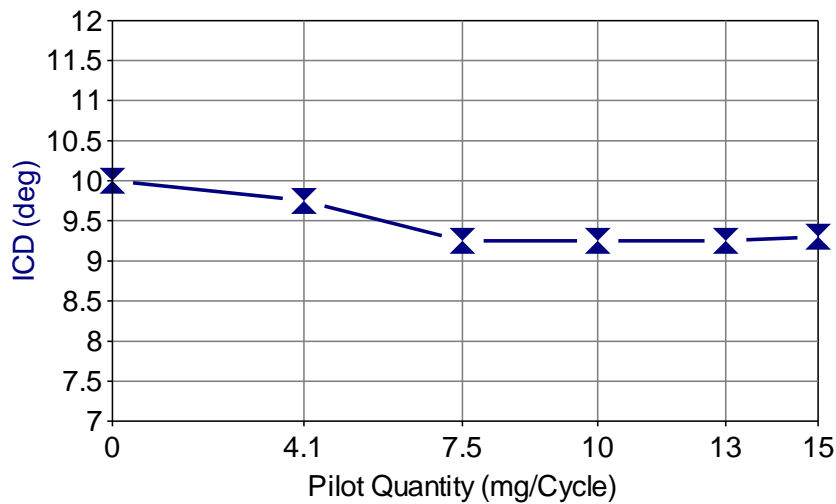


Figure 7.13. Ion current delay versus different amounts of pilot injection at constant SOPI 25° bTDC [IMEP 8 bar]

(iv) Resonance at IMEP 12 bar

Figure 7.14 and Figure 7.15 show the results obtain at IMEP of 12 bar. This condition is consider at high engine load and it is characterized by the following: long

injection duration, shorter ID, small premixed combustion fraction, large mixing and diffusion controlled combustion fraction, high soot formation, high thermal efficiency, high torque output, high cylinder gas temperature, high NO emissions, long combustion duration, and low rate of fuel burning.

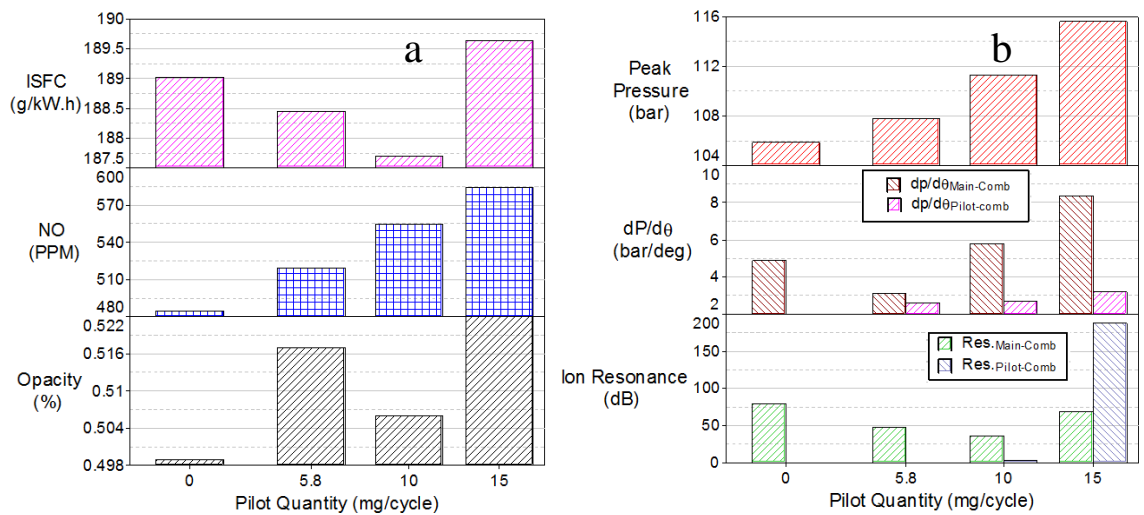


Figure 7.14. (a) Indicated specific fuel consumption, NO emissions and Opacity percentage (b) peak pressure, peak of pressure rise and combustion resonance at different amounts of pilot injection [IMEP 12 bar]

Introducing the pilot injection at IMEP 12 reduces the combustion resonance where it reaches a minimum value of 36 dB at pilot quantity of 10 mg/cycle and a minimum ISFC of 187 g/kW.h. At pilot quantity of 15 mg/cycle, the NO emission, soot, peak pressure, ISFC and rate of pressure rise reach their highest values as shown in Figure 7.14.

In Figure 7.15, the pressure traces and their corresponding ion current and RHR traces show that the pilot injection produced a very high rate of heat release due to the pre-combustion followed by an insignificant fraction of premixed combustion after the main injection and high fraction of diffusion and mixing controlled combustion.

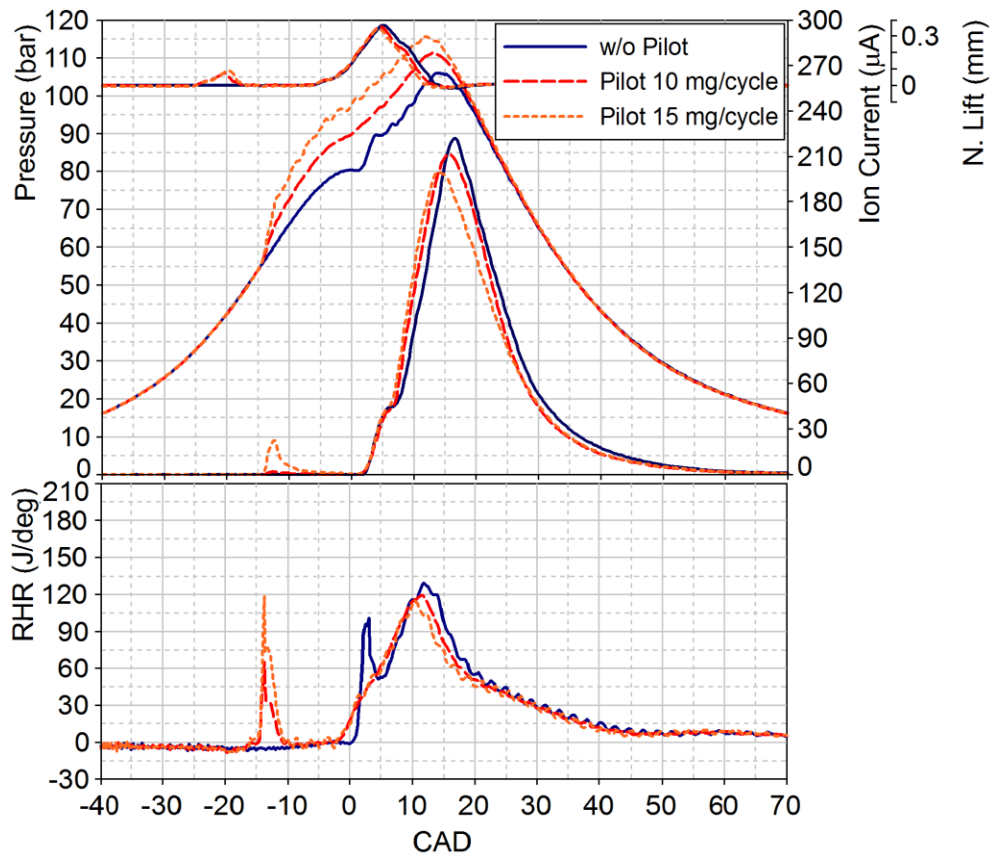


Figure 7.15. Different amounts of pilot injection at constant SOPI 25° bTDC [JD, ULSD, 1800 RPM, LPPC 4° aTDC, Inj. Press 1200 bar SOPI 25° bTDC, and IMEP 12 bar]

Figure 7.16 shows the ion current delay (ICD) for the main combustion plotted against different amounts of pilot injection at IMEP 12 bar. The ICD is 9.5 deg with single injection. the data in figures 7.7, 7.10, 7.13 and 7.1 indicates that the drop in ICD

due to the increase in the pilot injection quantity is smaller at this high load compared to the change at lower loads.

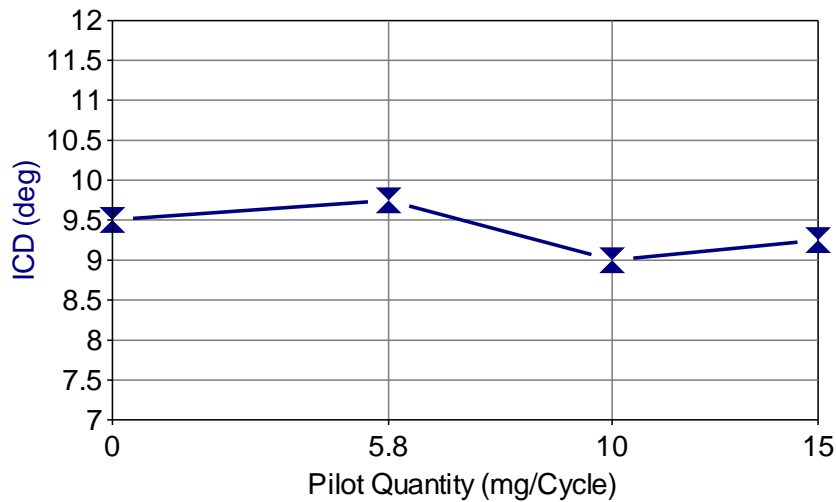


Figure 7.16. Ion current delay versus different amounts of pilot injection at constant SOPI 25° bTDC [IMEP 12 bar]

A summary of the NO emissions, percentage opacity, peak cylinder gas pressure and ISFC at the quantity of pilot injection that produces minimum combustion resonance at various loads is shown in Table 7.1. A comparison between the results obtained without pilot injection and with pilot injection indicates that the drop in combustion resonance is associated with the following: (a) an improvement in the indicated specific fuel consumption, (b) the peak cylinder pressure decreased at light and medium loads, but increased at higher loads, (c) NO emissions followed the peak pressure trend and (d) an increase in opacity.

Table 7.1. Percentage increase or decrease of different combustion and emissions output at the minimum combustion resonance achieved by varying the quantity of pilot injection, SOPI at 25° bTDC and LPPC at 4° aTDC

IMEP (bar)	I _{on} _{RES} (dB)	NO (ppm)	Opacity (%)	Peak Press (bar)	ISFC (g/kW.h)
	Percentage increase /decrease				
4	-94.8	-11.4	+33.7	-8.40	-1.10
6	-91.2	-1.20	+17.0	-3.70	-1.05
8	-82.6	+12.2	+3.60	+0.80	-1.62
12	-54.2	+10.3	+1.20	+4.90	-1.00

It can be concluded from this section that the trend for improving fuel economy, reducing peak pressure, reducing combustion resonance, and having a trade-off between NO and soot emissions were achieved by varying the quantity of pilot injection at light and medium loads. However, at higher engine loads, this is not the case. Therefore, the exclusive use of pilot injection quantity is not sufficient to improve the combustion process or to reduce engine emissions. Hence, the pilot injection timing is an important contributing parameter to be examined in improving the combustion process and engine out-emissions, and will, therefore, be investigated in the following section.

7.3.2 Effect of pilot injection timing at different engine loads

The timing of the pilot injection is varied at different loads in order to investigate its impact on combustion resonance, combustion characteristics, fuel consumption, and engine out emissions. The quantity of the pilot injection is fixed at 30% of the main injection which is dependent on the engine load. Figure 7.17 shows the results obtained for the combustion resonance at different pilot injection timings and engine loads. The

resonance produced from combustion shows the following: (1) at low and medium loads, combustion resonance reaches its highest value at very early SOPI, and it starts to drop down as the SOPI is retarded; (2) at high loads, the combustion resonance had an opposite trend, where it reaches its minimum values at advanced SOPI = 35 bTDC after it increases again. Further, the resonance produced from the combustion of the pilot injection shows the following: (1) at low load, the amount of fuel injection in pilot does not develop a pre-combustion as a result no resonance is detected; (2) at medium and high load, combustion resonance reaches its highest value at very late SOPI, and it starts to decay as the SOPI is advanced.

Figure 7.18 shows the needle lift, cylinder gas pressure, ion current, and RHR at IMEP of 4 bar at different pilot injection timings. The results are also compared with the case of single injection. The needle lift signal shows that the ID is the longest with the single injection which develops the highest premixed combustion observed in the first peak in both RHR and the ion current signal. Introducing the fuel of the pilot injection early at SOPI = 45° bTDC, where the cylinder gas pressure and temperature are low causes the following: (a) a slow rate of evaporation of the fuel due to the low pressure and temperature at the time of injection, (b) a slow rate of formation of the low temperature combustion reactions and the corresponding rise in gas temperature, (c) a small reduction of the ID of the main injection, (d) slower main combustion reactions and a low peak of the RHR due to the premixed combustion fraction, (e) a corresponding low peak of the ion current signal, (f) an increase in RHR from the mixing and diffusion controlled combustion fraction, and (g) a slight reduction in combustion resonance due to

the reduction in the maximum rate of pressure rise during the main combustion. Retarding the SOPI from 45° bTDC to 25° bTDC had the following effects: (a) a faster rate of evaporation of the fuel due to the higher pressure and temperature at the time of injection, (b) low temperature combustion detected at 10° bTDC, (c) NTC regime is formed, (d) short ID for the main injection, (e) a sharp drop in the peak of the premixed combustion fraction observed in the RHR and the ion current signal followed by an increase in the mixing and diffusion controlled combustion, and (f) a significant reduction in combustion resonance due to the large drop in the maximum rate of pressure rise during the main combustion.

The combustion resonance at light and medium loads is reduced by retarding the SOPI but the trend is reversed at high loads as seen in Figure 7.17. A plot representing the effect of pilot timing on the combustion process at IMEP of 12 bar is shown in Figure 7.19. The peak cylinder pressure is the lowest in case of single injection. By introducing a pilot injection at $\text{SOPI} = 25^\circ$ bTDC, premixed combustion takes place due to the fuel evaporated from the pilot bTDC; this results in an increase in the peak cylinder pressure and temperature, and NO emission. By advancing the timing for the pilot injection to $\text{SOPI} = 45^\circ$ bTDC, the pilot fuel is injected at lower cylinder pressure and temperature and results in the following: (a) low temperature combustion flame is formed, (b) lower peak pressure, and (c) slower rate of fuel burning.

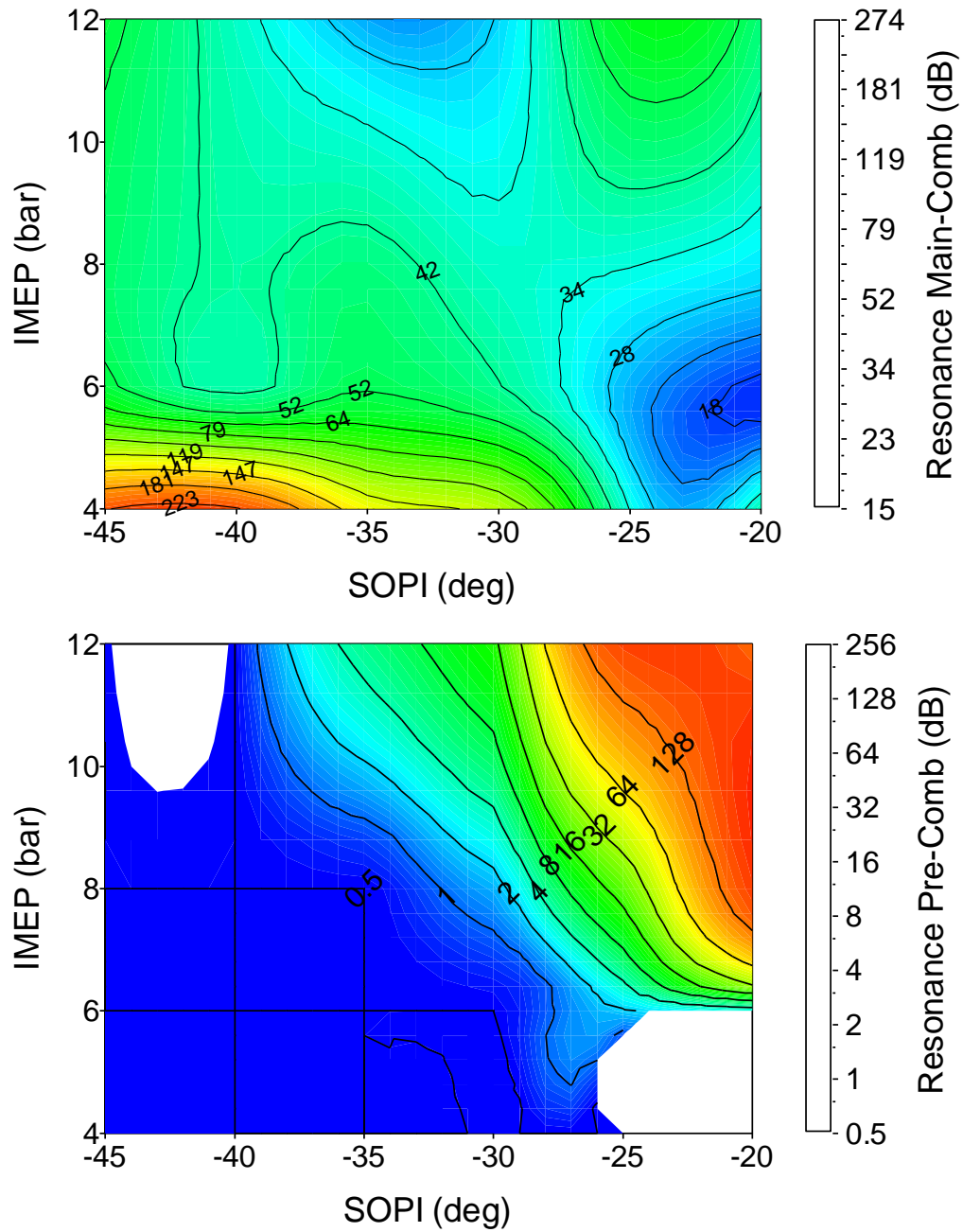


Figure 7.17. Combustion resonance at different SOPI [JD, ULSD, 1800 RPM, LPPC 4° aTDC ,inj. Press 1200 bar, and Pilot Q. 30% of the main inj.]

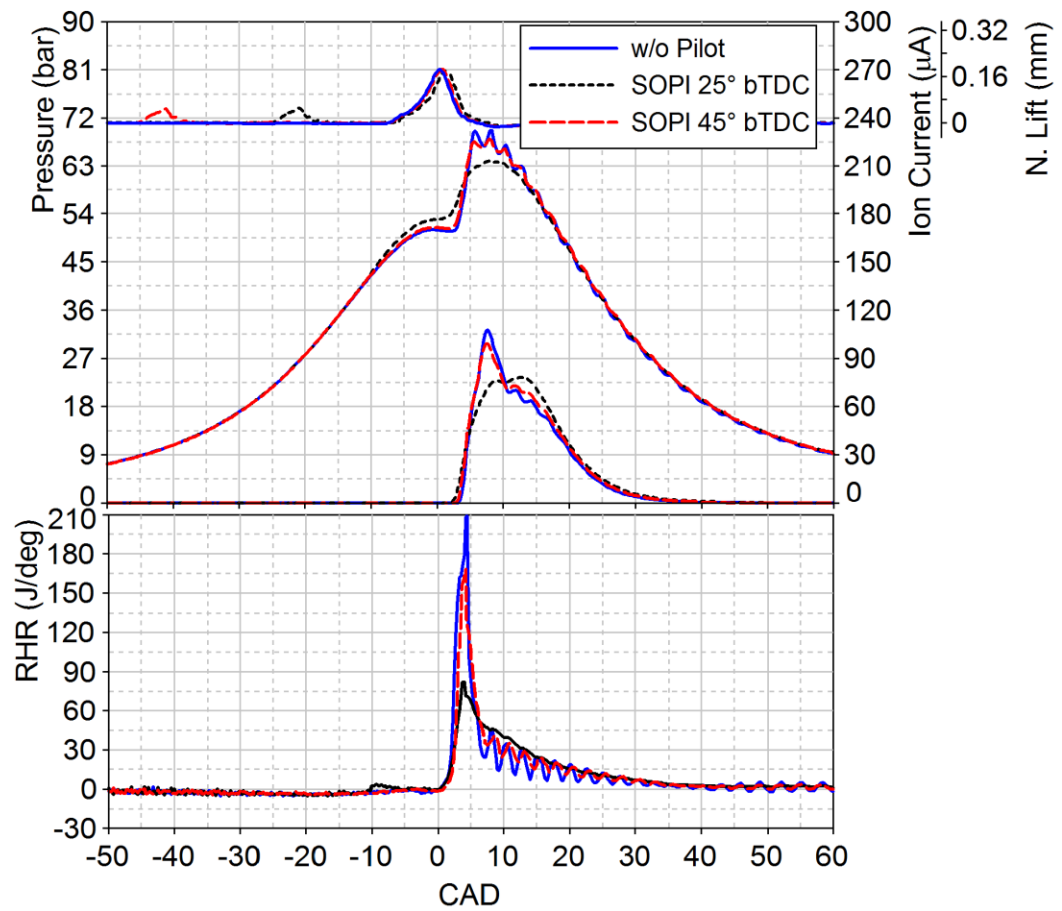


Figure 7.18. Different timings of pilot injection with pilot quantity of 5.2 mg/cycle [JD, ULSD, 1800 RPM, LPPC 4° aTDC, inj. Press 1200 bar, various SOPI, and IMEP 4 bar]

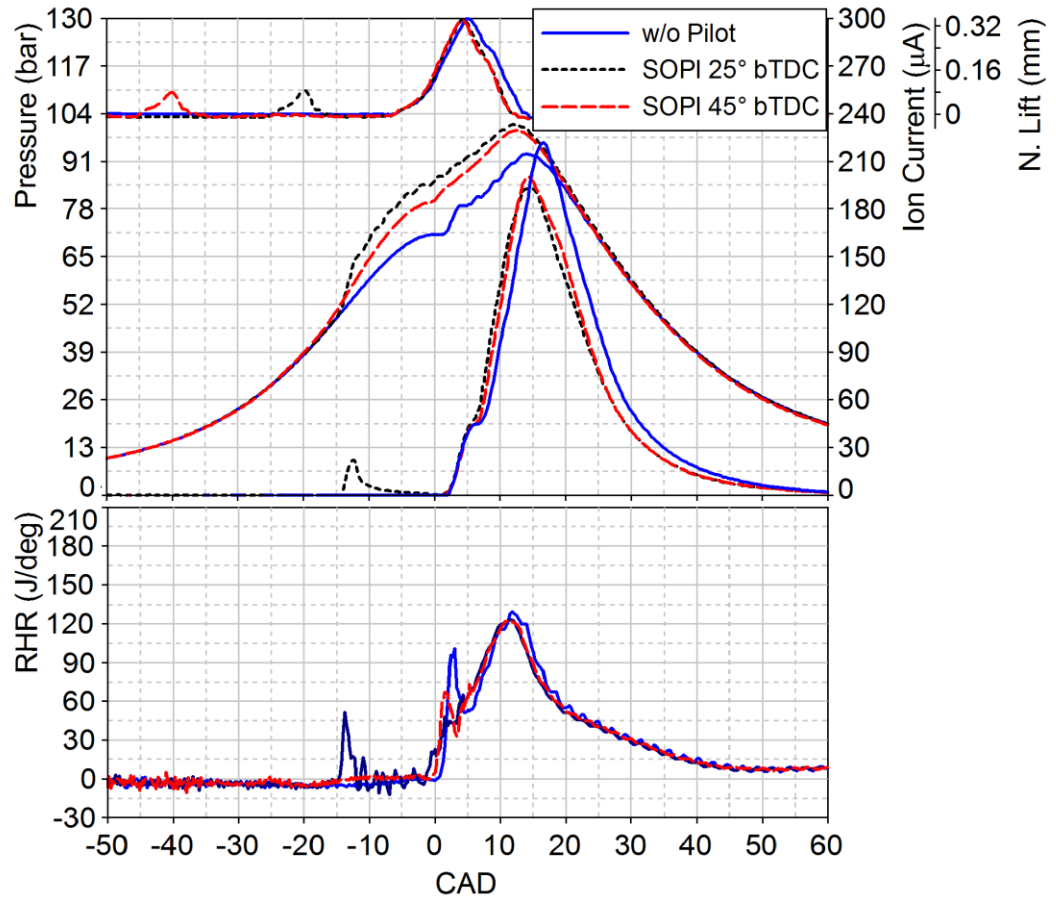


Figure 7.19. Different timings of pilot injection with pilot quantity of 10 mg/cycle [JD, ULSD, 1800 RPM, LPPC 4° aTDC, inj. Press 1200 bar, various SOPI, and IMEP 12 bar]

Figure 7.20 shows the effect of varying SOPI on the peak cylinder pressure at different engine loads. It is clear that the peak pressure increases with increasing engine load. Further, the contour lines indicate that the peak cylinder pressure is slightly lower at low loads with retarded SOPI. In contrast, a slightly lower peak pressure can be achieved with increasing load by advancing the SOPI.

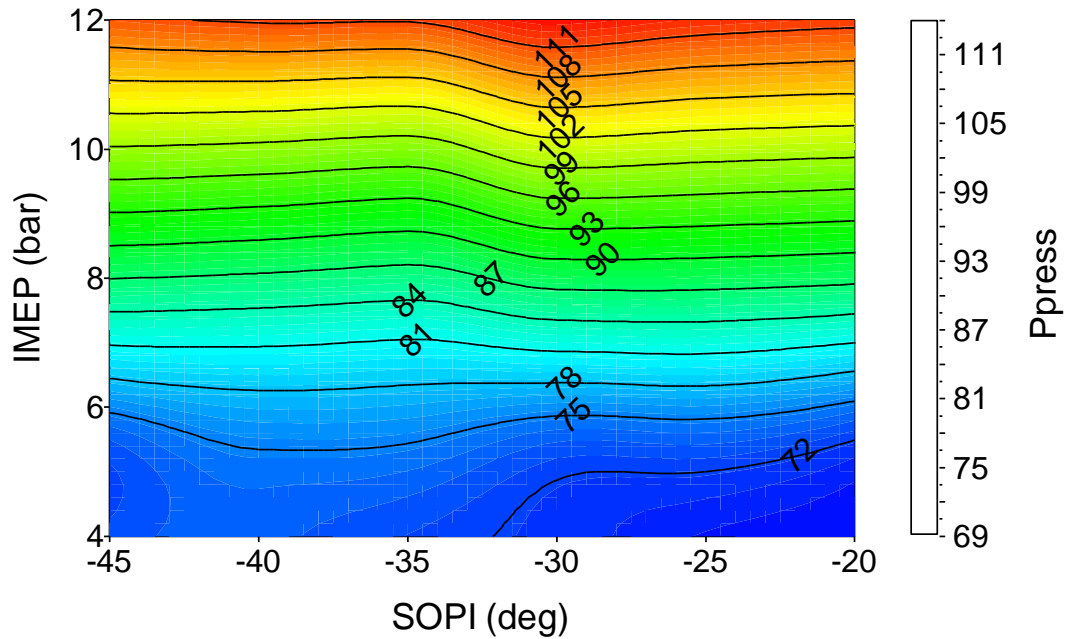


Figure 7.20. Peak cylinder pressure at different SOPI [JD, ULSD, 1800 RPM, LPPC 4° aTDC, inj. Press 1200 bar, and Pilot Q. 30% of the main injection]

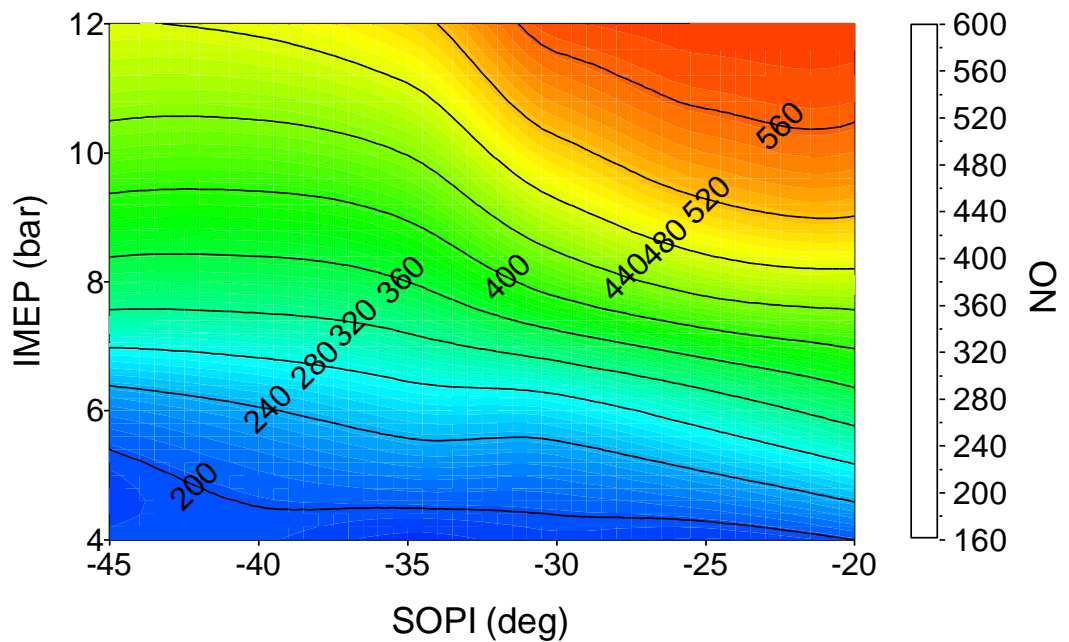


Figure 7.21. NO emissions at different SOPI [JD, ULSD, 1800 RPM, LPPC 4° aTDC, inj. Press 1200 bar, and Pilot Q. 30% of the main injection]

The NO emissions are plotted in Figure 7.21 at different engine load and SOPI. The contour plot shows that the NO emissions can be reduced at different engine loads by advancing the SOPI. In addition, the NO contour trend is observed to follow the same trend as of the peak cylinder pressure shown in Figure 7.20.

The Soot percentage at different loads and SOPI is also plotted in Figure 7.22. At low load, the soot percentage is observed to reach its minimum values at SOPI = -25° degs. As load increased, a bell type contours were observed with higher values for retarded SOPI.

Figure 7.23 shows the indicated specific fuel consumption contour plot at different loads and SOPI. The indicated specific fuel consumption is observed to decrease with increasing engine load. Further, it is observed that fuel consumption is low at late timing at light load and show an opposite trend at high loads.

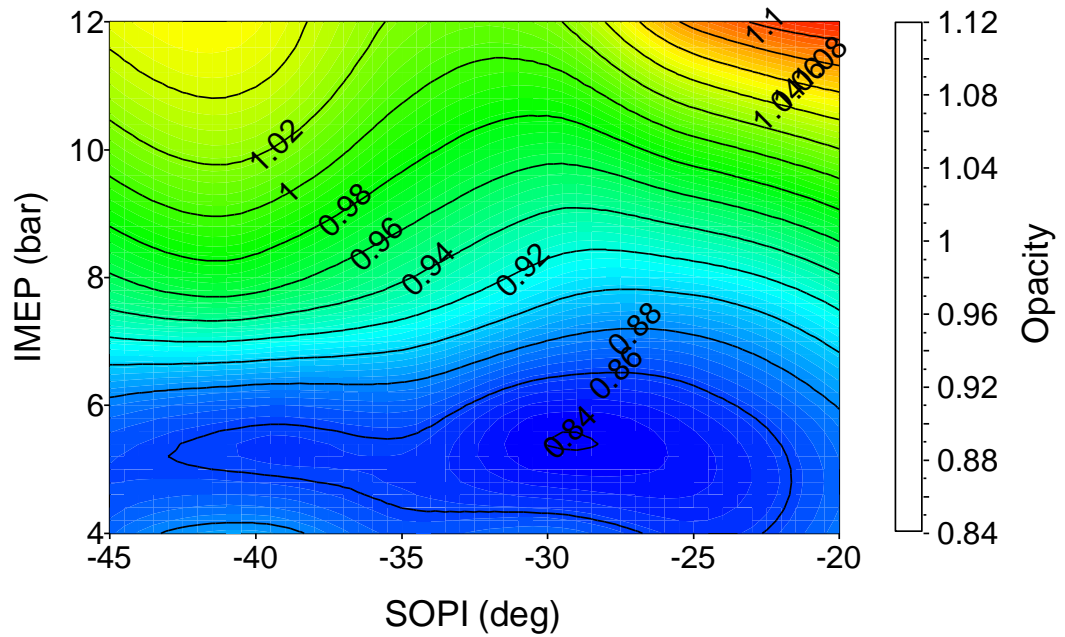


Figure 7.22. Soot percentage at different SOPI [JD, ULSD, 1800 RPM, LPPC 4° aTDC, inj. Press 1200 bar, and Pilot Q. 30% of the main injection]

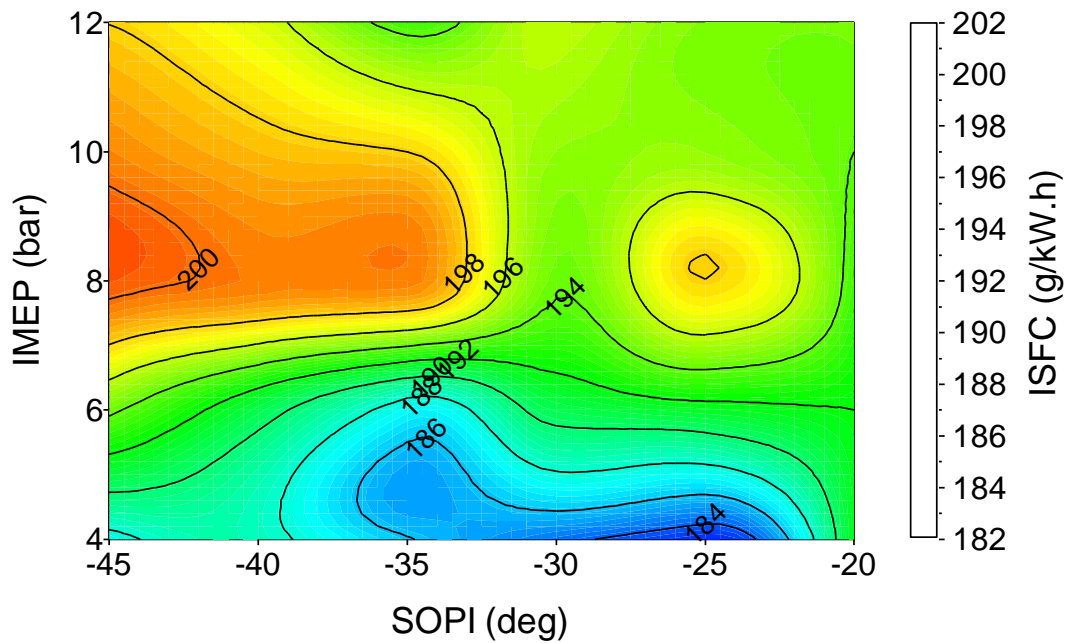


Figure 7.23. Brake specific fuel consumption at different start of pilot injection. [JD, ULSD, 1800 RPM, LPPC 4° aTDC, inj. Press 1200 bar, and Pilot Q. 30% of the main inj.]

The results show that SOPI has a strong impact on the combustion resonance, combustion characteristics, fuel consumption, and engine out emissions. In order to optimize the combustion process to reduce NO, peak cylinder pressure, fuel consumption and engine noise, the SPOI can be varied with varying engine load. It can be concluded from the analysis of the data that the SOPI can be advanced from 25° bTDC at IMEP 4 bar to 40° bTDC at IMEP of 12 bar incrementally. By adopting this strategy, the results thus obtained are compared with the single injection strategy as shown in Table 7.2. A significant reduction in the combustion resonance is noticed in addition to an improvement in other combustion and emissions characteristics. The peak cylinder pressure decreases at lighter loads, but increases at higher loads. NO emissions and brake specific fuel consumption are also reduced. But the soot percentage increased when using the pilot injection, particularly at the low loads.

Comparing the data in Table 7.1 and Table 7.2 reveals that each of the pilot timing strategy and pilot quantity has different effects on engine fuel economy, emissions and resonance. ISFC can be reduced by controlling the timing, particularly at light loads. NO_x emissions can be reduced by pilot injection timing control, at all loads. Soot emissions increase by different percentages by applying pilot injection depending on quantity and timing at different loads. Combustion resonance is substantially reduced by pilot injection quantity and/or timing at all loads. The reduction in resonance is slightly different at different loads.

Table 7.2. Percentage increase or decrease of different combustion and emissions output at the minimum combustion resonance achieved by varying the timing of the pilot injection.

IMEP (bar)	$I_{on_{RES}}$ (dB)	NO (ppm)	Opacity (%)	Peak Press (bar)	ISFC (g/kW.h)
Percentage increase /decrease					
4	-93.7	-20.9	+13.0	-7.32	-15.05
6	-90.5	-22.5	+16.0	-5.30	-4.09
8	-84.7	-9.36	+4.50	+1.25	-2.03
12	-56.5	-0.97	+2.00	+9.50	-0.03

7.4 Summary

An experimental investigation was conducted on a 4.5L turbocharged diesel engine at a constant engine speed of 1800 RPM in order to investigate the effect of injection pressure, EGR, pilot injection quantity and timing on cycle-resolved combustion resonance and other engine parameters while combustion phasing is kept constant LPPC at 4° aTDC.

The following are conclusions drawn from this chapter:

1. The injection pressure influences the combustion resonance mainly through the in-cylinder combustion temperature and the rate burning of the fuel.
2. The combustion resonance decreased at higher EGR percentage at constant combustion phasing. This is probably due to the lower combustion temperature developed inside the combustion chamber.
3. Pilot injection can be used to significantly reduce combustion resonance as compared to single injection strategy.

4. The pilot injection quantity for which the combustion resonance was the least, ISFC was also the least.
5. A considerable reduction in NO emission with an tolerable penalty in soot can be achieved using pilot injection strategy.
6. An improvement in overall combustion characteristics such as combustion resonance, ISFC and peak cylinder pressure, and a tradeoff between NO and soot emissions can be realized by adjusting the SOPI particularly at different engine loads.
7. The ion current sensor can be used to detect the combustion resonance for combustion diagnostics and can be implemented in close loop controller that adjust pilot injection quantity and timing to minimize the combustion resonance in addition to the reduction of NO, peak cylinder pressure, fuel consumption and engine noise.

CHAPTER 8

NO_x AND SOOT ESTIMATION MODELS

Estimation of NO_x and soot emissions from an in-cylinder measurement would help in the calibration of diesel engines to meet certain emission standards. Since the ion current signal carries information about the different ionized species, it can be used to indicate their concentrations. It is interesting to know that NO is a major contributor in the ion current. Similarly, some soot precursors are ionized. This chapter presents a detailed analysis of the ion current signal under steady state and transient conditions. Experiments are carried out on a 4.5L heavy duty, turbocharged diesel engine. An ion current/ glow plug sensor is used to measure the ion current signal inside the cylinder. , A method is developed to estimate NO_x and soot formed using the ion current signal on a cyclic basis. A comparison between the NO_x and soot measured and simulated results will be made

A non-linear multiple regression model (NLMR) is used to estimate NO_x concentration in PPM and opacity percentage from the ion current signal. The ion current signal acquired in each cycle is analyzed, and different parameters are extracted to be plugged as inputs to the NLMR model. Also, a sensitivity analysis for these parameters is evaluated to improve the estimation accuracy. The NLMR model developed is tested and results show that the ion current signal can effectively be used to estimate NO_x and soot percentage produced in diesel engines.

8.1 Introduction

Emission regulations for diesel engines are progressively reducing the standards for particulate matter (PM) (85; 86) and oxides of nitrogen (NO_x)(87-89). There is evidence that modern diesel engines still generate levels of NO and soot higher than the current emission standards (90; 91) in spite of implementing some engine strategies to reduce their formation (92-94), This made it necessary to apply after-treatment devices to reduce the tail-pipe emissions (95; 96). To reduce the demand on the after-treatment devices, there is a need for a technique to measure the soot and NO content of the combustion chamber. Currently, devices can measure the soot in exhaust tailpipe. Most of these devices are expensive and used only during development process such as opacity meter (97), micro-soot sensor (98), and particulate counter (99). More advanced technique used in research to measure soot particulate size distributions and mass inside the combustion chamber such as laser induced incandescence (100; 101) and laser light scattering (102). More advanced instruments to measure soot in the tailpipe include scanning mobility particle sizer (SMPS) (103; 104) and particulate spectrometer (105; 106). All of these devices are expensive, bulky, and cannot be implemented for the feedback control of the engine.

In the last decade, researchers focused on developing new sensors that can be implemented in modern diesel engine to accurately measure soot emissions. Warey et al. developed a soot sensor to monitor soot emissions in the exhaust line (107; 108). The sensor consists of two insulated electrodes, energized with a potential difference of 1000 DC Volt. The voltage drop ionizes the carbon particles flowing in the exhaust, thus a

current flow through the sensor circuit indicating the particulate carbon mass emissions. Ochs et al. and Kondo et al. designed a soot sensor for on-board measurements. It consists of two electrodes that measure the electric current that flow due to the soot accumulated on sensor surface, and a heater that burns the soot accumulated for regeneration (109; 110). The sensor signal representative of the soot concentration in the exhaust gases is the time between the regeneration and the current reaching a certain threshold. Allan et al. designed a spark plug with heated insulation that can estimate the smoke in exhaust, where they found a correlation between the smoke number and sensor signal (111). All these sensors are installed in the exhaust line and have slow response times.

Technologies proposed and developed to reduce NO_x emissions include three-way catalytic converter (112), exhaust gas recirculation (113), selective catalytic reduction system (SCR) (114). Other techniques to optimize engine strategies include multiple injection (115; 116) or injection rate shaping (117; 118). The reduction of NO_x emissions using the 3-way catalyst is limited due to the fact that diesel engines operate on an overall lean mixture. Diluting the charge using EGR can lower the combustion temperature and oxygen concentration to reduce NO_x formation but with a drawback for soot formation. SCR systems using urea injection provide an effective reduction of NO_x. However, overdose of urea injected could result in NH₃ slip in the exhaust tailpipe.

The traditional method for measuring NO_x is using a chemi-luminescence detector (CLD), where gases from exhaust or in-cylinder are being sampled to measure the concentration of NO (119-121). Although CLD is a very accurate measurement

device, it is can be used only in laboratory due device size and calibration procedure required. Other Solid-state NO_x sensors installed in the exhaust tailpipe are used for after-treatment system control and engine optimization (122-124).

Several methods can be used to develop mathematical regression models for linear and non-linear problems (125-128). There are many nonlinear regression functions that can be used in building a model such as logistic, gompertz, monomolecular, power, exponential (126-128) as well as multiple regression polynomial functions (125; 129). Most of the procedures of estimation and testing of hypotheses for nonlinear models are based on the least square method and mean square error. In this study, a non-linear multiple regression (NLMR) model is used to estimate the soot percentage cycle by cycle using the ion current signal. There are two main steps to develop the NLMR model: development and testing. In the development phase, the NLMR model undergoes regression procedure in order to reduce the error between output and target values. In the testing phase, the performance of the NLMR model is evaluated with an independent dataset.

In this study, a novel approach using the ion current signal measured during combustion is developed to estimate the NO_x and percentage of soot formed. The ion current signal and some characterization parameters are determined. These parameters are used as an input in a non-linear multiple regression model (NLMR). The output target used in the NLMR is either NO_x or opacity percentage. A sensitivity analysis is conducted on the ion current characterization parameters to optimize the model

parameters and evaluate the uncertainties of these parameters due to the cycle to cycle variation.

8.2 Characteristics of the ion current signal in diesel engine

The air/fuel mixture in diesel engines has heterogeneous distribution that depends on engine design such as piston bore, bowl shape, swirl inside the cylinder, number of fuel sprays and spray cone angle (9; 26; 130; 131). It also depends on operating parameters such as injection pressure, injection timing, and amount of fuel injected, EGR, engine speed, load, intake pressure and temperature (41; 77; 130-135). The auto-ignition and combustion of the heterogeneous charge depend on the properties of the local fuel – vapor/air mixture and its thermodynamic properties. Consequently, the ionization is affected by many parameters that impact the combustion process. Although the ion current signal has noticeable cycle-to-cycle variations, it has some characteristics indicative of the combustion process. These include the start, duration, number of peaks and their amplitudes. Also the ion current signal, averaged over many cycles, can indicate different combustion characteristics such as premixed combustion fraction, and diffusion and mixing controlled combustion fraction.

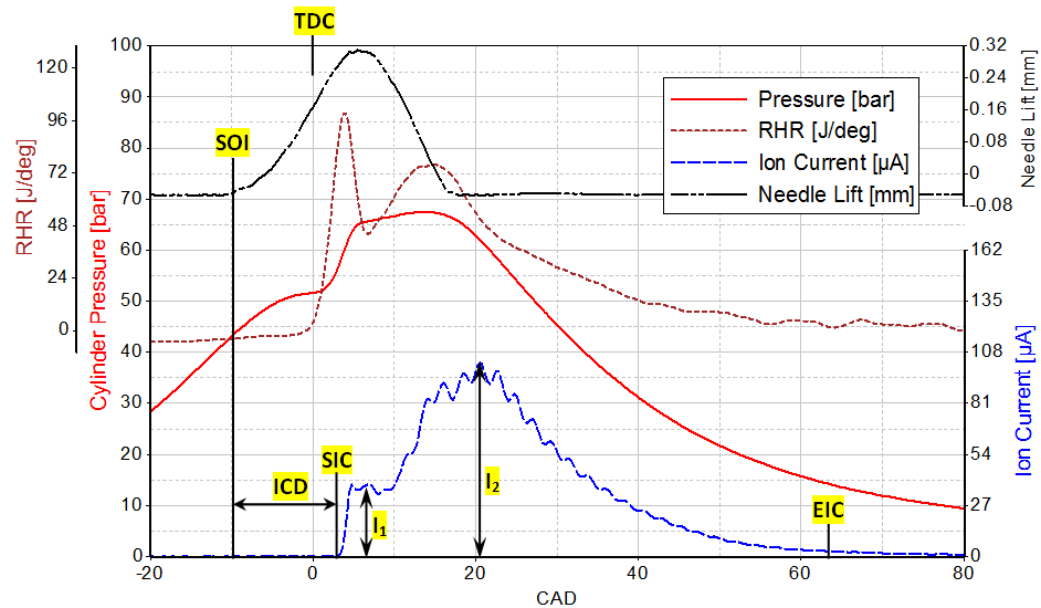


Figure 8.1. Cylinder gas pressure, needle lift, RHR, and ion current traces in a diesel engine [JD, IMEP=10 bar, Const. Speed=1800RPM, SOI=10° bTDC, Inj. Pres=600bar]

Figure 8.1 shows traces for cylinder gas pressure, rate of heat release (RHR), ion current and needle lift in 4.5L John Deere heavy duty turbocharged diesel engine. Engine operates at speed of 1800 rpm, injection pressure at of 600 bar, and engine load of 320 Nm (IMEP =10 bar). The needle lift indicates that the start of injection (SOI) is at 10° bTDC. The start of the increase of the ion current (SIC) is at 3.5° aTDC after an ion current delay (ICD) of 13.5 CAD. It reached a first peak I_1 of 36 μA at 6° aTDC, followed by a second peak I_2 of 101 μA at 20° aTDC. The first peak is produced from the premixed combustion fraction and the second peak is produced from the diffusion and mixing controlled combustion fraction. After the second peak, the signal decays down with slope (m), and terminates at EIC at 62° aTDC.

8.3 Basic concept of the soot and NO estimation

The experiential setup used in developing the algorithms for NO_x and soot estimation from the ion current signal is shown in Figure 8.2. One cylinder in the John Deere engine is fitted with a glow plug converted in house to act as an ion current sensor in addition to its basic function as a glow plug. (136). The soot content in the exhaust is measured by an opacity meter. The opacity meter has a response time of 0.1 sec and the time for one cycles = 0.067 sec at 1800 rpm. The NO emissions is measured by using CLD (40) Figure 8.2 A data acquisition system (DAQ) is used to record on a crank angle degree basis the ion current signal NO (ppm) and the soot percentage from the opacity readings.

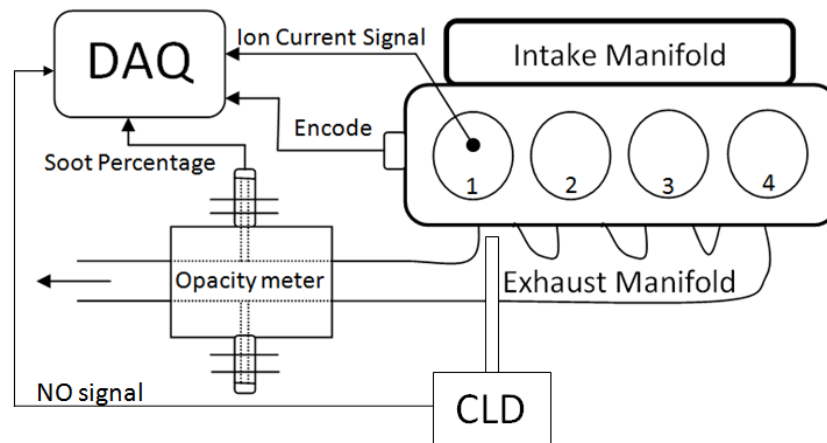


Figure 8.2. Engine Instrumentation for the ion current sensor, in-line opacity meter, and CLD

Although no ionization mechanism in diesel engines is available in the literature, the ion current signal characteristic parameters are used as an input to the NLMR model to estimate the soot percentage. These parameters are identified based on detailed analyses of several signals obtained in diesel engines of different makes and designs under steady state and transient operating conditions (9; 26; 29; 136).

8.4 NIMR model

Figure 8.3 shows the NLMR model used for the cycle to cycle soot estimation which consists of regressors block that receives inputs from the ion current signal and an input from soot measured by opacity meter. In this study, NLMR generates a set of linear and non-linear polynomial terms. The multiple regressions model is evaluated with least mean square error (MSE). Once the regression is computed, the output of the regression undergoes inverse transformation to obtain an initial estimate for the predicted soot percentage. The initial estimate is compared directly with the measured soot percentage. The predicted output block generates the NLMR model which can be used for the real-time estimation of the soot percentage using the ion current characterization parameters. Similar layout for the NO model is created using the NLMR model.

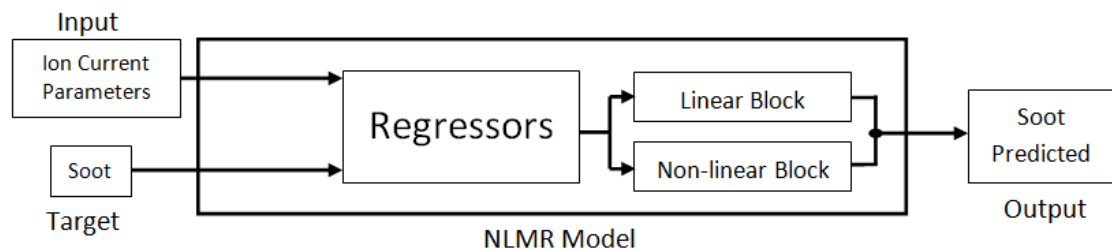


Figure 8.3. Layout of the NLMR model

8.5 Results and discussion for the soot model

The experiments conducted in this study include steady state and transient operation of the engine for various engine parameters. The range of the engine parameters covered in this study is listed in Table 8.1. The training for the NLMR model uses sets of engine operation for 11660 cycles using the ion current signal and the soot percentage measured in the exhaust.

Table 8.1. Operation range for experimental tests used in the study

Engine Parameters	Min	Max
Load (Nm)	50	450
IMEP (bar)	2.5	15
Speed (RPM)	1000	2000
Injection Pressure (bar)	350	1200
Start of injection	4	12
MAP (bar)	1.17	1.3

8.5.1 Sensitivity analysis for the ion current parameters

In order to examine the ion current parameters for accurate estimation of soot percentage, different combinations are tested in the NLMR model by increasing the number of input parameters. The results for the regression model are shown in Table 8.2. The best fit for the measured soot percentage is estimated using mean square error (MSE) and coefficient of determination (R^2). Each combination of input parameters generates a certain number of polynomial coefficients depending on the number of inputs to the NLMR model.

R^2 and MSE are calculated as follows:

$$\bar{y} = \frac{1}{n} \sum_i^n y_i \quad (5)$$

$$SS_{tot} = \sum_i (y_i - \bar{y})^2 \quad (6)$$

$$SS_{err} = \sum_i (y_i - f_i)^2 \quad (7)$$

$$R^2 = 1 - \frac{SS_{err}}{SS_{tot}} \quad (8)$$

$$DF = p \quad (9)$$

$$DF_{err} = n - p \quad (9)$$

$$MSE = \frac{SS_{err}}{DF_{err}} \quad (10)$$

Where

y_i is the soot input value (observed value)

\bar{y} is the mean value for soot input

f_i is the predicted soot value (modeled value)

SS_{tot} is the total sum of squares

SS_{err} is the residual sum of squares

MSE is the mean squared error

n is the total number of observations

p is the number of input parameters

DF_{err} is the degree of freedom for the error

DF is the degree of freedom for the model

Table 8.2. Results for MSE and R^2 for the NLMR model using different combination of the ion current parameters

# Input	DF	MSE	R^2
1	2	1.599	0.3845
2	5	0.994	0.6050
3	10	0.615	0.7409
4	19	0.526	0.8232

Table 8.2, four combinations are listed for the ion current parameters examined using the NLMR model. The table lists model degree of freedom, mean squared error (MSE), and coefficient of determination (R^2). It is observed that using one input to the model results in a low coefficient of determination $R^2 < 0.39$ and high MSE > 1.6 . Using combination of two inputs show a maximum $R^2 = 0.6$ and MSE= 0.994. A combination of three inputs has further improved the correlation for soot estimation $R^2 = 0.74$ and MSE= 0.615. By including four inputs in the LNMR model, the coefficient of determination R^2 reaches its maximum of 0.82 and the MSE reduces to 0.526. It should be noted that the NLMR model considers the interaction between different inputs in the nonlinear block, and the DF for the input variables is 19. Thus, the four ion current parameters are able to estimate the soot percentage with $R^2 = 0.82$. Figure 8.4 shows different trends between estimated and measured soot percentage using different inputs to the NLMR model. Varying the number of input parameters reflects different coefficient of determination R^2 and mean square error MSE at their DF.

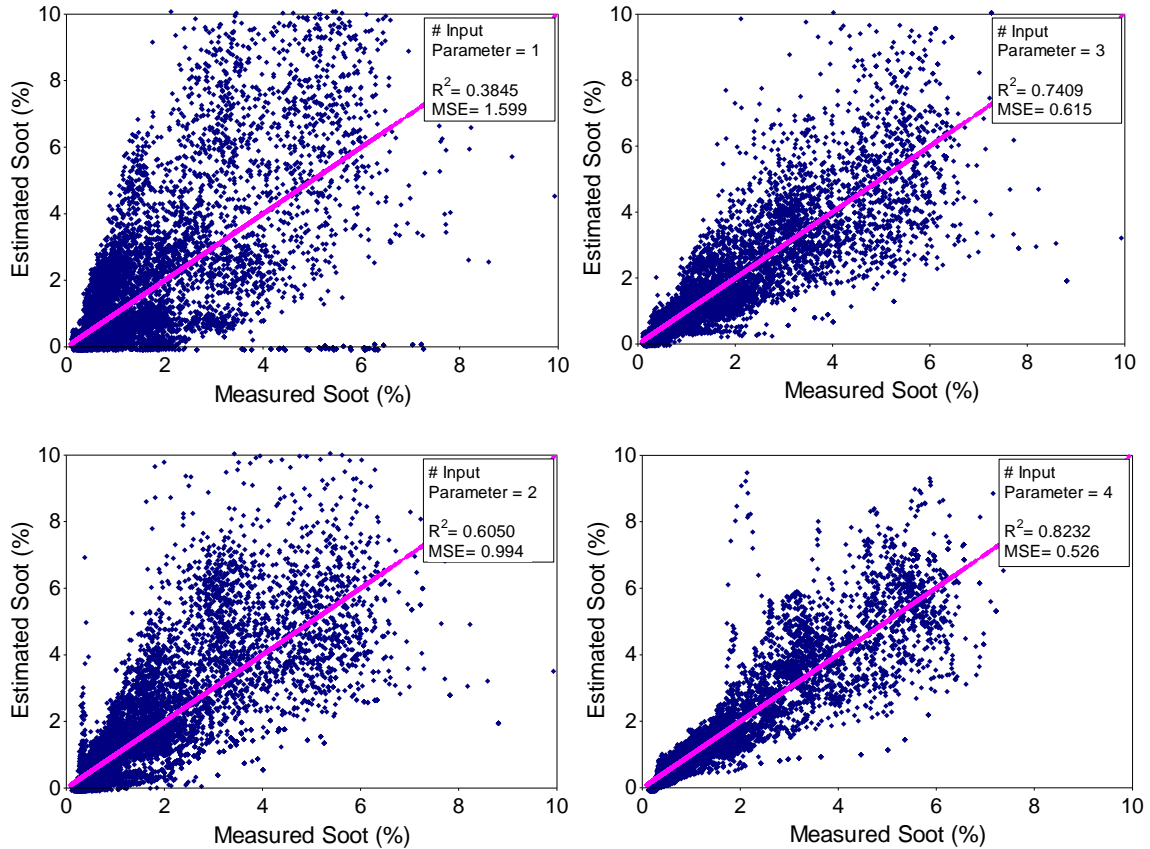


Figure 8.4. Estimated versus measured soot percentage using different inputs to the NLMR model

8.5.2 Ion current/ soot sensor

After the sensitivity analysis performed on the ion current parameters using the NLMR model, the NLMR model is ready to be tested in real-time and compared with soot measured using the opacity meter. The NLMR model built is shown in Figure 8.5, where the model is tested under various engine conditions such as different engine loads, speeds, injection pressures, intake pressures, and different rates of EGR. The ion current signal acquired cycle by cycle is analyzed to extract the four ion current parameters. The

parameters are supplied to the NLMR model, where estimated and measured soot percentage is compared.

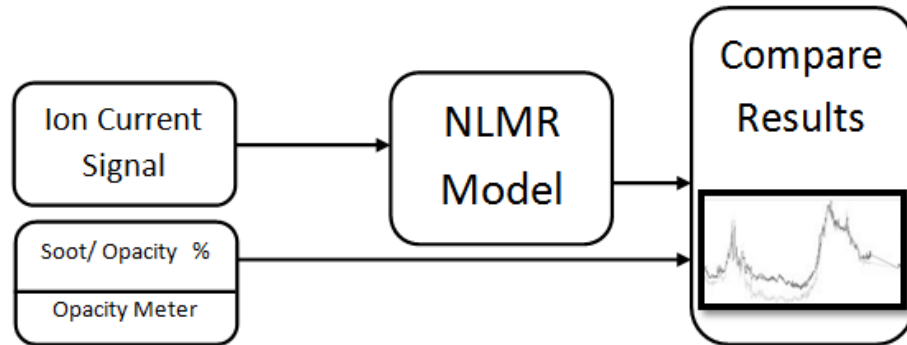


Figure 8.5. Testing the NLMR model layout

(i) Engine load and injection pressure

Figure 8.6 shows a comparison between the estimated soot (E_{soot}) calculated using the ion current parameters and the measured soot (M_{soot}) from the opacity meter. The load profile shows transient increase and decrease of engine load to test the performance of the soot model. The engine is operated at constant speed of 1800 rpm. The engine load is varied from a minimum of 12 Nm (IMEP =1.72 bar) to a maximum of 410 Nm (IMEP =14 bar) with four injection pressures 350, 500, 650, and 800 bar. The soot estimation using the ion current signal shows a fairly good agreement with the opacity soot percentage. The figure also shows that the estimation of the soot is very sensitive in low ranges soot as well as high ranges. In addition, the residual error plot shown in Figure 8.7 shows a normal distribution with a very high frequency at zero. In Figure 8.8, the

estimated soot (M_{soot}) is plotted versus the measured soot (E_{soot}), where the determination coefficient $R^2 = 0.92$ which indicates a very high accuracy and mean square error $\text{MSE} = 0.1615$.

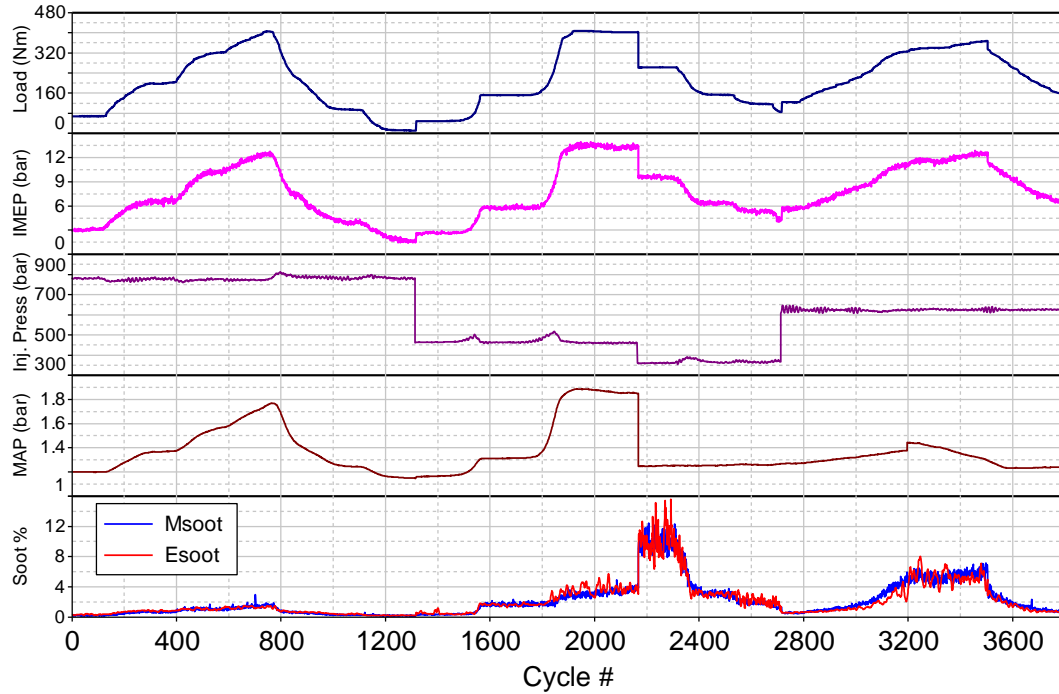


Figure 8.6. Engine Load data [JD, Const. Speed=1800RPM, EGR= 0%]

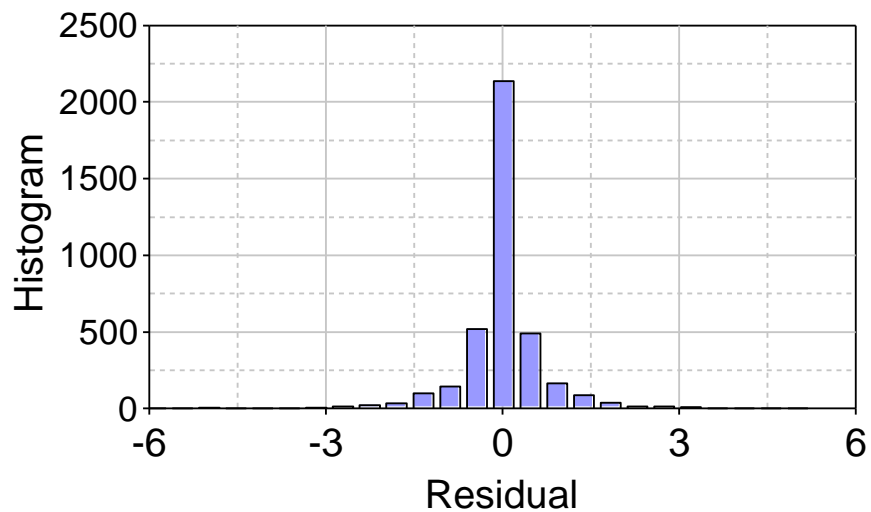


Figure 8.7. Histogram for the residual error between estimated and measured soot percentage for engine Load data

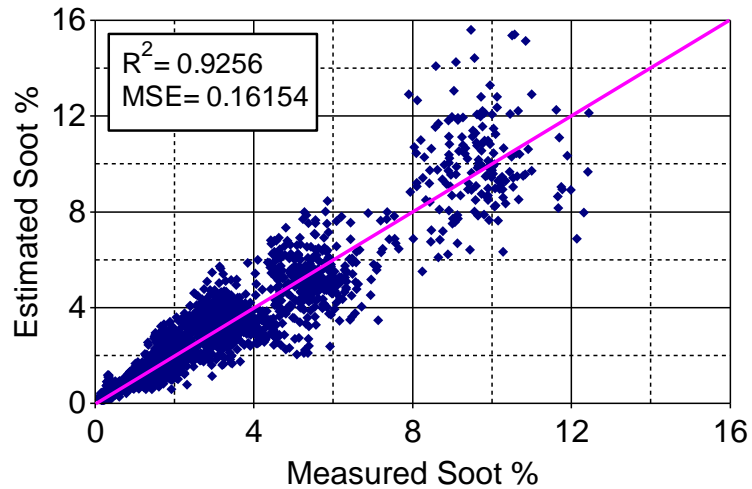


Figure 8.8. Measured versus estimated soot percentage for engine Load data

(ii) Engine speed

Figure 8.9 shows a comparison between the estimated soot (E_{soot}) and the measured soot (M_{soot}). The speed profile shows acceleration, deceleration and constant engine speed to test the performance of the soot model. The engine is operated at constant load of 150 Nm (IMEP= 6 bar). The engine speed is varied from 1000 to 2000 rpm, where intake pressure MAP ranged from 1.1 to 1.6 bar . The soot estimation using the ion current signal shows a fairly good agreement with the opacity soot percentage. In addition, the residual error plot shown in Figure 8.10 shows a normal distribution with a high frequency within $\pm 1\%$. In Figure 8.11, the estimated soot (M_{soot}) is plotted versus

the measured soot (M_{soot}), where the determination coefficient $R^2 = 0.79$ which indicates a good accuracy and mean square error $\text{MSE} = 0.5695$.

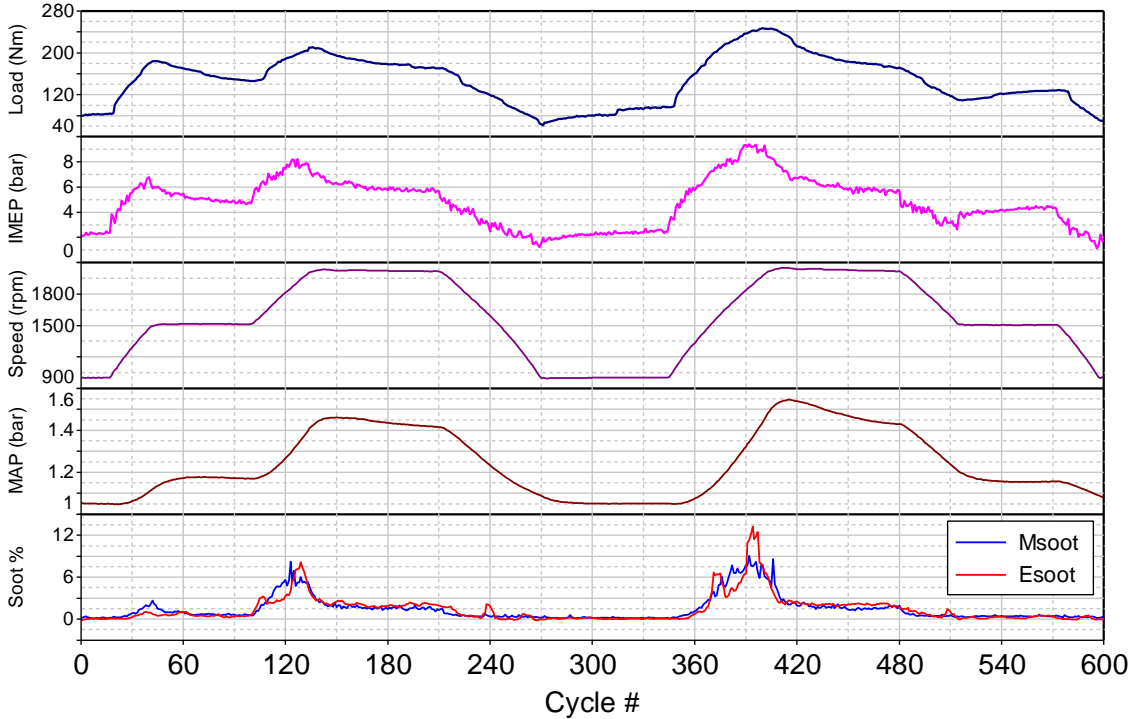


Figure 8.9. Engine speed data [JD, EGR= 0%]

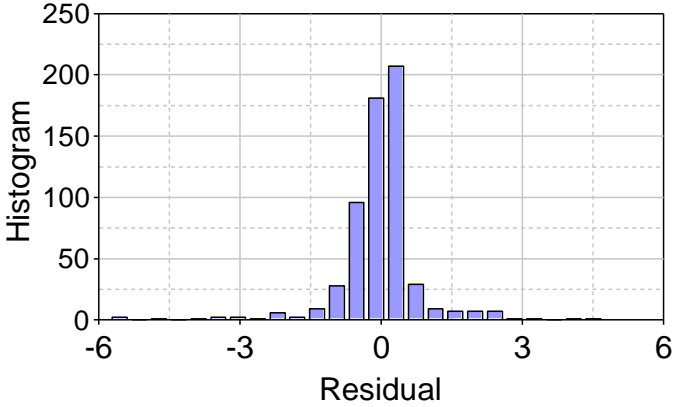


Figure 8.10. Histogram for the residual error between estimated and measured soot percentage for engine speed data

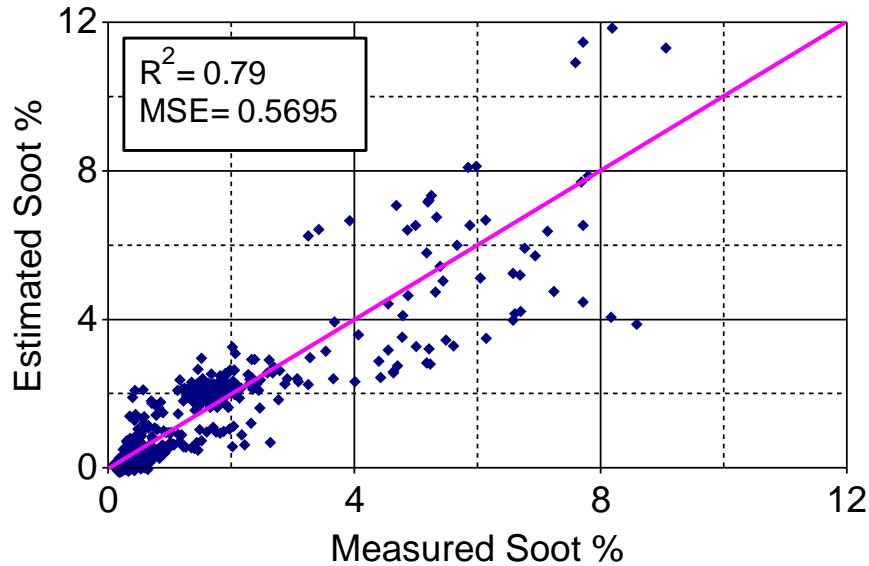


Figure 8.11. Measured versus estimated soot percentage for engine speed data

(iii) MAP

The soot model is tested under transient MAP as shown in Figure 8.12. A comparison between the estimated soot (E_{soot}) and the measured soot (M_{soot}) shows a good agreement. The engine is operated at constant load of 140 Nm (IMEP= 6 bar), engine speed = 1800 rpm, injection pressure = 800 bar, and EGR = 0 %. The intake pressure is varied from MAP = 1.15 to 1.27 bar. The residual error plot shown in Figure 8.13 shows a normal distribution with a high frequency within $\pm 0.25\%$. In Figure 8.14, the estimated soot (M_{soot}) is plotted versus the measured soot (E_{soot}), where the determination coefficient $R^2 = 0.35$ with very small mean square error $MSE = 0.0035$. Although the overall trend for the estimated and measured soot percentage is in agreement. R^2 is very small due two to two reasons: (1) very low range of soot percentage

that being measured, and (2) fast response cycle to cycle estimated soot does not match the lower response measured soot.

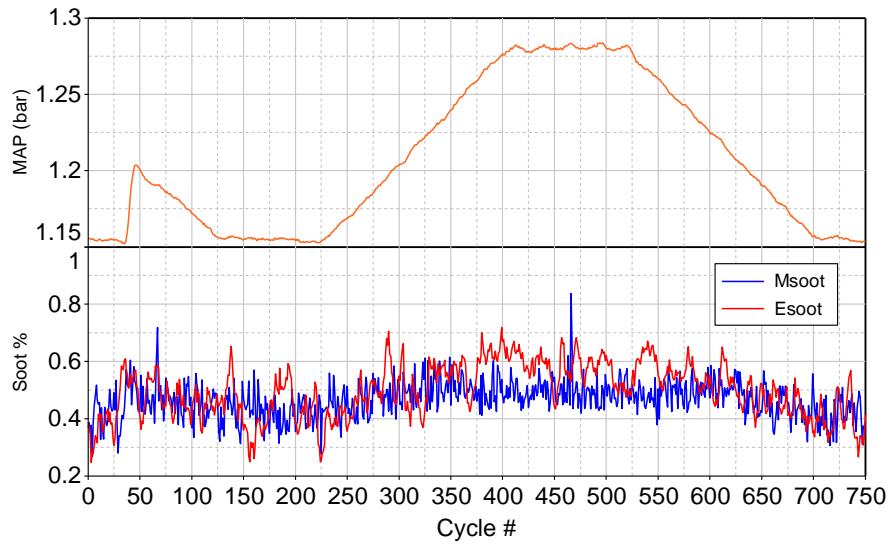


Figure 8.12. Engine speed data [JD, Speed=1800 rpm, Load=140 Nm , EGR= 0%]

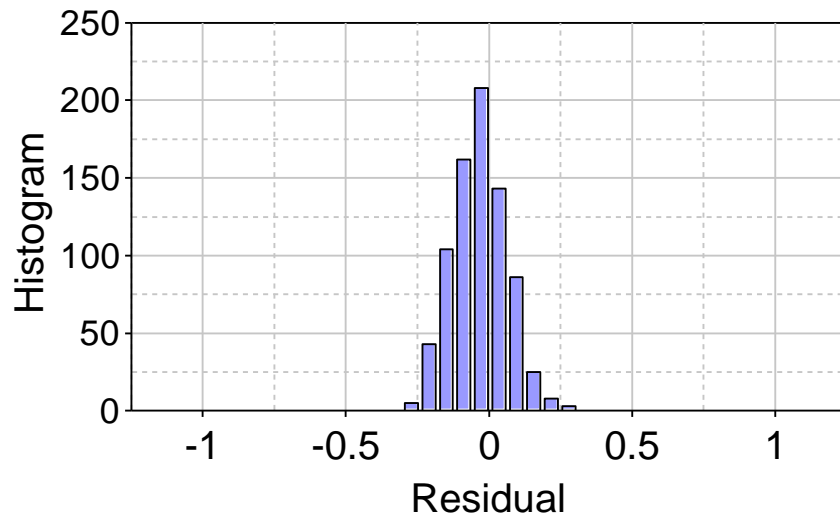


Figure 8.13. Histogram for the residual error between estimated and measured soot percentage for MAP data

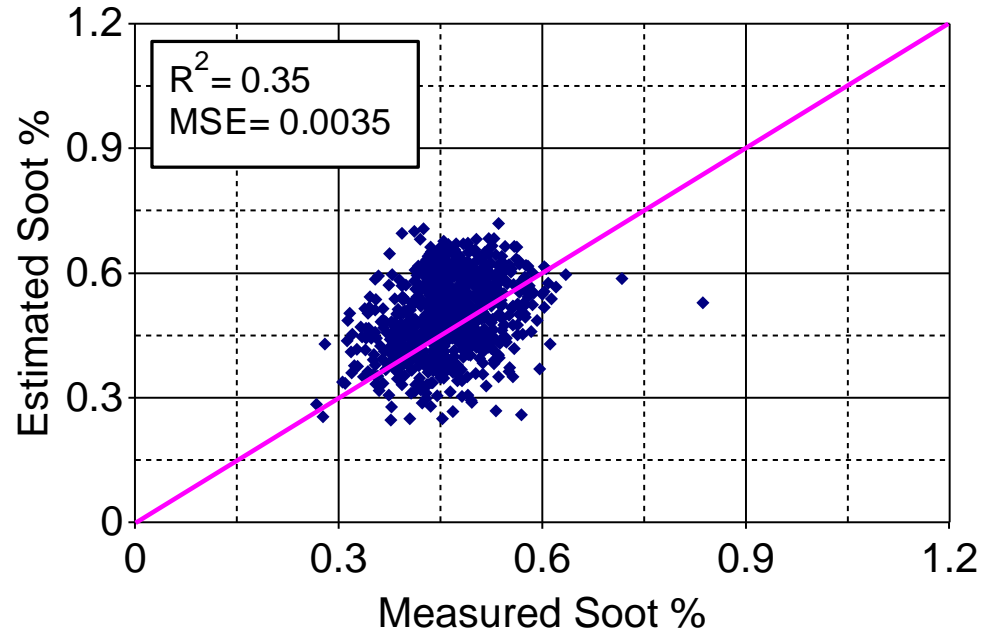


Figure 8.14. Measured versus estimated soot percentage for MAP data

8.6 Results and discussion for the NO model

The experiments conducted are the same as those used in the soot model and include operation under steady state and transients while varying different engine parameters. The training of the NLMR model uses sets of engine operation for 11660 cycles using the ion current signal and the NO measured in the exhaust of the cylinder # 1.

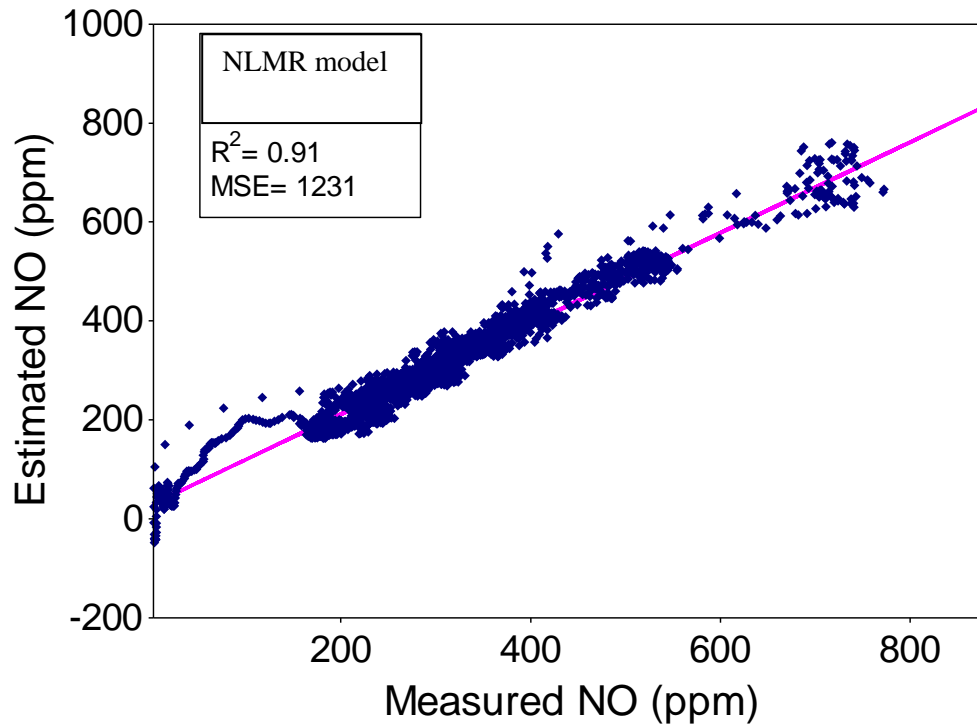


Figure 8.15. Estimated versus measured NO concentration using different inputs to the NLMR model

Figure 8.15 shows different trends between the estimated and measured NO concentrations using ion current as an input to the NLMR model. The coefficient of determination R^2 and minimum mean square error MSE at their DF are 0.91 and 1231.

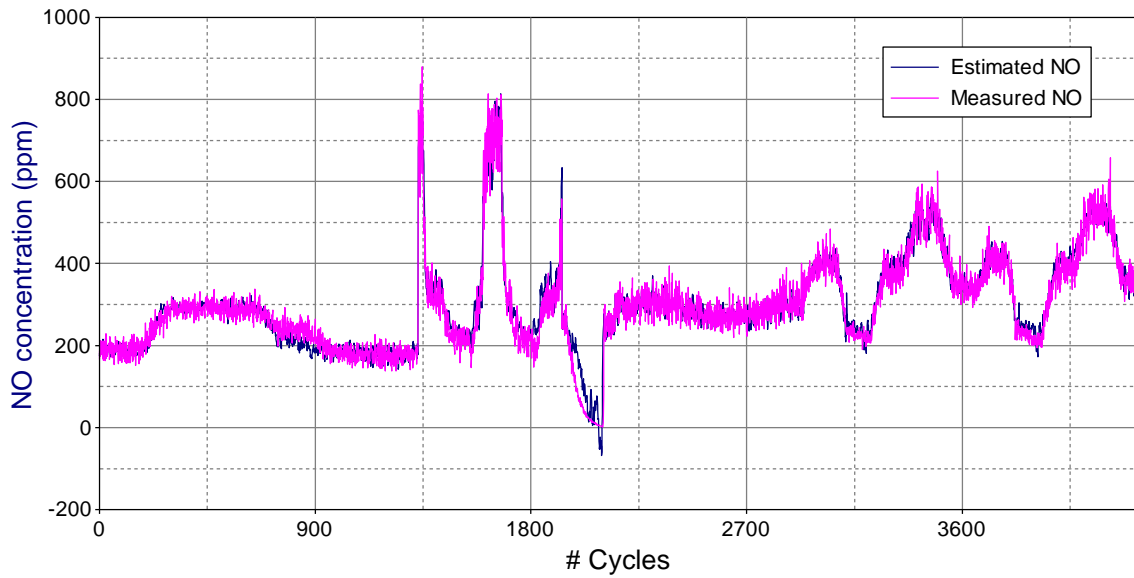


Figure 8.16. Estimated and measured NO concentration under different operating conditions

Figure 8.16 shows NO concentration measured in the exhaust port of cylinder #1 and NO concentration estimated from the ion current signal using the NLMR model. The agreement between the two traces under the steady state and transient operation is very good.

8.7 Summary

A new technique is described and tested to estimate the soot percentage and NO mole fraction on cyclic basis. This technique utilizes inputs derived from the ion current signal measured during the combustion process. Several advantages are demonstrated, including the insensitivity to uncertainties in the measurements. The non linear multiple regression model developed is able to estimate NO and soot under steady state and transient operating conditions. A summary of this study is as follows:

1. A new technique for estimating NO and soot in diesel combustion is developed based on the ionization signal measured inside the combustion chamber.
2. The combinations of inputs extracted from the ion current signal are able to estimate NO and soot on a cycle by cycle basis.
3. The predicted soot and NO emissions agreed fairly well with the measured values in the exhaust port of the instrumented cylinder under different steady state loads and speeds as well as under transient engine operating modes.

Therefore, introducing the ion sensor in advanced diesel engines can be of great advantage in engine development and calibration. By utilizing the model presented in this paper, the engine ECU can estimate simultaneously NO and soot percentage for feedback control of the parameters of engine and after-treatment devices to meet the production targets. Also, it has a potential for use as an on-board diagnostic tool..

CHAPTER 9

3D CFD MODEL SIMULATION AND VALIDATION OF IONIZATION

In order to better understand ionization produced in diesel combustion, a 3D CFD model is built using a commercial computational fluid dynamics software (STARCD). The CFD cycle simulation is coupled with a chemical kinetic solver (DARS-CFD) to compute the chemical reactions taking place inside the combustion chamber. In this chapter, an ionization model developed at WSU (42) is included in the chemical kinetic model and used to simulate combustion cycles at different operating conditions. The simulation data obtained are compared and validated with the experimental results.

9.1 Literature review

It is important to have a good understanding of the ionization processes in diesel combustion in order to fully utilize the ion current signal for engine diagnostics and feedback control. This can be accomplished by using CFD simulation coupled to a chemical kinetic ionization mechanism and chemical combustion model. A review is made of the ion formation includes ions formation in different hydrocarbon/air flames, positive and negative ions contribution, ions initiation reactions, role of ions in soot

formation, ionization mechanisms, and interpretation of the ionization in internal combustion engines.

9.1.1 Ions formation in flames

An early investigation of ions formation in flames was conducted by Calcote, where he modified a Langmuir probe to measure the electron concentration produced at different distances in the flame (137-139). Calcote discussed the production of ions by chemi-ionization and attempted to formulate the ion formation and recombination in flames. Also, experimental observations found that the concentrations of the positive ions are 4 times of the electrons.

Nicholson et. al. concluded that CH and O are the primary reactants in ionization in premixed flames which are formed in the blue luminous zone of CH emission and the ion concentration reaches a maximum in the violet zone of the flame, that is, downstream of the blue zone (140).

The reaction paths for positive and negative ionization in hydrocarbon flames were studied using the mass spectrometer and Langmuir probe (141-143). The mass spectrometer showed that the negative ions concentration is 2% of the positive concentration, where it is decided that negative ions were to be unimportant.

Calcote et. al. studied the ion formation in fuel rich and sooty flames such as acetylene-oxygen and benzene-oxygen, and proposed soot formation mechanism through a chemical ionization cycle that produces heavy hydrocarbon ions and PAH⁺ in rich flames (144-146). A mass spectrometer was used to measure the concentration profile in

low pressure rich fuel/air flames. The ionic theory postulates that small ions such as $C_3H_3^+$ acts as nuclei that react with species such as C_2H_2 and C_4H_2 to form larger positive polycyclic aromatic ions which ultimately become soot precursors.

Hall-Roberts et. al. showed a comparison between the soot formation through ions involved mechanisms and non ions involved mechanisms (147). They conducted an experimental test that introduces an aqueous CsCl into the burner to increase the concentration of (Cesium) Cs atoms in the flame. By introducing Cs atoms, a charge transfer takes place due to the low ionization potential of Cs that rapidly removes ions such as $C_3H_3^+$. This should have dramatically reduced the levels of soot in the flame if $C_3H_3^+$ was the only nuclei for soot. On the other hand, neither Cs showed any effect on the initial sooting behavior nor do hydrocarbon ions appear as major nuclei for soot.

Doherty et. al. showed additional results reported in reply to Calcote's comments on the origin of soot in flames (148). Although this study supported their claims shown earlier (147) which indicates that the ionic route to soot is not the major one, they indicated that the role of ions affecting the coalescence and agglomeration of soot particles is possible.

9.1.2 Modeling ions formation in internal combustion engines

Saitzkoff et. al. used the spark plug to measure the ionization produced in spark ignition engines (13; 14; 149). Three distinct phases in the ion current signal were defined. The first phase is a high current measured due to the discharge of the electric potential of the spark, second phase is a first peak at early stage of combustion dominated by chemical reactions, and third phase is a second peak coincides with peak pressure and

temperature inside the cylinder. An analytical model was proposed to predicate the ion current in the post flame, where an assumption of magnifying the NO concentration of the Zeldovich mechanism more than 12 times in order to predict ion current comparable to the experimental results.

Naoumov et. al. considered Saitzkoff and Reinmann model to simulate the ion current signal of spark ignition engine (16). They integrated a chemical kinetic mechanism for the first peak of the ion current and a non-equilibrium model for the second peak. The model showed a good prediction for the ion current signal compared to the experimental results.

A number of publication investigated the chemi-ionization mechanism for homogenous charge compression ignition engines (HCCI) considering the main ionization species are CHO^+ , CH_3^+ , H_3O^+ , NO^+ , and C_3H_3^+ (23; 25; 150). The model results showed a good agreement with the experimental findings at different equivalence ratios, intake temperatures, and fuel concentration.

In 2011, a complete ionization mechanism was developed by Estefanous for diesel combustion based on detailed chemical kinetics considering combustion in very lean to very rich air/fuel mixtures (42). A zero dimensional chemical kinetic model was used to evaluate the contribution of different species over a wide range of equivalence ratios. Also, thermal ionization was considered for NO^+ , CH_3^+ , HCO^+ and C_3H_3^+ in addition to detailed chemi-ionization reactions. Further, the ionization model was implemented into a 3D simulation mode, where simulation results showed a good

agreement with experimental results obtained under different injection pressures and loads.

9.2 Simulation model and assumption

The engine is a 4.5L John Deere Turbocharged diesel engine, bore = 106 mm, stroke = 123 mm and compression ratio = 17:1. The engine is equipped with a common rail injection system and a solenoid type injector, 6-hole nozzle (0.095 mm in diameter). A detailed description of the experimental setup and engine instrumentation can be found in Ref. (40). Figure 9.1 shows the geometry of piston bowl used in this work for creating the CFD mesh for the combustion simulation.

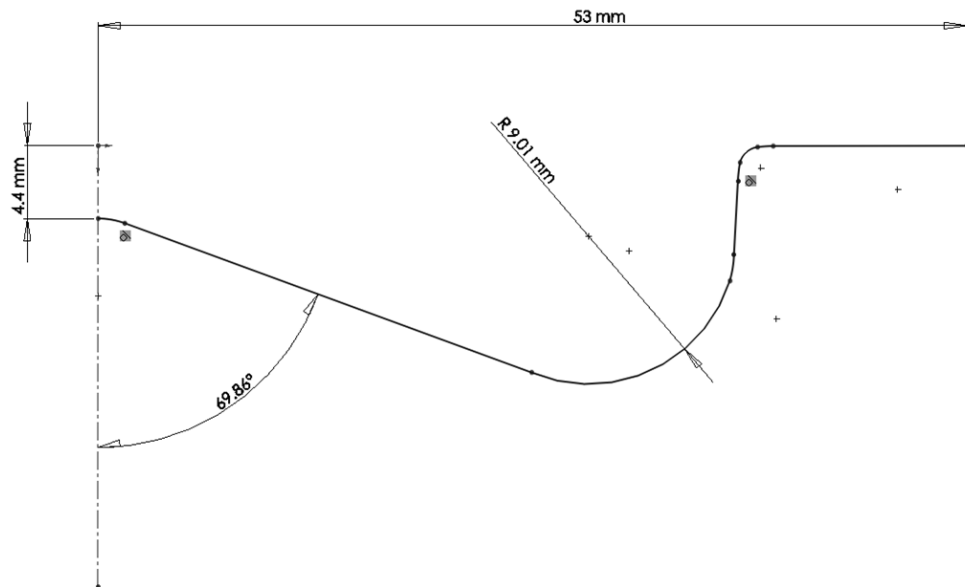


Figure 9.1. Piston bowl profile used in the CFD simulation

STAR-CD, commercial CFD simulation software coupled with chemical kinetics solver (DARS-CFD), was used to simulate combustion cycles. Es-ice was used to generate the sector mesh of the combustion chamber and is responsible for defining moving-grid, boundary conditions, and initial conditions. Further, Pro-STAR was used to set other parameters such as fuel atomization model, combustion model, injection parameters, time-step resolutions etc. STAR-CD has the capability to compress, expand trim, add, and remove cells in the mesh based on piston location. The mesh created for the diesel engine simulation is shown in Figure 9.2. The total number of cells is 99144 with piston at BDC and 18168 at TDC.

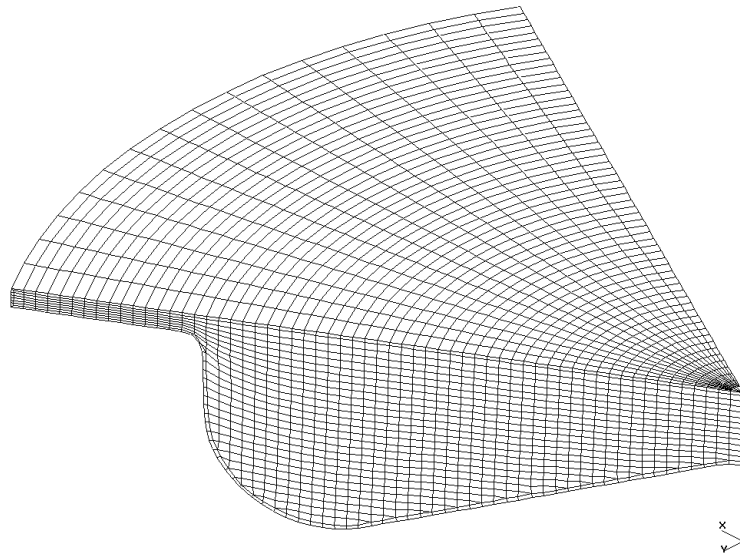


Figure 9.2. Computational Sector mesh used in the engine simulation at TDC

The simulation model is computed using the following assumptions: (1) Lagrangian approach to define droplet behavior, (2) Reitz break-up model, (3) Bai Droplet wall interaction, (4) Huh spray model, (5) wall heat transfer and droplet

evaporation, (6) Droplet Physical model including turbulence dispersion, gravity effect and collision model. Table 9.1 shows simulation parameters setting used in this study.

Table 9.1. Simulation parameters setting

Engine Speed (RPM)	1800
Spray Angle (deg)	103°
Swirl Ratio (SR)	2.66
Droplet Physical properties	N-heptane (L) NC7H16 (NIST Table)
Cylinder wall, combustion dome, and piston crown temperatures	450, 500, and 500 K
Chemical Kinetic mechanism	33 species N-heptane mechanism (151)

The combustion simulation starts at 40° bTDC and ends at 180° aTDC with two time step resolution of 0.25 CAD from start of simulation till start of injection, and 0.1 CAD from start of injection till the exhaust valve opening at 180° aTDC. The initial pressure and temperature conditions are set based on the experimental data obtained from the intake manifold for each test conducted.

9.3 Ionization mechanism and ion current probe configuration

The ionization mechanism used in this study is generated for diesel combustion considering the heterogeneity of the charge, and it accounts for wide equivalence ratio from very lean, stoichiometric, very rich and soot producing mixture. Also, the ionization mechanism accounts for chemi-ionization as well as thermal ionization. The major ion

species considered are CHO^+ , CH_3^+ , H_3O^+ , CH^+ , C_3H_3^+ , C_5H_3^+ , C_7H_5^+ , C_9H_7^+ , $\text{C}_{11}\text{H}_9^+$, NO^+ , and electrons.

In order to validate the results of the ionization obtained from the simulation, a number of virtual probes are defined inside the combustion chamber to sense the ionization produced locally inside the combustion chamber. Further, the ion current data measured from the experimental test is compared with the simulation results. Figure 9.3 illustrate the location of 23 virtual probes defined in the CFD simulation model to monitor the electrons and other species of interest during the combustion process. The virtual probe is defined in es-ice input file, where the probe radius and its protrusion inside the combustion chamber are defined. The location of the original ion current probe is # 13 marked with red circles in Figure 9.3.

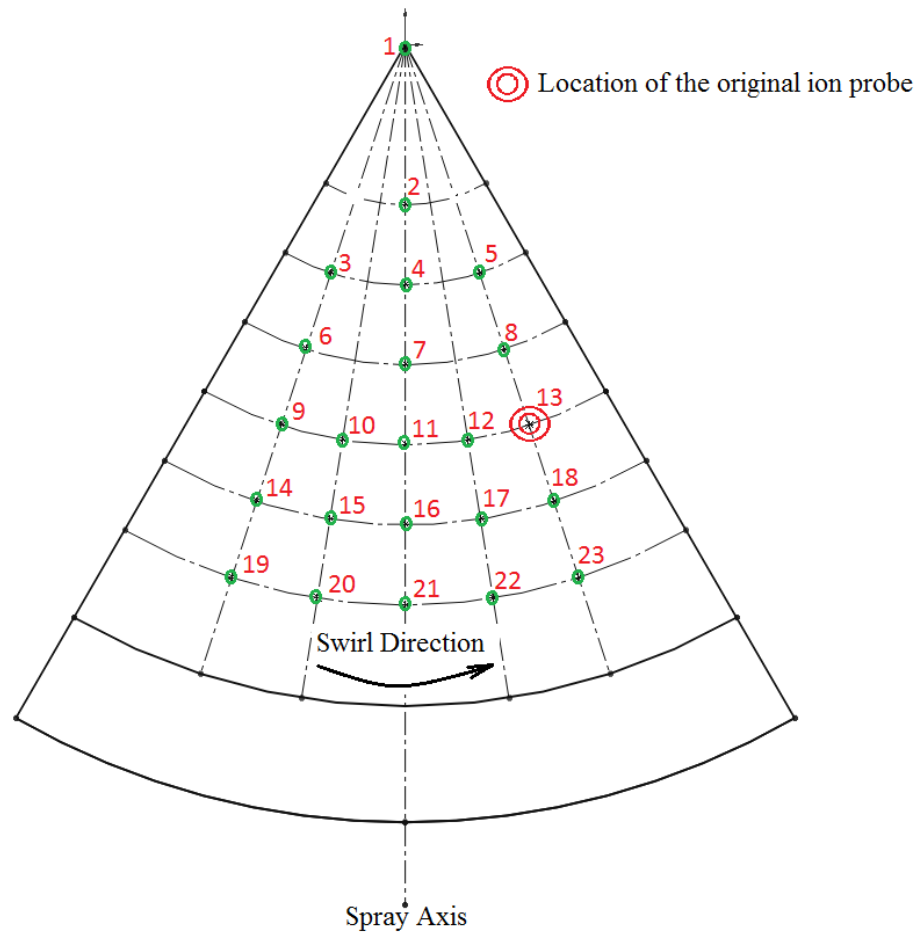


Figure 9.3. Virtual probes defined in the CFD model

9.4 Effect of probe diameter and protrusion in the CFD

results

The probe functions as a data collector in the boundary defined by the radius and center of the probe sphere which is different from the ion current probe used in the experimental setup. Also, there is no electric field defined in for the virtual probes which can be approximated to a case with low potential difference between the ion current electrodes. According to recent publications (11; 18; 26; 29), the increase in voltage and

probe area increase the amplitude of the signal but do not change its characteristics (number of peaks and shapes).

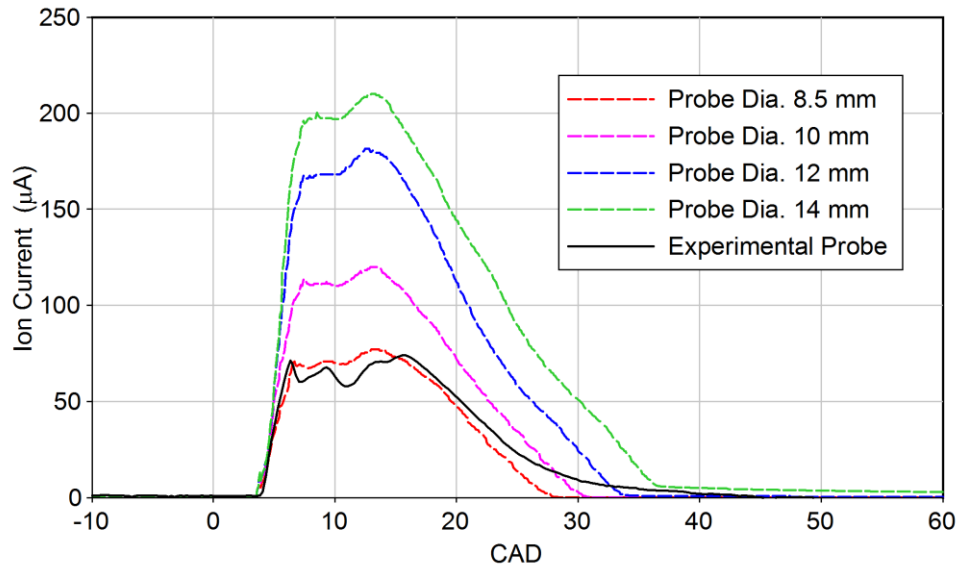


Figure 9.4. Different probe diameter CFD simulation [JD, 1800 RPM, LPPC 4° aTDC, ,inj. press 1200 bar, and IMEP 4 bar]

Figure 9.4 shows simulation results for the effect of the probe diameter at an engine IMEP of 4 bar. The ionization resulted from simulation is scaled against the experiential results of Diameter 8.5 mm which shows a very good agreement in peaks and slopes. By increasing the probe diameter the following is observed: (1) the amplitude of the ion current signal 1st and 2nd peak increase, (2) the ion current duration increases, and (3) location 1st and 2nd peak slightly retard. These observations are in agreement with experimental test conducted under different probe areas (18).

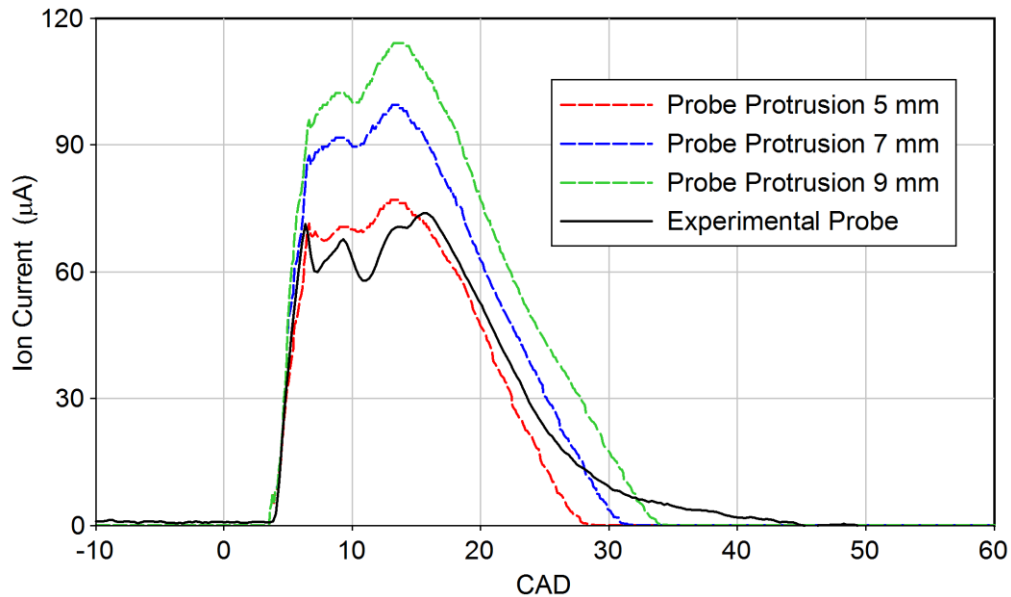


Figure 9.5. Different probe protrusion in the CFD simulation [JD, 1800 RPM, LPPC 4° aTDC, inj. press 1200 bar, and IMEP 4 bar]

Figure 9.5 shows simulation results for the effect of different probe protrusion at an engine IMEP of 4 bar. The ionization resulted from simulation is scaled against the experiential results of protrusion 5 mm. Increasing the probe protrusion inside the chamber has the following effects: (1) the amplitudes of the ion current signal 1st and 2nd peaks increase, and (2) the ion current duration increases. These observations are in agreement with results of experimental test conducted under different probe lengths (26).

It can be concluded from Figure 9.4 and Figure 9.5 that the diameter of the ion current probe is more effective in increasing the signal amplitude compared to sensor protrusion. The results of simulation will be validated with the experimental results using the probe # 13 with the following configuration: radius 8.5 mm and protrusion 5 mm.

9.5 Effect of probe location in the CFD results

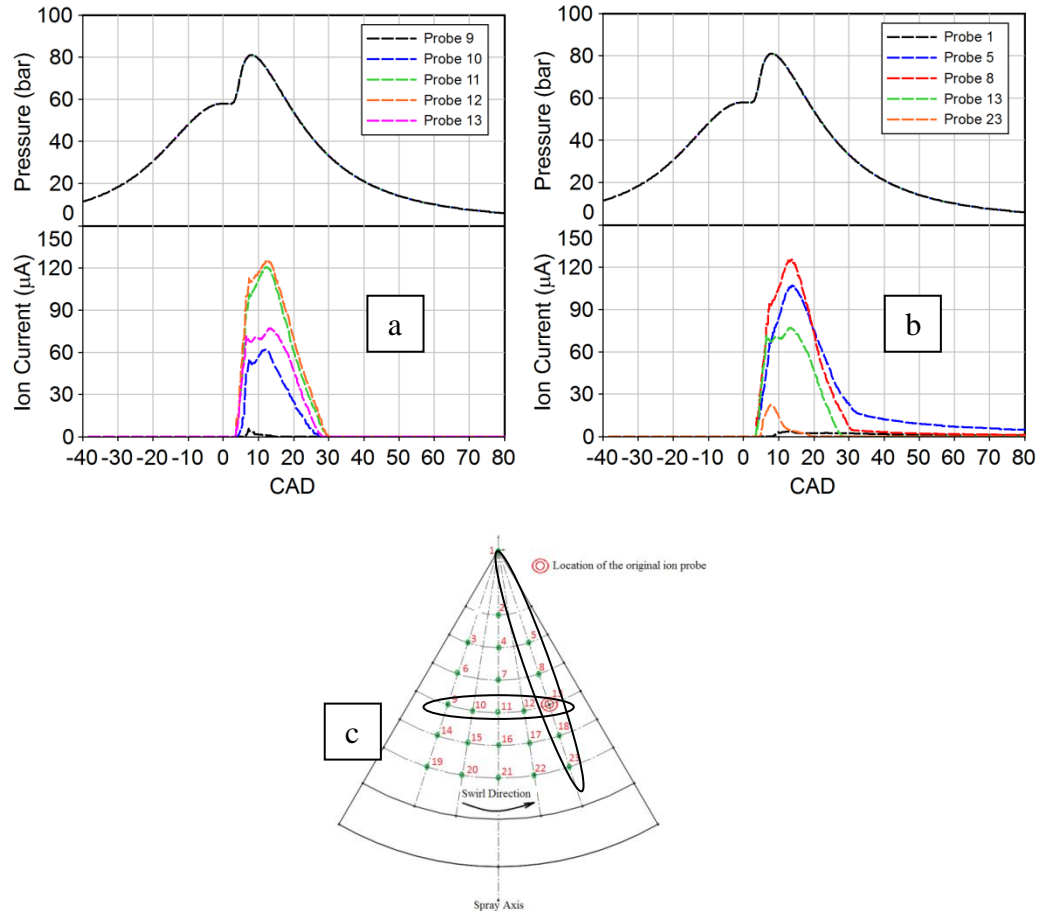


Figure 9.6. Different probe location in the CFD simulation [JD, 1800 RPM, LPPC 4° aTDC, inj. press 1200 bar, and IMEP 4 bar]

Figure 9.6 shows the ion current signal plotted for different probe locations inside the combustion chamber. The probes on the azimuthal and radial axes intersecting probe13 are considered for plotting the ion current along their axes. Figure 9.6c indicates the location of the virtual probes inside the combustion chamber and the direction of the gas swirl motion relative to the probe locations. Figure 9.6a shows the ion current signals from five probes on the azimuthal axis. The following observations are made (1) the SIC

is consistent for the probes located on the spray axis and in the direction of the swirl whereas the far probes 9 and 10 showed some retardation, (2) the location of the 1st and 2nd peaks of the ion current is consistent for all the probes, and (3) the amplitude of the ion current signal is the highest at probe 12 (location of the probe is adjacent to the spray axis in the swirl direction) whereas the amplitude decay for far probes.

Figure 9.6b shows the ion current signals from five probes located on the radial axis located 18° from the spray axis. The following observations are made (1) the SIC is consistent for all the probes except for a small retardation in the signal detected by probe 1 near the injector and probe 23 near the wall of the piston bowl, (2) the location of the 1st and 2nd peaks of the ion current is consistent for all the probes, and (3) the amplitude of the ion current signal is the highest at probe 8 where signal decays for probes far from probe 8. Meanwhile, the pressure signals recorded at all probes show no difference regardless of their location.

The limitation of an actual probe installed in-line with the spray axis inside the combustion chamber for detecting the ion current signal was reported (29) which resulted from wetting the sensor surface by the liquid spray. The liquid film formed on the probe surface prevents the sensor from detecting the ion current signal. This effect was not considered in modeling the virtual probe in the CFD simulation.

In addition, the location of the maximum amplitude for the ion current signal can change based on engine parameters such as spray angle, nozzle diameter, swirl ratio, and type combustion chamber geometry. Also, the SIC and location of the maximum amplitude for the ion current signal can change based on the operating parameter such as

injection pressure, timing, speed and load. Some of these parameters and conditions will be studied in details later in this chapter.

9.6 Simulation results validation with experimental data

In this section, the results for the gas pressure, rate of heat release, ion current, NO, and soot emissions are results obtained from the CFD simulation under different loads and injection pressure are validated with the experimental data.

9.6.1 Effect of engine load

The results obtained from the experiments and CFD simulation are compared at four different engine loads as shown in Figure 9.7. The combustion phasing is kept constant at LPPC of 4° aTDC; therefore, the SOI in the simulation is adjusted accordingly to match the experimental combustion phasing. The results in Figure 9.7 show a good agreement between the simulation and experiments. At IMEP 4 bar, the fuel is injected at 5° bTDC where a high premixed combustion is produced. The simulation showed a very good prediction of the ion current in term of peaks location, amplitudes, duration, rising and decaying slopes.

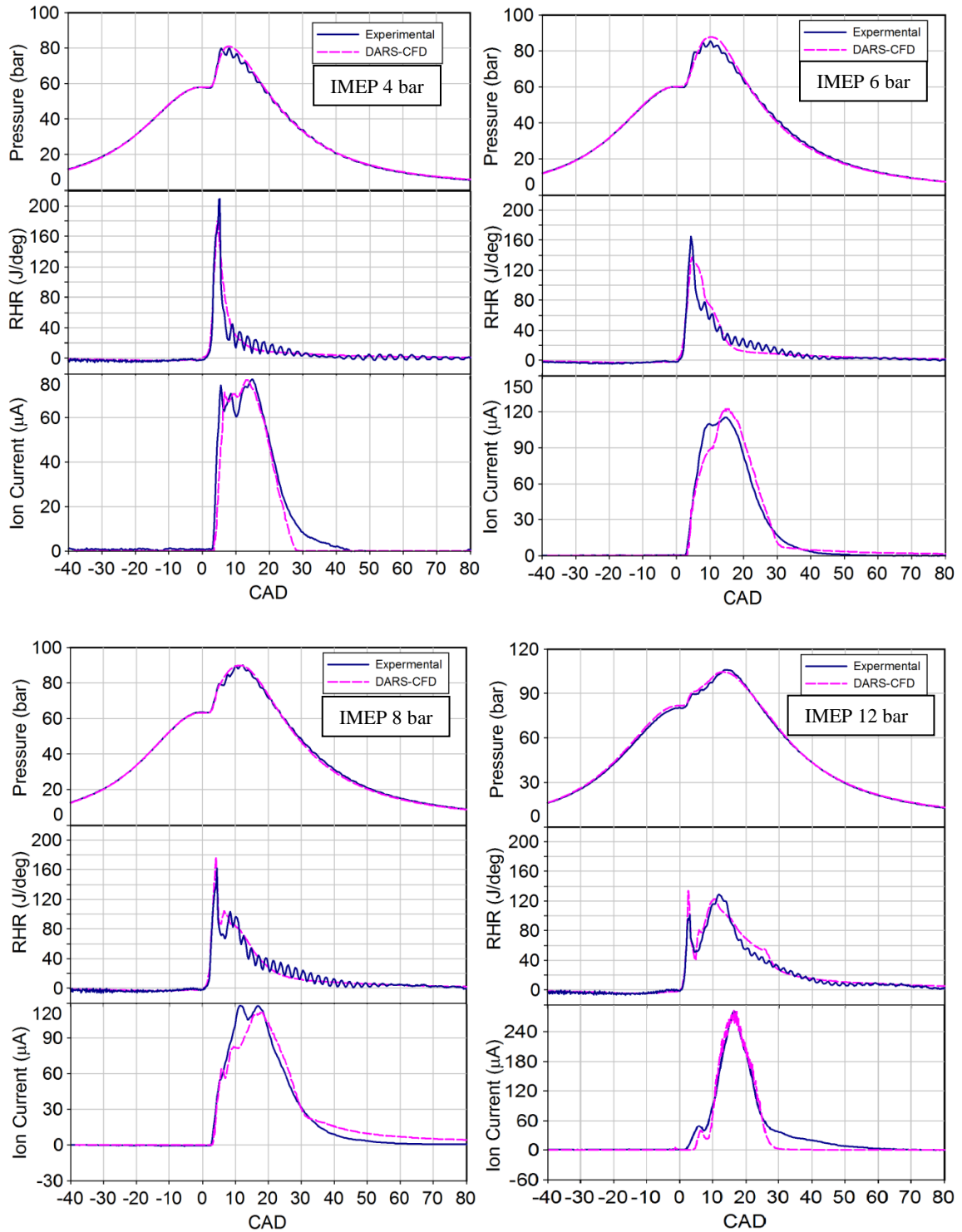


Figure 9.7. Simulation at different loads [JD, 1800 RPM, LPPC 4° aTDC, and inj. press 1200 bar]

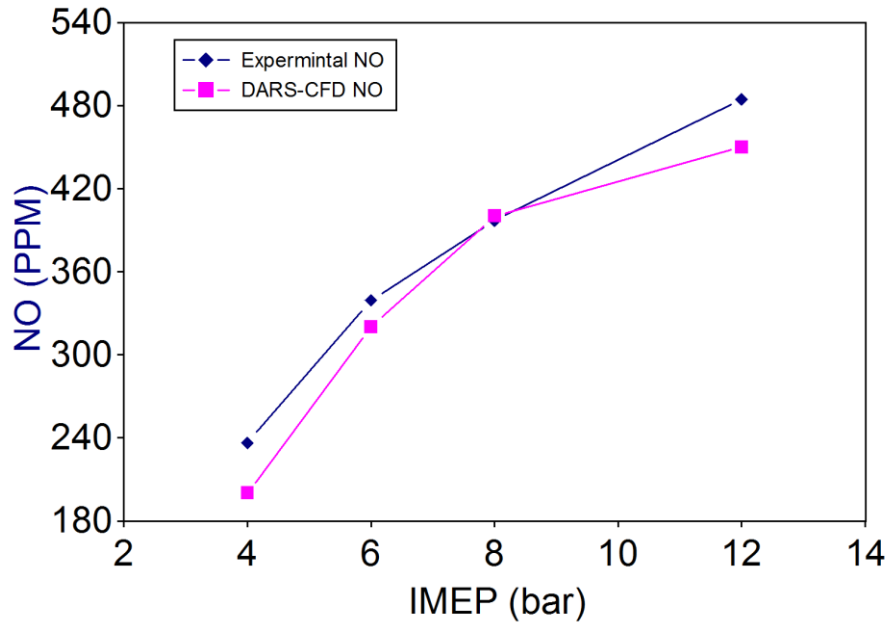


Figure 9.8. Simulated and experimental NO emissions at different loads [JD, 1800 RPM, LPPC 4° aTDC, and inj. press 1200 bar]

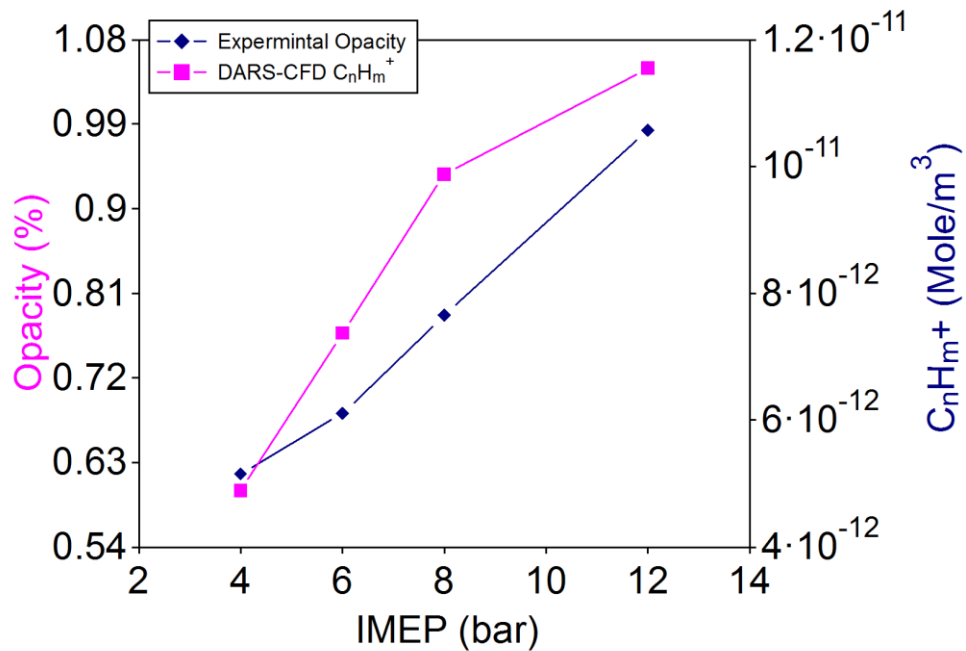


Figure 9.9. Simulated soot precursor and experimental opacity emissions at different loads [JD, 1800 RPM, LPPC 4° aTDC, and inj. press 1200 bar]

At IMEP 6 bar, the fuel is injected at 4.8° bTDC as the reduced ignition delay results in a lower RHR due to the premixed combustion and higher RHR due to the diffusion combustion. Further an increase in load to IMEP 8 and 12 causes shorter ignition delay, whereas the SOI is 4.1° and 3.1° bTDC respectively and the premixed combustion is reduced significantly as indicated by the RHR and the ion current signal.

Additionally, the experimental NO and soot emissions are compared to the CFD simulation results as shown in Figure 9.8 and Figure 9.9. Figure 9.8 shows the NO emission predicted from the CFD model is in agreement with the experimental NO measured whereas the NO emissions increase at higher engine load. The chemical kinetic model did not have soot species produced from the ionization mechanism due to the limitation for the number of species allowed by the software but the heavy hydrocarbon ions contribute to soot production based on the ionization mechanism (42; 144-146; 152; 153). Although the soot nucleus is not only sourced from the ion mechanism (148; 153; 154), it can be used as a precursor to indicated the soot trend (145). Therefore, the concentration of $C_nH_m^+$ is plotted with the opacity measured from the engine exhaust as shown in Figure 9.9. A good agreement with the soot percentage measured is noticed with increase in engine load.

9.6.2 Effect of injection pressure

The results obtained from the experiments and CFD simulation at three different injection pressures are shown in Figure 9.10. The combustion phasing is kept constant at LPPC 4° aTDC; therefore, the SOI in the simulation is adjusted accordingly to match the experimental combustion phasing. The results in Figure 9.10 show a very good agreement between the simulation and experiments. The simulation showed a very good prediction of the ion current in term of peaks location, duration, rising and decaying slopes.

Moreover, the experimental NO and soot emissions are compared with the CFD simulation results as shown in Figure 9.11 and Figure 9.12. Figure 9.11 shows the NO emission predicted from the CFD model is in agreement with the experimental NO measured whereas the NO emissions increase at higher injection pressure. Also, the concentration of $C_nH_m^+$ is plotted with the opacity measured from the engine exhaust as shown in Figure 9.12 and a good agreement is noticed between the soot percentage measured with increase in engine load.

The CFD results of the 1st peak of the ion current signal are observed to be lower than the 1st peak in the experimental data. Since the 1st peak of the ion current signal represents the ions produced due to the premixed combustion which is mainly resulted from $CH^* + O \rightarrow CHO^+ + e$ (26; 29; 40; 42; 144; 145; 148; 152), the CH^* concentration varies based on the surrogate mechanism used (155). Therefore, the n-heptane mechanism used in this study (151) impacts the accuracy in predicting the amplitude of the 1st peak of the ion current signal through CFD simulation.

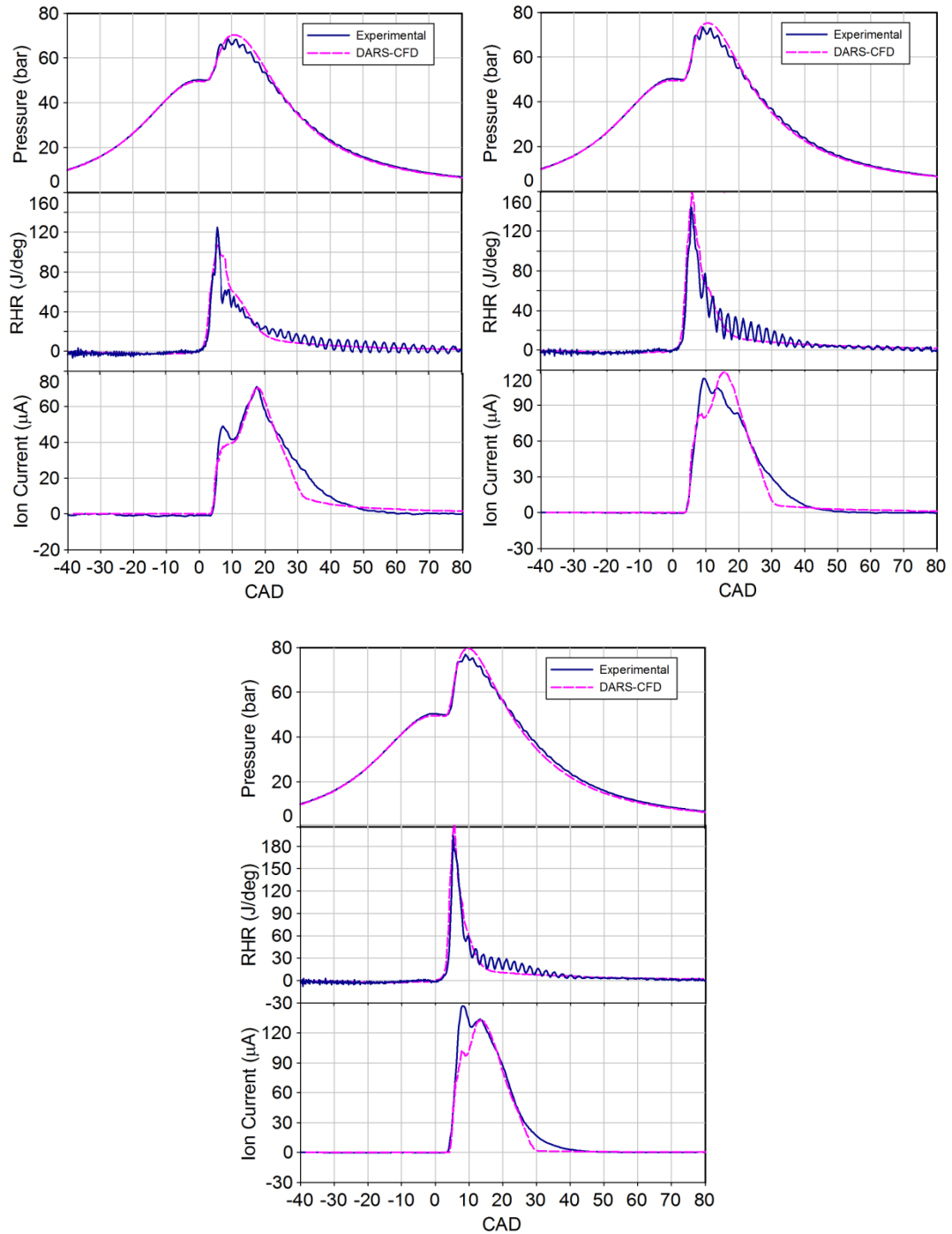


Figure 9.10. Simulation at different injection pressures [JD, 1800 RPM, LPPC 4° aTDC, and IMEP 6 bar]

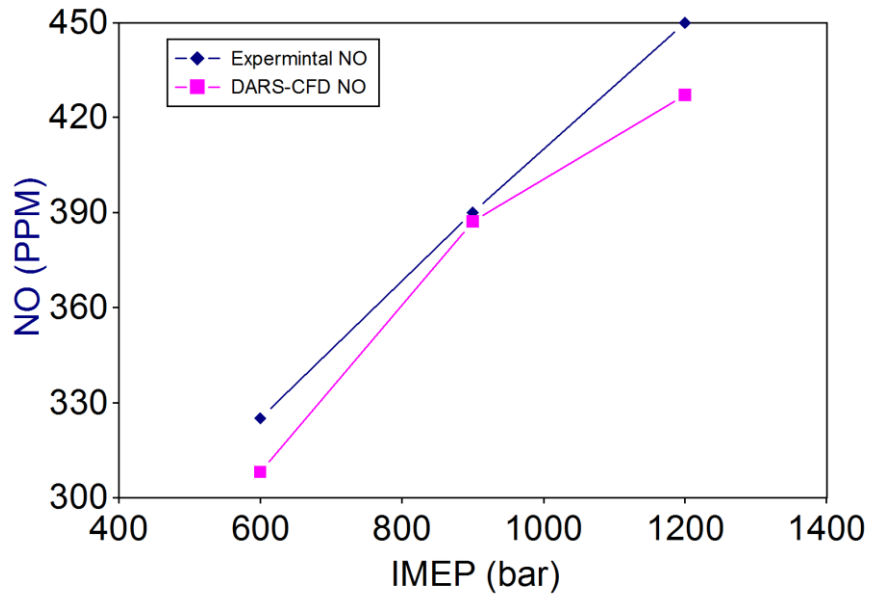


Figure 9.11. Simulated and experimental NO emissions at different injection pressure [JD, 1800 RPM, LPPC 4° aTDC, and IMEP 6 bar]

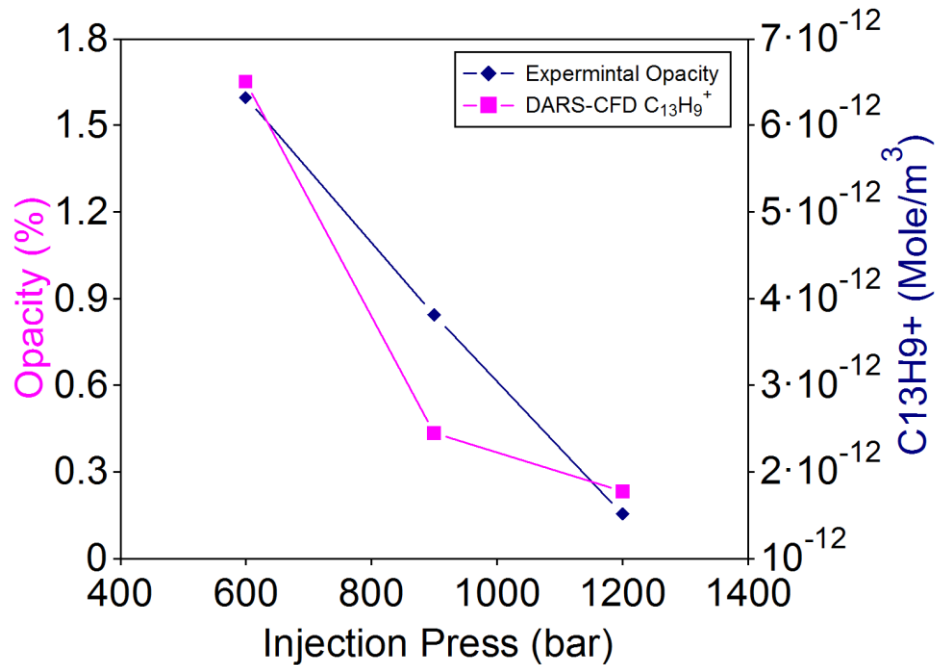


Figure 9.12. Simulated soot precursor and experimental opacity emissions at different injection pressure [JD, 1800 RPM, LPPC 4° aTDC, and inj. IMEP 6 bar]

9.7 Swirl ratio effect on the ion current using CFD simulation

A CFD simulation is conducted to study the effect of different swirl ratios on the characteristics of the ion current signal. The study also includes a detailed analysis of the simulated ion current signal under the effect of different operating parameters and swirl ratios. This is a preliminary attempt to find any correlation between the swirl ratio and the ion current signal characteristics. Figure 9.13 shows simulation results for swirl ratios (SR) from 0 to 3.72 at engine speed of 1800 RPM and IMEP of 6 bar.

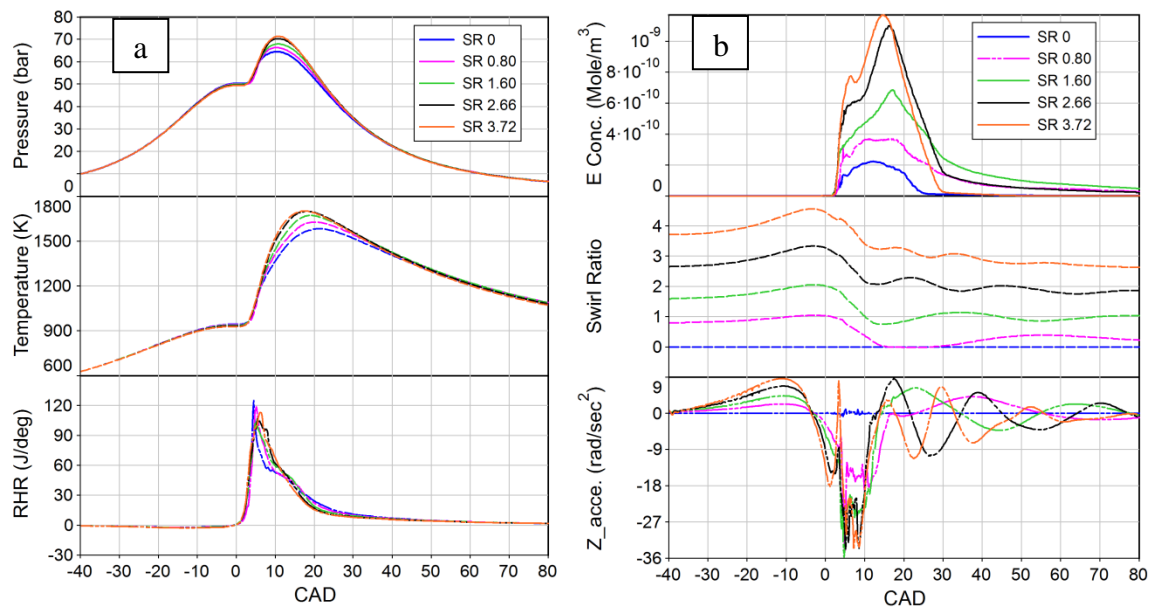


Figure 9.13. Simulation at different swirl ratios [JD, 1800 RPM, LPPC 4° aTDC, inj. press 1200 bar and IMEP 6 bar]

Figure 9.13a shows the cylinder gas pressure, temperature and rate of heat release for different swirl ratios. It is observed that the peak cylinder pressure and temperature is the lowest at zero swirl and it increases at higher swirl ratios. This is explained clearly from the RHR trace where the premixed combustion fraction is improved at higher swirl due to the enhancement in air/fuel mixing and faster evaporation at higher swirl ratio.

Figure 9.13b shows the electron concentration (ion current), swirl ratio, and swirl acceleration in the cycle at different swirl ratios. The characteristics of the ion current signal are significantly affected by the swirl ratio. The ionization signal has the lowest amplitude at SR of 0 and it reached its maximum value at SR of 3.72. The variation in the amplitude of the ionization signal is mainly attributed to two factors (1) the in-cylinder gas temperature and (2) the local equivalence ratio of the air/fuel mixture. Further, it is observed that the SIC and SOC are not affected by the change in swirl but the duration of combustion from the ion current and RHR decrease at higher swirl ratios.

Both swirl ratio and in-cylinder charge swirl acceleration are plotted in Figure 9.13. The in-cylinder charge swirl velocity and acceleration will be explained based on a SR of 3.72. The swirl ratio initial simulation condition is 3.72 with zero acceleration. As the charge is undergoing compression, the charge air accelerates gradually reaching a 9 rad/sec². The charge velocity starts to slow down after the SOI and rapidly decelerates at the SOC reaching a valley of -34 rad/sec². The swirl starts to accelerate back at the start of the diffusion combustion, followed by an oscillation in the swirl due to combustion heterogeneity with an overall swirl ratio below 3.

9.7.1 Correlation between the swirl ratio and the ion current signal

In order to find a correlation between the ion current produced during combustion and the swirl ratio, two different approaches are considered. The first approach is by utilizing two probes and the other approach is through a direct correlation between the rate of ion production or decay during the diffusion combustion and their instant swirl ratio.

The fundamental understand for the fuel/air mixture formation of the diesel spray is highlighted in this section as it plays an important role in determining the local equivalence ratio that affects the combustion developed locally and ultimately the SIC. Figure 9.14 is a schematic of a fuel spray injected in a swirl air of a direct injection diesel engine, without fuel impingement on the wall (156). The atomized liquid droplets are carried away in the direction of the swirl and their concentration decreases downstream edge driven by the swirl. Therefore, the ion current signal produced locally at different probe location would be affected by the swirl in two aspects (1) a shift of the fuel spray distribution further downstream at higher swirl and (2) enhanced air/fuel mixing at higher swirl which affects the local equivalence ratios developed at different probe locations.

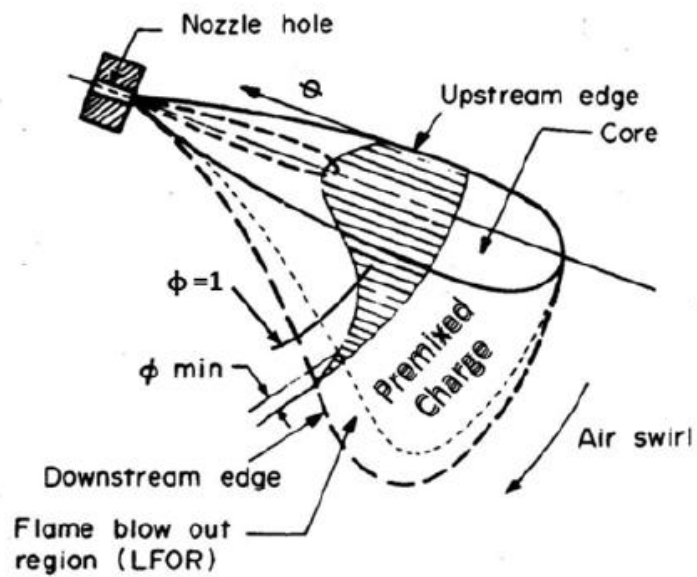


Figure 9.14. Schematic of fuel spray injected in a swirl air of a diesel engine (156)

Two probes approach

Two probes are considered to determine the SIC at different locations. The difference in SIC represents the time for the ionization to form at different locations inside the combustion chamber. Figure 9.15a shows the difference in SIC of probe 13 and 10 plotted against the swirl ratio at different operating conditions. A polynomial trend of 2nd order is observed with a determination coefficient $R^2=0.86$.

Probe 10 and 13: At no swirl condition, the difference between the SIC detected by the two probes is -0.7 deg because the spray develops a symmetric mixing distribution around the spray; therefore, the SIC will be detected earlier for the nearest probe to the spray which in this case is probe 10. At swirl ratio of 0.8, the difference in SIC is 0.4 as the direction of the swirl drifts the spray towards probe 13. Further increase in the swirl ratio, the difference in SIC increases till it reached 1.2 deg at swirl ratio 3.77. Thus, the

increase of the swirl ratio can be detected from the difference in the SIC using these two probes such as 10 and 13.

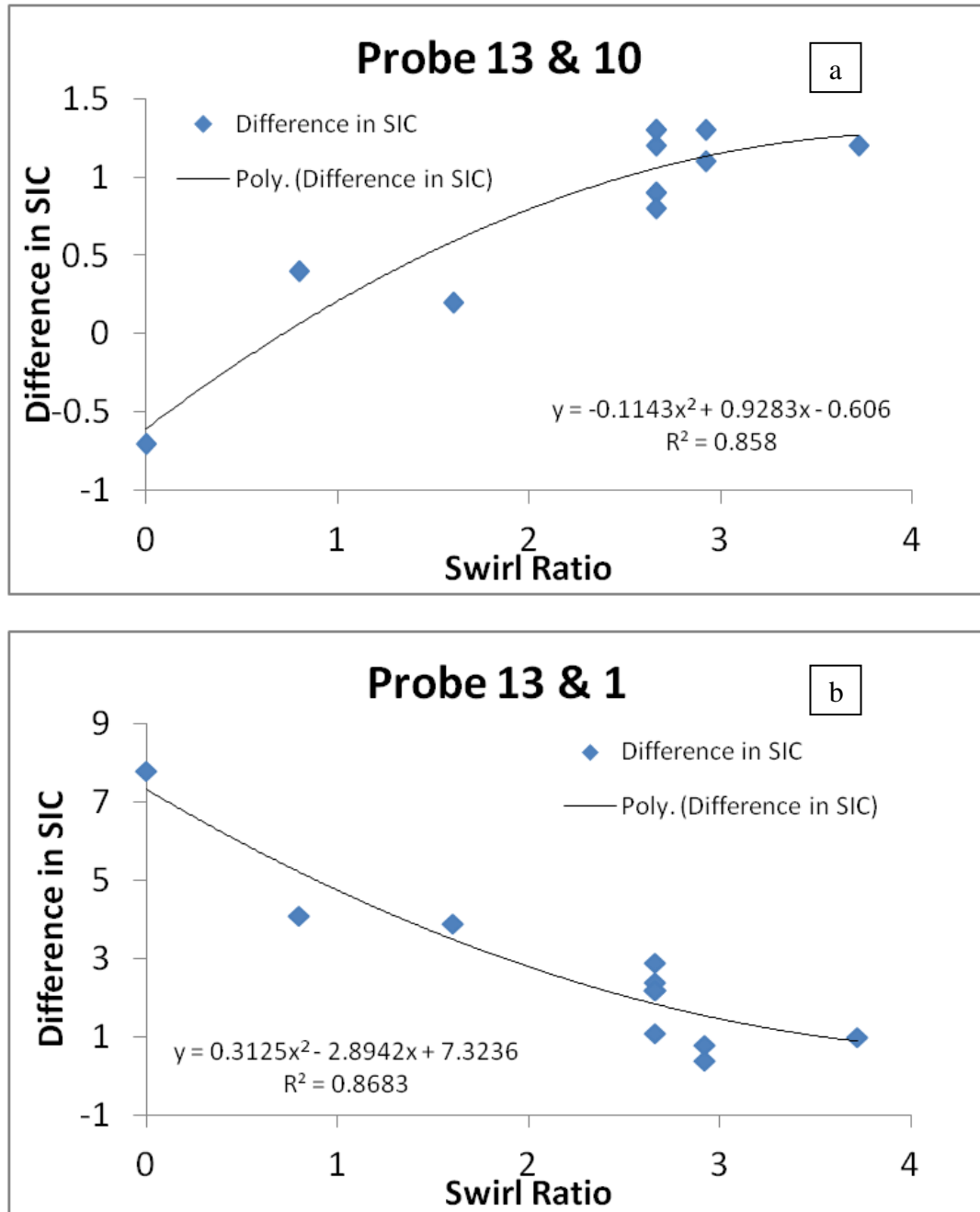


Figure 9.15. Correlation between difference in SIC of two probes and swirl ratio at different operating conditions

Probe 1 and 13: At no swirl condition, the difference between the difference in SIC is 7.8 deg because the worst mixing occurs at the tip of probe 1 at the center of the swirl motion (injector probe) compared to probe 13 which is far from the center of the swirl motion. Also probe 13 is near the atomized fuel spray. At swirl ratio 0.8, the difference in SIC is 4.1 and the swirl start to enhance the air/fuel mixture around probe 1. Further increase in the swirl ratio, the difference in SIC decreased till it reached 1 deg at swirl ratio 3.77. Thus, the swirl ratio increases with decrease in the difference in the SIC using probes 1 and 13.

Therefore, a correlation between the difference in SIC and swirl ratio exists and many precautions such as probe locations, spray distribution should be carefully understood in order to utilize this correlation for engine diagnostics and feedback control.

Direct correlation between the rate of ion current and swirl ratio

Another attempt is made to find a direct correlation between the engine swirl and the swirl ratio calculated from the ion current signal characteristics. In this section, a comparison is made between the rate of ion production and decay during the diffusion combustion and their instant swirl ratios as shown in Figure 9.16. The derivative of the ion current at point 1 and 2 is computed and plotted versus their corresponding CAD swirl ratios for different operating condition as shown in Figure 9.17. Ascending rate of ion current at point 1, the rate $\frac{dE}{d\theta}$ decreases at higher instantaneous swirl ratio, where a linear trend is observed with determination coefficient $R^2 = 0.87$. Descending rate of ion

current at point 2, the rate $\frac{dE}{d\theta}$ increases at higher instantaneous swirl ratio, where a linear trend is observed with determination coefficient $R^2 = 0.74$. It is observed that the slope for the rate of formation or decay of the ion current (shown in both the equations in Figure 9.17 and indicates the absolute value for the rate $\frac{dE}{d\theta}$ is correlated to the instantaneous swirl ratio during the start and end of the diffusion controlled combustion.

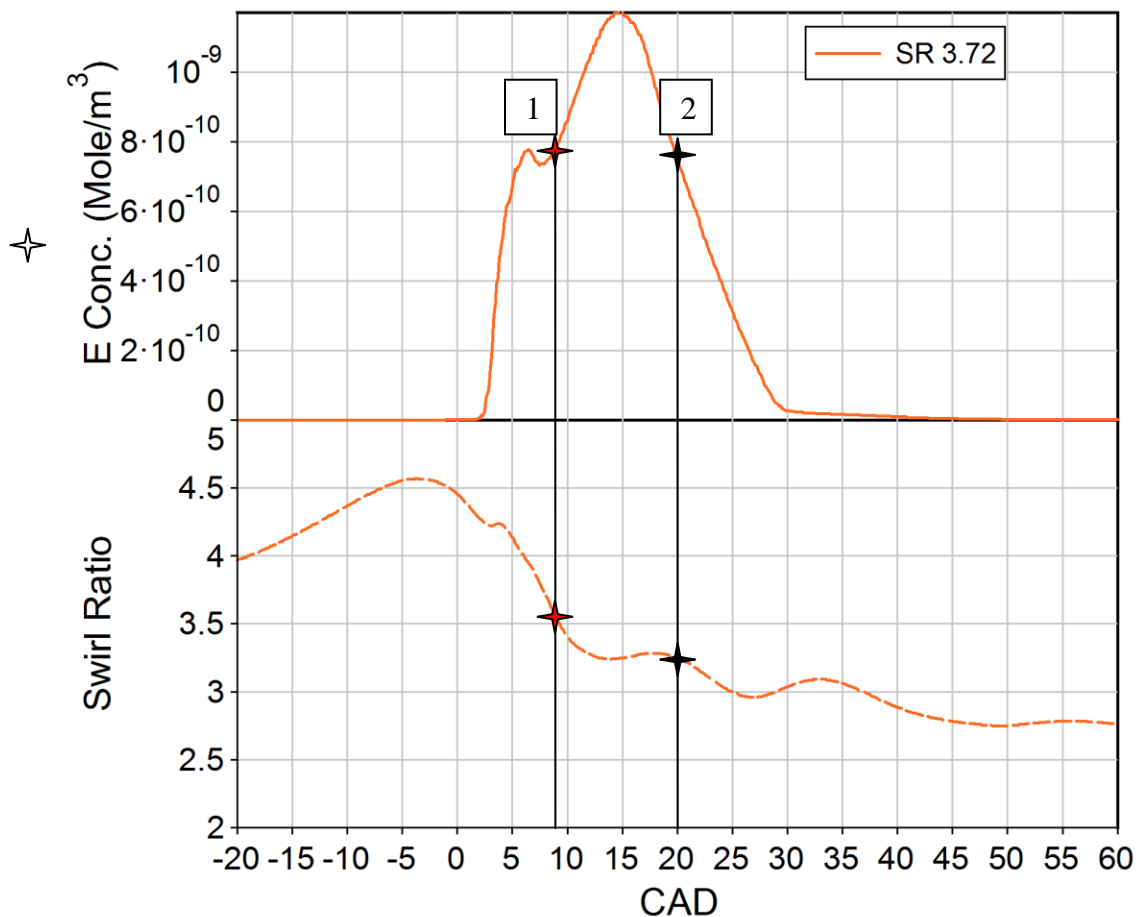


Figure 9.16. Electron concentration (Ion Current) and swirl ratio profile during a combustion cycle (SR = 3.72)

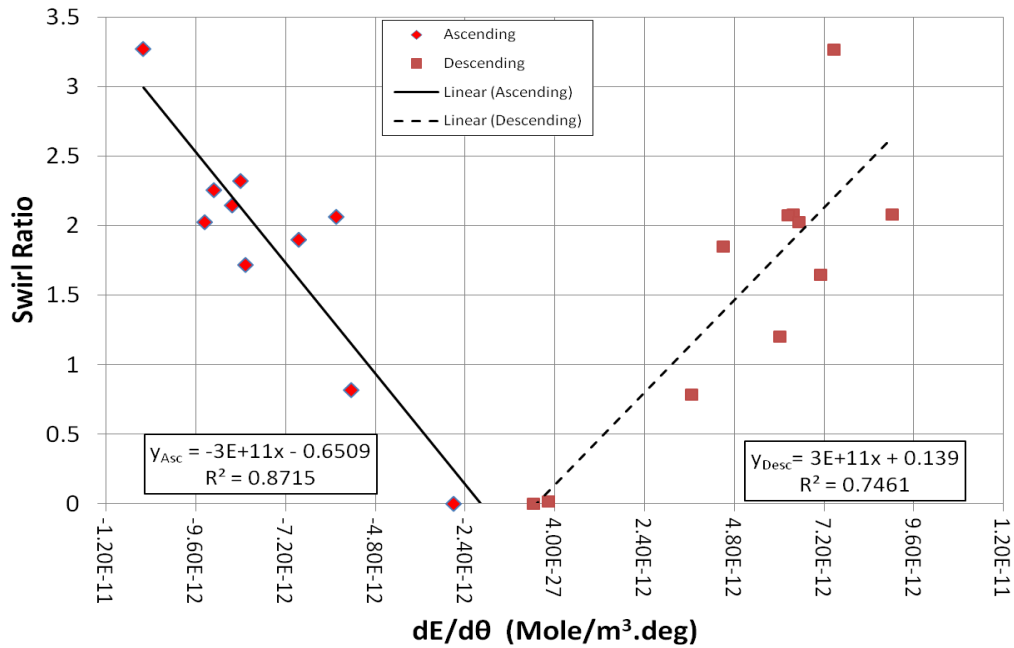


Figure 9.17. Correlation between the rates of ion formation and dissociation and swirl ratio at different operating conditions

9.8 SIC and peak I_{max} distribution inside the chamber

9.8.1 Swirl ratio

Figure 9.18 shows the distribution of the SIC in CAD and the maximum amplitude of the ion current I_{max} in mole/cm³ at different swirl ratios. It is clear that the distribution of the SIC and I_{max} inside the combustion chamber is affected by the fuel distribution in the spray as explained earlier. The combustion chamber can be divided into four annular zones. The first zone is in the center where the injector is located, and the fourth zone is at the combustion chamber periphery. The extent of combustion in each of these zones

depends on many parameters such as the injection pressure, number of nozzle holes, hole geometry. The simulation is made for engine operating at 1800 rpm, injection pressure of 1200 bar and IMEP of 9 bar.

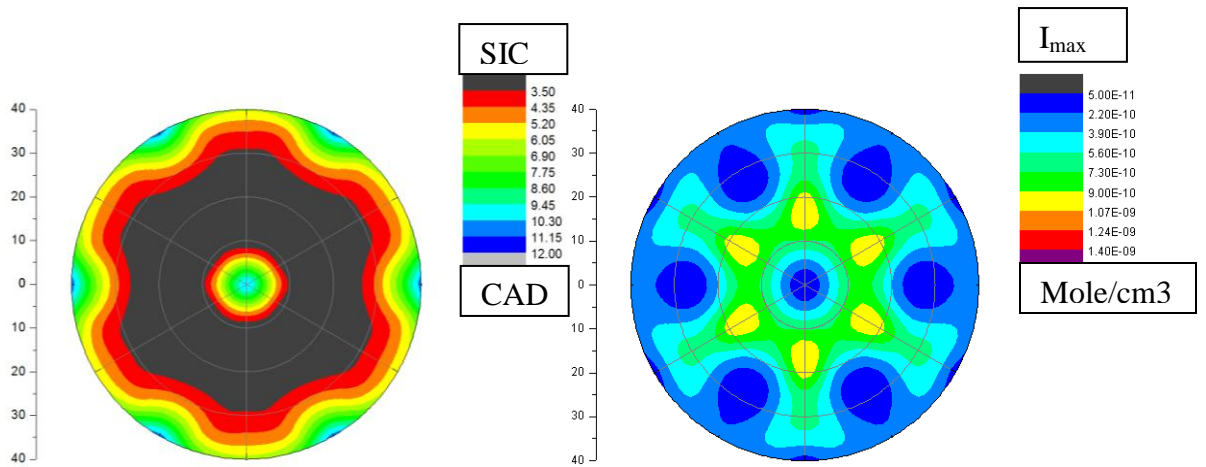
At zero swirl, the fuel injected is not well mixed with the air but the SIC distribution show that almost the second and third zones having the core of combustion with SIC of 3.5 CAD. The symmetric distribution of the I_{\max} around the spray axis clearly confirm stagnation of the ions produced inside the combustion chamber. Meanwhile, the SIC around the injector (first zone) was very late approximately 4 CAD later than the second and third zones, and the I_{\max} was very low. The retardation of the SIC is due to the very rich mixture and the low temperature around the injector. Further, the SIC was retard at the chamber periphery (fourth zone) by approximately 2 CAD relative to the second and third zones. The fourth zones is very lean mixture due to poor mixing at zero swirl and resulted in low combustion temperature and low I_{\max} concentration.

At 0.80 swirl ratio, distortion is noticed in both distribution of SIC and I_{\max} along the swirl direction. The core of combustion is crawling toward the center compared to zero swirl, where the SIC is 3.5 CAD at outer half of the first zone, second zone, and inner half of the third zone. I_{\max} reached its highest concentration in the second zone at a point slight shifted from the spray axis. The SIC is retarded around the injector approximately 3 CAD compared with the core zones. The retardation of the SIC in the fourth zone relative to the zero swirl case can be explained by the much leaner mixture at the combustion chamber periphery, where the spray penetration is reduced by the action of the swirl motion.

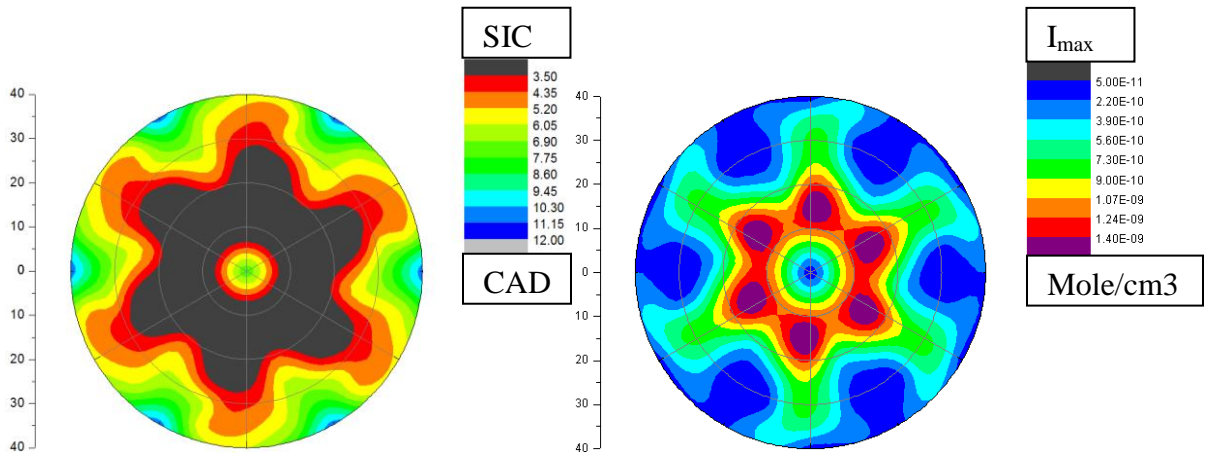
At 1.60 swirl ratio, more distortion in both distribution of SIC and I_{\max} along the swirl direction is observed. The distribution of SIC in first, second and third zones has not changed compared at 0.80 swirl ratio. A better combustion is indicated by having small areas in the fourth zone near to the spray axis with SIC of 3.5 CAD. This is reflected in the distribution of the I_{\max} , where larger area inside the combustion chamber indicate high concentration of I_{\max} compared to 0.8 swirl ratio.

Increasing the swirl ratio to 2.66, the SIC and I_{\max} distribution inside the combustion chamber which is in proportion to the spray distortion and fuel/air distribution. At this high swirl ratio, the SIC is retarded around the injector approximately 1 CAD compared to the core of combustion. Expanding area of high concentration of I_{\max} is observed due to better mixing and higher temperature reached at the core zones. Further increase in swirl ratio to 3.72, caused the area of high concentration of I_{\max} to be smaller than at swirl 2.66. Although the global in-cylinder temperature increased, the local temperatures at the probe levels are lower due to the higher heat loss at this elevated swirl ratio.

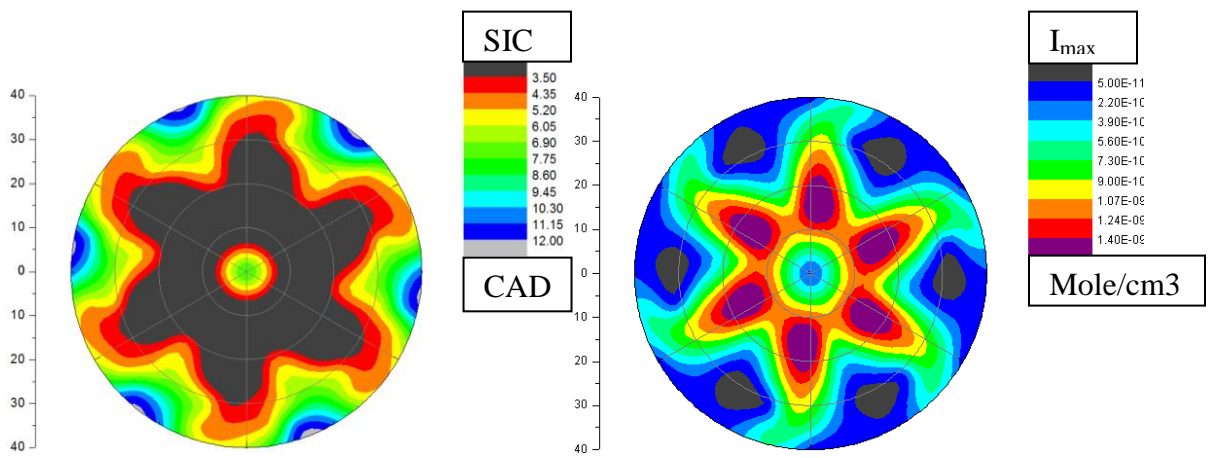
More retardation of the SIC and low I_{\max} are observed at higher swirl at the combustion chamber periphery of the fourth zone. The concentration of I_{\max} is observed to increase at higher swirl ratio particularly at the core zones. The SIC in of the core zone at higher swirl ratio expands particularly toward the center of the chamber and collapses at the periphery of the chamber.



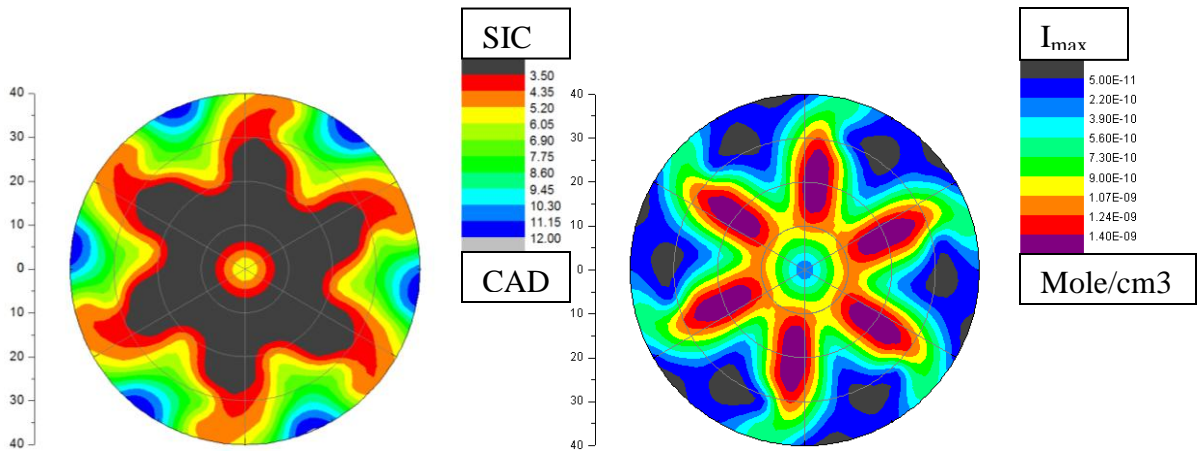
0 rad/sec [Swirl Ratio 0]



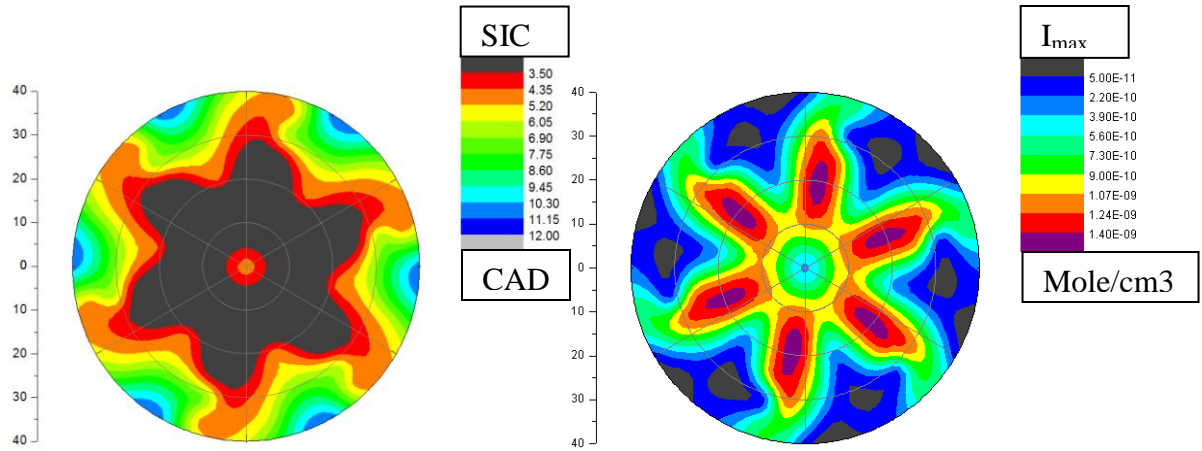
150 rad/sec [Swirl Ratio 0.80]



300 rad/sec [Swirl Ratio 1.60]

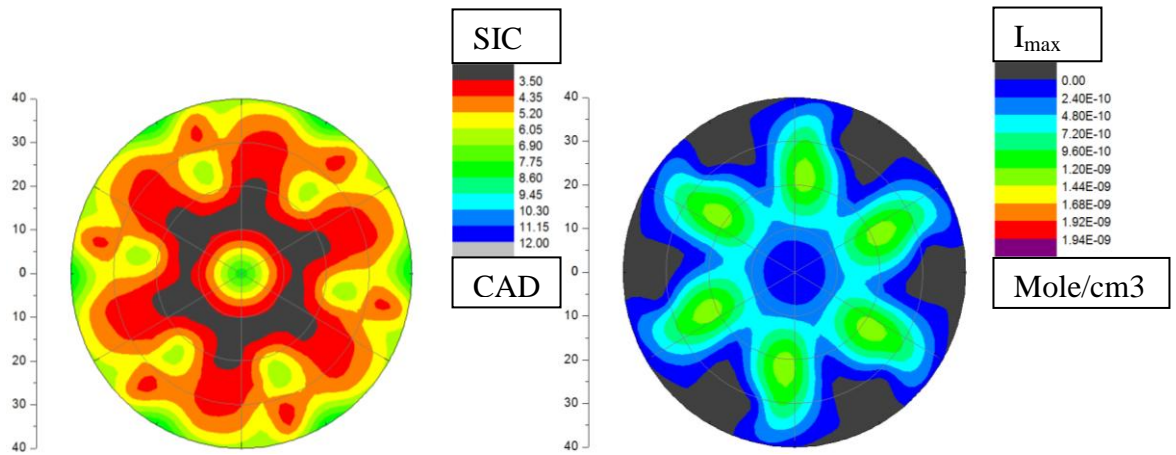


500 rad/sec [Swirl Ratio 2.66]

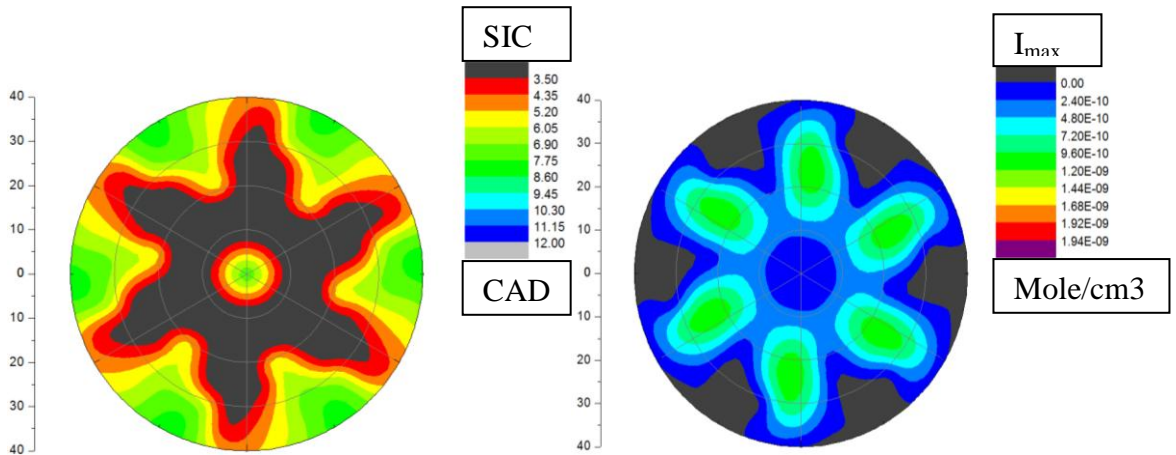


700 rad/sec [Swirl Ratio 3.72]

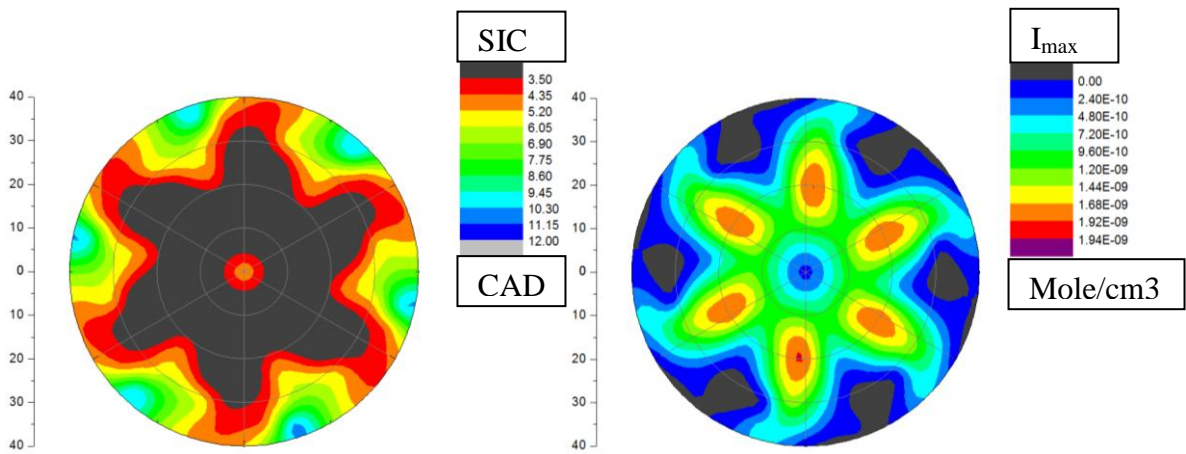
Figure 9.18. SIC and I_{max} distribution inside the combustion chamber by multiple ion probes at different swirl ratios [inj. press 1200 bar, and IMEP 6 bar]



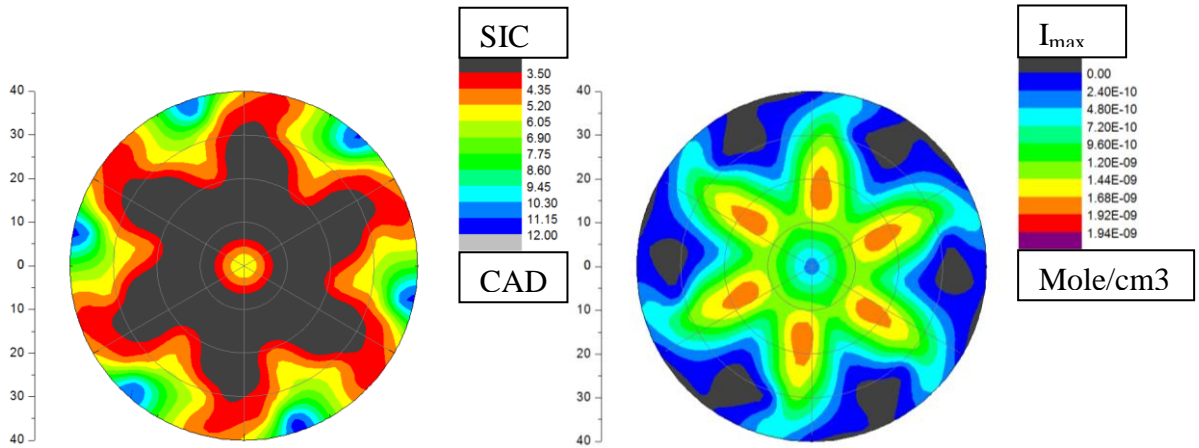
IMEP 2 bar



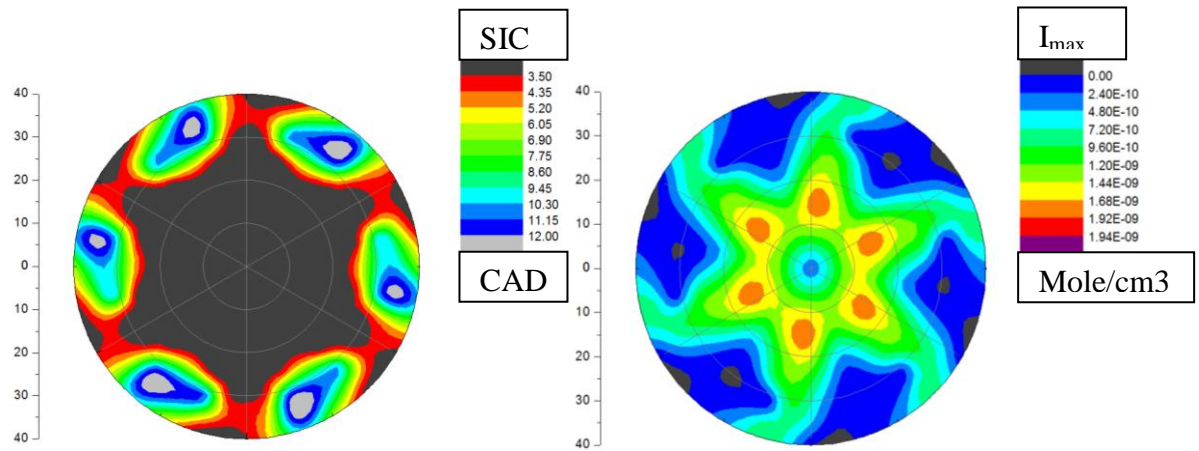
IMEP 4 bar



IMEP 6 bar



IMEP 8 bar



IMEP 12 bar

Figure 9.19. SIC and I_{max} distribution inside the combustion chamber by multiple ion probes at different engine loads [Inj. press 1200 bar]

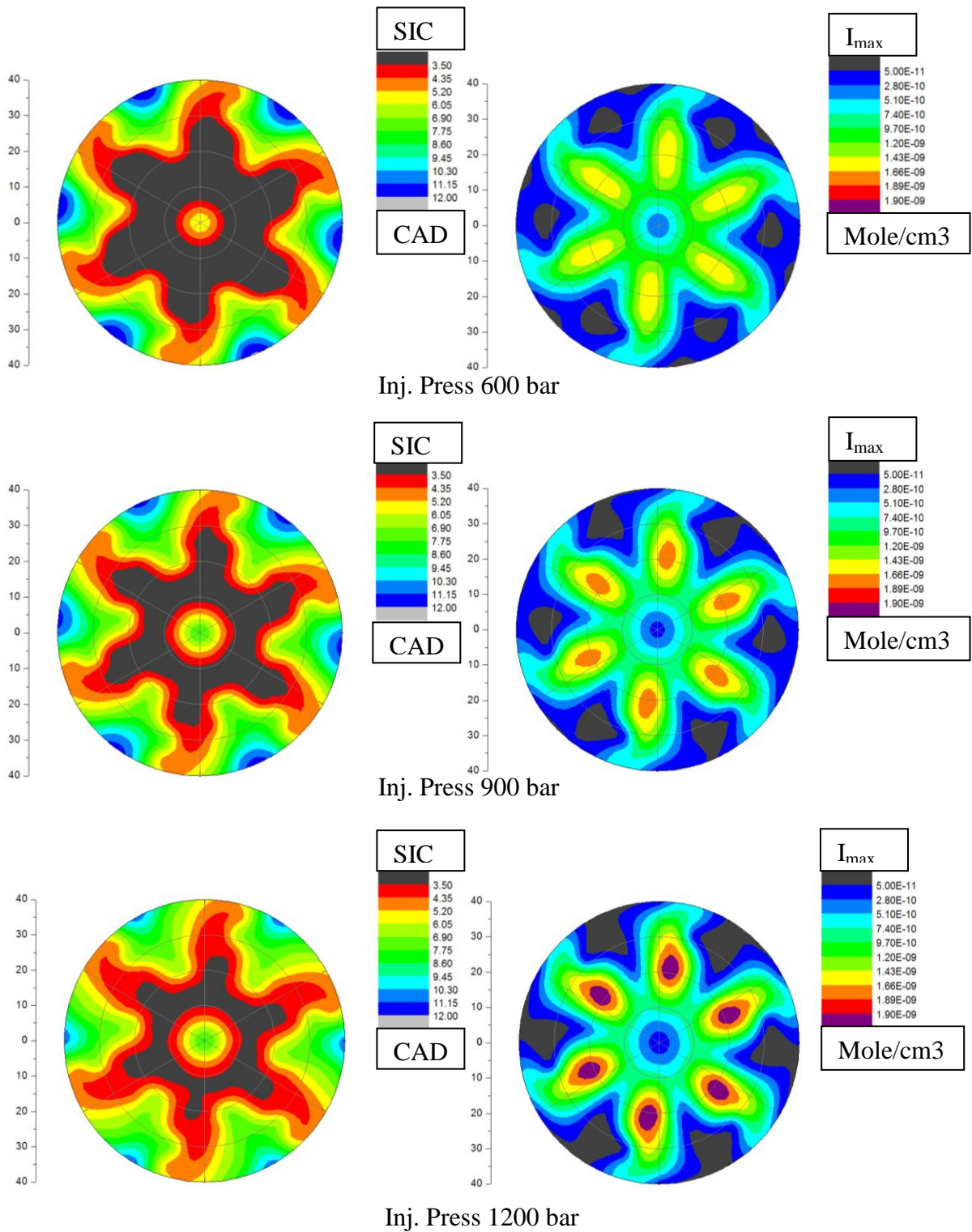


Figure 9.20. SIC and I_{max} distribution inside the combustion chamber by multiple ion probes at different injection pressures [IMEP 6 bar]

9.8.2 Engine load

Figure 9.19 shows the distribution of the SIC in CAD and the maximum amplitude of the ion current I_{\max} in mole/cm³ with increasing engine load. The distribution of the SIC and I_{\max} inside the combustion chamber is affected by the quantity of fuel injected, fuel spray penetration and combustion temperature at different engine loads. The core of the combustion process is concentrated within the second and third zones inside the combustion chamber. The simulation results are obtained for engine operating at injection pressure of 1200 bar and swirl ratio of 2.66.

At IMEP 2 bar, a small amount of fuel is injected into the combustion chamber, where fuel vapor mixes with the air to produce combustion of a fairly lean mixture. This is reflected by the low amplitude of I_{\max} distribution inside the combustion chamber. The core of combustion represented by the SIC distribution at 3.5 CAD, indicates small area within the second zone. SIC is slightly retarded at the third and fourth zones by about 1.5 CAD due to lean mixture and low temperature reached at these zones. The I_{\max} distribution shows that swirl shifted the combustion developed around the spray axis in the clockwise direction of about 15° from spray axis. However, large areas within the fourth zone indicate no ions, where combustion does not exist.

At IMEP 4 bar, the SIC distribution shows that core of combustion is swarming inside the combustion chamber compared to IMEP 2bar. The second and third zones indicate SIC at 3.5 CAD. Also, the distribution of I_{\max} indicate a slight increase in amplitude compared to lower load but the swirl shifted the combustion only 6.72° from the spray axis compared to 15° at IMEP 2 bar.

Further increase in IMEP, caused the core of the combustion to spread in more areas inside the combustion chamber; where SIC of 3.5 CAD is dominant in the first, second, and third zones as shown for IMEP 6 and 8 bar in Figure 9.19. The I_{\max} distribution reaches higher amplitudes with increase in engine load due to the increase of in-cylinder temperature. At IMEP 12 bar, the combustion starts in most of the combustion chamber at SIC 3.5 CAD except for fourth zone, where the rich mixture is present due liquid wall impingement. Although the I_{\max} is distribution in all the combustion chamber, the amplitude is lower than IMEP 8 bar. This is due to the very rich fuel/air mixture that develops combustion with low burning rate, where lower combustion temperature is reached.

9.8.3 Injection pressure

Figure 9.20 shows the distribution of the SIC in CAD and the maximum amplitude of the ion current I_{\max} in mole/cm³ with the increase in injection pressures from 600 bar to 1200 bar. It is very obvious that the distribution of the SIC and I_{\max} inside the combustion chamber is affected by the spray penetration, fuel atomization and rate of evaporation at different injection pressures. The core of the combustion process is concentrated mainly at the second and third zones inside the combustion chamber. The simulation results are obtained for engine operation at IMEP of 9 bar and Swirl ratio 2.66.

At injection pressure 600 bar, it is observed that the core of combustion with SIC at 3.5CAD is present in outer half of the first zone, second and third zones. The retardation in SIC of about 1.5 - 2 CAD (red and orange contours) around the injector and at around the spray axis at the chamber wall is due to the rich mixture and the low temperature

locally present. But the retarded SIC by about 5 - 8 CAD (green and blue contours) located away from the spray axis at the chamber wall is due to very lean mixture and the low gas temperature. This is reflected by the amplitude of I_{\max} distribution inside the combustion chamber. The I_{\max} amplitude is located between the second and third zones is slightly shifted away from the spray axis due to the swirl motion.

Further increase in injection pressure to 900 bar, caused the area with SIC at 3.5 CAD to shrink towards the spray axis where the core of combustion is mainly located in the second zone. Larger areas inside the chamber indicate retardation of the SIC. On the other hand, the I_{\max} distribution showed higher amplitudes due to the higher in-cylinder gas temperature. The I_{\max} amplitude is located in third zone is shifted away from the second zone due to the longer spray penetration at higher injection pressure.

At injection pressure 1200 bar, it is observed that a very small area represents SIC at 3.5 CAD as shown in the figure. The first zone indicates a retardation of SIC from 1.5 CAD at its periphery to 5.25 CAD at the center of the injector. The I_{\max} distribution shows higher amplitude at the higher injection pressure but less shrinking in the I_{\max} contours can be observed inward the spray axis. It can be concluded that a 50% decrease in the area of SIC at 3.5 CAD and a 35% increase in the I_{\max} amplitude occurred when injection pressure increased from 600 to 1200 bar.

9.9 Summary

This chapter covers 3D- CFD simulation of the combustion process in the diesel engine. The CFD simulation is coupled to a chemical kinetic solver that includes the ions and electrons species. A validation of the simulation model is performed at different engine operating conditions. The conclusions are as follows:

1. The simulation model is able to predict the ion current signal detected by the glow plug/ ion sensor at different engine operating conditions.
2. By introducing virtual ion current probes in the simulation for the ion current signal, it was possible to study the effect of the probe geometry on the ion current characteristics. The simulation results agreed with results of early experiments on the effects of sensor diameter and protrusion on the ion current signal.
3. The model is validated by experimental in-cylinder data under different loads and injection pressures, where a good agreement between the local virtual probe and the measured ion current is found.
4. The model is also validated by the agreement between the predicted NO mole fraction from the ion current signal and experimental measurements of the NO mole fraction in the engine exhaust.
5. The model results for soot indicators such as $C_nH_m^+$ showed the same trends as soot measurements made by an opacity meter under different loads and injection pressures.

6. Two different approaches have been illustrated to determine the swirl ratio from the ion current signal. The first method is by measuring the ion current from two probes located at different locations inside the combustion chamber. The second method is by correlation the rate of formation and decay of the ion current to the instantaneous swirl ratio inside the combustion chamber.
7. Utilizing virtual ion current probes in the CFD model, produced contours for SIC and I_{\max} in the combustion chamber under different operating conditions.

CHAPTER 10

CONCLUSIONS

1. The ion current signal characteristics has been investigated in a heavy duty diesel engine at different steady state and transient operating conditions. There is high cycle to cycle variation in the ion current signal peak location, shape and amplitude but the start of the ion current signal provides a reproducible characteristic at various engine operating conditions.
2. The correlation between the location of the start of the ion current signal sensed locally by the ion current probe and the location of the maximum rate of heat release due to the premixed combustion fraction has been established. The correlation has been also verified by combustion images at different operating conditions.
3. There is a strong evidence of the ion current misdetection in the diesel engine at low loads, where the overall equivalence ratio is lean and combustion temperature is not high enough to produce detectable ionization.
4. Investigations on the optically accessible engine at different loads indicated the absence of a flame in some areas of the combustion chamber at low loads, which explains the reason for misdetection of the ion current observed in the production engine at light loads
5. A detailed analysis of the ion current signal indicated that it carries basic information about combustion resonance which could not detected from the signals produced by a cylinder gas pressure transducer and an acceleration sensor fitted to the cylinder block.

The oscillations observed in the ion current signal are studied in frequency domain using different representation such as FFT, STFT, and CWT.

6. The injection pressure has an impact on combustion resonance due to the increase in rate of pressure rise caused by the volumetric combustion of the premixed charge.

7. A benchmarking for the combustion resonance for the 1st shape mode (highest resonance amplitude) with its corresponding resonance from the cylinder pressure and vibration signals showed a linear relationship. Therefore, the ion current sensor can be used in replacement to the cylinder pressure sensor or accelerometer to detect combustion resonance for the purpose of engine diagnostics and control.

8. The time frequency representation of the combustion resonance using STFT and CWT gives more understanding during the development and progress of the combustion resonance using different sensors. Manipulation of the CWT is made in order to have the combustion resonance "time-resolved". The resonance derived from the ion current signal shows clear explanation for the evolution of the combustion resonance at different combustion phases compared to the resonance derived from cylinder pressure or vibration signals.

9. Time- resolved resonance detected by the ion current signal was studied at different operating conditions such as injection pressure, EGR, and pilot injection. Further, engine and emission parameters were studied at the same operating conditions. A significant improvement in overall combustion characteristics such as ISFC and peak cylinder pressure, and a tradeoff between NO and soot emissions can be realized by adjusting the SOPI to achieve minimum combustion resonance.

10. The ion current sensor can be used to detect the combustion resonance for combustion diagnostics and can be implemented in close loop controller that adjust pilot injection quantity and timing to minimize the combustion resonance in addition to the reduction of NO, peak cylinder pressure, fuel consumption and engine noise.

11. An Incremental fuzzy logic controller (IFLC) is developed to control the phasing of the combustion process in a direct injection diesel engine, utilizing the ion current as feedback signal to the ECU. The IFLC demonstrated a fast response and accounted for the low amplitude or missing ion current signals. This enabled the autonomous operation of a diesel engine on fuels of different physical and chemical properties without additional cost in engine production while maintaining the production target in power and fuel economy.

12. A new model was developed and tested for the estimation of soot and NO_x concentrations on cyclic basis. This technique utilizes inputs derived from the ion current signal measured during the combustion process. Several advantages are demonstrated, including the insensitivity to uncertainties in the measurements.

13. A 3D- CFD model coupled with chemical kinetic solver which includes the mechanism of ionization in diesel combustion is used to determine the cycle resolved concentrations of the different ionized species in the combustion chamber. This enhanced the development of diagnostics techniques for the engine performance and emission parameters.

14. The simulation model is validated by experimental in-cylinder data under different loads and injection pressures, where a good agreement between the local virtual probe

and the measured ion current is established. Further, the model was also validated against experimental emissions data, where a good agreement between the measured and simulated NO and between soot indicator $C_nH_m^+$ indicated the same trend for the soot percentage measured by the opacity meter.

15. Two different approaches have been illustrated to determine the swirl ratio from the ion current signal. The first method is by measuring the ion current from two probes located at different locations inside the combustion chamber. The second method is by correlation the rate of formation and decomposition of the ion current to the instantaneous swirl ratio inside the combustion chamber.

REFERENCES

- [1] Włodarczyk , M. T., Poorman , T., Xia , L., Arnold , J., and Coleman , T., "In-Cylinder Fiber-Optic Pressure Sensors for Monitoring and Control of Diesel Engines," *SAE Technical Paper 981913*, 1998.
- [2] Willems , F., Doosje , E., Engels , F., and Seykens , X., "Cylinder Pressure-Based Control in Heavy-Duty EGR Diesel Engines Using a Virtual Heat Release and Emission Sensor," *SAE Technical Paper 2010-01-0564*, 2010.
- [3] Jan, O., Tunest+Ñl , P., and Johansson , B., "Closed-Loop Control of an HCCI Engine," *SAE Technical Paper 2001-01-1031*, 2001.
- [4] Marek, T., "High Accuracy Glow Plug-Integrated Cylinder Pressure Sensor for Closed Loop Engine Control," *SAE Technical Paper 2006-01-0184*, 2006.
- [5] Moriwaki , J., Murai , H., and Kameshima , A., "Glow Plug with Combustion Pressure Sensor," *SAE Technical Paper 2003-01-0707*, 2003.
- [6] Geiser , F., Wytrykus , F., and Spicher , U., "Combustion Control with the Optical Fibre Fitted Production Spark Plug," *SAE Technical Paper 980139*, 1998.
- [7] Hunicz , J., Piernikarski , D., and Niewczas , A., "Transient In-Cylinder AFR Management Based on Optical Emission Signals," *SAE Technical Paper 2004-01-0516*, 2004.
- [8] Piernikarski , D. and Hunicz , J., "Investigation of Misfire Nature Using Optical Combustion Sensor in a SI Automotive Engine," *SAE Technical Paper 2000-01-0549*, 2000.

- [9] Henein, N. A., Bryzik, W., Abdel-Rehim, A., and Gupta, A., "Characteristics of Ion Current Signals in Compression Ignition and Spark Ignition Engines," *SAE International Journal of Engines*, Vol. 3, No. 1, 2010, pp. 260-281.
- [10] Kubach, H., Velji, A., Spicher, U., and Fischer, W., "Ion Current Measurement in Diesel Engines," *SAE Technical Paper 2004-01-2922*, 2004.
- [11] Larsson, M., Denbratt, I., and Koopmans, L., "Ion Current Sensing in an Optical HCCI Engine with Negative Valve Overlap," *SAE Technical Paper 2007-01-0009*, 2007.
- [12] Yoshiyama, S., Tomita, E., and Hamamoto, Y., "Fundamental Study on Combustion Diagnostics Using a Spark Plug as Ion Probe," *SAE Technoical Paper 2000-01-2828*, 2000.
- [13] Reinmann, R., Saitzkoff, A., and Mauss, F., "Local Air-Fuel Ratio Measurements Using the Spark Plug as an Ionization Sensor," *SAE Technical Paper 970856*, 1997.
- [14] Saitzkoff, A., Reinmann, R., Berglind, T., and Glavmo, M., "An Ionization Equilibrium Analysis of the Spark Plug as an Ionization Sensor," *SAE Technical Paper 960337*, 1996.
- [15] Abdel, R., Naeim, A., and VanDyne, E., "Impact of A/F Ratio on Ion Current Features Using Spark Plug with Negative Polarity," *SAE Int.J.Passeng.Cars - Electron.Electr.Syst.*, Vol. 1, No. 1, 2008, pp. 432-445.

- [16] Naoumov , V., Demin , A., Andersson , I., and Sokolov , A., "Modeling of Combustion and Non-Equilibrium Ionization in Spark Ignition Engines," *SAE Technical Paper 2002-01-0009*, 2002.
- [17] Eric, N., Edward, A., Alexandre, M., Ratton , K., and Ming, C., "In-Cylinder Air/Fuel Ratio Approximation Using Spark Gap Ionization Sensing," *SAE Technical Paper 980166*, 1998.
- [18] Abdel, R., Naeim, A., and VanDyne , E., "Ion Current in a Spark Ignition Engine using Negative Polarity on Center Electrode," *SAE Technical Paper 2007-01-0646*, 2007.
- [19] Franke , A., Einewall , P., Johansson , B., and Reinmann , R., "Employing an Ionization Sensor for Combustion Diagnostics in a Lean Burn Natural Gas Engine," *SAE Technical Paper 2001-01-0992*, 2001.
- [20] KITAJIMA , T., KUMADA , M., SHIMODAIRA , H., YOSHIDA , K., and SHOJI , H., "A Study on Ion Current and OH Radical Luminescence Behavior in a Two-Stroke Engine," *SAE Technical Paper 2000-01-1424*, 2000.
- [21] Kai, W., Bernhardt , S. r., Spicher , U., Gegg , T., K+lmel , A., Paa , A., Weissgerber , T., and Westecker , M., "Ion-Current Measurement in Small Two-Stroke SI Engines," *SAE Technical Paper 2008-32-0037*, 2008.
- [22] Oakley , A., Zhao , H., Ladommatos , N., and Ma , T., "Experimental Studies on Controlled Auto-ignition (CAI) Combustion of Gasoline in a 4-Stroke Engine," *SAE Technical Paper 2001-01-1030*, 2001.

- [23] Bogin, J., Chen, J. Y., and Dibble, R. W., "The effects of intake pressure, fuel concentration, and bias voltage on the detection of ions in a Homogeneous Charge Compression Ignition (HCCI) engine," *Proceedings of the Combustion Institute*, Vol. 32, No. 2, 2009, pp. 2877-2884.
- [24] Yoshiyama , S., Tomita , E., Mori , M., and Sato , Y., "Ion Current in a Homogeneous Charge Compression Ignition Engine," *SAE Technical Paper 2007-01-4052*, 2007.
- [25] Guangyu, D., Zhijun, W., Liguang, L., Fafa, L., and Yingnan, G., "Method of ion current detection for HCCI combustion on SI/HCCI dual mode engine," *Intelligent Vehicles Symposium, 2009 IEEE*, 2009, pp. 1221-1226.
- [26] Henein, N. A., Badawy, T., Rai, N., and Bryzik, W., "Ion Current, Combustion and Emission Characteristics in an Automotive Common Rail Diesel Engine," *ASME 2010 Internal Combustion Engine, Technical Paper ICEF2010-35123*, 2010.
- [27] Glavmo , M., Spadafora , P., and Bosch , R., "Closed Loop Start of Combustion Control Utilizing Ionization Sensing in a Diesel Engine," *SAE Technical Paper 1999-01-0549*, 1999.
- [28] Keßler. Ionenstrom sensorik im Diesel motor. 2002. Düsseldorf, VDI-Verlag, Germany, Fortschritt-Berichte VDI, Reihe 12.

Ref Type: Thesis/Dissertation

- [29] Badawy, T., Rai, N., Singh, J., Bryzik, W., and Henein, N., "Effect of design and operating parameters on the ion current in a single-cylinder diesel engine," *International Journal of Engine Research*, 2011.
- [30] Gargo, S., Badawy, T., Estefanous, F., and Henein, N., "Simulation of Ionization in Diesel Engines Premixed Combustion," *ICARAME'11: International Conference on Advanced Research and Applications in Mechanical Engineering*, 2011.
- [31] Haskara, I., Zhu, G., Daniels, C., and Winkelman, J., "Closed Loop Maximum Dilution Limit Control using In-Cylinder Ionization Signal," *SAE Technical Paper 2005-01-3751*, 2005.
- [32] Zhu, G. G., Haskara, I., and Winkelman, J., "Closed-Loop Ignition Timing Control for SI Engines Using Ionization Current Feedback," *Control Systems Technology, IEEE Transactions on*, Vol. 15, No. 3, 2007, pp. 416-427.
- [33] Kumar, D., Ramesh, A., Babu, M. K. G., and Manivannan, P. V., "An Ionization Current based Cylinder Gas Pressure Estimation for Knock Detection and Control in a Single Cylinder SI Engine," *Technical Paper 2009-32-0118*, 2009.
- [34] Einewall, P., Tunestål, P., and Johansson, B., "The Potential of Using the Ion-Current Signal for Optimizing Engine Stability - Comparisons of Lean and EGR (Stoichiometric) Operation," *SAE Technical Paper 2003-01-0717*, 2003.
- [35] Byttner, S. and Holmberg, U., "Closed-loop control of EGR using ion currents," *Technical Committee on Modelling and Simulation, Technical Committee on*

- Control, World Modelling and Simulation Forum (WMSF) KW*, ACTA Press, 2008.
- [36] Dong , G., Yu , S., and Li , L., "Misfiring Control in Current Cycle at Engine Start Employing Ion Sensing Technology," *SAE Technical Paper 2009-01-2713*, 2009.
- [37] Panousakis , D., Gazis , A., Patterson , J., Chen , R., Turner , J., Milovanovic , N., and Blundel , D., "Using Ion-current Sensing to Interpret Gasoline HCCI Combustion Processes," *SAE Technical Paper 2006-01-0024*, 2006.
- [38] Aulin , H., Bentioulis , P., Tunest+Ñl , P., Hyv+ñnen , J., and Johansson , B., "Improving Ion Current Feedback for HCCI Engine Control," *SAE Technical Paper 2007-01-4053*, 2007.
- [39] Rivara , N., Paul, B., and Thomas, A., "Peak Pressure Position Control of Four Cylinders through the Ion Current Method," *SAE Technical Paper 2009-01-0235*, 2009.
- [40] Badawy, T., "Investigation of the ion current signal in Gen-set turbocharged diesel engine," *ETD Collection for Wayne State University, Paper AAI1482418 "Master Thesis"*, 2010.
- [41] Zhong , L., Singh , I. P., Han , J., Lai , M.-C., Henein , N. A., and Bryzik , W., "Effect of Cycle-to-Cycle Variation in the Injection Pressure in a Common Rail Diesel Injection System on Engine Performance," *SAE Technical Paper 2003-01-0699*, 2003.

- [42] Estefanous, F., "Ionization in diesel combustion: Mechanism, new instrumentation and engine applications," *Wayne State University Dissertations.Paper 272*, 2011.
- [43] Estefanous , F. and Henein , N., "Multi Sensing Fuel Injector for Electronically Controlled Diesel Engines," *SAE Technical Paper 2011-01-0936*, 2011.
- [44] Yu , X., Zha , K., Florea , R., and Jansons , M., "Comparison of In-Cylinder Soot Evolution in an Optically Accessible Engine Fueled with JP-8 and ULSD," *SAE Int.J.Fuels Lubr., Technical Paper 2012-01-1315*, Vol. 5, No. 2, 2012, pp. 875-891.
- [45] Zha, K., Florea, R. C., and Jansons, M., "Comparison of Soot Evolution Using High-Speed CMOS Color Camera and Two-Color Thermometry in an Optical Diesel Engine Fueled With B20 Biodiesel Blend and Ultra-Low Sulfur Diesel," *ASME Conference Proceedings*, Vol. 2011, No. 44427, 2011, pp. 273-294.
- [46] Yen, J. and Langari, R., *Fuzzy Logic: Intelligence, Control and Information Prentice Hall*, New Jersey, USA, 1999.
- [47] Khaled, N., *Virtual Reality and Animation for MATLAB® and Simulink® Users: Visualization of Dynamic Models and Control Simulations*, Springer 2011.
- [48] Lee, A. and Pyko, J., "Engine Misfire Detection by Ionization Current Monitoring," *SAE Technical Paper 950003*, 1995.
- [49] Chiavola, O., Chiatti, G., Arnone, L., and Manelli, S., "Combustion Characterization in Diesel Engine via Block Vibration Analysis," *SAE Technical Paper 2010-01-0168*, 2010.

- [50] Arnone, L., Boni, M., Manelli, S., Chiavola, C. S., and Recco, E., "Block Vibration Measurements for Combustion Diagnosis in Multi-Cylinder Common Rail Diesel Engine," *Technical Paper 2009-01-0646*, 2009.
- [51] Arnone, L., Manelli, S., Chiatti, G., and Chiavola, O., "In-Cylinder Pressure Analysis through Accelerometer Signal Processing for Diesel Engine Combustion Optimization," *SAE Technical Paper 2009-01-2079*, 2009.
- [52] Hariyanto, A., Bagiasna, K., Asharimurti, I., Wijaya, R. I. K., and Arismunandar, W., "Application of Wavelet Analysis to Determine the Start of Combustion of Diesel Engines," *SAE Technical Paper 2007-01-3556*, 2007.
- [53] Goldwine, G., deBotton, G., Rivin, B., and Sher, E., "Studying the Relationship between the Vibration Signature and the Combustion Process in Diesel Engines," *SAE Technical Paper 2004-01-1786*, 2004.
- [54] Anas, M., Paling, R. J., Nailon, W. H., and Cumming, D. R. S., "Real-time combustion knock processing using a single instruction multiple data automotive PowerPC system-on-a-chip," *IEEE Control Conference*, Vol. 1, 2004, pp. 1296-303.
- [55] Lujá'n, J. M., Bermu'dez, V., Guardiola, C., and Abbad, A., "A methodology for combustion detection in diesel engines through in-cylinder pressure derivative signal," *Mechanical Systems and Signal Processing*, Vol. 24, No. 7, 2010, pp. 2261-2275.
- [56] Payri, F., Broatch, A., Tormos, B., and Marant, V., "New methodology for in-cylinder pressure analysis in direct injection diesel engines - application to

- combustion noise," *Measurement Science and Technology*, Vol. 16, No. 2, 2005, pp. 540.
- [57] Broatch , A., Margot , X., Gil , A., and Donayre , J. C., "A CFD APPROACH TO DIESEL ENGINE COMBUSTION CHAMBER RESONANCE," *SAE Technical Paper 2007-24-0043*, 2007.
- [58] Millo, F. and Ferraro, C., "Knock in S.I. Engines: A Comparison between Different Techniques for Detection and Control," *SAE Technical Paper 982477*, 1998.
- [59] Mittal , V., Bridget, M., and John, B., "Phenomena that Determine Knock Onset in Spark-Ignition Engines," *SAE Technical Paper 2007-01-000*, 2007.
- [60] Elmqvist , C., Lindström , F., Hans, E., Grandin , B. r., and Kalghatgi , G., "Optimizing Engine Concepts by Using a Simple Model for Knock Prediction," *SAE Technical Paper 2003-01-3123*, 2003.
- [61] Asano , M., Ito , A., Kuma , T., Kajitani , M., Takeuchi , M., Fukumura , Y., and Izumi , M., "Further Development of an Ion Current Combustion Control System (ICCS)," *SAE Technical Paper 2001-01-0266*, 2001.
- [62] Ohashi , Y., Koiwa , M., Okamura , K., and Ueda , A., "The Application of Ionic Current Detection System for the Combustion Condition Control," *SAE Technical Paper 1999-01-0550*, 1999.
- [63] Torregrosa, A. J., Broatch, A., Margot, X., Marant, V., and Beauge, Y., "Combustion chamber resonances in direct injection automotive diesel engines: A

- numerical approach," *International Journal of Engine Research*, Vol. 5, No. 1, 2004, pp. 83-91.
- [64] Ren, Y., Randall, R. B., and Milton, B. E., "Influence of the resonant frequency on the control of knock in diesel engines," *Proceedings of the Institution of Mechanical Engineers, Part D: Journal of Automobile Engineering*, Vol. 213, No. 2, 1999, pp. 127-133.
- [65] Khaira, S. S., Singh, A., and Jansons, M., "Effect of Injection Parameters and Strategy on the Noise From a Single Cylinder Direct Injection Diesel Engine," *ASME Conference Proceedings*, Vol. 2011, No. 44427, 2011, pp. 471-480.
- [66] Baral , B. and Raine , R., "Knock in a Spark Ignition Engine Fuelled with Gasoline-Kerosene Blends," *SAE Technical Paper 2008-01-2417*, 2008.
- [67] Merkisz , J., Tomaszewski , F., Szymański , G., and Waligórski , M., "Application of the Time-Frequency Selection of the Vibration Signal for Misfire Sensing in Diesel Engines," *SAE Technical Paper 2009-01-0242*, 2009.
- [68] Jonathan, M., Saikalis , G., Oho , S., and Ka, C., "Knock Signal Analysis Using the Discrete Wavelet Transform," *SAE Technical Paper 2006-01-0226*, 2006.
- [69] Gerardin, R., Huallpa, B., Alves, M., and de França Arruda, J., "Analysis of Spark Ignition Engine Knock Signals using Fourier and Discrete Wavelet Transform," *SAE Technical Paper 2009-36-0312*, 2009.
- [70] Selim, M. Y. E., "Pressure-time characteristics in diesel engine fueled with natural gas," *Renewable Energy*, Vol. 22, No. 4, 2001, pp. 473-489.

- [71] Jose, C. and Folkerts, C., "Knock Detection and Estimation Based on Heat Release Strategies," *SAE Technical Paper 2011-01-140*, 2011.
- [72] Guzzella, L. and Onder, C., *Introduction to Modeling and Control of Internal Combustion Engine Systems* 2010.
- [73] Hickling, R., Feldmaier, D. A., Chen, F. H. K., and Morel, J. S., "Cavity resonances in engine combustion chambers and some applications," *The Journal of the Acoustical Society of America*, Vol. 73, No. 4, 1983, pp. 1170-1178.
- [74] Scholl, D., Davis, C., Russ, S., and Barash, T., "The Volume Acoustic Modes of Spark-Ignited Internal Combustion Chambers," *SAE Technical Paper 980893*, 1998.
- [75] Ajovalasit, M. and Giacomini, J., "Analysis of variations in diesel engine idle vibration," *Proceedings of the Institution of Mechanical Engineers, Part D: Journal of Automobile Engineering*, Vol. 217, No. 10, 2003, pp. 921-933.
- [76] Chen, V. and Ling, H., *Time-frequency transforms for radar imaging and signal analysis*, Artech House, Boston-London, 2002, pp. 77-79.
- [77] Henein, N. A., Singh, I. P., Zhong, L., Lai, M.-C., and Bryzik, W., "New Integrated "O.P.E.R.A.S." Strategies for Low Emissions in HSDI Diesel Engines," *SAE Technical Paper 2003-01-0261*, 2003.
- [78] Keiichi, O., Kazutoshi, M., Shiroh, S., Kiyoharu, Y., and Yusuke, M., "Effects of Multiple Injections on Diesel Emission and Combustion Characteristics," *SAE Technical Paper 2007-01-4178*, 2007.

- [79] Long, Z. and oshinori, I., "Effect of pilot injection on combustion noise and other emissions in a diesel engine," *SAE Technical Paper 1999-10-0050*, 1999.
- [80] Mallamo, F., Badami, M., and Millo, F., "Analysis of Multiple Injection Strategies for the Reduction of Emissions, Noise and BSFC of a DI CR Small Displacement Non-Road Diesel Engine," *SAE Technical Paper 2002-01-2672*, 2002.
- [81] Murari, M. R. and Hideyuki, T., "Effect of Injection Pressure and Split Injection on Exhaust Odor and Engine Noise in DI Diesel Engines," *SAE Technical Paper 2002-01-2874*, 2002.
- [82] Sylvain, M. and Benoist, T., "Using Multiple Injection Strategies in Diesel Combustion: Potential to Improve Emissions, Noise and Fuel Economy Trade-Off in Low CR Engines," *SAE technical Paper 2008-01-1329*, 2008.
- [83] Wang, P., Song, D., Zhou, H., MA, X., and GE, Y., "Effect of Combustion Process on DI Diesel Engine Combustion Noise," *SAE Technical Paper 2007-01-2076*, 2007.
- [84] Zhang, L., "A Study of Pilot Injection in a DI Diesel Engine," *SAE Technical Paper 1999-01-3493*, 1999.
- [85] Bertola , A., Schubiger , R., Kasper , A., Matter , U., Anna, M., Mohr , M., Boulouchos , K., and Lutz , T., "Characterization of Diesel Particulate Emissions in Heavy-Duty DI-Diesel Engines with Common Rail Fuel Injection Influence of Injection Parameters and Fuel Composition," *SAE Technical Paper 2001-01-3573*, 2001.

- [86] Matsumoto , T., Hori , M., Nakane , T., Horiuchi , M., Pfeifer , M., Spurk , P., Gieshoff , J., van, S., Lox , E., Garr , G., and Crocker , M., "Advanced Emission Control Technologies for PM Reduction in Heavy-Duty Applications," *SAE Technical Paper 2003-01-1862*, 2003.
- [87] Kitamura , Y., Mohammadi , A., Ishiyama , T., and Shioji , M., "Fundamental Investigation of NO_x Formation in Diesel Combustion Under Supercharged and EGR Conditions," *SAE Technical Paper 2005-01-0364*, 2005.
- [88] Fischer , S. and Jens, O., "Investigation on the Effect of Very High Fuel Injection Pressure on Soot-NO_x Emissions at High Load in a Passenger Car Diesel Engine," *SAE Int.J.Engines, Technical Paper 2009-01-1930*, Vol. 2, No. 1, 2009, pp. 1737-1748.
- [89] Jong, H., Soon, H., Kwang, M., and Kyo, S., "Comparison of NO_x Level and BSFC for HPL EGR and LPL EGR System of Heavy-Duty Diesel Engine," *SAE Technical Paper 2007-01-3451*, 2007.
- [90] Cai , W. and Ma , L., "Numerical Investigation of an Optical Soot Sensor for Modern Diesel Engines," 2009.
- [91] Morgan , R. E., Gold , M. R., Laguitton , O., Crua , C., and Heikal , M. R., "Characterisation of the Soot Formation Processes in a High Pressure Combusting Diesel Fuel Spray," 2003.
- [92] Merkel , S., Eckert , P., Wagner , U., Velji , A., and Spicher , U., "Investigation of a New Injection Strategy for Simultaneous Soot and NO_x Reduction in a Diesel

- Engine with Direct Injection," *SAE Int.J.Fuels Lubr.*, Vol. 1, No. 1, 2008, pp. 1433-1442.
- [93] Bobba , M., Musculus , M., and Neel , W., "Effect of Post Injections on In-Cylinder and Exhaust Soot for Low-Temperature Combustion in a Heavy-Duty Diesel Engine," *SAE Int.J.Engines*, Vol. 3, No. 1, 2010, pp. 496-516.
- [94] Higashi, M., Uchida, S., Suzuki, N., and Fujii, K., "Soot elimination and NO_x and SO_x reduction in diesel-engine exhaust by a combination of discharge plasma and oil dynamics," *Plasma Science, IEEE Transactions on*, Vol. 20, No. 1, 1992, pp. 1-12.
- [95] Wagner , U., Merkel , S., Eckert , P., and Spicher , U., "Comparative Study to Assess the Soot Reduction Potential of Different In-Cylinder Methods and Exhaust Gas Aftertreatment Systems for Direct Injection Diesel Engines," *SAE Technical Paper 2007-01-4016*, 2007.
- [96] Ishizawa , T., Yamane , H., Sato , H., Sekiguchi , K., Watanabe , K., and Ohtsubo , Y., "IP Filter with DOC-Integrated DPF for an Advanced PM Aftertreatment System (1): A Preliminary Evaluation," *SAE Technical Paper 2007-01-0924*, 2007.
- [97] Singer , W., Schindler , W., and Friedl , H., "High Sensitive Smoke Measurement for Dynamic Engine Tests," *SAE Technical Paper 1999-01-3077*, 1999.
- [98] Scott, A., Christopher, A., Jay, S., Lundberg , C., Silvis , W., and Pankratz , H., "Measurement of Dry Soot and Particulate Matter from Two-Stroke and Four-Stroke Snowmobiles," *SAE Technical Paper 2010-32-0042*, 2010.

- [99] Li , W., John, F., Joseph, M., David, R., and Sawant , A., "Assessment of Particulate Matter Emissions from a Sample of In-Use ULEV and SULEV Vehicles," *SAE Technical Paper 2006-01-1076*, 2006.
- [100] Inagaki , K., Takasu , S., and Nakakita , K., "In-cylinder Quantitative Soot Concentration Measurement By Laser-Induced Incandescence," *SAE Technical Paper 1999-01-0508*, 1999.
- [101] Schraml , S., Heimgärtner , C., Will , S., Leipertz , A., and Hemm , A., "Application of a New Soot Sensor for Exhaust Emission Control Based on Time Resolved Laser Induced Incandescence (TIRE-LII)," *SAE Technical Paper 2000-01-2864*, 2000.
- [102] Zhao, H. and Ladommatos, N., "Optical diagnostics for soot and temperature measurement in diesel engines," *Progress in Energy and Combustion Science*, Vol. 24, No. 3, 1998, pp. 221-255.
- [103] Kawano , D., Kawai , T., Naito , H., Goto , Y., Odaka , M., and William, D., "Comparative Measurement of Nano-Particulates in Diesel Engine Exhaust Gas by Laser-Induced Incandescence (LII) and Scanning Mobility Particle Sizer (SMPS)," *SAE Technical Paper 2004-01-1982*, 2004.
- [104] Johnson , T., Caldow , R., Pöschel , A., Mirme , A., and Kittelson , D., "A New Electrical Mobility Particle Sizer Spectrometer for Engine Exhaust Particle Measurements," *SAE Technical Paper 2004-01-1341*, 2004.

- [105] Gerald, Z., Edward, M., Caldow , R., and Timothy, R., "Transient Performance of Diesel Particulate Filters as Measured by an Engine Exhaust Particle Size Spectrometer," *SAE Technical Paper 2005-01-0185*, 2005.
- [106] Reavell , K., Hands , T., and Collings , N., "A Fast Response Particulate Spectrometer for Combustion Aerosols," *SAE Technical Paper 2002-01-2714*, 2002.
- [107] Warey , A., Hendrix , B., Hall , M., and Nevius , T., "A New Sensor for On-Board Detection of Particulate Carbon Mass Emissions from Engines," *SAE Technical Paper 2004-01-2906*, 2004.
- [108] Warey , A. and Matthew, J., "Performance Characteristics of a New On-Board Engine Exhaust Particulate Matter Sensor," *SAE Technical Paper 2005 - 01-3792*, 2005.
- [109] Ochs , T., Schittenhelm , H., Genssle , A., and Kamp , B., "Particulate Matter Sensor for On Board Diagnostics (OBD) of Diesel Particulate Filters (DPF)," *SAE Int.J.Fuels Lubr.*, Vol. 3, No. 1, 2010, pp. 61-69.
- [110] Kondo , A., Yokoi , S., Sakurai , T., Nishikawa , S., Egami , T., Tokuda , M., and Sakuma , T., "New Particulate Matter Sensor for On Board Diagnosis," *SAE Int.J.Engines*, Vol. 4, No. 1, 2011, pp. 117-125.
- [111] Allan , W. D. E., Freeman , R. D., Pucher , G. R., Faux , D., Bardon , M. F., and Gardiner , D. P., "Development of a Smoke Sensor for Diesel Engines," *SAE Technical Paper 1999-01-0856*, 2003.

- [112] Lee, J. H., Schmieg, S. J., and Oh, S. H., "Improved NO_x reduction over the staged Ag/Al₂O₃ catalyst system," *Applied Catalysis A: General*, Vol. 342, No. 1GÇô2, 2008, pp. 78-86.
- [113] Nuccio, P. and Bertone, M., "Reduction in Pollutant Emissions in an "Off-Road" DI Diesel Engine by Means of Exhaust Gas Recirculation," *SAE Technical Paper 2011-32-0610*, 2011.
- [114] Prabhakar, S., Karthikeyan, M., Annamalai, K., and Banugopan, V. N., "Control of emission characteristics by using Selective Catalytic Reduction (SCR) in D.I. diesel engine," *Frontiers in Automobile and Mechanical Engineering (FAME)*, 2010, 2010, pp. 104-107.
- [115] Chen, S. K., "Simultaneous Reduction of NO_x and Particulate Emissions by Using Multiple Injections in a Small Diesel Engine," *SAE Technical Paper 2000-01-3084*, 2000.
- [116] Rajkumar, S., Pramod, S., and Bakshi, S., "Parametric Investigation for NO_x and Soot Emissions in Multiple-injection CRDI Engine using Phenomenological Model," *SAE Technical Paper 2011-01-1810*, 2011.
- [117] Benajes, J., Payri, R., Molina, S., and Soare, V., "Investigation of the Influence of Injection Rate Shaping on the Spray Characteristics in a Diesel Common Rail System Equipped with a Piston Amplifier," *Journal of Fluids Engineering*, Vol. 127, No. 6, 2005, pp. 1102-1110.
- [118] Ghaffarpour, M. and Baranescu, R., "NO_x Reduction Using Injection Rate Shaping and Intercooling in Diesel Engines," *SAE Technical Paper 960845*, 1996.

- [119] Wallace, I. G. and Powell, R. J., "The application of a chemiluminescence NO_x analyser to stability and compatibility testing," *Journal of Hazardous Materials*, Vol. 5, No. 4, 1982, pp. 373-386.
- [120] Mark, S., Finch, A., and Campbell, B., "Analysis of Transient HC, CO, NO_x and CO₂ Emissions from a GDI Engine using Fast Response Gas Analyzers," *SAE Int.J.Engines*, Vol. 4, No. 1, 2011, pp. 1513-1522.
- [121] Hagen, J. R., Assanis, D. N., and Filipi, Z. S., "Cycle-resolved measurements of in-cylinder constituents during diesel engine transients and insight into their impact on emissions," *Proceedings of the Institution of Mechanical Engineers, Part D: Journal of Automobile Engineering*, Vol. 225, No. 9, 2011, pp. 1103-1117.
- [122] Zhuiykov, S., Ono, T., Yamazoe, N., and Miura, N., "High-temperature NO_x sensors using zirconia solid electrolyte and zinc-family oxide sensing electrode," *Solid State Ionics*, Vol. 152/153, No. 0, 2002, pp. 801-807.
- [123] Shimizu, Y. and Maeda, K., "Solid electrolyte NO_x sensor using pyrochlore-type oxide electrode," *Sensors and Actuators B: Chemical*, Vol. 52, No. 1/2, 1998, pp. 84-89.
- [124] Hibino, T., Ushiki, K., and Kuwahara, Y., "Electrochemical oxygen pump using CeO₂-based solid electrolyte for NO_x detection independent of O₂ concentration," *Solid State Ionics*, Vol. 93, No. 3/4, 1997, pp. 309-314.
- [125] Montgomery, D. C., Peck, E. A., and Vining, G. G., *Introduction to Linear Regression Analysis*, 4th ed. 2011.

- [126] Pinheiro, J. C. and Bates, D. M., *Mixed-Effects Models in S and S-PLUS*, Springer, New York, 2000.
- [127] Gallant, A. R., *Nonlinear Regression*, The American Statistician 29 ed. 1975, pp. 73-81.
- [128] Gallant, A. R., *Nonlinear Statistical Models*, Wiley, New York, 1987.
- [129] Bostic, D. R., Watson, D. G., and Harrison, T. V., "Modeling NO Emissions of an Off-Road Diesel Engine Based on Emission Tests," *Agricultural Engineering International: The CIGRE Journal*, Vol. XI, 2009.
- [130] Heywood, J., *Internal Combustion Engine Fundamentals*, McGraw-Hills and Hall, London, 1988.
- [131] Rakopoulos , C. D., Giakoumis , E. G., Hountalas , D. T., and Rakopoulos , D. C., "The Effect of Various Dynamic, Thermodynamic and Design Parameters on the Performance of a Turbocharged Diesel Engine Operating under Transient Load Conditions," *SAE Technical Paper 2004-01-0926*, 2004.
- [132] Monica, A. C., Ehleskog , M., Gjirja , S., and Denbratt , I., "Effects of Varying Engine Settings on Combustion Parameters, Emissions, Soot and Temperature Distributions in Low Temperature Combustion of Fischer-Tropsch and Swedish Diesel Fuels," *SAE Technical Paper 2009-01-2787*, 2009.
- [133] Buom, S. and Jung, H., "The Effects of Injection Parameters on a Heavy-Duty Diesel Engine with TICS System," *SAE Technical Paper 981070*, 1998.

- [134] Lapuerta , M. n., Armas , O., and Juan, J., "Effect of the Injection Parameters of a Common Rail Injection System on Diesel Combustion Through Thermodynamic Diagnosis," *SAE Technical Paper 1999-01-0194*, 1999.
- [135] Mito , Y., Tanaka , D., Seang, W., Daisho , Y., and Kusaka , J., "The Effect of Intake, Injection Parameters and Fuel Properties on Diesel Combustion and Emissions," *SAE Technical Paper 2003-01-1793*, 2003.
- [136] Badawy, T., Shrestha, A., and Henein, N., "Detection of combustion resonance using an ion current sensor in diesel engines," *Technical Paper ICEF2011-60068*, 2011.
- [137] Calcote, H. F., "Ion production and recombination in flames," *Symposium (International) on Combustion*, Vol. 8, No. 1, 1961, pp. 184-199.
- [138] H.F., C., *9th International Symposium on Combustion*, New York, 1963, pp. 662.
- [139] Calcote, H. F., "Mechanisms for the formation of ions in flames," *Combustion and Flame*, Vol. 1, No. 4, 1957, pp. 385-403.
- [140] Nicholson, A. J. C. and Swingler, D. L., "Ion formation in the flame ionization detector," *Combustion and Flame*, Vol. 39, No. 1, 1980, pp. 43-52.
- [141] Hayhurst, A. N. and Kittelson, D. B., "The positive and negative ions in oxy-acetylene flames," *Combustion and Flame*, Vol. 31, No. 0, 1978, pp. 37-51.
- [142] T.M., S., "A Survey of Flame Ionization Work at the University of Cambridge," *Paper presented at the ARS Conference*, 1962.
- [143] A.B., F., "Investigations on ions in flames," *Progress in Energy and Combustion Science* 23, 1997, pp. 399-528.

- [144] Calcote, H. F., Olson, D. B., and Keil, D. G., "ARE IONS IMPORTANT IN SOOT FORMATION?," Vol. 32, 1987, pp. 524-533.
- [145] Calcote, H. F., "IONIC MECHANISMS OF SOOT FORMATION," Vol. 7, 1983, pp. 197-215.
- [146] Olson, D. B. and Calcote, H. F., "Ions in fuel-rich and sooting acetylene and benzene flames," *Symposium (International) on Combustion*, Vol. 18, No. 1, 1981, pp. 453-464.
- [147] Hall-Roberts, V. J., Hayhurst, A. N., Knight, D. E., and Taylor, S. G., "The origin of soot in flames: is the nucleus an ion?," *Combustion and Flame*, Vol. 120, No. 4, 2000, pp. 578-584.
- [148] Calcote, H. F., "Comments on the origin of soot in flames: is the nucleus an ion? by V. J. Hall-Roberts, A. N. Hayhurst, D. E. Knight, and S. G. Taylor," *Combustion and Flame*, Vol. 126, No. 12, 2001, pp. 1607-1610.
- [149] Saitzkoff, A., Reinmann, R., Mauss, F., and Glavmo, M., "In-Cylinder Pressure Measurements Using the Spark Plug as an Ionization Sensor," *SAE Technical Paper 970857*, 1997.
- [150] Mehresh, P., Souder, J., Flowers, D., Riedel, U., and Dibble, R. W., "Combustion timing in HCCI engines determined by ion-sensor: experimental and kinetic modeling," *Proceedings of the Combustion Institute*, Vol. 30, No. 2, 2005, pp. 2701-2709.

- [151] Patel , A., Song, C., and Rolf, D., "Development and Validation of a Reduced Reaction Mechanism for HCCI Engine Simulations," *SAE Technical Paper 2004-01-0558*, 2004.
- [152] Calcote, H. F. and Keil, D. G., "Ion-molecule reactions in sooting acetylene+oxygen flames," *Combustion and Flame*, Vol. 74, No. 2, 1988, pp. 131-146.
- [153] H.F., C. and D.G., K., "The role of ions in soot formation," *Pure Appl.Chem.*, Vol. 62, No. 5, 1990, pp. 815-824.
- [154] Egsgaard, H., "Investigation of the initial reactions of the Calcote mechanism for soot formation," *Journal of The American Society for Mass Spectrometry*, Vol. 7, No. 6, 1996, pp. 559-564.
- [155] Walsh, K. T., Long, M. B., Tanoff, M. A., and Smooke, M. D., "Experimental and computational study of CH, CH*, and OH* in an axisymmetric laminar diffusion flame," *Symposium (International) on Combustion*, Vol. 27, No. 1, 1998, pp. 615-623.
- [156] Henein, N. A., "Analysis of Pollutant Formation and Control and Fuel Economy in Diesel Engines," *Prog.EnergyCombust.Sci.(1)*, 1976, pp. 165-207.

ABSTRACT**IONIZATION IN DIESEL COMBUSTION FOR ON-BOARD
DIAGNOSTICS AND ENGINE CONTROL**

by

TAMER H. BADAUWY

May 2013

Advisor: Prof. Naeim Henein**Major:** Mechanical Engineering**Degree:** Doctor of Philosophy

Diesel engines have been known for their high thermal efficiency and specific power output, but there is concern about engine-out NO_x and particulate matter emissions. To meet the current emission standards, advanced diesel engines are fitted with electronically controlled fuel injection systems and sophisticated and expensive after-treatment devices. Further improvements are still needed to meet future goals in better fuel economy and the more stringent emission standards. In order to meet these goals, there is a need for the control of the combustion process to reduce engine-out emissions in real-time and reduce the demand on the after-treatment devices. This requires a signal indicative of the in-cylinder conditions to be fed in the ECU (Engine Control Unit). The most promising sensors in internal combustion engines are the cylinder gas pressure transducer and the combustion produced ion current sensor. Ion current probes have many advantages over pressure transducers because they are less

expensive, more rugged, and are sensitive to the in cylinder gas temperature, and the composition of the combustion products.

The ion current technique has been used in some SI engines, based on an understanding of the ionization produced from the combustion of a homogeneous charge. This is not the case in diesel engines where different types of flames are produced from the combustion of the heterogeneous mixture. This study investigates in details the characteristics of the ion current signal in diesel engines and its use for combustion diagnostics and feedback control of the engine. Experimental investigations and CFD simulation models are used to understand the characteristics of the ion current signal under different operating conditions. The investigations proved that the ion current signal carry basic information about combustion. 3-D mathematical models developed gave more insight into the distribution of the ionized species in the combustion chamber and enhanced the development of feedback control of the combustion process and enable the engine to autonomously operate properly on fuels of a wide range of physical and chemical properties. In addition, algorithms have been developed to use the signal for on-board diagnostics of different combustion, performance and engine-out emissions parameters.

AUTOBIOGRAPHICAL STATEMENT

I was born in Milan, Italy on Dec. 23rd,1984. I completed my high school from Toukh secondary school in Egypt. I had been dreaming to become an engineer, Therefore; I started my studies to pursue an engineering degree from Shoubra Faculty of Engineering in Cairo, Egypt. After the first year, it was clear to me that mechanical engineers are the pillar of engineering. One of the interesting fields that always attracted me was automotive industry. I joined thermal combustion group, where I gained experience in engine testing and instrumental setup for test cells. I worked for one year under supervision of Dr. Ahmed Abdel Rehim. After I completed my Bachelor degree in May 2006, I joined “Wayne State University”, Detroit to pursue Ph.D. in mechanical engineering. I was thrilled when I got an opportunity to work as GRA (Graduate Research Assistant) under the guidance of Prof. Naeim Henein at the Center of Automotive Research since September 2007. I was assigned to a new project where engine setup and instrumentation were part of my job. I was able to conduct extensive research on single cylinder diesel engine as well as multi-cylinder Gen-set diesel engine for the investigation of the characteristics of the ion current signal. I believe that when a man's curiosity is keyed up, it will keep him eager to know more and more for the rest of his life.